

Sheffield Hallam University

Metal-aluminium gallium nitride Schottky contacts formation.

BOUDJELIDA, Boumedienne.

Available from the Sheffield Hallam University Research Archive (SHURA) at:

<http://shura.shu.ac.uk/19373/>

A Sheffield Hallam University thesis

This thesis is protected by copyright which belongs to the author.

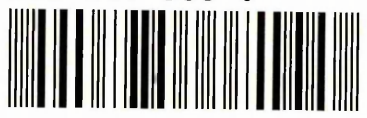
The content must not be changed in any way or sold commercially in any format or medium without the formal permission of the author.

When referring to this work, full bibliographic details including the author, title, awarding institution and date of the thesis must be given.

Please visit <http://shura.shu.ac.uk/19373/> and <http://shura.shu.ac.uk/information.html> for further details about copyright and re-use permissions.

Sheffield Centre City Campus
Sheffield S1 1WB

101 857 355 0



REFERENCE

10 of issue
10

ProQuest Number: 10694254

All rights reserved

INFORMATION TO ALL USERS

The quality of this reproduction is dependent upon the quality of the copy submitted.

In the unlikely event that the author did not send a complete manuscript and there are missing pages, these will be noted. Also, if material had to be removed, a note will indicate the deletion.



ProQuest 10694254

Published by ProQuest LLC (2017). Copyright of the Dissertation is held by the Author.

All rights reserved.

This work is protected against unauthorized copying under Title 17, United States Code
Microform Edition © ProQuest LLC.

ProQuest LLC.
789 East Eisenhower Parkway
P.O. Box 1346
Ann Arbor, MI 48106 – 1346

Metal - Aluminium Gallium Nitride Schottky Contacts Formation

Boumedienne BOUDJELIDA

A thesis submitted in partial fulfilment of the requirements of
Sheffield Hallam University
for the degree of Doctor of Philosophy

August 2006

Abstract

X-ray photoelectron spectroscopy (XPS) has been used to investigate the effect of various surface cleaning procedures on $\text{Al}_x\text{Ga}_{1-x}\text{N}$ surfaces for $x = 0.20$ and 0.30 . Results show that wet chemical etch in a HF solution followed by a 600°C *in-situ* annealing under ultra-high vacuum (UHV) is very effective in removing oxygen from the surface. Downward band bending of 0.87 eV and 0.99 eV also occurs between the solvents-treated and the annealed $\text{Al}_x\text{Ga}_{1-x}\text{N}$ surfaces for $x = 0.20$ and 0.30 , respectively.

Increasing *in-situ* temperature annealing in increments of 100°C up to 600°C shows a re-ordering at the surface and subsurface with Ga and Al moving deeper in the surface, whereas N goes to the topsurface. In addition, the Fermi level movement observed when increasing the temperature could be interpreted by the change in surface stoichiometry or by a creation of vacancies due to the *ex-situ* surface treatment which may, in turn, be activated/deactivated by temperature annealing. Atomic hydrogen clean (AHC) followed by 400°C *in-situ* UHV annealing is also found effective in removing O and C from $\text{Al}_x\text{Ga}_{1-x}\text{N}$ surface ($x = 0.20$).

The formation of Ag/ $\text{Al}_x\text{Ga}_{1-x}\text{N}$ ($x = 0.20$) and Ni/ $\text{Al}_x\text{Ga}_{1-x}\text{N}$ ($x = 0.30$) interfaces, where the substrate was subjected to HF etch followed by 600°C *in-situ* UHV anneal, has been studied by a combination of XPS, atomic force microscope (AFM), scanning tunneling microscope (STM) and current-voltage (I-V) measurements.

XPS results suggest a layer-by-layer followed by islanding growth mode of Ag and Ni on $\text{Al}_x\text{Ga}_{1-x}\text{N}$. This is confirmed by the presence of metal islands at the metal-covered surfaces using AFM and *in-situ* STM. XPS investigation shows a more abrupt, well-defined Ag/ $\text{Al}_x\text{Ga}_{1-x}\text{N}$ interface compared to Ni/ $\text{Al}_x\text{Ga}_{1-x}\text{N}$. Ag deposition on $\text{Al}_x\text{Ga}_{1-x}\text{N}$ substrates causes upward band bending of 0.30 eV and 0.40 eV between the "clean" surface and the last metal deposition, for $x = 0.20$ and 0.30 , respectively, while Ni induces downward band bending of 0.3 eV for $x = 0.20$. I-V measurements of Ag/ $\text{Al}_x\text{Ga}_{1-x}\text{N}$ ($x = 0.30$), where the substrate was cleaned using N^+ bombardment followed by 600°C annealing, yield a Schottky barrier height of 0.82 eV with ideality factor $n = 1.21$.

XPS and I-V results on Ag/ $\text{Al}_x\text{Ga}_{1-x}\text{N}$ and Ni/ $\text{Al}_x\text{Ga}_{1-x}\text{N}$ are compared and discussed in terms of current models of Schottky barrier formation.

Publications

1. **B. Boudjelida**, M.C. Simmonds, I. Gee, S.A. Clark, "The influence of chemical treatment and thermal annealing on $\text{Al}_x\text{Ga}_{1-x}\text{N}$ surfaces: an XPS study", *Appl. Surf. Science*, **252**(14), 5189-5196, (2006).
2. **B. Boudjelida**, I. Gee, J. Evans-Freeman, S.A. Clark, M. Azize, J.-M. Bethoux, P. De Mierry, "Structural and electrical characteristics of $\text{Ag}/\text{Al}_{0.2}\text{Ga}_{0.8}\text{N}$ and $\text{Ag}/\text{Al}_{0.3}\text{Ga}_{0.7}\text{N}$ Schottky contacts: an XPS study", *Phys. Stat. Solidi (c)* **3**(6), 1824-1827, (2006).
3. **B. Boudjelida**, I. Gee, J. Evans-Freeman, M. Gad, S.A. Clark, T.G.G.. Maffei, V. Teng, M. Azize, J.-M. Bethoux, P. De Mierry, "The formation of Ag and Ni Schottky contacts to $\text{Al}_x\text{Ga}_{1-x}\text{N}$ ", in preparation.

Acknowledgements

I would like to thank all the people who have interacted with this research work, especially my supervisors: Dr. Mike Simmonds who was my supervisor during the first year of this project, Dr. Simon Clark who has always provided me with helpful guidance and Prof. Jan Evans-Freeman for her support at the Materials and Engineering Research Institute (MERI). I am grateful to Dr. Ian Gee for his kind support with XPS at Sheffield Hallam University and NCESS at Daresbury. Thanks to Dr. Gad for his valuable help on electrical measurements at MERI, P. Haines for diode processing at Sheffield University.

I would like to express my gratitude to Dr. T.G.G. Maffei and Dr. V. Teng at the Semiconductor Interface Lab at Swansea University for their technical help and support, but also for valuable discussions.

I would also like to thank Dr. P.J. Parbrook at Sheffield University and the CNRS-CRHEA Nice Sophia Antipolis (Dr. J.-M. Bethoux, Dr. M. Azize, Dr. P. De Mierry and Dr. P. Vennegues) for kindly providing the valuable samples and for helpful discussions.

Special thanks go to my family members, especially Imen, for their moral support.

Contents

Abstract	i
Publications	ii
Acknowledgements	iii
Contents	iv
Chapter 1: Introduction	1
References	7
Chapter 2: Literature review	8
2.1. Al_xGa_{1-x}N Properties	9
2.1.1. Growth techniques	9
2.1.2. Importance of the substrate	11
2.1.3. Properties of the materials	13
2.2. Metal-Al_xGa_{1-x}N contacts	15
2.2.1. Introduction	15
2.2.2. Ohmic contacts to Al _x Ga _{1-x} N	16
2.2.3. Schottky contacts to Al _x Ga _{1-x} N	20
a) Cleaning the surface	20
b) Metal- Al _x Ga _{1-x} N contacts	23
2.3. Summary	27
References	28
Chapter 3: Theory of Metal-Semiconductor Contacts	32
3.1. Introduction	32
3.2. Models of Schottky barrier formation	33
3.2.1. Schottky-Mott model	33
3.2.2. Origin of surface states	36
3.2.3. Bardeen Model	36
3.2.4. Unified Defect Model (UDM)	38
3.2.5. Metal Induced Gap States (MIGS)	38
3.2.6. Electronegativity	40
3.2.7. MIGS-and-electronegativity model	42
3.2.8. Effective work function model	43

3.2.9. Cowley-Sze model	44
3.2.10. Intimate contacts	44
3.3. Current transport mechanisms	45
3.4.1. Thermionic emission	46
3.4.2. Quantum mechanical tunneling	47
3.4.3. Recombination current	49
3.4. Extraction of the Schottky parameters	50
3.4.1. Current-voltage measurement	50
3.4.2. X-ray Photoelectron Spectroscopy (XPS)	52
References	55
Chapter 4: Experimental Techniques	56
4.1. Principles	57
4.2. Photoemission process	59
4.3. Surface sensitivity	62
4.3.1. Inelastic mean free path (IMFP)	62
4.3.2. Escape depth and surface sensitivity	64
4.3.3. Photo-ionisation cross-section	65
4.4. Spectrum features	65
4.4.1. Auger peaks	66
4.4.2. X-ray satellites and ghosts	67
4.4.3. Core-level data analysis	68
4.4.3.1. Broadening effects	68
4.4.3.2. Spin-orbit splitting	69
4.4.3.3. Chemical shifts	70
4.4.3.4. Fermi shifts	71
4.4.3.5. Asymmetric metal core-levels	72
4.4.3.6. Core-level intensities	72
4.4.3.7. Curve-fitting	74
4.4.3.8. Charging	75
4.5. XPS at Materials and Engineering Research Institute	77
4.5.1. Experimental set-up	77
4.5.2. Electron energy analyser	80

4.6. XPS at Swansea University	82
4.7. High resolution XPS at Daresbury Laboratory	83
4.8. Scanning Probe Microscopy	85
4.8.1. Atomic force microscope (AFM)	85
4.8.2. Scanning Tunnelling Microscope (STM)	86
4.9. I-V measurement	88
References	89
Chapter 5: Cleaning of Al_xGa_{1-x}N	90
5.1. Introduction	90
5.2. Solvents cleaning and wet chemical etch	92
5.3. <i>In-situ</i> UHV annealing	96
5.4. Ion bombardment and annealing (IBA)	106
5.4.1. Atomic H sputtering	106
5.5. Summary	109
References	110
Chapter 6: Metal - Al_xGa_{1-x}N Schottky contacts	112
6.1. Introduction	112
6.2. Experimental details	114
6.2.1. Ag/ Al _x Ga _{1-x} N contact formation	114
6.2.2. Ni/Al _{0.2} Ga _{0.8} N contact formation	114
6.2.3. Electrical measurements	116
6.3. Ag - Al_xGa_{1-x}N contacts	117
6.3.1. Core-level intensity	117
a) Ag deposition on Al _{0.2} Ga _{0.8} N surfaces	117
b) Ag deposition on Al _{0.3} Ga _{0.7} N surfaces	121
6.3.2. Core-level binding energy	124
a) Ag deposition on Al _{0.2} Ga _{0.8} N surfaces	124
b) Ag deposition on Al _{0.3} Ga _{0.7} N surfaces	129
6.3.3. AFM results	134
6.3.4. Electrical characterisation	136

6.4. Ni - Al_{0.2}Ga_{0.8}N contacts	140
6.4.1. Core-level intensity	140
6.4.2. Core-level binding energy	142
6.4.3. STM results	148
6.5. Discussion	150
6.5.1. Ag/Al _x Ga _{1-x} N interface formation	150
6.5.2. Ni/Al _x Ga _{1-x} N interface formation	153
6.5.3. Metal- Al _x Ga _{1-x} N Schottky barrier formation	154
6.5.4. Conclusions	161
References	164
Chapter 7: Conclusion and future work	166
References	170

Chapter 1

Introduction

Semiconductor devices can be found everywhere in most modern societies, from personal computers to mobile phones, to laser-related technology such as CD/DVD players, storage systems, medicine, etc... Semiconductor properties and related devices have been studied for over a century. The first study of metal-semiconductor contacts was carried out by Braun¹ in 1874 who discovered the rectifying properties of such interfaces. Later, in 1947, Bardeen and Brattain invented the first transistor², known as the point-contact transistor, by using the properties of gold contacts to Germanium. This invention was considered as a major advance in semiconductor technology and has stimulated considerable progress in semiconductor research since then. In 1960, Kahng and Atalla³ demonstrated the first metal-oxide-semiconductor-field-effect-transistor (MOSFET). This device is still playing a major role in modern microelectronics industry, such as integrated circuits.

Various semiconductor substrate materials have been studied for potential applications in devices but Silicon has been and is still the most commonly used

substrate in semiconductor industry. The semiconducting properties of III-V materials were pointed out with a study of Gallium Arsenide and its related compounds⁴ in 1952. These materials have attracted a lot of interest for potential use in optoelectronic devices. The As-based and P-based ability of tuning the bandgap by selecting the appropriate alloy material has been successful in applications such as light emitting diodes (LED) and laser diodes (LD). However, the wavelengths covered by these materials do not allow potential applications over the full visible spectrum, and only range from infra red to yellow, as shown in figure 1-1. Therefore, wider bandgaps are needed in order to achieve the full range of visible colours.

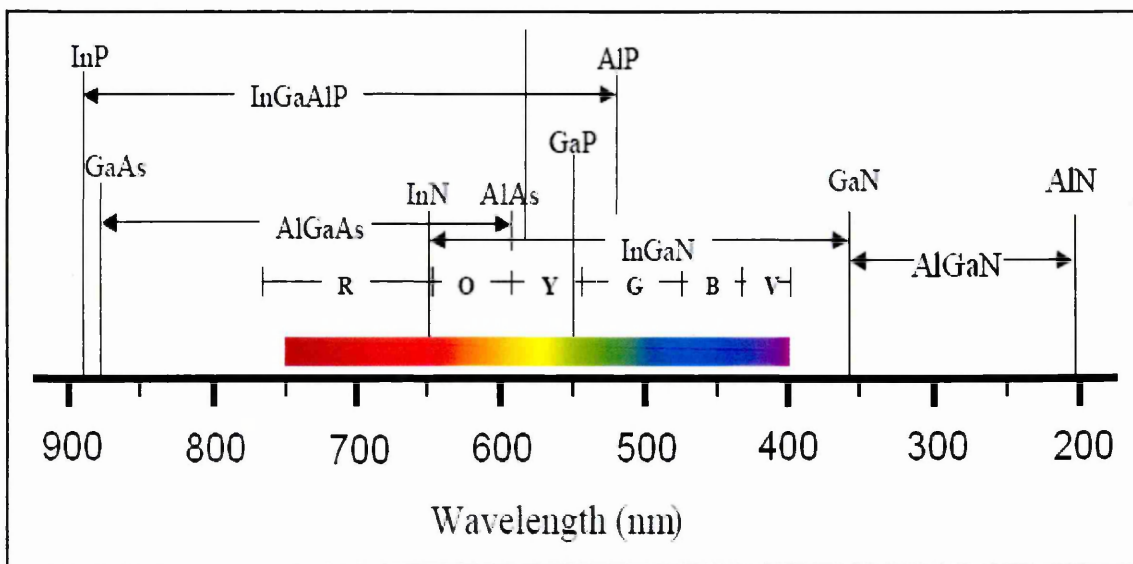


Figure 1-1: III-V substrate materials and related alloys used for potential use in optoelectronic devices over the spectrum of light (from ref. [5]).

III-V nitrides such as InN, GaN and AlN have been considered as promising materials for potential use in optoelectronic devices, mainly because of their wide direct bandgaps ranging from 1.9 eV for InN, to 3.4 eV for GaN, to 6.2 eV for AlN. However, these materials have mostly presented two problems to researchers. It has been found difficult to grow high-quality materials because of the lack of lattice match substrates, and all nitrides have had high n-type background carrier concentration. Therefore, even when reasonable material quality was achieved, p-type doping could not be successful. There was considerable interest in these materials⁶ (mainly GaN) in the 70's but efforts

to make the materials p-type failed and the research activity in the field therefore lightened.

In 1986, Amano *et al.*⁷ significantly improved the GaN surface quality by deposition of a thin low-temperature AlN buffer layer prior to the high temperature growth of GaN. Three years later, the same authors developed a technique that converts Mg acceptors in GaN into p-type material with the use of energy beam irradiation⁸. Later, Nakamura *et al.*⁹ pointed out a procedure to produce low-Ohmic p-type GaN by annealing in N₂, and soon after demonstrated the first high luminescence blue LED¹⁰ using nitrides. Both blue GaN-based LED and LD are now available commercially¹¹.

Most semiconductor devices are optimized by heterojunctions which are commonly achieved through the use of alloys¹². Al_xGa_{1-x}N has received special attention because of the wide range of applications potentially possible for AlGa_xN/GaN heterostructure devices, with the possibility of tuning Al_xGa_{1-x}N bandgap by changing the Al content x.

These semiconductors are suitable for device applications in optical devices such as violet laser, LEDs with colours ranging from red to UV, white LEDs, photodetectors, UV cameras, to high-frequency power devices such as High Electron Mobility Transistors (HEMTs)¹³. Lasers can be widely used for lighting applications and displays as well as for storage and retrieval of digital information. For example¹⁴, it is predicted that the use of nitride-based lasers will increase the data storage density of DVDs by a factor of 40. Moreover, these materials and their alloys have many valuable key properties for device fabrication and processing:

- Their wide bandgap nature enables high temperature applications because they become intrinsic at much higher temperature than other materials used (Ge, Si, GaAs...). They would require less cooling to operate, which would lead to less device processing and lower cost.
- Such materials have high breakdown field (> 4MV/cm for GaN) which makes the fabrication of high voltage devices easier as they will not need a high doping concentration and semiconductor thickness⁵.

The high thermal conductivity and chemical stability of such semiconductors make heterostructures based on these materials very attractive for high power, high frequency and high temperature devices.

However, it is important to note the central role of metal-semiconductor contacts in such devices. Ohmic contacts are essential for the connection between devices and the outside world. Such contacts should have low contact resistance while Schottky contacts should exhibit little or no reverse current with electron transport mechanism being dominated by thermionic emission. The fact that devices are expected to operate at high temperature also means that the thermal stability of metal contacts should be ensured. Schottky contacts to $\text{Al}_x\text{Ga}_{1-x}\text{N}$ are mainly used on UV detection devices¹⁵ and HEMTs¹⁶. The precise mechanisms of electron transport across such interfaces and the possible chemical reaction between the metal and semiconductor need be understood in order to exploit the full potential of GaN-based devices.

The properties of the surface may differ from those in the bulk and it strongly depends on the cleanliness of the surface¹⁷. Hence, metal-semiconductor contacts may be mainly divided into two categories: real, or practical contacts, and intimate contacts. Real contacts are very common in semiconductor industry as they are processed without an *in-situ* surface treatment. The substrate material is usually cleaned before metal deposition. However, even if the *ex-situ* surface treatment is very effective in removing contaminants from the surface, the surface atoms will still react with air to form a thin interfacial layer¹⁸. Intimate contacts refer to metallization onto atomically clean surfaces. These surfaces can only be generated under certain ideal conditions, involving the use of ultra-high vacuum (UHV) environment, for example by cleavage or by *in-situ* cleaning techniques such as high temperature UHV annealing. Metal contacts on these clean surfaces can also be obtained by *in-situ* metallization straight after epitaxial growth. The resulting metal-semiconductor interface is however more complex, mainly because metal and semiconductor atoms are not separated by an insulating layer and can interact freely. Therefore, the electronic properties at the interface may be dependent on the possible chemical reactions between the metal and semiconductor, the possible structural change at metal and semiconductor surfaces, semiconductor or metal interdiffusion, and the creation of interface states such as metal-induced gap states (MIGS)¹⁹. Hence, the precise knowledge of the electronic and structural properties of the clean surface would be a major asset towards the understanding of the metal-semiconductor contacts formation.

The formation of Schottky contacts on GaN has been extensively studied in the last decade but additional work is still needed in order to understand the precise mechanisms of electron transport across the barrier. $\text{Al}_x\text{Ga}_{1-x}\text{N}$ is increasingly more

complex compared to GaN, mainly because the presence of Al in the alloy and metal contacts on this alloy are by far less known than for GaN. The increase in Al concentration in $\text{Al}_x\text{Ga}_{1-x}\text{N}$ alloys also induces more imperfections due to growth in the lattice such as dislocations and cracks^{20, 21} which may, in turn, have an influence on the transport mechanisms across the Schottky barrier.

The experimental work carried out in this research is divided into two main parts: the effect of cleaning procedures on the electronic and structural properties of $\text{Al}_x\text{Ga}_{1-x}\text{N}$, and the formation of metal contacts on these substrates. *Ex-situ* and *in-situ* cleaning techniques such as solvents rinse, HF etch followed by 600°C UHV anneal were investigated on $\text{Al}_x\text{Ga}_{1-x}\text{N}$ ($x = 0.20$) and ($x = 0.30$) using x-ray photoelectron spectroscopy (XPS). After each step, the relative O and C composition was measured and the band bending was checked. The influence of UHV annealing was also investigated using XPS. Chemically etched $\text{Al}_x\text{Ga}_{1-x}\text{N}$ ($x = 0.20$) were annealed up to 600°C by increments of 100°C. By changing the angle of detection, relative concentrations of the substrate atoms and contaminants were measured at the surface and topsurface, as well as band bending at the surface. Finally, using the same spectroscopic technique, atomic hydrogen cleaning (AHC) followed by 400°C UHV anneal were used on $\text{Al}_x\text{Ga}_{1-x}\text{N}$ ($x = 0.20$), in increments of 100°C.

Then, the formation $\text{Ag}/\text{Al}_x\text{Ga}_{1-x}\text{N}$ ($x = 0.20$ and $x = 0.30$) and $\text{Ni}/\text{Al}_x\text{Ga}_{1-x}\text{N}$ ($x = 0.20$) contacts was investigated through a combination of XPS, atomic force microscope (AFM), scanning tunneling microscope (STM) and current-voltage (I-V) measurements. For each contact, the metal was deposited on the substrate from sub-monolayer to thick coverage while XPS was used to assess the formation of the Schottky barrier. The metal-covered surfaces were then analysed with AFM and *in-situ* STM and I-V measurements were carried to extract the Schottky parameters.

To the best of my knowledge, no investigation of $\text{Al}_x\text{Ga}_{1-x}\text{N}$ Schottky contacts using simultaneously XPS, AFM, STM and I-V measurements has been reported to date.

Chapter 2 presents a brief review of GaN and $\text{Al}_x\text{Ga}_{1-x}\text{N}$ material properties and metal contacts on these substrates.

Chapter 3 explains the basic theory of metal-semiconductor contacts with the current model of Schottky barrier formation and gives the theoretical background of current transport mechanisms across metal-semiconductor interfaces.

Chapter 4 describes the experimental techniques used in the course of this work, with special focus on XPS.

Chapter 5 discusses the XPS results on the different procedures used to clean $\text{Al}_x\text{Ga}_{1-x}\text{N}$ ($x = 0.20$ and $x = 0.30$).

Chapter 6 presents the formation of Ag and Ni Schottky contacts to $\text{Al}_x\text{Ga}_{1-x}\text{N}$ using a combination of XPS, AFM, STM and I-V measurements. The results are compared and discussed through the current model of Schottky barrier formation.

Chapter 7 offers conclusions of the current work and presents an outlook of the future research.

References

1. F. Braun, *Ann. Phys. Chem.* **153**, 556, (1874).
2. J. Bardeen, W.H. Brattain, *Phys. Rev.* **71**, 230, (1948).
3. D. Kahng, M.M. Atalla, IRE Device Research Conference, Pittsburgh, (1960).
4. H. Welker, *Z. Naturforsch.* **7a**, 744, (1952).
5. S.J. Pearton, F. Ren, A.P. Zhang, K.P. Lee, *Mat. Sci. and Eng.* **R30**, 55, (2000).
6. J.I. Pankove, E.A. Miller, J.E. Berkeyheiser, *RCA Review* **32**, 383, (1971).
7. H. Amano, N. Sawaki, I. Akasaki, and T. Toyoda, *Appl. Phys. Lett.* **48**, 353, (1986).
8. H. Amano, M. Kito, K. Hiramatsu, I. Akasaki, *Jpn. J. Appl. Phys.* **28**, L2112, (1989).
9. S. Nakamura, N. Iwasa, M. Senoh, T. Mukai, *Jpn. J. Appl. Phys.* **31**, 1258, (1992).
10. S. Nakamura, T. Mukai, M. Senoh, *Appl. Phys. Lett.* **64**, 1687, (1994).
11. S. Nakamura, S. Pearton, G. Fasol, "The Blue Laser Diode. The Complete Story", 2nd Ed., Springer, Berlin, (2000).
12. S. Strite, H. Morkoc, *J. Vac. Sci. Technol. B* **10**(4), 1237, (1992).
13. H. Morkoc, A. Di Carlo, R. Cingolani, *Solid-State Electronics* **46**, 157, (2002).
14. R.F. Davis, S. Einfeldt, E.A. Preble, A.M. Roskowsky, Z.J. Reitmeier, P.Q. Miraglia, *Acta Materialia* **51**, 5961, (2003).
15. E. Munoz, E. Monroy, J.L. Pau, F. Calle, F. Omnes, P. Gibart, *J. Phys.: Condens. Matter* **13**, 7115, (2001).
16. B. Monemar, G. Pozina, *Progress in Quantum Electronics*, **24**, 239, (2000).
17. S.M. Sze, "Semiconductor Devices. Physics and Technology", 2nd Ed., Wiley, New-York, (2002).
18. E.H. Rhoderick, R.H. Williams, "Metal-semiconductor contacts", 2nd Ed., Oxford university press, (1988).
19. V. Heine, *Physical Review A* **138**, 1689, (1965).
20. J.-M. Bethoux, P. Vennegues, F. Natali, E. Feltin, O. Tottereau, G. Nataf, P. De Mierry, F. Semond, *J. Appl. Phys.* **94**(10), 6499, (2003).
21. J.-M. Bethoux, P. Vennegues, *J. Appl. Phys.* **97**(12), 123504, (2005).

Chapter 2

Literature Review

Extensive work has been done on III-V nitrides in the last 15 years because they attracted a lot of interest since the demonstration of the first blue GaN laser diode¹. The main properties of GaN and AlN remain their large bandgaps (3.4 eV and 6.2 eV, respectively) and the possibility of tuning the bandgap by changing the Al concentration x in the alloy $\text{Al}_x\text{Ga}_{1-x}\text{N}$. In order to produce electronic devices based on such materials, good Ohmic and Schottky contacts are needed. However, the formation of reliable, reproducible Schottky contacts on such materials is still challenging.

In this chapter, we present a brief review of the advances made on $\text{Al}_x\text{Ga}_{1-x}\text{N}$ materials, composed of two major parts. First, $\text{Al}_x\text{Ga}_{1-x}\text{N}$ properties and fabrication are reviewed; in the second part, a short survey on metal- $\text{Al}_x\text{Ga}_{1-x}\text{N}$ contact formation is presented.

2.1. Al_xGa_{1-x}N Properties

2.1.1. Growth techniques

Many different growth techniques have been developed since the 1960's but two main techniques have been extensively and successfully used: Chemical Vapour Deposition (CVD) (and its related techniques) and more recently Molecular Beam Epitaxy (MBE). However, many other techniques have been used to produce high quality GaN and Al_xGa_{1-x}N.

Ohta *et al*² have recently used Pulsed Laser Deposition (PLD) to grow AlN and GaN on different substrates and investigated the roughness and interfaces using grazing incidence X-ray reflectivity (GIXR) and atomic force microscopy (AFM). In laser ablation, high-power laser pulses are used to evaporate matter from a target surface such that the stoichiometry of the material is preserved in the interaction. As a result, a supersonic jet of particles (plume) is ejected normal to the target surface. The plume, similar to the rocket exhaust, expands away from the target with a strong forward-directed velocity distribution of the different particles. The ablated species condense on the substrate placed opposite to the target. PLD enables epitaxial growth of nitrides using less stable substrates because of the less reactive N₂ or NH₃ atmosphere. The same group fabricated AlN on (Mn,Zn)Fe₂O₄ substrates, although GIXR results seemed to show the presence of an interfacial layer between AlN and the substrate.

Ito *et al*³ achieved for the first time the epitaxial growth of GaN on MnO(111) substrates using PLD. They noticed that this could not be allowed with more common techniques such as MOCVD because PLD can operate with substrates vulnerable to chemical attack.

Epitaxial growth of GaN has been achieved on sapphire (Al₂O₃) single crystal substrates using Nebulized Spray Pyrolysis⁴. That inexpensive technique led to the fabrication of high quality films according to photoluminescence studies.

Molecular Beam Epitaxy (MBE) is an epitaxial process where one or more thermal beams of atoms or molecules impinge on a crystalline surface, under UHV conditions^{5,6}. Figure 2-1 shows a schematic of the MBE machine mainly composed of the effusion cells and the sample holder in an UHV environment.

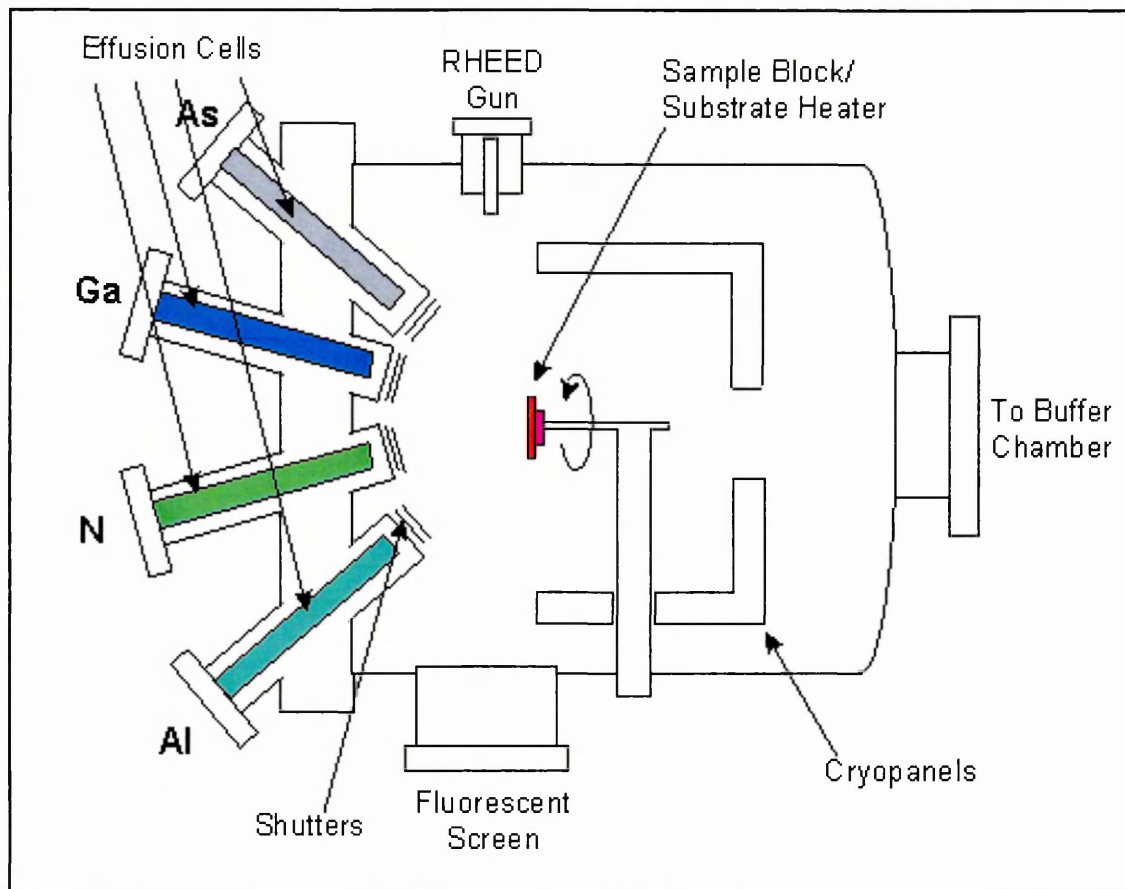


Figure 2-1: Schematic diagram of the MBE process of $\text{Al}_x\text{Ga}_{1-x}\text{N}$ and $\text{Al}_x\text{Ga}_{1-x}\text{As}$ materials (from ref. [5], [6]).

The low substrate temperatures make out-diffusion of impurities more difficult but also lead to more accurate control of dopants in the sample growth. High quality $\text{Al}_x\text{Ga}_{1-x}\text{N}$ films have been grown on various substrates using MBE^{7, 8}.

The most commonly used family of techniques for nitride growth is Chemical Vapor Deposition (CVD) also known as Vapour Phase Epitaxy (VPE). Hydride VPE (HVPE) can be used to grow thickness of 200-300 μm on a reasonable timescale. The principle of that method is quite simple. HCl vapour reacts with the Ga melt to produce a mixture of GaCl and NH_3 according to the reaction⁹:



The main advantage of that process is the fast growth rate and achievement of thick nitride film deposition and it has been successful in producing and $\text{Al}_x\text{Ga}_{1-x}\text{N}$ based materials^{10, 11}.

Metalorganic CVD (MOCVD) or OMVPE is a reliable technique and has evolved into a leading technique for production of III-V compound semiconductors. In this process, TriMethylGallium (TMG) and TriMethylAluminum (TMA) react with NH_3 at a substrate annealed at approximately 1000°C to form GaN and AlGaN surfaces as shown in figure 2-2. This technique is widely used to obtain high quality samples by varying the temperature and other growth parameters.

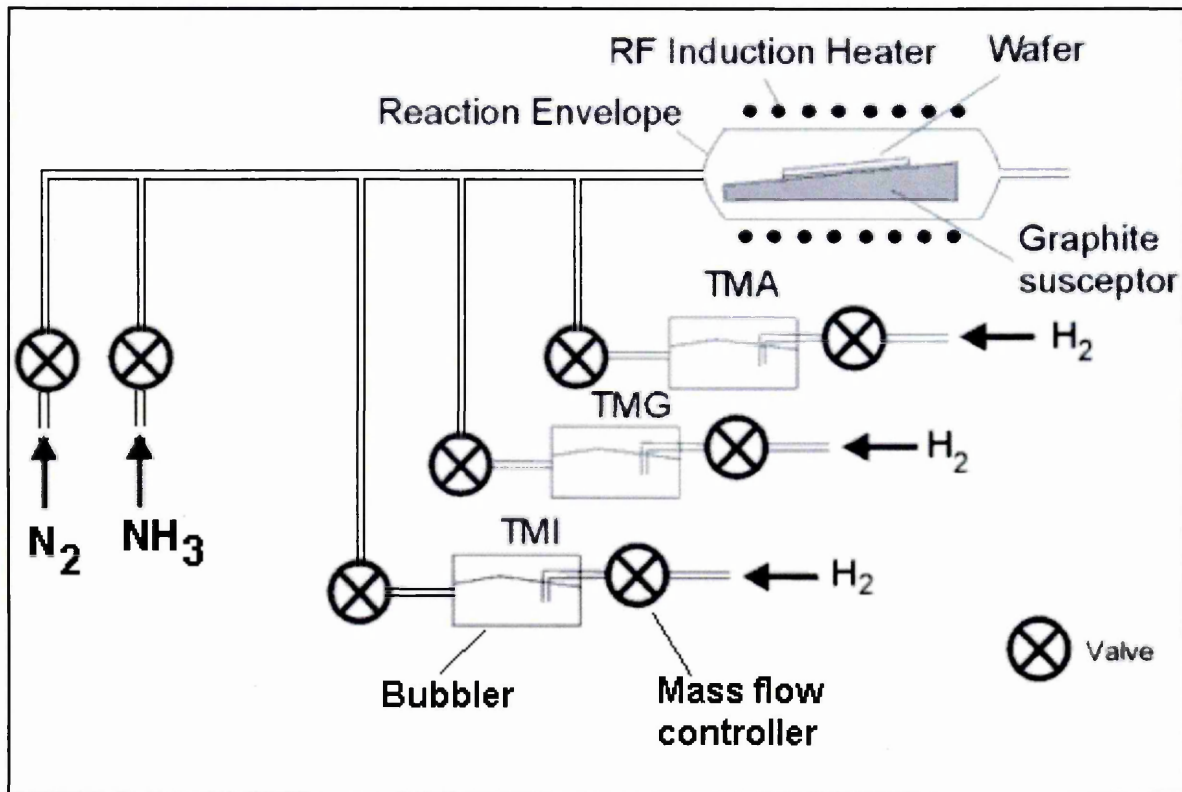


Figure 2-2: Schematic diagram of the MOCVD process for the growth of $\text{Al}_x\text{Ga}_{1-x}\text{N}$, $\text{In}_x\text{Ga}_{1-x}\text{N}$ and related alloys (from ref. [9]).

2.1.2. Importance of the substrate

One of the main problems in growing stable $\text{Al}_x\text{Ga}_{1-x}\text{N}$ surfaces relies in the difficulty of finding a suitable substrate that can lattice match and be thermally compatible with the material. This has influenced the evolution of nitrides semiconductor device fabrication and is still a source of discussion as different researches are focusing on the influence of the substrate. The lattice mismatch is a very important parameter in the choice of the substrate as it could be responsible for many defects, surface cracks and other thermal instabilities. However, several researchers

have deposited GaN epitaxial thin films onto substrates such as Al₂O₃, 6H-SiC, ZnO, SiC, Si, GaP, InP, ZnO, MgAl₂O₄, TiO₂, MgO etc.

In the case of lattice matched epitaxy, the substrate and the film have the same lattice constant. However, for lattice mismatches, if the substrate lattice constant is smaller than the film one, then the epitaxial layer will be compressed and will conform to the substrate spacing⁹. In that case, the substrate thermal expansion plays a crucial role. Properties of some frequently used substrates are summarized in table 2-1.

Substrate	Crystal structure	Lattice parameters (Å)	Coefficient of thermal expansion × 10 ⁻⁶ /K
Wurtzite GaN	Hexagonal	a= 3.189	5.59
		c=5.185	3.17
Wurtzite AlN	Hexagonal	a= 3.112	4.2
		c=4.982	5.3
α-Al ₂ O ₃	Hexagonal	a= 4.758	7.5
		c=12.991	8.5
6H-SiC	Hexagonal	a= 3.08	/
		c=15.12	/
ZnO	Hexagonal	a= 3.252	2.9
		c=5.213	4.75
LiAlO ₂	Tetragonal	a=5.1687	7.1
		c=6.2679	15
LiGaO ₂	Orthorhombic	a=5.402	6
		b=6.372	9
		c=5.007	7
Si	Cubic	a= 5.4301	3.59
GaAs	Cubic	a= 5.6533	6
3C-SiC	Cubic	a= 4.36	/
InP	Cubic	a= 5.8693	4.5
GaP	Cubic	a= 5.4512	4.65
MgO	Cubic	a= 4.216	10.5
MgAl ₂ O ₄	Cubic	a= 8.083	7.45

Table 2-1: Crystallographic and physical properties of frequently used substrates for GaN growth (from [1], [12] and [13])

Possible substrate materials should have low thermal expansion and lattice mismatch with the grown crystals. Also, they should be unaffected by the growth

chemistries (such as NH₃ or H₂) at high growth temperatures (sometimes over 1000 °C). According to these requirements, sapphire and SiC are the most popular substrate materials used currently. At the start, the growth of GaN was performed directly on these substrates, with large crystalline defects threading vertically from the substrate interface through the deposited thin film. This usually resulted in rough material surfaces. In 1986, Amano *et al.*¹⁴ significantly improved the GaN surface quality by deposition of a thin low-temperature AlN buffer layer prior to the high temperature growth of GaN. This led to threading dislocation densities in the order of 10¹⁰-10⁹ cm⁻² (about 10⁶ times higher than common semiconductors) which may affect the long-term stability of the devices. Epitaxial lateral overgrowth (ELO)¹⁵ was successfully used to produce low dislocation density GaN. In this technique, SiO₂ or Si_xN_y masks are used to stripe the underlying GaN layer. Then, regrowth is performed in such way to allow the growth on GaN only, and eventually lateral overgrowth takes place. Using this method, dislocation densities as low as about 10⁶ cm⁻² were achieved on GaN¹⁶.

The growth of AlGaN is mainly performed on GaN because of the reduced lattice mismatch between deposited film and substrate (less than 2.4%). However, surface crack networks are also created which depends on the Al mole fraction and quality of the GaN template. Nevertheless, large area crack-free AlGaN samples have been produced with threading dislocation density as low as 5×10⁸ cm⁻² using plastic relaxation through buried cracks^{17,18}.

2.1.3. Properties of the materials

Al_xGa_{1-x}N is a ternary alloy whose properties vary from those of GaN (when x = 0), to those of AlN (when x = 1). Due to their wide bandgap, mechanical properties and physical properties, GaN and AlN are expected to play a major role in various applications in the future, in addition to the application in light emitting devices. A brief summary of these material properties are shown in table 2-2.

The Al_xGa_{1-x}N energy bandgap is found to vary depending on the Al mole fraction and can be expressed as follows²⁰:

$$E_g(Al_xGa_{1-x}N) = xE_g(AlN) + (1-x)E_g(GaN) - bx(1-x) \quad [2-1]$$

where b is the bowing parameter.

The values reported in literature vary from $b=0.53$ to 2.6 eV, but most studies report values around 1 eV^{20,21,22}.

	GaN	AlN	4H SiC	GaAs	InP	Si
Crystal Structure	Wurtzite	Wurtzite				
Energy Gap (eV)	3.39	6.2	3.26	1.42	1.35	1.1
Static Dielectric Constant	8.9	8.5				
Density (g/cm ³)	6.15	3.23				
Lattice Constant, a (Å)	3.189	3.11				
Lattice Constant, c (Å)	5.185	4.98				
Electron mobility (cm ² /Vs)	1000	135	700	8500	5400	1500
Hole mobility (cm ² /Vs)	30	14				
Saturation velocity (cm/s)	2.5×10^7	1.4×10^7	2.0×10^7	1.0×10^7	1.0×10^7	1.0×10^7
Peak velocity (cm/s)	3.1×10^7	1.7×10^7	2.0×10^7	2.1×10^7	2.3×10^7	1.0×10^7
Thermal Conductivity (W/cmK)	1.5	2	4.5	0.5	0.7	1.5
Critical breakdown (MV/cm)	> 5		2.0	0.4	0.5	0.3

Table 2-2: Summary of properties of GaN, AlN and various semiconductors at 300K (from [1], [12], and [19])

2.2. Metal-Al_xGa_{1-x}N contacts

2.1.1. Introduction

An ohmic contact is defined as a metal-semiconductor contact that has a very small contact resistance compared to the bulk or series resistance of the semiconductor. The specific contact resistance (ρ_C) which is an important characteristic when analysing ohmic contacts in metal-semiconductor interfaces is defined as follows⁹ :

$$\rho_C = \left(\frac{\partial J}{\partial V} \right)_{V=0}^{-1} \quad (\Omega \cdot \text{cm}^2) \quad [2-2]$$

where J is the current density across the junction and V the applied voltage.

Hence, the lower the specific contact resistance, the better the Ohmic contact is. Furthermore, for the high concentrations ($n \geq 10^{19} \text{ cm}^{-3}$), the contact resistance strongly depends on the doping concentration: ρ_C is dominated by tunnelling effect (see section 3.3.2.). However, for lower doping concentrations ($n \leq 10^{17} \text{ cm}^{-3}$), the current created by electrons is caused by thermionic emission (see section 3.3.1.) and ρ_C is essentially independent of doping⁹. To form low-resistance Ohmic contacts, either the Schottky barrier height needs to be low or the semiconductor needs to be highly doped in order to make the electrons tunnel through the barrier, or both.

The main characteristic of Schottky contacts relies in the Schottky barrier height Φ_B . A good Schottky contact should have a high metal-semiconductor barrier where current transport mechanisms are dominated by thermionic emission. More details about electron transport mechanisms and metal-semiconductor contact formation are presented in the next chapter.

Schmitz *et al.*²⁴ investigated the influence of the metal on the metal-GaN interface properties. They pointed out that the contact characteristics generally depended on the metal work function, as shown in table 2-3. For low work function metals, the (I-V) characteristics exhibit a linear evolution showing an Ohmic-like behaviour, whereas higher work function metals led to Schottky-like behaviour.

This section presents some experimental data taken from literature focusing on the formation of Ohmic and Schottky contacts to n-type and p-type Al_xGa_{1-x}N.

Metal	Ag	Al	Ti	Cr	W	Mo	Cu	Au	Pd	Ni	Pt
Work function (eV)	4.26	4.28	4.33	4.50	4.55	4.6	4.65	5.10	5.12	5.15	5.65

Table 2-3: Work function for various metals used as Schottky or Ohmic contact to $\text{Al}_x\text{Ga}_{1-x}\text{N}$ (ref. [23]).

2.2.1. Ohmic contacts to $\text{Al}_x\text{Ga}_{1-x}\text{N}$

The choice of the metal is a very important parameter in order to obtain good Ohmic contacts. The use of low work function metals such as Al or Ti has proven to be very effective in reducing the contact resistance on n-type materials. Table 2-4 presents a compilation of results obtained for metal- $\text{Al}_x\text{Ga}_{1-x}\text{N}$ Ohmic contacts.

Hence, it can be noted that Ohmic contacts have generally been performed using a Ti/Al metallization scheme and the use of Ni/Au^{30,33}, Pt/Au³⁴ or Mo/Au³⁶ overlayers has been developed in order to minimize the effect of Al oxidation.

Fan *et al.*³⁰ investigated the influence of a composite metal layer Ti/Al/Ni/Au as a function of the thickness of the layers. They first formed an AlTi layer (crystal) over GaN in order to avoid Ga out-diffusion (thick Ti layer) and interdiffusion of excess Ni (and possibly Au). Besides, the deposition of Ti may produce TiN and create N vacancies acting as donors hence leading to highly doped interface making tunnelling predominant. They increased the Al thickness and concluded that a thick Al layer is needed to prevent Ni interdiffusion into Ga. That result was confirmed by Jacobs *et al.*³³ while optimising Ti/Al/Ni/Au ohmic contacts on AlGaN/GaN FET structures. They also concluded that the Ni layer should act as diffusion barrier for Al and Au to avoid the formation of a highly resistive alloy.

The influence of the doping was found to be a key factor as the lowest specific contact resistance ($\rho_C = 3.6 \times 10^{-8} \Omega\text{cm}^2$) was obtained by Burn *et al.*²⁶ who used a highly doped GaN to form their Ti/Au Ohmic contact. The implanted Si was implanted near the surface in order to create a highly doped region and the depletion layer caused by the Schottky barrier became very thin making current transport across the barrier enhanced by tunnelling. The temperature is also a major parameter as Foresi *et al.*²⁵ measured the contact characteristics before and after annealing (575° C, 10 min). They found that Au-GaN contact went from rectifying to Ohmic after annealing and attributed to Au diffusion into GaN creating N vacancies.

It is also possible to reduce the metal-GaN specific contact resistance by using a thin n-type $\text{Al}_x\text{Ga}_{1-x}\text{N}$ layer on top of n-type GaN. This approach relies on polarization effects in the thin $\text{Al}_x\text{Ga}_{1-x}\text{N}$ layer. With this method, the best results were obtained by Li *et al.*³⁷ using the thinner $\text{Al}_x\text{Ga}_{1-x}\text{N}$ thickness ($w = 4$ nm) together with the higher Al concentration ($x = 0.5$) and led to $\rho_C = 8.5 \times 10^{-5} \Omega\text{cm}^2$ for Ti/Al/Ni/Au (20/120/30/30) without annealing ($\rho_C = 7.6 \times 10^{-6} \Omega\text{cm}^2$ when annealed at 800°C for 30s in N_2).

Metal (thickness in nm)	ρ_C (Ωcm^2)	Material	Doping (cm^{-3})	Anneal conditions	Ref.
Al	$10^{-3} - 10^{-4}$	GaN	$n = 3 \times 10^{18}$	575°C, 10 min	[25]
Au	$10^{-4} - 10^{-4}$	GaN			
Ti/Au (3/300)	3.6×10^{-8}	GaN	$n = 4 \times 10^{20}$	No anneal	[26]
PtIn ₂	1.2×10^{-2}	GaN	$n = 5 \times 10^{17}$	No anneal	[27]
	$< 1 \times 10^{-3}$	GaN		800°C, 1 min	
Ti/Al/Ti/Au (30/100/30/30)	7×10^{-5}	GaN	$n = 6 \times 10^{17}$	No anneal	[28]
Ti/Al (40/100)	$5-8 \times 10^{-5}$	GaN	$n = 5-7 \times 10^{16}$	600°C, 1 min, N_2	[29]
Ti/Al/Ni/Au (15/220/40/50)	8.9×10^{-8}	GaN	$n = 4 \times 10^{17}$	900°C, 30 s	[30]
Ti/Ag (15/150)	6.5×10^{-5}	GaN	$n = 1.7 \times 10^{19}$	No anneal	[31]
Al	9×10^{-5}	GaN	$n = 2.8 \times 10^{17}$	No anneal	[32]
Ti/Al (25/100)	6×10^{-6}	GaN		550°C, 30 s	
Ti/Al/Ni/Au (20/120/30/30)	7.3×10^{-7}	$\text{Al}_{0.25}\text{Ga}_{0.75}\text{N}/\text{GaN}$ FET	$n = 2.8 \times 10^{17}$	900°C, 30 s, N_2	[33]
Ti/Al/Pt/Au (25/100/45/80)	5.5×10^{-5}	GaN	$n \approx 1 \times 10^{18}$	No anneal	[34]
	5.7×10^{-6}	GaN		850°C, 30 s, N_2	
	1.69×10^{-5}	$\text{Al}_{0.25}\text{Ga}_{0.75}\text{N}$		850°C, 90 s, N_2	
	8.89×10^{-6}	$\text{Al}_{0.25}\text{Ga}_{0.75}\text{N}$		850°C, 120 s, N_2	
Ti/Al (30/100)	10^{-4}	AlGaN	undoped	No anneal	[35]
Ti/Al/Mo/Au (15/60/35/50)	4.5×10^{-7}	$\text{Al}_{0.20}\text{Ga}_{0.80}\text{N}/\text{GaN}$ FET	$n = 2 \times 10^{18}$	800° C, 30 s, N_2	[36]

Table 2-4: Specific contact resistance of various metals and alloys Ohmic contacts to n-type $\text{Al}_x\text{Ga}_{1-x}\text{N}$.

Ohmic contacts to p-type GaN and $\text{Al}_x\text{Ga}_{1-x}\text{N}$ play a crucial role in the semiconductor device performance. However, p-type GaN and $\text{Al}_x\text{Ga}_{1-x}\text{N}$ Ohmic

contacts are difficult to achieve and contact resistances on p-type materials remain much higher than those measured on other p-type semiconductors. Table 2-5 shows some results for $\text{Al}_x\text{Ga}_{1-x}\text{N}$ Ohmic contacts from literature.

Ishikawa *et al.*⁴³ led a wide investigation on the influence of the metal on the characteristics of p-GaN and compared results using a wide range of metals and alloys (Ni, Au, Pd, Pt, Ta, Ti, Al and Ni/Au). They measured a contact resistance of $10^{-2} \Omega\cdot\text{cm}^2$ for Ni/Au (40/100) Ohmic contacts annealed at 500°C (10 min) and concluded that metals with large work functions should be used to perform low-resistance Ohmic contacts to p-GaN.

Until 1989, such nitride semiconductors were not exploited at full potential because a good p-n junction is required for producing LED's and LD. The main breakthrough was in 1989 with the achievement of p-type GaN using Mg doping with samples grown by MOCVD and treated by Low Energy Electron Beam Irradiation (LEEBI) for the activation of Mg by acceptors¹. Then, the interest was moved to the p-type doping concentration that would enable low resistance Ohmic contacts for suitable device application. Nakamura *et al.*⁴⁵ fabricated blue LEDs for the first time. They obtained carrier concentrations in the 10^{18}cm^{-3} range using GaN buffer layers (AlN were usually used) and produced a successful heterostructure using the p-type GaN (p-GaN/n-InGaN/n-GaN). The device was twice better (output power and external quantum efficiency) than previous II-VI-based blue LEDs.

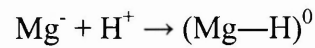
Ohmic contact formation to $p\text{-Al}_x\text{Ga}_{1-x}\text{N}$ alloys has been difficult to realize. There are two main obstacles to developing device quality ohmic contacts to these materials. The first derives from the difficulty in growing high-quality $p\text{-AlGaN}$ having high carrier concentrations with high Al contents. The second arises from the absence of metals having a work function larger than that of $p\text{-AlGaN}$. For these reasons, only very limited results have been reported so far.

Park *et al.*⁴⁴ measured contact resistance of the $10^{-4} \Omega\cdot\text{cm}^2$ range for Ni/Au and Pd/Au -pGaN Ohmic contacts. This result was mainly attributed to special annealing conditions. They found that cryogenic cooling after annealing at 600°C decreased the value of ρ_c for Ni/Au metallization and had an influence on recrystallization and surface morphology.

Metal (thickness in nm)	ρ_c (Ωcm^2)	Material	Doping (cm^{-3})	Anneal conditions	Ref.
Pd	3×10^{-3}	$\text{Al}_{0.06}\text{Ga}_{0.94}\text{N}$	$p = 3 \times 10^{18} - 10^{19}$	800°C, 20 s, N_2	[38]
Pt/Pd/Au (5/5/10)	3.1×10^{-4}	$\text{Al}_{0.11}\text{Ga}_{0.89}\text{N}$	$p = 1.5 \times 10^{17}$	600°C, 1 min, N_2	[39]
Pt (70)	1.5×10^{-2}	GaN	$p = 4.6 \times 10^{17}$	600°C, 1 min, N_2	[40]
Ni/Pt (50/100)	1.8×10^{-2}			800°C, 1 min	
Ni/Au (10/5)	$< 10^{-4}$	GaN	$p = 2 \times 10^{17}$	400°C, 10 min, air	[41]
Ta/Ti (60/40)	3×10^{-5}	GaN	$p = 7 \times 10^{17}$	800° C, 20 min, UHV	[42]
Ni/Au (10/40)	1×10^{-2}	GaN	$p = 3 \times 10^{17}$	500°C, UHV	[43]
Ni/Au (30/15)	$3 - 9.5 \times 10^{-2}$	GaN	$p = 1.41 \times 10^{17}$	No anneal	[44]
	9.84×10^{-4}			600°C, 10 min, N_2	
	2.65×10^{-4}			600°C, 10 min, N_2 + C.T. (LN_2)	
Pd/Au (25/15)	$5 - 8.5 \times 10^{-4}$		$p = 1.41 \times 10^{17}$	No anneal	
	1.80×10^{-4}			600°C, 10 min, N_2	
	3.34×10^{-4}			600°C, 10 min, N_2 + C.T. (LN_2)	

Table 2-5: Specific contact resistance of various metals and alloys Ohmic contacts to p -type $\text{Al}_x\text{Ga}_{1-x}\text{N}$. The abbreviation "C.T." stands for cryogenic cooling in liquid nitrogen.

The lowest contact resistance on p-GaN published to date was reported by Suzuki *et al.*⁴² as they obtained a value of $3 \times 10^{-5} \Omega\cdot\text{cm}^2$ for ρ_c using Ti/Ta metallization scheme. Moreover, they pointed out an important characteristic in the improvement of Ohmic contacts to p-GaN. They selected the metals in order to improve H out-diffusion from p-type GaN. In fact, interdiffusion of atomic hydrogen can result in the formation of a neutral complex with the Mg acceptors present in the GaN for p-doping as follows:



This reaction could lead to the passivation of Mg acceptors⁴⁶, the decrease in the hole concentration, and the increase in the barrier height^{1,13}.

Stampfl *et al.*^{46, 47} investigated the behaviour of doping for $\text{Al}_x\text{Ga}_{1-x}\text{N}$ as a function of x using theoretical simulations. They noticed that the ionisation energy of

the Mg acceptor increased with x but didn't find any other element that could replace Mg for p-doping.

Different investigations have led to the improvement of p-GaN Ohmic contacts but it is still challenging to obtain contact resistances low enough for electronic device applications, as ρ_c on the $10^{-5} \Omega \cdot \text{cm}^2$ range are desirable¹. The various studies pointed out different problems such as the lack of metals with low enough work functions, the deep ionization level of Mg acceptor ($\sim 170 \text{ meV}$)⁴⁸ responsible for the low hole concentration or the creation of N vacancies making the surface more n-type²⁵.

2.2.2. Schottky contacts to $\text{Al}_x\text{Ga}_{1-x}\text{N}$

Understanding the precise mechanisms of Schottky barrier formation would lead to more accurate predictions of metal-semiconductor characteristics. In this sub-section, the major role of $\text{Al}_x\text{Ga}_{1-x}\text{N}$ surface cleaning is presented; then the Schottky contacts on these materials are discussed.

a) Cleaning the surface

The selection of the metal for Schottky contact to $\text{Al}_x\text{Ga}_{1-x}\text{N}$ is a key parameter. Such semiconductors have ionic bonds which induces that the Fermi level at the interface with the metal shows little or no pinning. Schottky barrier heights of metal- $\text{Al}_x\text{Ga}_{1-x}\text{N}$ are expected to show a dependence on the metal⁶⁵. The pre-metallization surface treatment is found to strongly influence the current-voltage (I-V) characteristics of the diodes because of the presence of an interfacial layer between the metal and semiconductor. Hence, Schottky contacts can be classified in two distinct categories: intimate contacts, meaning that the semiconductor surface is atomically clean; and practical contacts, where an interfacial layer prevents the semiconductor from interacting freely with the metal. Intimate contacts can only be achieved using UHV equipments, often with high temperature annealing, or with a combination of *in-situ* and *ex-situ* surface treatments (or on a cleaved facet which is not yet possible in a large scale).

Ishikawa *et al.*⁴³ identified a contamination layer at GaN surfaces mainly composed of GaO_x and adsorbed carbon, with a thickness layer of $\sim 2 \text{ nm}$ on the as-grown surface. Besides, the presence of native oxides such as Ga_2O_3 was reported⁶⁶.

Cleaning GaN with wet chemical etch was put forward as a way to remove C and O from the surface. King *et al.*⁶⁷ investigated the effect of surface cleaning in order

to produce abrupt, clean Schottky contacts. They found that using HF/HCl treatment removes the lowest oxygen coverage on GaN even if they found residual F and Cl at the surface. Furthermore, complete thermal desorption of C contaminants occurred at temperatures higher than 900°C which corresponds to the GaN sublimation temperature. This is in very good agreement with the study of Smith *et al.*⁶⁸ who found HF combined with methanol followed by high temperature UHV anneal capable of removing C and O from GaN surfaces.

Atomically clean as well as stoichiometric GaN surfaces have been obtained⁶⁷ by annealing at 700-800°C in NH₃. This result is however at variance with the study of Bermudez *et al.*⁶⁹ as this cleaning technique was only found partly effective. Similarly, Widstrand *et al.*⁷⁰ who did not witness complete removal of C and O at GaN surface.

Ion sputtering and annealing (ISA) technique has also been studied to produce clean nitride surfaces. Nitrogen sputtering and annealing resulted in nearly stoichiometric, clean and well-ordered GaN surface^{66, 69, 71}, and a better ordered GaN surface was obtained compared to Ar⁺ ISA⁷². In addition, when nitrogen is used for ISA, it may also compensate the preferential loss of N caused by ion bombardment.

On the other hand, atomic hydrogen clean (AHC) has been widely used to clean InN surfaces mainly because the temperature required for this technique is lower than those needed using other ions⁷³. H₂ is cracked and then deposited onto the surface to be annealed at temperature around 400°C. Recently, AHC was successfully used to remove all contaminants from AlN surfaces^{74, 75}.

Clean GaN surfaces can also be obtained by annealing at 900°C in a Ga flux or by desorbing Ga-covered surfaces at the same temperature. The Ga deposited onto the surface may react with C and O at the surface, then high temperature annealing causes the evaporation of the Ga-reacted from the top surface leaving the surface free of contaminants. This technique was found to give essentially the same surface quality as for nitrogen ISA⁶⁹.

Al_xGa_{1-x}N was found more difficult to clean, even though the alloy properties are very close to GaN for low x. The addition of Al in the lattice makes this ternary alloy more reactive, with a dominant Al-oxide on the top surface which was drastically reduced using hot NH₄OH solution⁷⁶. Besides, growing crack-free, low dislocations Al_xGa_{1-x}N layers is still challenging and remains more difficult to achieve than GaN, especially for high Al mole fractions¹⁷. Oxygen was also found to be preferentially incorporated in the vicinity of cracks or surface defects in Al_xGa_{1-x}N and crack regions

would allow oxygen to move easily along the AlGa_xN layer⁷⁷. This is in accordance with the study of Nienhaus *et al.*⁷⁸ who cleaned Al_xGa_{1-x}N samples by N⁺ ISA cycles but could not completely remove O contaminants. The residual oxygen contamination was then correlated to the Al content in the alloy⁷⁹ and was believed to be incorporated into the bulk layers⁷⁸.

The pre-metallization surface treatment is an important parameter as band bending may occur before the deposition of the metal, hence influencing the Schottky barrier height. Table 2-6 presents some results on the effects of various surface treatments to Al_xGa_{1-x}N surfaces.

Surface Treatment	Material	E _F - E _V (eV)	Band bending (eV)	Reference
NH ₄ OH	n-GaN		0.4 ± 0.2	[80]
HCl	p-GaN	0.62	- 0.51	[57]
Aqua regia	p-GaN	0.30	- 0.20	
Reactive ion etch (RIE)	n-GaN		≈ 1.4	[81]
Oxidation + HF + (NH ₄) ₂ S _x	n-Al _{0.2} Ga _{0.8} N	2.14	≈ 1.26 + 2.8y **	[82]
	p-Al _{0.2} Ga _{0.8} N	- 2.08	≈ -2.08	
NH ₃ flux annealing	n-GaN	3.0 ± 0.1	0.3 ± 0.1	[83]
	p-GaN	1.1 ± 0.1	- 0.8 ± 0.1	
NH ₃ flux annealing + Ga reflux	n-GaN	2.4 ± 0.1	≈ 1	[70]
N ⁺ ISA	n-GaN	2.4 ± 0.2	0.9 ± 0.2	[80]
	n-GaN	2.6 ± 0.1	0.75 ± 0.1	[71]
	p-GaN	1.0 ± 0.1	- 0.75 ± 0.1	

Table 2-6: Summary of several experimental results reported on the electronic properties of cleaned n-type and p-type GaN and AlGa_xN. **In this study⁸², the authors reported 0 ≤ y < 0.2.

In this table, the column labelled “band bending (eV)” represents the potential barrier at the free surface, without any metal deposition. It is also known as the bare surface barrier height. For all studies presented in this table, the “band bending” was calculated using the position of the Fermi level relative to the valence band maximum (E_F – E_V). This value was measured using spectroscopic techniques such as XPS or UPS (Ultra-violet photoemission spectroscopy); except for [81] where the surface band bending was directly measured by potential electric force microscopy (a variant of atomic force microscopy).

All studies on the determination $\text{Al}_x\text{Ga}_{1-x}\text{N}$ surface band bending in this table show a significant band bending at the cleaned surface. The clean surface in these works was also found to be, to some extent, free of contaminants. Hence, the removal of the oxide/contaminant layer from the surface does not lead to flat band situation (like in the bulk) but the Fermi level is rather pinned by surface states caused by the surface treatment.

However, cleaning the surface predominantly appears to drag the Fermi level closer to the conduction band, causing upward band bending. Cho *et al.*⁸¹ measured the surface band bending at the as-grown and clean surface n-GaN and found an upward band bending of 1 eV and 1.4 eV, respectively. This is good agreement with Sabuktagin *et al.*⁸⁴ who found that the as-grown n-GaN surfaces presented an upward band bending of 0.9 eV. Similarly, the surface of atomically clean GaN showed an upward band bending of 0.9 eV, while GaN surface which was chemically cleaned and air-exposed exhibited an upward band bending of 0.4 eV⁸⁰. Some studies have also reported downward band bending with increased cleanliness. Wu *et al.*⁷¹ reported upward band bending of 0.75 eV for clean n-type, but witnessed a reduction of the upward banding as the surface was progressively cleaned and annealed. Similar behaviour was also observed on $\text{Al}_{0.2}\text{Ga}_{0.8}\text{N}/\text{GaN}$ HFET³⁶ and very recently on n-type $\text{Al}_{0.2}\text{Ga}_{0.8}\text{N}$ surface⁸².

b) Metal- $\text{Al}_x\text{Ga}_{1-x}\text{N}$ contacts

A review of metal- $\text{Al}_x\text{Ga}_{1-x}\text{N}$ practical and intimate Schottky contacts is presented in tables 2-7 to 2-9. Most of the studies showed Schottky barrier heights measured by electrical techniques such as current-voltage (I-V). The transport mechanisms can be assessed by the measurement of the ideality factor n . Hence, it can be noted that the ideality factor and barrier height vary with the pre-metallization surface treatment. Cleaner surfaces that exhibit band bending at the free surface might be responsible for higher Schottky barrier heights. Intimate contacts formed *in-situ* tend to yield lower ideality factor whereas for the same metal, Schottky barrier heights show discrepancies depending on the measurement technique. Barrier heights derived from (I-V) may be found lower than XPS ones. This might be explained by the fact that XPS barrier heights are measured as average in the sampling area, whereas electrons crossing the barrier in (I-V) measurements find the lowest barrier

Metal	Work function (eV)	Doping (cm ⁻³)	Growth	Surface treatment		Φ_B (eV)	Ideality factor n	Ref.
				<i>in-situ</i>	<i>ex-situ</i>			
Ag	4.26	$n=5-7 \times 10^{17}$	sapphire - MBE	/	Organic solvents	0.92	1.24	[29]
		$n=5-7 \times 10^{17}$	sapphire - MBE	/	NH ₄ OH	0.79	1.08	[24]
		$n=1 \times 10^{17}$	sapphire - LP MOCVD	/	Cleaned oxygen plasma + HCl sol.	0.54	1.24	[49]
		$n=1 \times 10^{17}$	SiC - MOVPE	NH ₃ flux annealing	Organic solvents + HCl sol.	0.6	1.2	XPS, UPS
		$n=6 \times 10^{16}$	sapphire - MBE	Ga reflux	HF:H ₂ O, H ₂ O	0.77	1.6	[50]
Au	5.10	$n=5-7 \times 10^{17}$	sapphire - MBE	/	Organic solvents	0.88	1.54	[29]
		$n=5-7 \times 10^{17}$	sapphire - MBE	/	NH ₄ OH	1.03	1.07	[51]
		$n=1 \times 10^{17} - 10^{18}$	sapphire - MOCVD	UHV annealing (600°C, 10 min)	Organic solvents + hot KOH and aqua regia	1.15 ± 0.15	XPS	[24]
		$n=1 \times 10^{17}$	sapphire - LP MOCVD	/	Cleaned oxygen plasma + HCl sol.	0.86	1.04	[52]
		$n=1.2 \times 10^{17}$	sapphire - MOCVD	/	Hot KOH and aqua regia	~1.05	BEEEM	[53]
		$n=2 \times 10^{15}$	sapphire - MOVPE	UHV annealing (600°C, 10 min)	HF:H ₂ O, H ₂ O	1.24	1.03	[54]
		$n=2 \times 10^{15}$	sapphire - MOVPE	Ga reflux	HF:H ₂ O, H ₂ O	0.84	1.18	[55]
		$n=2 \times 10^{15}$	sapphire - MOCVD	UHV annealing (600°C, 10 min)	HF:H ₂ O, H ₂ O	1.35	1.12	[55]
		$p=5 \times 10^{17}$	SiC - MOCVD	cycles of N ⁺ ISA (900°C, 10 min)	/	Organic solvents + aqua regia	1.2	XPS
		$n=1 \times 10^{19}$	SiC - MOCVD	cycles of N ⁺ ISA (900°C, 10 min)	/	Organic solvents	1.25	XPS
Pt	5.65	$n=7 \times 10^{17}$	sapphire - MBE	/	Organic solvents	0.98	1.4	[29]
		$n=5-7 \times 10^{17}$	sapphire - MBE	/	NH ₄ OH	0.7	1.1	[24]
		$n=5-7 \times 10^{17}$	sapphire - MBE	/	Cleaned oxygen plasma + HCl sol.	0.88	1.05	[57]
		$n=1 \times 10^{17}$	sapphire - LP MOCVD	/	HCl sol.	1.08	SRPES	
		$p=1.9 \times 10^{17}$	sapphire - MOCVD	/	aqua regia	0.5	~1.10	
Pd	5.12	$n=1 \times 10^{17}$	sapphire - MOCVD	/	Buffered oxide etch, 30s	1.13	BEEEM	
		$n=1.2 \times 10^{17}$	sapphire - MOCVD	/	Hot KOH and aqua regia	~0.95	~1.10	
		$n=1 \times 10^{17}$	sapphire - MOCVD	/	Buffered oxide etch, 30s	1.11	1.04	
		$n=1 \times 10^{17}$	sapphire - LP MOCVD	/	Cleaned oxygen plasma + HCl sol.	0.9	1.04	
		$n=1 \times 10^{17}$	sapphire - MOCVD	/				

Table 2-7: Summary of reported experimental studies of Schottky contacts to GaN. Results have been obtained using (I-V) measurements, unless stated otherwise.

Metal	Work function (eV)	Doping (cm ⁻³)	Growth	Surface treatment		Φ_B (eV)	Ideality factor n	Ref.
				<i>in-situ</i>	<i>ex-situ</i>			
Pt/Au (40/150)	5.65/5.10	n=8×10 ¹⁶	sapphire - RF MBE	/	HCl/HF	0.81	1.6-1.8	[59]
		n=1×10 ¹⁷		/	(NH ₄) ₂ S	0.58	1.8-1.9	
		p=1×10 ¹⁷		/	HCl/HF	0.99	1.4-1.6	
				/	(NH ₄) ₂ S	0.83	1.3-1.8	
Ni	5.15	n=1×10 ¹⁷	sapphire - LP MOCVD	/	HCl/HF	0.49	~2	[24]
		n=2×10 ¹⁷		/	(NH ₄) ₂ S	0.47	~2	
				/	Cleaned oxygen plasma + HCl sol.	0.99	1.04	
			sapphire - MOCVD	Ga reflux	/	0.98	1.4	[60]

Table 2-8: Summary of reported experimental studies of Schottky contacts to GaN

Metal	Work function (eV)	Doping (cm ⁻³)	Growth	Surface treatment	x	Φ_B (eV)	Ideality factor n	Reference
Au	5.1	n=8.39×10 ¹⁶	sapphire - OMVPE	/	0.00	0.91	1.04	[61]
		n=2.68×10 ¹⁶		/	0.08	0.99±0.02	1.2	
		n=1.03×10 ¹⁷		/	0.11	1.09±0.05	1.57	
		n=3.50×10 ¹⁷		/	0.14	1.17±0.03	1.22	
		n=9.55×10 ¹⁶		/	0.20	1.36±0.08	2.3	
Pt/Ti/Au	5.65/4.33/5.10	n=2.5×10 ¹⁸	sapphire - MOVPE	HF:H ₂ O + 550°C UHV anneal, 15 min	0.31	2.0±0.1	1.2-1.6	[62]
Ti	4.33	n=1×10 ¹⁷	SiC - MOVPE	HCl/HF/H ₂ O	0.15	0.84	1.08	[63]
Ni	5.15					1.25	1.23	
Ni	5.15	n=1.5×10 ¹⁷	SiC - MOVPE	Organic solvents + HCl:HF:H ₂ O	0.00	0.84	1.12	[64]
		n=3.5×10 ¹⁶			0.11	0.94	1.13	
		n=1.6×10 ¹⁶			0.15	1.04	1.21	
		n=4.7×10 ¹⁶			0.17	1.11	1.15	
		n=1.4×10 ¹⁷			0.23	1.02	1.37	

Table 2-9: Summary of reported experimental studies of Schottky contacts to Al_xGa_{1-x}N.

As explained earlier, due to its ionicity, the $\text{Al}_x\text{Ga}_{1-x}\text{N}$ Fermi level is said to be unpinned which suggests metal- $\text{Al}_x\text{Ga}_{1-x}\text{N}$ Schottky barrier heights to be dependent on the metal work function. Schmitz *et al.*²⁴ investigated the metal-nGaN contact behaviour using 17 different metals. It was found that an increase in metal work function correlated with an increase in the barrier height. A similar result was obtained by Wu *et al.*⁵⁵ who noticed that higher Schottky barrier heights on n-GaN (p-GaN) were obtained using higher (lower) work function metals.

The index of behaviour S , or slope factor, is defined as the variation of the barrier height over the variation of metal work function and gives an estimate of the density of surface states D_{SS} (see section 3.2.8). Deviations from the ideal Schottky-Mott model, where $S = d\phi_B/d\phi_M = 1$, were often witnessed. Hence, both groups^{24, 55} found an index of behaviour $S \sim 0.39$ which gives a density of surface states $D_{\text{SS}} \sim 1.6 \times 10^{13} \text{ cm}^{-2} \text{ eV}^{-1}$. Similarly, Tracy *et al.*⁴⁹ measured a slope parameter $S \sim 0.44$, whereas the study of Bermudez *et al.*⁶⁰ on Al and Ni Schottky contacts yields $S \sim 0.92$. In this case, the dependence of the Schottky barrier on the metal work function is amongst the strongest ever reported to date and closely approaches the Schottky-Mott limit ($D_{\text{SS}} \sim 8.7 \times 10^{11} \text{ cm}^{-2} \text{ eV}^{-1}$).

However, the influence of the metal work function on metal- $\text{Al}_x\text{Ga}_{1-x}\text{N}$ Schottky barrier heights has hardly been studied with $x > 0$. To the best of our knowledge, the study published by Yu *et al.*⁶³ is the only investigation of metal Schottky contacts to bulk $\text{Al}_x\text{Ga}_{1-x}\text{N}$. They measured the Schottky barrier heights of Ni and Ti on thick $\text{Al}_{0.15}\text{Ga}_{0.85}\text{N}$. The slope parameter S , taken between the two data points shown in table 2-9, can be estimated to ~ 0.50 which yields a density of surface states $D_{\text{SS}} \sim 1.0 \times 10^{13} \text{ cm}^{-2} \text{ eV}^{-1}$. Besides, metal- $\text{Al}_x\text{Ga}_{1-x}\text{N}$ Schottky barrier heights are found to increase with increasing Al content^{61, 64} which is consistent with the Schottky-Mott rule (see section 3.2.1.).

For different metals deposited on the same surface, the formation of Schottky barrier may be attributed to the contribution of metal-induced gap states (MIGS). Furthermore, the MIGS-and-electronegativity model (see section 3.2.6.) predicts the barrier to be dependent on the electronegativity difference between the metal and semiconductor. Excellent agreement between experimental data and predictions based on the MIGS-and-electronegativity model has been found for binary^{85,86,87,88} and ternary⁸⁹ compound Schottky contacts.

Besides, as shown in table 2-6, the free surface generally exhibits significant band bending. Hence, the Cowley-Sze model predicts the barrier height to be expressed as a sum of the "bare surface barrier height" or band bending before metal deposition, and a Schottky-Mott term induced by the metal. As well, this model was found to agree with experimental data on metal-GaN⁹⁰.

2.3. Summary

In this chapter, the main Al_xGa_{1-x}N growth processes and properties have been briefly reviewed in order to get a better understanding of Schottky contact formation on such materials. The main results of Ohmic and Schottky contacts on n-type and p-type Al_xGa_{1-x}N have also been presented.

MOCVD and MBE have been extensively used to grow Al_xGa_{1-x}N on various substrates with increasingly high crystalline quality up to now. The best substrate candidate for the growth of Al_xGa_{1-x}N is GaN and dislocation densities as low as 5×10^8 cm⁻² over large area crack-free have been achieved for low Al mole fractions ($x < 0.30$).

Ohmic and Schottky contacts have been successfully formed in order to allow device applications. The best results on Ohmic contacts have been obtained with the following scheme for metal selection: low work function metals are used for n-type materials whereas high work function metals are more suitable for p-type contacts. Al/Ti and Ni/Au metallization schemes have been demonstrated to exhibit the lowest contact resistances on n-type and p-type Al_xGa_{1-x}N, respectively. Achieving low contact resistance Ohmic contacts on such p-type materials is however still challenging. Schottky contact formation on n-type Al_xGa_{1-x}N has been shown to exhibit increased Schottky barrier height with increasing metal work function. The barrier height was also found to vary depending on the pre-metallization surface treatment and intimate contacts are predominantly expected to result in high barriers with thermionic emission as main electron transport mechanism. It is however more difficult to obtain the clean, oxide-free Al_xGa_{1-x}N surfaces compared to GaN mainly because of the strong Al-oxide bonding and the poorer crystalline quality with higher Al content. Discrepancies in Schottky barrier heights might be due to various phenomena such as the bare surface barrier height, the measurement technique, surface treatment or the quality of the material. The Cowley-Sze and the MIGS-and-electronegativity models are amongst the current models used to predict Schottky barrier heights.

References

1. S. Nakamura, S. Pearton, G. Fasol, "The Blue Laser Diode. The Complete Story", 2nd Ed., Springer, Berlin, (2000).
2. J. Ohta, H. Fujioka, H. Takahashi, M. Oshima, Appl. Surf. Sci. **190**, 352, (2002).
3. S. Ito, J. Ohta, H. Fujioka, M. Oshima, Appl. Surf. Sci. **197-198**, 384, (2002).
4. A.R. Raju, K. Sardar, C.N.R. Rao, Mat. Sci. in Semicond. Processing **4**, 549, (2001).
5. M.A. Herman, H. Sitter, "Molecular Beam Epitaxy. Fundamentals and Current Status", Springer-Verlag, Berlin, 1989.
6. E.H.C.Parker, "The Technology and Physics of Molecular Beam Epitaxy", Plenum Press, New York, (1985).
7. M.A.L. Johnson et al., J. Vac. Sci. Technol. B **14**(3), 2349, (1996).
8. E. Calleja, M.A. Sanchez-Garcia, F. Calle, F.B. Naranjo, E. Munoz, U. Jahn, K. Ploog, J. Sanchez, J.M. Calleja, K. Saarinen, P. Hautajarvi, Mat. Sci. and Eng. B **82**, 2, (2001).
9. S.M. Sze, "Semiconductor Devices. Physics and Technology", 2nd Ed., Wiley, New-York, (2002).
10. R. Fornari, M. Bosi, D. Bersani, G. Attolini, P.P. Lottici, C. Pelosi, Semicond, Sci. Technol. **16**, 776, (2001).
11. A. Castaldini, A. Cavallini, L. Polenta, C. Diaz-Guerra, J. Picqueras, J. Phys: Condens. Matter **14**, 13095, (2002).
12. S. Strite, H. Morkoc, J. Vac. Sci. Technol. B **10**(4), 1237, (1992).
13. H. Morkoc, "Nitride Semiconductors and Devices", Springer-Verlag, Berlin, (1999).
14. H. Amano, N. Sawaki, I. Akasaki, and T. Toyoda, Appl. Phys. Lett. **48**, 353, (1986).
15. P. Ruterana, M. Albrecht, J. Neugebauer, "Nitride Semiconductors: Handbook on Materials and Devices", Wiley-WCH, Weinheim, (2003).
16. B. Beaumont, P. Venngues, P. Gibart, Phys. Stat. Sol. (b) **227**(1), 1, (2001).
17. J.-M. Bethoux, P. Venngues, F. Natali, E. Feltn, O. Tottereau, G. Nataf, P. De Mierry, F. Semond, J. Appl. Phys. **94**(10), 6499, (2003).
18. J.-M. Bethoux, P. Venngues, J. Appl. Phys. **97**(12), 123504, (2005).
19. R.T. Kemerly, H.B. Wallace, M.N. Yoder, "Impact of Wide Bandgap Microwave Devices on DoD systems", Proceedings of the IEEE, **90**(6), 1059, (2002).
20. S.P. Grabowski, M. Schneider, H. Nienhaus, W. Monch, R. Dimitrov, O. Ambacher, M. Stutzmann, Appl. Phys. Lett. **78**(17), 2503, (2001).
21. M.J. Murphy, B.E. Foutz, K. Chu, H. Wu, W. Yeo, W.J. Schaff, O. Ambacher, L.F. Eastman, T.J. Eustis, R. Dimitrov, M. Stutzmann, W. Rieger, MRS Internet J. Nitride Semicond. Res. **4S1**, G8.4, (1999).
22. S.R. Lee, A.F. Wright, M.H. Crawford, G.A. Petersen, J. Han, R.M. Biefeld, Appl. Phys. Lett. **74**, 3344, (1999).
23. D.A. Neamen, "Semiconductor Physics and Devices", Irwin, (1992).
24. A.C. Schmitz, A.T. Ping, M.A. Khan, Q. Chen, J.W. Yang, I. Adesida, J. Electronic Materials **27**(4), 255, (1998).
25. J.S. Foresi, T.D. Moustakas, Appl. Phys. Lett. **62**(22), 2856, (1993).
26. J. Burn, K. Chu, W.A. Davis, W.J. Schaff, T.J. Eustis, Appl. Phys. Lett. **70**(4), 464, (1997).

27. D. B. Ingerly, Y. A. Chang, N. R. Perkins and T. F. Kuech, *Appl. Phys. Lett.* **70**(1), 108, (1997).
28. A. Motayed, M. Jah, A. Sharma, W.T. Anderson, C.W. Litton, S.N. Mohammad, *J. Vac. Sci. Technol. B* **22**(2), 663, (2004).
29. Y. Koyama, T. Hashizume, H. Hasegawa, *Solid-State Electronics* **43**, 1483, (1999).
30. Z. Fan, S.N. Mohammad, W. Kim, O. Oktas, A.E. Botcharev, H. Morkoc, *Appl. Phys. Lett.* **68**(12), 1672, (1996).
31. J. D. Guo, C. I. Lin, M. S. Feng, F. M. Pan, G. C. Chi, C. T. Lee, *Appl. Phys. Lett.* **68**(2), 235 (1996).
32. A.T. Ping, M. Asif Khan, I. Adesida, *J. of Elec. Mat.*, **25**(5), 819 (1996).
33. B. Jacobs, M.C.J.C.M. Kramer, E.J. Geluk, F. Karouta, *J. Crystal Growth* **241**, 15, (2002).
34. B. Luo, J. Kim, R. Mehandrou, F. Ren, K.P. Lee, S.J. Pearton, A.Y. Polyanov, N.B. Smirnov, A.V. Govorkov, E.A. Kozhukhova, A.V. Osinsky, P.E. Norris, *Solid-State Electronics* **46**, 1345, (2002).
35. C.M. Jeon, H.W. Jang, K.J. Choi, S-B Bae, J-H. Lee, J-L. Lee, *Solid-State Electronics* **46**, 695, (2002).
36. D. Selvanathan, L. Zhou, V. Kumar, I. Adesida, *Phys. Stat. Sol. (a)* **194** (2), 583, (2002).
37. Y.L. Li, J.W. Graff, E.L. Waldron, T. Gessmann, E.F. Schubert, *Phys. Stat. Sol. (a)* **188**(1), 359, (2001).
38. T. V. Blank, Y. A. Goldberg, E. V. Kalinina, O. V. Konstantinov, A. E. Nikolaev, A. V. Formin, and A. E. Dherenkov, *Semiconductors* **35**, 529, (2001).
39. H.K. Kim, T.Y. Seong, I. Adesida, C.W. Tang, K.M. Lau, *Appl. Phys. Lett.* **84**(10), 1710, (2004).
40. J. M. Delucca, H. S. Venugopalan, S. E. Mohny, R. F. Karlicek, Jr, *Appl. Phys. Lett.* **73**(23), 3402, (1998).
41. J-K Ho, C-S Jong, C. C. Chiu, C-N Huang, C-Y Chen, K-K Shih, *Appl. Phys. Lett.* **74**(9), 1275, (1999).
42. M. Suzuki, T. Kawakami, T. Arai, S. Kobayashi, Y. Koide, T. Uemura, N. Shibata, M. Murakami, *App. Phys. Lett.* **74**(2), 275, (1999).
43. H. Ishikawa, S. Kobayashi, Y. Koide, S. Yamasaki, S. Nagali, J. Umezaki, M. Koike, M. Murakami, *J. Appl. Phys.* **81**(3), 1315, (1997).
44. M-R. Park, Y-J. Song, W.A. Anderson, *ETRI Journal* **24**(5), 349-359, (2002).
45. S. Nakamura, M. Senoh, T. Mukai, *Jpn. J. Appl. Phys.* **32**, Part 2, No 1A/B, L8-L11, (1993).
46. A.Y. Polyanov, N.B. Smirnov, A.V. Govorkov, K.H. Baik, S.J. Pearton, B. Luo, F. Ren, J.M. Zavada, *J. Appl. Phys.* **94**(6), 3960, (2003).
47. C. Stampfl, J. Neugebauer, C.G. Van De Walle, *Mat. Sci. and Eng.* **B59**, 253, (1999).
48. S.J. Pearton, F. Ren, A.P. Zhang, K.P. Lee, *Mat. Sci. and Eng.* **R30**, 55, (2000).
49. K.M. Tracy, P.J. Hartlieb, S. Einfeldt, R.F. Davis, E.H. Hurt, R.J. Nemanich, *J. Appl. Phys.* **94**(6), 3939, (2003).
50. T.G.G. Maffei, S.A. Clark, P.R. Dunstan, S.P. Wilks, D.A. Evans, F. Peiro, R. Riechert, P.J. Parbrook, *Phys. Status Solidi (a)* **176**, 751, (1999).
51. R. Sporcken, C. Silien, F. Malengrau, K. Grigorov, R. Caudano, F. J. Sanchez, E. Cajella, E. Munoz, B. Beaumont and P. Gibart, *MRS Internet J. Nitride Semicond. Res.* **2**, 23, (1997).
52. L.D. Bell, R.P. Smith, B.T. McDermott, E.R. Gertner, R. Pittman, R.L. Pierson, G.J. Sullivan, *J. Vac. Sci. Technol. B***16**(4), 2286, (1998).
53. T.G.G. Maffei, M.C. Simmonds, S.A. Clark, F. Peiro, P. Haines, P.J. Parbrook, *J. Phys. D: Appl. Phys.***33**(20), L115, (2000).

54. T.G.G. Maffei, M.C. Simmonds, S.A. Clark, F. Peiro, P. Haines, P.J. Parbrook, *J. Appl. Phys.* **92**(6), 3179-3186, (2002).
55. C.I. Wu, A. Kahn, *J. Vac. Sci. Technol. B* **16**(4), 2218, (1998).
56. Y. Kribes, I. Harrison, B. Tuck, T.S. Cheng, C.T. Foxon, *Semicond. Sci. Technol.* **12**, 913, (1997).
57. J.K. Kim, J.L. Lee, *J. Electrochemical Soc.* **150**(3), G209, (2003).
58. L. Wang, M.I. Nathan, T-H. Lim, M.A. Khan, Q. Chen, *Appl. Phys. Lett.* **68**(9), 1267, (1996).
59. X.A. Cao, S.J. Pearton, G. Dang, A.P.Zhang, F. Ren, J.M. Van Hove, *Appl. Phys. Lett.*, **75**(26), 4130, (1999).
60. V. M. Bermudez, T.M. Jung, K. Doverspike, A.E. Wickenden, *J. Appl. Phys.* **79**(1), 110, (1996).
61. M.R.H. Khan, N. Nakayama, T. Derchprohm, K. Hiramatsu, N. Sawaki, *Solid-State Electronics* **41**(2), 287, (1997).
62. E. Monroy, F. Calle, R. Ranchal, T. Palacios, M. Verdu, F.J. Sanchez, M.T. Montojo, M. Eickhoff, F. Omnes, Z. Bougrioua, I. Moerman, *Semicond. Sci. Technol.* **17**, L47-L54, (2002).
63. L.S. Yu, D.J. Qiao, Q.J. Xing, S.S. Lau, K.S. Boutros, J.M. Redwing, *Appl. Phys. Lett.* **73**(2), 238, (1998).
64. D. Qiao, L.S. Yu, S.S. Lau, J.M. Redwing, J.Y. Lin, H.X. Jiang, *J. Appl. Phys.* **87**(2), 801, (2000).
65. S. Kurtin, T. C. McGill, C. A. Mead, *Physical review letter* **22**, 1433 (1969).
66. K. Prabhakaran, T.G. Andersson, K. Nozawa, *Appl. Phys. Lett.* **69** (21), 3212, (1996).
67. S.W. King, J.P. Barnak, M.D. Bremser, K.M. Tracy, C. Ronning, R.F. Davis, R.J. Nemanich, *J. Appl. Phys.*, **84**(9), 5248, (1998).
68. L.L. Smith, S.W. King, R.J. Nemanich, R.F. Davis, *J. Electron. Mater.* **25**, 805, (1996).
69. V.M. Bermudez, D.D. Koleske, A.E. Wickenden, *Appl. Surf. Sci.* **126**, 69, (1998).
70. S.M. Widstrand, K.O. Magnusson, L.S.O. Johansson, E. Moons, M. Gurnett, H.W. Yeom, H. Miki, M. Oshima, *MRS Internet J. Nitride Semicond. Res.* **9**, 4, (2004).
71. C.I. Wu, A. Kahn, N. Taskar, D. Dorman, D. Gallagher, *J. Appl. Phys.* **83**(8), 4249, (1998).
72. Y.H. Lai, C.T. Yeh, J.M. Hwang, H.L. Hwang, C.T. Chen, W.H. Hung, *J. Phys. Chem. B* **105**(41), 10029, (2001).
73. T. Ohashi, Y. Saito, T. Maruyama, Y. Nanishi, *J. Cryst. Growth* **237-239**, 1022, (2002).
74. T.D. Veal, I. Mahboob, L.F.J. Piper, C.F. McConville, Hai Lu, W.J. Schaff, *J. Vac. Sci. Technol. B* **22**(4), 2175, (2004).
75. L.F.J. Piper, T.D. Veal, M. Walker, I. Mahboob, C.F. McConville, Hai Lu, W.J. Schaff, *J. Vac. Sci. Technol. A* **23**(4), 617, (2005).
76. T. Hashizume, S.Y. Ootomo, R. Nakasaki, S. Oyama, M. Kihara, *Appl. Phys. Lett.* **76**(20), 2880, (2000).
77. S. Rajasingam, A. Sarua, M. Kuball, A. Cherodian, M.J. Miles, C.M. Younes, B. Yavich, W.N. Wang, N. Grandjean, *J. Appl. Phys.* **94**(10), 6366, (2003).
78. H. Nienhaus, M. Schneider, S.P. Grabowski, W. Monch, R. Dimitrov, O. Ambacher, M. Stutzmann, *Mat. Res. Soc. Symp. Proc.* **680E**, E4.5.1, (2001).
79. S.P. Grabowski, M. Schneider, H. Nienhaus, W. Monch, R. Dimitrov, O. Ambacher, M. Stutzmann, *Appl. Phys. Lett.* **78**(17), 2503, (2001).
80. V.M. Bermudez, *J. Appl. Phys.* **80**(2), 1190 (1996).
81. S.-J. Cho, S. Dogan, S. Sabuktagin, M. A. Reshchikov, D.K. Johnstone, H. Morkoc, *Appl. Phys. Lett.* **84**(16), 3070, (2004).

82. Y.J. Lin, Y.L. Chu, W.X. Lin, F.T. Chien, C.S. Lee, *J. Appl. Phys.* **99**(7), 073702, (2006).
83. K.M. Tracy, W.J. Mecoach, R.F. Davis, R.J. Nemanich, *J. Appl. Phys.* **94**(5), 3163, (2003).
84. S. Sabuktagin, M. A. Reshchikov, D. K. Johnstone, H. Morkoc, *Mat. Res. Soc. Symp. Proc.* **798**, Y5.39.1, (2004).
85. T.U. Kampen, W. Monch, *MRS Internet J. Nitride Semicond. Res.* **1**(41), (1996).
86. T.U. Kampen, W. Monch, *Appl. Surf. Sci.* **117/118**, 388, (1997).
87. W. Monch, *J. Vac. Sci. Technol. B* **17**(4), 1867, (1999).
88. H.P. Hall, M.A. Awaah, K. Das, *Semicond. Sci. Technol.* **19**, 176, (2004).
89. W. Monch, *Appl. Phys. Lett.* **67**(15), 2209, (1995).
90. V.M. Bermudez, *J. Appl. Phys.* **86**(2), 1170 (1999).

Chapter 3

Theory of Metal-Semiconductor Contacts

3.1. Introduction

When a metal and a semiconductor are brought into intimate contact, an interface barrier is formed. In 1938, Schottky suggested that rectifying behaviour could arise from a potential barrier as a result of the stable space charge in the semiconductor¹. The barrier arising from this model is known as the Schottky barrier. The properties of electronic devices are often dependant on the quality of Ohmic, or nonrectifying, and Schottky, or rectifying, contacts. In order to define the characteristics of such devices, it is important to understand the electron transport mechanisms across metal-semiconductor contacts.

This chapter is composed of three main parts. The first section reviews the current models of Schottky barrier formation used to interpret the experimental data. The second section presents the mechanisms of current transport across the barrier and the third part briefly describes the Schottky parameter extraction from experimental data.

3.2. Models of Schottky barrier formation

3.2.1. Schottky-Mott model

The model proposed by both Schottky¹ and Mott² is solely based on bulk properties. Figure 3-1 shows the energy band diagram of the Schottky barrier formation according to the Schottky-Mott model.

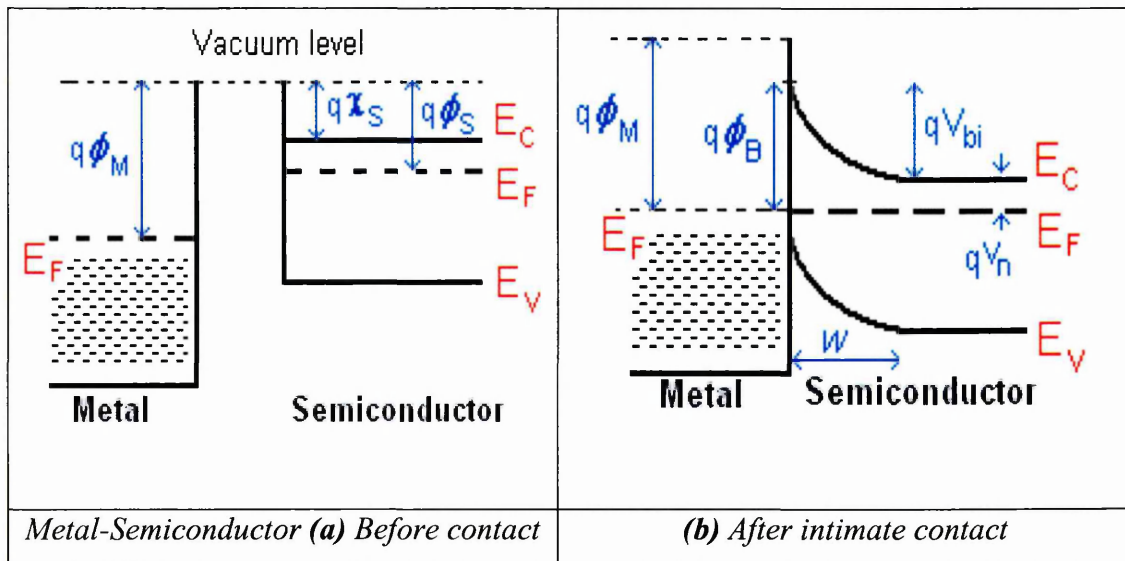


Figure 3-1: Energy band diagram of a metal-semiconductor junction (a) isolated, and (b) after intimate contact. In this example, the semiconductor is n-type and $\Phi_M > \Phi_S$.

On figure 3-1 (a), the metal and semiconductor are isolated from each other. The semiconductor bands are initially flat and the material is characterised by its electron affinity χ_S and work function Φ_S . The work function is defined as the energy difference between the Fermi level and the vacuum level; whereas the electron affinity represents the energy difference between the conduction band edge and the vacuum level. The electron affinity is a more convenient and more realistic way to characterise semiconductors as there are no electrons in the Fermi level. On this figure, the energy band diagram represents the situation where the metal work function is higher than the electron affinity.

When the metal and semiconductor are brought into intimate contact, the two Fermi levels must be equal at thermal equilibrium which means that electrons move from the semiconductor to the metal, as shown in figure 3-1 (b). This results in an excess negative charge at the metal surface and an excess positive charge at the

semiconductor surface due to ionised donors. This semiconductor region formed by the charge transfer is called the depletion region and expands to a width W in the semiconductor surface. However, as the electron concentration in the metal is much greater than the donor concentration in the semiconductor, the depletion region in the semiconductor side is larger than in the metal side (hundreds of Angstroms compared to a few Angstroms). As a result of the charge transfer across the interface, semiconductor bands bend upwards and the interface barrier, or Schottky barrier, ϕ_B is then the difference between metal work function and semiconductor electron affinity:

$$\phi_B = \phi_M - \chi_S \quad [3-1]$$

where

$$\chi_S = \phi_S - V_n \quad [3-2]$$

and

$$V_n = E_C - E_F = \frac{kT}{q} \ln \frac{N_C}{N_D} \quad [3-3]$$

where V_n is the energy difference between the bottom of the conduction band and the Fermi level, N_C and N_D are the effective density of states in the conduction band and donor concentration respectively, k is the Boltzmann constant, T the temperature in Kelvin and q the elemental electronic charge.

Similarly, when the semiconductor is p-type, and according to the Schottky-Mott model, then the Schottky barrier may be expressed as follow:

$$\phi_B = E_g - (\phi_M - \chi_S) \quad [3-4]$$

where E_g is the band gap.

Figure 3-1 showed the energy band diagram in the situation where $\Phi_M > \Phi_S$. In the same way, when the metal work function is smaller than the semiconductor work function ($\Phi_M < \Phi_S$), then the electrons flow from the metal to the semiconductor which results in downward band bending. The metal-semiconductor contact is called Ohmic, or nonrectifying, because the contact has a negligible contact resistance relative to the

bulk or series resistance of the semiconductor. When such a contact is biased, electrons encounter no barrier flowing from the semiconductor to the metal and the reverse direction current is eased by the high concentration of electrons in the region where the bands are bent downward.

Figure 3-2 shows the energy band diagram of a metal-semiconductor contact under different biasing situations with the same conditions as described in figure 3-1 (n-type semiconductor, $\Phi_M > \Phi_S$).

The built-in diffusion potential V_{bi} is represented as the potential that electrons have to overcome in order to move from the conduction band into the metal. If a positive voltage V_F is applied to the metal, this is a forward bias as shown in figure 3-2 (a), then the semiconductor-to-metal barrier height decreases. Hence, electrons can move more easily from the semiconductor into the metal because of the built-in potential reduction. Similarly, when a negative voltage V_R is applied to the metal, this is a reverse bias as shown in figure 3-2 (b), then the built-in potential is increased and it becomes more difficult for electrons to flow from the semiconductor into the metal. Figure 3-2 (c) shows the situation where the applied forward voltage is equal to the built-in diffusion potential V_{bi} . This is the flat-band case where semiconductor bands are not bent anymore.

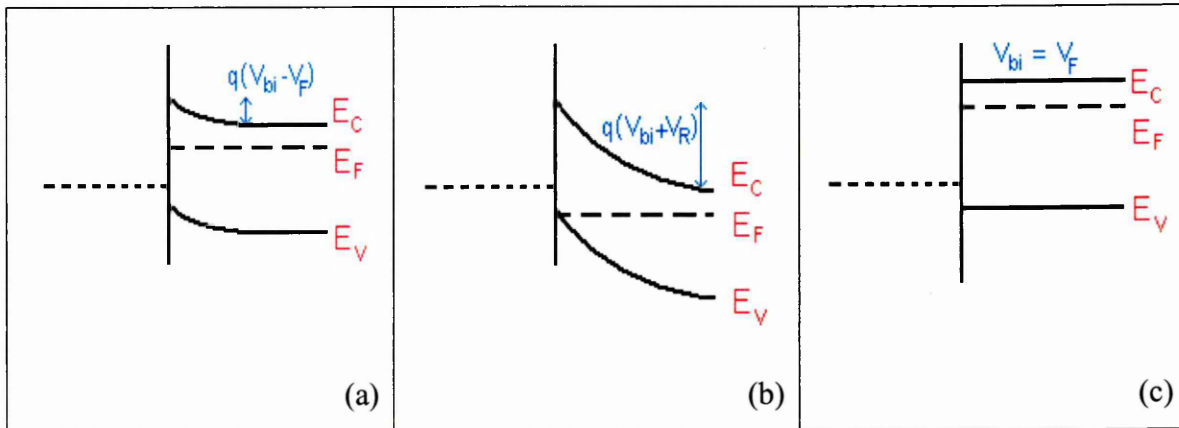


Figure 3-2: Energy band diagram of metal n-type semiconductor under the different biasing conditions: (a) forward bias; (b) reverse bias; (c) when the forward bias equals the built-in diffusion potential.

The depletion width W can be expressed as follows³:

$$W = \sqrt{\frac{2\epsilon_s}{qN_D}(V_{bi} - V)} \quad [3-5]$$

where ϵ_s is the semiconductor permittivity, V is the applied voltage which equal $+V_F$ for forward bias and $-V_R$ for reverse bias.

According to equation [3-5], the depletion width increases with increasing reverse bias, decreases with increasing forward bias, and the depletion region disappears when the applied voltage is equal to the diffusion potential (flat-band situation).

3.2.2. Origin of surface states

In a crystalline structure, the electrons are influenced by the periodic structure and arrangement of atoms. On the other hand, at the surface of a solid, the bulk periodic potential is abruptly terminated which means that the bulk material properties are no longer valid at the surface. At the surface, atoms have neighbours on one side only and the valence electrons on the vacuum side have no other partners with which to form covalent bonds. These unpaired electrons ('dangling bonds') act either as donors (giving electrons) or acceptors (accepting electrons), creating two surfaces states per surface atom. Therefore, surface states may exist whose wave-functions decay exponentially from the surface into the bulk and often have energies within the forbidden bandgap. These kinds of surface states which exist on a perfect free surface of an ideal solid are also intrinsic states, as opposed to interface states discussed in the next paragraphs.

3.2.3. Bardeen Model

This model points out the central role of surface states at a metal-semiconductor interface when the Schottky barrier is formed. Bardeen⁴ showed that if a density of localised surface states having energy distributed in the semiconductor bandgap is sufficiently high, the resulting metal-semiconductor contact will be practically independent of the metal. This model, as opposed to the Schottky-Mott model, takes into account the presence of an interfacial layer which is very often true for practical metal-semiconductor contacts. The energy band diagram is shown in figure 3-3. The contribution of surface states has been represented in red dashes.

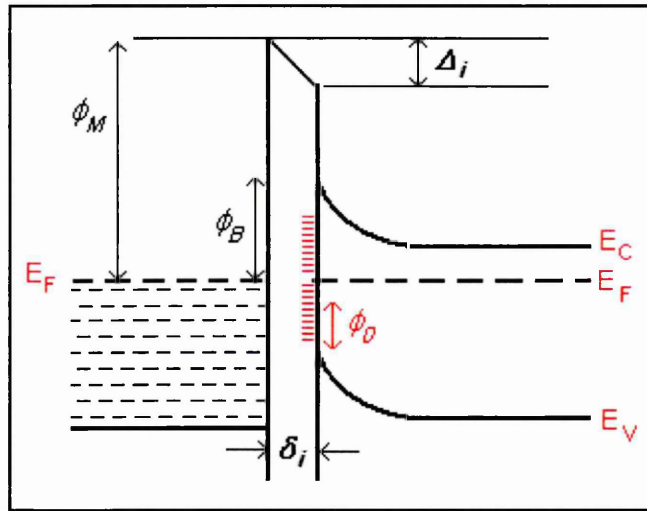


Figure 3-3: Energy band diagram of practical metal-semiconductor contact separated by an interfacial layer. Interface surface states are represented with small red lines.

The important parameter which is used to characterise the surface states is the neutrality level of these states ϕ_0 . This energy is measured relative to the valence band edge. Hence, states below ϕ_0 are called donor-like (positive when empty and neutral when full) while states above ϕ_0 are acceptor-like (neutral when empty and negative when full). The contribution of these states must be taken into account in the space charge neutrality of the contact. In addition, the presence of surface states tends to diminish the energy between the neutrality of these states ϕ_0 and the Fermi level E_F .

The final position of the Fermi level relative to ϕ_0 is then determined by the total density of surface states D_{SS} . If this quantity is high enough, then $\phi_0 \approx E_F$ and the barrier height is not dependant on the metal work function anymore. The Fermi level is said to be pinned and the Schottky barrier height may be expressed as follows:

$$\phi_B = E_g - \phi_0 \quad [3-6]$$

In the same way, when metal and semiconductor are separated by a thin interfacial layer as shown in figure 3-3, then the barrier height is given by:

$$\phi_B = \gamma(\phi_M - \chi_S) + (1 - \gamma)(E_g - \phi_0) \quad [3-7]$$

and

$$\gamma = \frac{\epsilon_i}{\epsilon_i + e\delta_i D_{SS}} \quad [3-8]$$

where ϵ_i is the permittivity of the interfacial layer, δ_i the interfacial layer thickness and D_{SS} the density of surface states ($\text{eV}^{-1}\text{cm}^{-2}$).

According to equation [3-8], if there is a large density of states ($D_{SS} \rightarrow \infty$), then $\gamma = 0$ and the Bardeen model is observed. If there are no surface states ($D_{SS} = 0$), then $\gamma = 1$ and the Schottky-Mott model is observed.

3.2.4. Unified Defect Model (UDM)

The unified defect model (UDM) was introduced by Spicer *et al.*⁵ and relies on the assumption that the Schottky barrier is caused by defects generated at the interface following the deposition of the metal contact. The defects are mainly native lattice defects such as substitutional impurities, vacancies or lattice mismatch with metal. It is pointed out that the intrinsic surface states are then perturbed by the effect of adatoms to the surface. In addition, the deposition of metal on the semiconductor surface might also result in the creation of additional surface states near the interface. These additional states, created by defects, can be generated by surface imperfections such as atomic steps (i.e. cleaved surface), vacancies, etc...

If the surface states created and/or modified by the formation of defects after deposition of metal are present in sufficiently high density, then they might cause Fermi level pinning.

3.2.5. Metal Induced Gap States (MIGS)

The origins of surface states at the interface between the metal and semiconductor were reviewed by Heine⁶ in 1965. The properties of metal-semiconductor contacts and the free semiconductor were usually described by the presence of surface states. However, these localised states should not exist. At metal-semiconductor interfaces, the electrons wavefunctions of the metal exponentially decay into the semiconductor and result in complex solutions.

Heine pointed out the existence of metal-induced interface states, derived from the virtual gap states (ViGS) of the complex band structure of the semiconductor. This

results in a continuum of states resulting from the tails of the electron wavefunctions of the metal decaying into the semiconductor, called metal-induced gap states (MIGS), with energies inside the bandgap⁷. Figure 3-4 shows the energy band diagram with the presence of MIGS at the semiconductor interface.

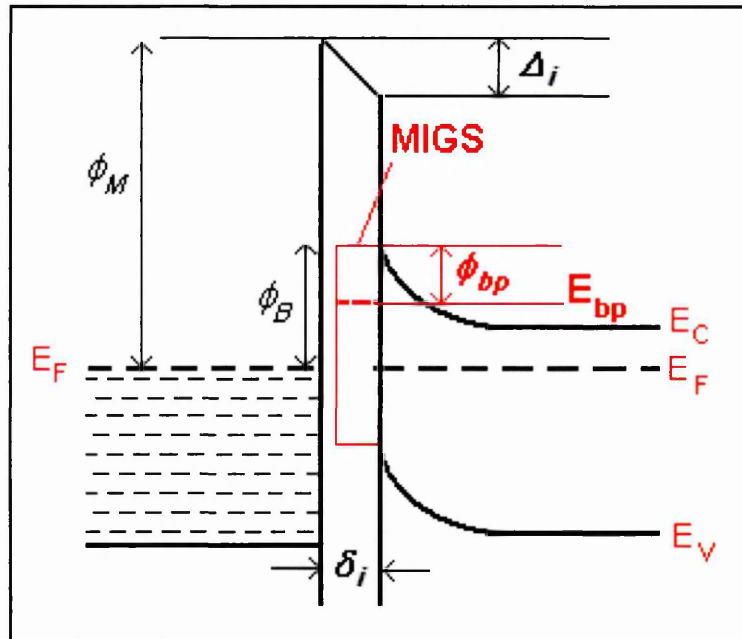


Figure 3-4: Energy band diagram of a metal-semiconductor contact separated by a thin interfacial layer. The continuum of MIGS is represented by the red box and covers the bandgap.

Similarly to the surface states described in the Bardeen model, a charge neutrality level of the MIGS can be defined. They are predominantly donor-like closer to the valence band maximum E_V and become mostly acceptor-like nearer to the conduction band minimum E_C . The energy level E_{bp} at which their dominant character changes is defined as the branch point. Hence, the net charge in these intrinsic gap states is positive, vanishes, and becomes negative when the branch point E_{bp} is above, coincides with, or lies below the Fermi level, respectively.

In the same way as for the Bardeen model, if these MIGS have a density high enough, they can cause Fermi level pinning at the surface and be responsible for the Schottky barrier formation. Depositing metal on top of the semiconductor will cause a charge transfer between the MIGS and the metal. Essentially, a thin interfacial layer of thickness δ_i is formed at the surface that does not contain conduction electrons. This

layer however, is thin enough to allow electron tunnelling. As a result, we can use the analysis of the previous section. However, due to their origins, Fermi level pinning caused by the MIGS is theoretically a reversible event, as opposed to the one initiated by the states described in the UDM. According to the MIGS model, re-evaporation of the metal after Schottky contact formation should drag the Fermi level to its original position before metal deposition.

3.2.6. Electronegativity

Electronegativity is a measure of the ability of an atom or molecule to attract electrons in the context of a chemical bond and was proposed by Pauling⁸. The distinction is made between covalent and ionic bond depending on the difference in electronegativity ΔX between the atoms involved. When the electronegativity difference is high, the bond is considered to be ionic, while low electronegativity difference leads to covalent bond. Hence, for ionic materials, the valence electrons will be localised near the atom with the higher electronegativity which will create an imbalance in the electronic charge allocation.

Kurtin *et al.*⁹ investigated the influence of the metal work function on the Schottky barrier height for various metals of different electronegativities X_M and three n-type semiconductors of different ionicity, as shown in figure 3-5.

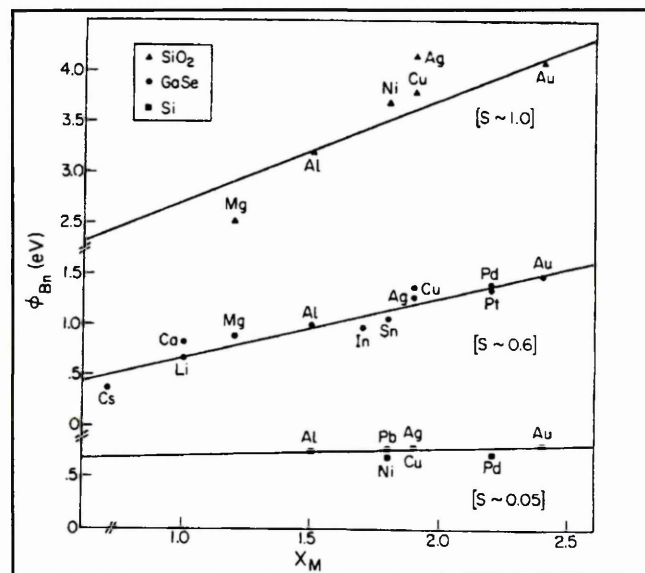


Figure 3-5: Influence of the metal electronegativity on the Schottky barrier height for various n-type semiconductors (from [9]).

The slope S of the straight lines fitted to the experimental data is then defined as the variation of the barrier height over the variation of the metal electronegativity for a given semiconductor ($S = d\Phi_B/dX_M$). This slope is found to be ≈ 1 (Schottky-Mott behaviour) for ionic semiconductors such as SiO_2 and ≈ 0 (Bardeen model dominated by surface states) for covalent bound Si.

Figure 3-6 shows the evolution of S with the ionicity measured by ΔX . The curve exhibits a well defined transition between covalent semiconductor, where the $\Delta X < 0.6$ and $S < 0.1$, and ionic compounds, where $\Delta X > 0.8$ and $S > 0.9$. These two regions are separated by an abrupt transition region where the electronegativity difference varies from 0.6 and 0.8.

$\text{Al}_x\text{Ga}_{1-x}\text{N}$ is a ternary compound whose chemical and electronic properties vary from that of AlN to GaN depending on the Al mole fraction in the matrix. In this work, only low Al contents ($x \leq 0.3$) are considered, but it can be noted that both binary compounds exhibit ionic behaviour ($\Delta X_{\text{GaN}} = 1.4$ and $\Delta X_{\text{AlN}} = 1.5$). For that reason, the Schottky barrier height of metal- $\text{Al}_x\text{Ga}_{1-x}\text{N}$ is expected to show a dependence on the metal electronegativity.

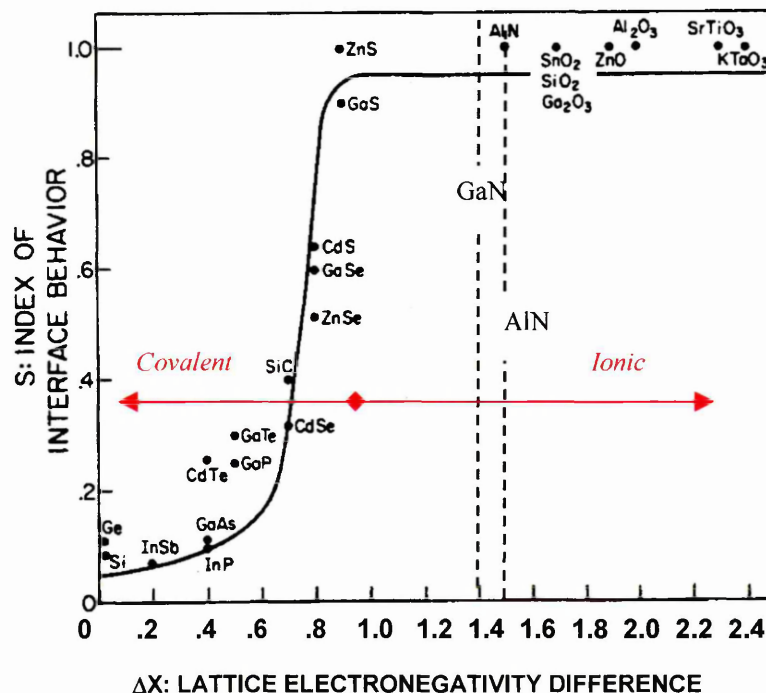


Figure 3-6: Index of interface behaviour S for different semiconductors as a function of the electronegativity difference ΔX between the atoms in the compounds (from [9]).

3.2.7. MIGS-and-electronegativity model

This model is mainly based on the contribution of the MIGS at the interface between the metal and semiconductor (see section 3.2.4.), and generalizing the concept of electronegativity presented in the previous section. Monch used the principles of Pauling's electronegativity concept to model the charge transfer across the metal-semiconductor interface¹⁰. He proposed that charge transfer across these interfaces varies proportionally to the electronegativity difference between the metal and semiconductor. The electronegativity of the semiconductor should be calculated by taking the geometric mean of the atomic electronegativities of the constituents^{11,12}:

$$X_{AB} = (X_A X_B)^{1/2} \quad [3-9]$$

Hence, according to this model, at the interface with the metal, the charge in the MIGS varies proportional to the difference ($X_M - X_S$). This means that if that difference is 0, then the Fermi level E_F coincides with the charge neutrality level, or branch point E_{bp} , of the MIGS. Consequently, according to the MIGS-and-electronegativity model, the Schottky barrier height may be expressed as follows¹³:

$$\phi_B = \phi_{bp} + S(X_M - X_S) \quad [3-10]$$

and

$$\phi_{bp} = E_g - E_{bp} \quad [3-11]$$

where ϕ_{bp} is the zero-charge transfer barrier height or energy position of the branch point E_{bp} relative to the semiconductor conduction band, S is the slope defined in the previous section, X_M and X_S are the metal and semiconductor electronegativities, respectively.

Excellent agreement between experimental data and predictions based on the MIGS-and-electronegativity model has been found for binary^{14,15,16,17} and ternary¹⁸ compound Schottky contacts. Figure 3-7 shows an example of comparison between experimental data taken for metal-GaN contacts and the MIGS-and-electronegativity calculations¹⁷. The metals (Au, Pt, Cr, Ni and Cu) were sputter-deposited on n-GaN surfaces and barrier heights were measured using (I-V) and (C-V) techniques.

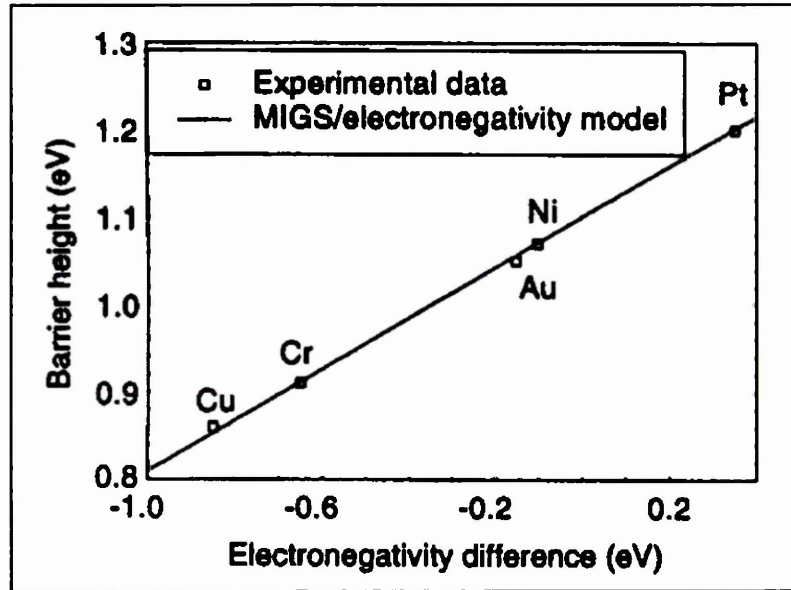


Figure 3-7: Metal-GaN Schottky barrier height as a function of the electronegativity between metals and GaN (from ref. [17]). The straight line gives the MIGS-and-electronegativity model prediction using the zero-charge-transfer barrier height $\phi_{bp} = 1.07$ eV and the slope parameter $S = 0.29$ /Miedema-unit.

3.2.8. Effective work function model

This model suggests that the Fermi level at the surface of a semiconductor or at a metal-semiconductor interface is not fixed by surface states but rather is related to the work functions of microclusters of one or more interface phases resulting from either oxygen contamination or metal-semiconductor reactions which occur during metallization. Good agreement was found with the Schottky-Mott model when the metal work function is replaced by an effective work function¹⁹. According to this assumption, the ideal Schottky-Mott relationship may be written as:

$$\phi_B = \phi_{eff} - \chi_s \quad [3-12]$$

where ϕ_{eff} is an appropriately weighted average of the work function of the different interface phases.

3.2.9. Cowley-Sze model

This model put forward by Cowley and Cze²⁰ assumes a uniform density of surface states D_{SS} ($\text{cm}^{-2}\text{eV}^{-1}$), throughout the bandgap. Neglecting any image charge effect, the barrier height ϕ_B is expressed as a sum of the “bare surface barrier height” ϕ_0 or band bending before metal deposition, and a Schottky-Mott term induced by the metal:

$$\phi_B - \phi_0 = S(\phi_M - \chi_S) - S\phi_0 \quad [3-13]$$

where ϕ_M is the metal work function and χ_S the semiconductor electron affinity. S is a constant depending only on the density of surface state D_{SS} and can be expressed as follows:

$$D_{SS} \approx 10^{13} \frac{(1-S)}{S} \quad [3-14]$$

3.2.10. Intimate contacts

The theory of metal-semiconductor contact formation has attracted a lot of interest because of its importance for semiconductor device technology. Normally, a thin insulating layer is formed between the metal and semiconductor but the interfacial oxide layer is thin enough (about 10 to 20 Angstroms) to allow electrons to tunnel through it and the semiconductor surface is effectively decoupled from the metal.

However, it is possible to obtain intimate contact between the metal and semiconductor, formed on a clean semiconductor surface, using a wide range of cleaning techniques. It is important to note that the pre-metallization cleaning procedures should take place in an UHV environment in order to avoid surface contamination which may lead to the formation of an insulating layer. The cleaning techniques such as wet chemical cleaning (acid etch, boiling solutions), high temperature annealing or ion bombardment may cause surface damage. For this reason, some equipment is available to grow the sample and allows *in-situ* metal deposition. In this case, the sample should be free of contamination and/or cleaning-induced defects.

When intimate contacts between the metal and semiconductor are achieved, the surface is likely to change after the deposition of the metal. This may be the result of

chemical reactions at the surface, or interdiffusion, which could lead to the formation of an interfacial compound layer. Metal deposition may also induce defects at the surface which might pin the Fermi level if present in sufficiently high density, as described in the UDM model. Similarly, MIGS are likely to be present at the surface after metal deposition and may represent the main cause of the Schottky barrier formation.

3.3. Current transport mechanisms

There are three main transport mechanisms by which electrons can cross from the semiconductor into the metal under applied bias, as shown in figure 3-8:

- (a) Emission over the barrier;
- (b) Quantum-mechanical tunnelling through the barrier;
- (c) Recombination.

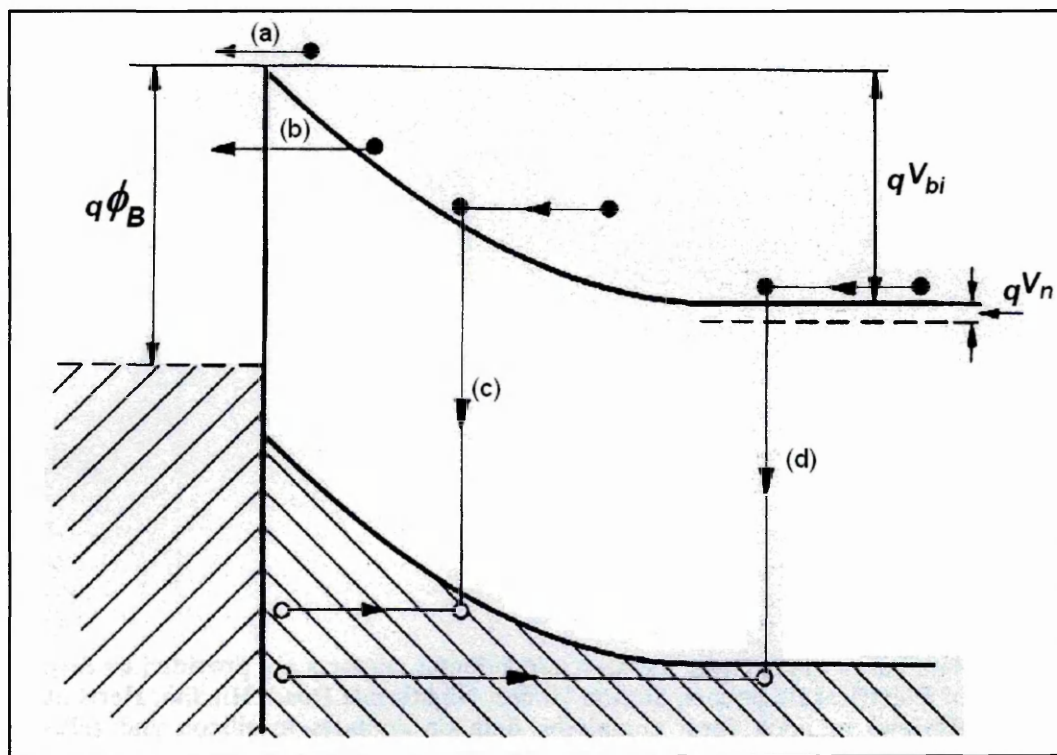


Figure 3-8: Schematic diagram of current transport mechanisms across metal/n-type semiconductor under forward bias. Process (d) represents the recombination mechanism outside the depletion region (from ref. [21]).

The different transport mechanisms across the Schottky contact may be identified through the current-voltage (I-V) characteristics of the diode. In the ideal case,

the current transport across the barrier is entirely dominated by mechanism (a), while in practical situations, mechanisms (b) and (c) are not negligible. Emission over the barrier is represented by the transfer of electrons across the barrier and occurs following different processes: the thermionic emission happens together with the drift and diffusion current. In traversing the semiconductor depletion region, the electrons motion is governed by the mechanisms of diffusion and drift in the electric field of the barrier. According to the diffusion theory, the impediment to current flow across the barrier is only related to the processes of drift and diffusion in the semiconductor depletion region, where the semiconductor has relatively low doping and low mobility. On the other hand, the thermionic emission theory assumes that the interface barrier represents an important impediment to the current flow.

Although the real current is a combination of these two theories, experimental results show that the thermionic emission is the dominant process²¹ mainly because of the relatively high mobility of the semiconductor materials. Therefore, as the materials system used in this work has very high electron mobility, the processes of drift and diffusion may be neglected. In this part, the different electron transport mechanisms are presented.

3.3.1. Thermionic emission

Bethe *et al.*²² investigated the theory of the influence of thermionic emission on the electron transfer across metal-semiconductor interfaces. They presented a theory where the effect of drift and diffusion in the depletion region is negligible. The current is controlled by the transfer of electrons across the barrier. According to the kinetic theory of gases, only a limited number of electrons can cross the barrier in unit time. Boltzmann statistics are used to derive the electron density probability, and the number of electrons with velocity between v_x and v_x+dx , which pass unit cross-section in unit time, is given by²³:

$$dn = n_e v_x \sqrt{\frac{m}{2kT}} \exp\left(\frac{-mv_x^2}{2kT}\right) dv_x \quad [3-15]$$

where n_e is the equilibrium electron concentration and m the standard electron mass. The minimum velocity v_{x0} required to cross the barrier from the semiconductor (under forward bias) can be written as:

$$E_0 = \frac{1}{2} m^* v_{x0}^2 = q(V_{bi} - V_F) \quad [3-16]$$

where V_{bi} is the built-in diffusion potential and V_F the applied bias ($V_F > 0$).

The current density in the forward direction j_+ can be expressed as follows:

$$j_+ = q \int_{x_0}^{\infty} dn = n_e q \sqrt{\frac{kT}{2\pi m^*}} \exp\left(\frac{-q(V_D - V_F)}{kT}\right) \quad [3-17]$$

The electron concentration at the interface is given by:

$$n_e = 2 \left(\frac{2\pi m^* kT}{h^2} \right)^{3/2} \exp\left(\frac{-q(\phi_B - V_F)}{kT}\right) \quad [3-18]$$

The total current density $j = j_+ + j_-$ must be zero when $V = 0$, which leads to:

$$j = j_0 \left[\exp\left(\frac{qV}{kT}\right) - 1 \right] \quad [3-19]$$

and:

$$j_0 = A^* T^2 \exp\left(\frac{-q\phi_B}{kT}\right) \quad [3-20]$$

where $A^* = 4\pi q m^* k^2 / h^3$ is the effective Richardson constant and m^* the electron effective mass.

3.3.2. Quantum mechanical tunneling

Electrons can overcome a potential barrier if their energy is higher than the energy of the barrier. However, electron tunneling through the barrier may be possible even if the temperature is not high enough for the electrons to be thermally excited over the barrier. In quantum mechanics, an electron has a non-zero probability of crossing a barrier potential greater than its energy. The wave vector of the electron wave function becomes imaginary within the barrier and the wave function decays exponentially with the distance.

Figure 3-9 shows the tunneling process which may occur following two mechanisms. The field emission mechanism operates when the semiconductor is heavily doped (degenerate semiconductors) at very low temperature. Electrons whose energy is close to the Fermi level can tunnel through the barrier, hence creating a forward current.

The other type of tunneling is the thermionic-field emission. This may occur when the temperature is increased so that electrons are excited to higher energies where the barrier is thinner and tunneling more likely to happen. However, if the temperature is further increased, electron energies may be greater than the barrier and pure thermionic emission will be predominant.

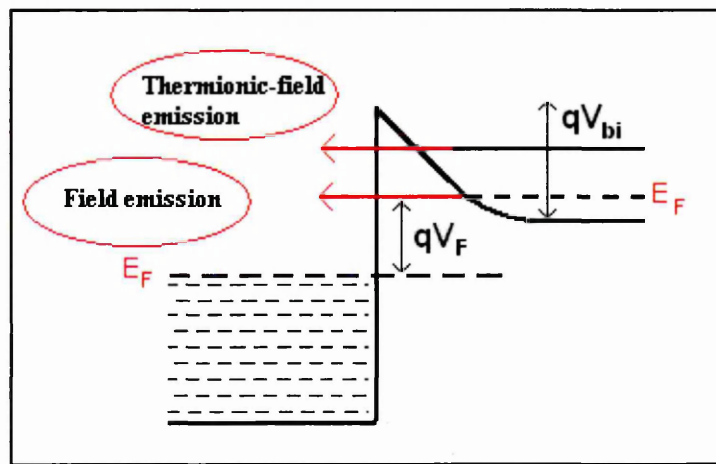


Figure 3-9: Schematic diagram of the two tunneling mechanisms at metal-semiconductor interface under forward bias.

By applying the WKB (from G. Wentzel, H.A. Kramers and L. Brillouin) approximation to a triangular barrier, the probability P , of a triangular barrier being tunnelled by an electron with energy ΔE less than the barrier height is given by²¹:

$$P = \exp \left\{ \frac{-2(\Delta E)^{3/2}}{3E_{00}} \sqrt{V_{bi}} \right\} \quad [3-21]$$

and

$$E_{00} = \frac{h}{2\pi} \sqrt{\frac{N_D}{m^* \epsilon_s}} \quad [3-22]$$

where N_D is the donor concentration in the semiconductor and ϵ_s its permittivity.

Parameter E_{00} is used to assess the primary electron transport mechanism across the potential barrier. If $E_{00} \gg kT/q$, field emission is likely to occur; if $E_{00} \approx kT/q$, thermionic-field emission is expected; and if $E_{00} \ll kT/q$, then pure thermionic emission is dominant²⁴. Hence, increasing the doping leads to higher E_{00} which may make field emission more likely to happen. This is why field emission only occurs in degenerate semiconductors. Therefore, for Ohmic contacts formed with degenerate semiconductors, the high resistivity of the barrier may be overcome by electrons tunneling from semiconductor into the metal via field emission.

The current-voltage relationship can be written similarly to that of thermionic emission theory and is given by²⁴:

$$j = j_s \exp\left(\frac{V}{E_0}\right) \left\{ 1 - \exp\left(-\frac{qV}{kT}\right) \right\} \quad [3-23]$$

where $E_0 = E_{00}$ for field emission and $E_0 = E_{00} \coth(qE_{00}/kT)$ for thermionic field emission. For thermionic field emission, the pre-exponential term j_s is given by²⁴:

$$j_s = A^* T^2 \exp\left(-\frac{qV_n}{kT}\right) \frac{q}{kT} \frac{\{\pi E_{00} (\phi_B - V - V_n)\}^{1/2}}{\cosh(qE_{00}/kT)} \exp\left(-\frac{\phi_B - V_n}{E_0}\right) \quad [3-24]$$

3.3.3. Recombination current

Although recombination currents are relatively small, electron-hole recombination process can occur in the depletion region through localised states or in the bulk of the semiconductor due to hole injection. This may occur in metal-semiconductor (n-type) contacts when the Schottky barrier height is greater than half of the bandgap, in which case the semiconductor region bordering the metal has become p-type and consists of a high density of holes.

For low forward bias, the recombination current density can be expressed as follows²⁵:

$$j = j_0 \exp\left(\frac{qV}{2kT}\right) \left\{ 1 - \exp\left(-\frac{qV}{kT}\right) \right\} \quad [3-25]$$

and

$$j_0 = qn_i \frac{W}{2\tau_r} \quad [3-26]$$

where n_i is the intrinsic electron concentration, W the depletion width and τ_r the lifetime within the depletion region (or electron-hole recombination time).

3.4. Extraction of the Schottky parameters

In order to achieve the desired Schottky contact, it is important to be able to extract the Schottky parameters such as the barrier height and ideality factor n . Various measurement techniques such as current-voltage (I-V), capacitance-voltage (C-V), photoelectron spectroscopy have been used to extract these parameters. It is also important to measure the same interface using different techniques, as the possible discrepancies may give useful information about the transport mechanisms across the contact.

In this work, current-voltage (I-V) and X-ray photoelectron spectroscopy (XPS) have been used to extract the metal- $\text{Al}_x\text{Ga}_{1-x}\text{N}$ Schottky contact parameters. Therefore, this part is composed of two sections: extraction of the ideality factor n and Schottky barrier from (I-V) measurements is presented, and then the determination of Φ_B through XPS scans is explained.

3.4.1. Current-voltage measurement

This technique is based on the thermionic emission theory explained in section 3.1.1. However, according to equations [3-19] and [3-20], the Schottky barrier height should be corrected by considering an effective barrier height ϕ_{eff} which would be bias dependant.

In fact, the image-force lowering barrier would affect the Schottky barrier height. Electrons approaching the metal surface experience an attractive force as if a positive charge of magnitude q was located at the mirror image of the electron with respect to

the interface. This effect gives the electrons a negative potential energy, which has to be added to the potential energy due to the Schottky barrier thus leading to a lowering of the barrier by an amount $\Delta\phi_{Bi}$.

Hence, the effective barrier height, ϕ_{eff} can be expressed as follows:

$$\phi_{eff} = \phi_{B0} - (\Delta\phi_{Bi})_0 + \beta V \quad [3-27]$$

where ϕ_{B0} and $(\Delta\phi_{Bi})_0$ are the barrier height and image-force lowering at zero-bias. The variation of the effective barrier height with bias is assumed to be linear, with

$$\beta = \frac{\partial\phi_{eff}}{\partial V} = \text{constant.}$$

According to that, rewriting equations [3-19] and [3-20] lead to the following current densities²¹:

$$j = j_0 \exp\left(\frac{qV}{nkT}\right) \left\{ 1 - \exp\left(-\frac{qV}{kT}\right) \right\} \quad [3-28]$$

and

$$j_0 = A^* T^2 \exp\left[-\frac{q}{kT}(\phi_B - \Delta\phi_{Bi})\right] \quad [3-29]$$

where $1/n=1-\beta$. n is called the ideality factor because real diodes become "ideal" when n is close to unity (n cannot be smaller than one because β is always positive in the forward direction). For applied voltages such as $V > 3kT/q$, and using the current notation, equation [3-19] can be simplified as²¹:

$$I = I_0 \exp\left(\frac{qV}{nkT}\right) \quad [3-30]$$

and

$$I_0 = AA^* T^2 \exp\left(\frac{-q\phi_B}{kT}\right) \quad [3-31]$$

where A is the contact area and A^* is the effective Richardson constant.

Extraction of the ideality factor and Schottky barrier from current-voltage measurements is carried out using equations [3-30] and [3-31]. The plot $\ln I = f(V)$ should exhibit a straight line for $V > 3kT/q$ where the slope yields n and intercept at $V = 0$ is I_0 which yields ϕ_B .

This extraction method is the simplest and is therefore widely used to obtain the Schottky parameters from I-V curves. However, it may be possible that the linear region is hidden by series resistances even at low voltage. This is the reason why more extraction methods have been investigated²¹ (Norde plot, Small signal conductance, etc...) and are still of interest²⁶. For high values of n , the diode becomes far from ideal and the assumption of purely thermionic emission is no longer valid which leads to errors in evaluation of the barrier height. The best diodes are always referred to those with lowest ideality factor where the measurement of the barrier height is more reliable. The departure from ideality may be due to the presence of a thick interfacial layer or to tunnelling and recombination currents²¹.

3.4.2. X-ray Photoelectron Spectroscopy (XPS)

This surface sensitive technique has been used to assess the chemical and electronic changes occurring at the interface between the metal and semiconductor. Details of the XPS technique will be presented in the next chapter.

Figure 3-10 shows the EDC (Energy distribution curve) for metal and semiconductor together with the corresponding energy band diagram. The sharp discrete peaks on the EDC can be used to identify the elements present at the surface, as core-level binding energies are characteristic of the elemental species.

Thin layers of metal are successively deposited to the semiconductor surface and XPS scans of the surface are taken before and after metallization. Schottky barrier heights were determined from the XPS data using the relation previously used by Waldrop and Grant^{27, 28} for metal-SiC and metal-GaAs barrier height calculations:

$$\phi_B = E_g - E_{VBM}^i + (E_{core}^i - E_{core}^m) \quad [3-32]$$

where E_g is the band gap, E_{VBM}^i is the binding energy of the valence band maximum of the semiconductor, E_{core}^i is the initial binding energy of the core-level peak and E_{core}^m is the binding energy of the material core-level peak following metal deposition.

All binding energies are measured relative to the Fermi energy. Hence, it is important to calibrate the analyser by scanning a metal to determine the position of the Fermi level. The E_{VBM}^i value can be obtained by finding the intersection of a line fitted to the leading-edge of the XPS valence band with one fitted to background points above the valence-band maximum.

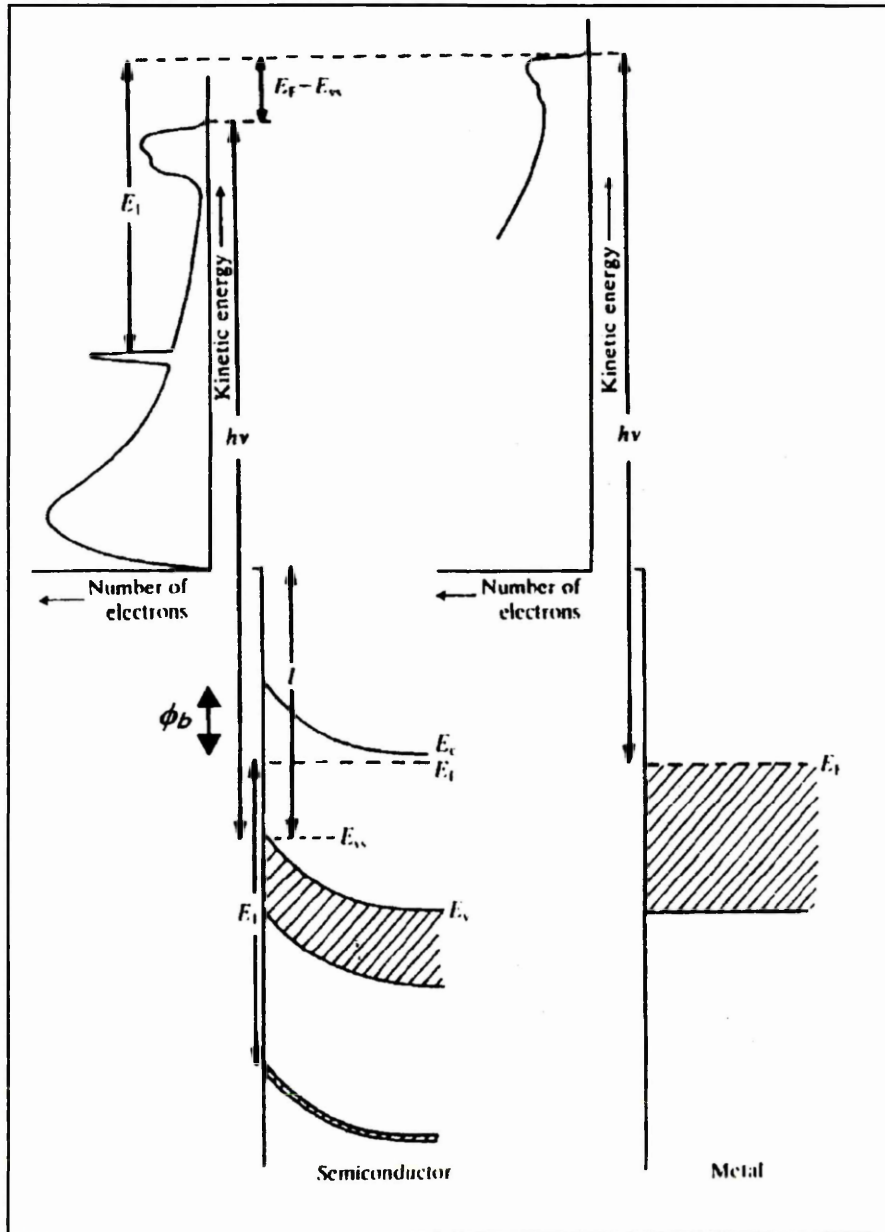


Figure 3-10: Energy band diagrams of metal and semiconductor with their corresponding energy distribution curves (EDC) in the photoelectron spectra (from ref. [21]).

It is very difficult to determine E_{VBM}^i via XPS using standard X-ray non-monochromated sources, and the position of the valence band is often measured using low energy X-rays, tuneable synchrotron radiation or ultra-violet photons. However, some XPS equipment using high-power monochromated X-rays sources operating at high resolution may allow the measurement of the valence band maximum (i.e. XPS at NCESS, see next chapter). The difference ($E_{core}^i - E_{core}^m$) is known as total band bending between the clean surface and the last metal deposition.

This extraction method has been used on metal-GaN Schottky contacts and the Schottky barrier height measured with XPS was in accordance with those measured with (I-V), (C-V) and UPS²⁹.

References

1. W. Schottky, *Naturwissenschaften*, **26**, 843, (1938).
2. N.F. Mott, *Proc. Cambr. Phil. Soc.*, **34**, 568, (1938).
3. S.M. Sze, "Semiconductor Devices Physics and Technology", 2nd Edition, John Wiley & Sons, (2002).
4. J. Bardeen, *Phys. Rev.* **71**, 717, (1947).
5. W.E. Spicer, I. Lindau, P. Skeath, C.Y. Su and P. Chye, *Phy. Rev. Lett.* **44**, 420, (1980).
6. V. Heine, *Physical Review A* **138**, 1689, (1965).
7. J. Tersoff, *Phys. Rev.Lett.* **52**(6), 465, (1984).
8. L.N. Pauling, "The nature of the chemical bond", 2nd ed., Cornell University Press, Ithaca, NY, (1960).
9. S. Kurtin, T. C. McGill, C. A. Mead, *Physical review letter* **22**, 1433 (1969).
10. W. Monch, *Festkorperprobleme (Advances in Solid State Physics)*, Vol. 26, Ed. P. Grosse (Vieweg, Braunschweig), (1986).
11. W. Monch, *Rep. Prog. Phys.* **53**, 221, (1990).
12. W. Monch, *Surf. Sci.* **299/300**, 928, (1993).
13. W. Monch, *Phys. Rev. Lett.* **58**, 1260 (1987).
14. T.U. Kampen, W. Monch, *MRS Internet J. Nitride Semicond. Res.* **1**(41), (1996).
15. T.U. Kampen, W. Monch, *Appl. Surf. Sci.* **117/118**, 388, (1997).
16. W. Monch, *J. Vac. Sci. Technol. B* **17**(4), 1867, (1999).
17. H.P. Hall, M.A. Awaah, K. Das, *Semicond. Sci. Technol.* **19**, 176, (2004).
18. W. Monch, *Appl. Phys. Lett.* **67**(15), 2209, (1995).
19. J.L. Freeouf, J.M. Woodall, *Appl. Phys. Lett.* **39**, 727, (1981).
20. A.M. Cowley and S.M. Sze, *J. Appl. Phys* **36**, 3212 (1965).
21. E.H. Rhoderick and R.H. Williams, "Metal-semiconductor contacts", Oxford university press, (1988).
22. H.A. Bethe, *M.I.T. Radiat. Lab. Rep.*, 43-12, (1942).
23. H.K. Henisch, "Semiconductor contacts", Oxford university press, (1988).
24. F.A. Padovani and R. Stratton, *Solid state electronics* **9**, 695, (1966).
25. C.T. Sah, R.N. Noyce and W. Shockley, *Proc. IRE* **45**, 1228, (1957).
26. J. Osvald, E. Dobrocka, *Semicond. Sci. Technol.* **11**, 1198, (1996).
27. J.R. Waldrop, R.W. Grant, *Appl. Phys. Lett.* **52**, 1794, (1988).
28. J.R. Waldrop, R.W. Grant, *Appl. Phys. Lett.* **62**, 2685, (1993).
29. K.M. Tracy, P.J. Hartlieb, S. Einfeldt, R.F. Davis, E.H. Hurt, R.J. Nemanich, *J. Appl. Phys.* **94**(6), 3939, (2003).

Chapter 4

Experimental Techniques

The formation of metal- $\text{Al}_x\text{Ga}_{1-x}\text{N}$ Schottky contacts was carried out through a combination of current-voltage measurements (I-V), scanning probe microscopies such as atomic force and scanning tunneling microscopy (STM and AFM), and X-ray photoelectron spectroscopy (XPS).

This analytical technique has been chosen to investigate the electronic and chemical changes at the metal- $\text{Al}_x\text{Ga}_{1-x}\text{N}$ interface, when the interface is formed. As a main analysis technique, it is important to explain the fundamental theory and underlying principles in order to analyse the data in a sensible way.

Hence, in this chapter, the basic theory of XPS will be developed in order to facilitate the data interpretation. The experimental details of the three ultra high vacuum systems used in this project will be briefly presented, together with the different surface heating setups and metal deposition systems.

4.1. Principles

XPS relies on the photoelectric effect discovered by Einstein¹, which is the primary interaction of photons with solids and gives rise to the photoemission process. In the XPS system, the sample is subjected to an X-ray photon flux with energy $h\nu$. The photon energy must be high enough for the electrons to overcome the work function of the solid in order to lead to photoemission as shown in figure 4-1.

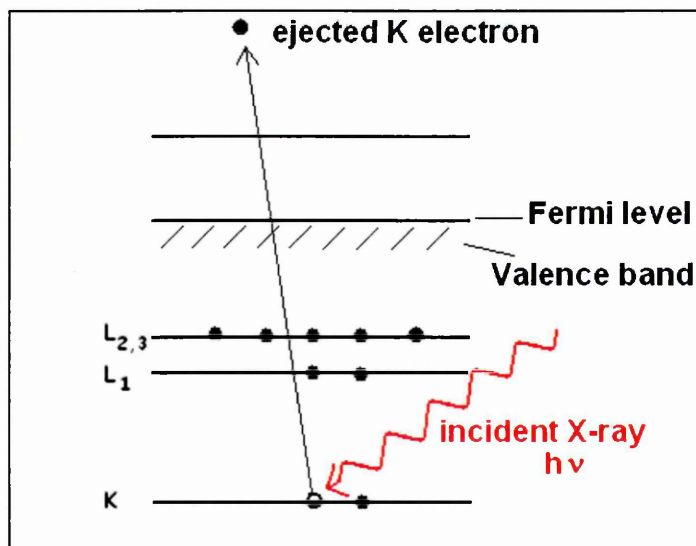


Figure 4-1: The photoemission process.

The kinetic energy of the emitted photoelectron can be expressed using the following relation:

$$E_k = h\nu - E_i - \phi \quad [4-1]$$

where $h\nu$ is the energy of the incident X-ray beam, E_i is the initial state energy of an electron in the solid, and ϕ is the work function of the solid. Then, using Koopman's theorem², the initial state energy can be approximated to the binding energy of the electron in the solid. However, this approximation doesn't take into account the effect of the core hole left after photoionisation. The remaining electrons will relax to a lower state in order to screen the photo-hole from the nucleus which in turn creates an excess

energy transmitted to the photoelectron. Hence, the photoelectron kinetic energy of the ejected photoelectron is increased resulting in an apparent reduced binding energy.

After escaping from the surface, the emitted photoelectrons are collected and then counted according to their kinetic energies in a spectrometer. The result from the analyser is presented as an energy distribution curve (EDC) as shown in figure 4-2.

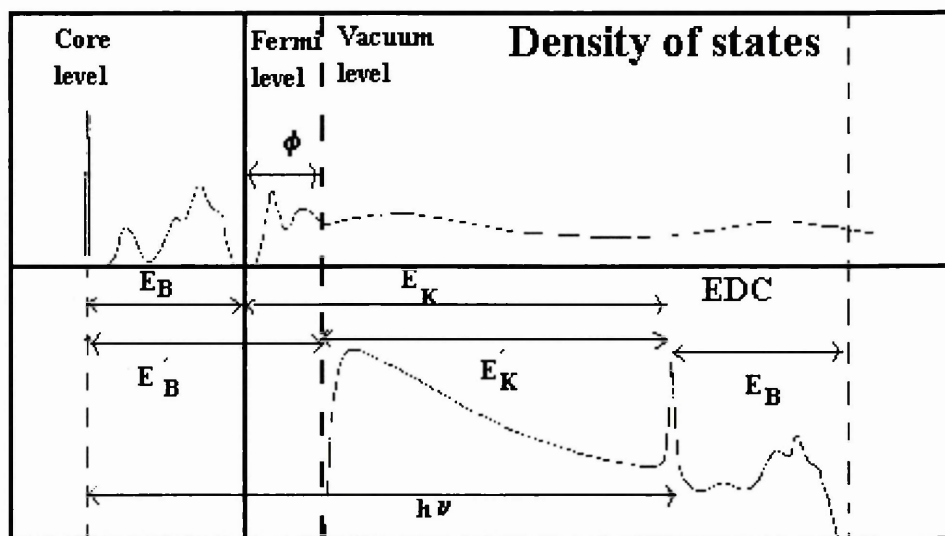


Figure 4-2: Schematic diagram showing the density of states in a solid and the corresponding photoelectron energy distribution curve (EDC) with photoemission process (from ref. [4]).

The EDC is mainly composed of sharp discrete peaks representing the core level electron emission and a broader valence band at higher kinetic energy. The large featureless background represents the emission of electrons that have undergone inelastic scattering and lost energy while escaping from the surface. Hence, the EDC cannot directly represent the density of filled states.

The sharp discrete peaks on the EDC can be used to identify the elements present at the surface, as core-level binding energies are characteristic of the elemental species. This allows an identification of the chemical composition near the surface and is the reason why XPS is also known as electron spectroscopy for chemical analysis (ESCA).

In the same way, the examination of core-level binding energy changes give useful information on structural, chemical, and electronic changes near the surface. Additionally, the fact that photoemission is a non-destructive process makes XPS very attractive for semiconductor surface and interface analysis.

4.2. Photoemission process

There are many models that have been proposed to describe the photoemission process, the most accurate ones being those that describe it as a single quantum mechanical event, from the absorption of a photon through to the emission and detection of the photoelectron³.

However, these theories are extremely complex. Hence, for the purpose of explaining the photoemission process and the phenomena observed in the photoemission data presented here, a simpler model, "The Three Step Model", is discussed^{6,7}. This model neglects many body-effects such as electron-electron interactions and inelastic scattering and focuses on the elastically scattered electrons.

The Three Step Model describes the photoemission process in three stages, which are all dependent on the initial electron energy (E) and the energy of the incident photons ($h\nu$). These stages are:

- Photoexcitation of the electron $P(E, h\nu)$
- Transport and propagation through the solid $T(E, h\nu)$
- Escape from the solid surface into vacuum $D(E, h\nu)$

The intensity of the resulting photocurrent $I(E, h\nu)$ is given by the relation,

$$I(E, h\nu) = P(E, h\nu)T(E, h\nu)D(E, h\nu) \quad [4-2]$$

Step one: Photoexcitation

Details of quantum physics calculations and the different approximations leading to the expression of the photocurrent may be found elsewhere^{6, 7, 8, 9}.

The resulting photocurrent is given by the following equation:

$$P(E, h\nu) = \frac{2\pi}{\hbar} \sum_i \left| \langle \psi_f | \hat{W} | \psi_i \rangle \right|^2 \delta(E_f - E_i - h\nu) \quad [4-3]$$

where ψ_i and ψ_f are the initial state and final state wavefunctions, having energies E_i and E_f , respectively. The δ -term ensures that there is energy conservation between $h\nu$ and the transition energy ($E_f - E_i$). \hat{W} is the electron-radiation interaction Hamiltonian.

The summing over all initial states is an approximation, with a more accurate summation being one that incorporates all final states as well. However, for a large density of final states, the modulation of the photocurrent will be negligible. Only for low final state energies (≤ 20 eV) does this final state density become significant to the observed photocurrent and hence for XPS experiments this effect will be trivial resulting in the photocurrent being characteristic of the initial density of states.

Step two: Transport and propagation of the electron through the solid

Once the electrons have been excited due to the absorption of a photon, they must travel through the surface of the solid where they will be emitted and detected. On the way to the surface, it is highly likely that the electrons will be scattered and hence the resulting photocurrent will be modified. The propagation probability $T(E, h\nu)$ can be expressed in terms of the inelastic mean free path of the electron $\lambda(E)$, which is defined as the average distance an electron with energy E can travel through a solid before being inelastically scattered. If one considers the number of electrons (N_o) that are photoexcited at a distance x from the surface, then the number of electrons (N) that actually reach the surface without losing any energy is given by the following equation:

$$N = N_o \exp\left(\frac{-x}{\lambda(E)}\right) \quad [4-4]$$

Hence, the propagation probability can be written as follows⁹:

$$T(E, h\nu) = \exp\left(\frac{-x}{\lambda(E)}\right) \quad [4-5]$$

If the penetration depth (x) of the photon is assumed to be much larger than λ , then the above equation is thought to be a constant.

Step three: Electron escape from the solid

Once the electrons have propagated to the surface of the solid, they must possess enough energy to escape into vacuum. The electrons must have a component of momentum normal to the surface and enough energy to overcome the work function of the solid.

Therefore, the probability of escape from the solid $D(E)$ may be simply described as zero when the electrons do not have enough energy to escape and one when they do, as follows:

$$D(E) = 0 \quad \text{when } E_{norm} - E_{vac} < \phi \quad [4-6]$$

$$D(E) = 1 \quad \text{when } E_{norm} - E_{vac} \geq \phi \quad [4-7]$$

where E_{norm} is the component of final state energy normal to the surface and E_{vac} is the vacuum level of the solid.

The final expression for the photocurrent can be written as a product of the three steps described previously, as follows:

$$I(E, h\nu) = \frac{2\pi}{\hbar} \sum_i \left| \langle \psi_f | \hat{\mathbf{W}} | \psi_i \rangle \right|^2 \delta(E_f - E_i - h\nu) \exp\left(\frac{-x}{\lambda(E)}\right) D(E) \quad [4-8]$$

The Three Step Model is relatively basic as it neglects many-body effects. However, it is useful for interpreting the EDC's obtained by the photoemission technique and makes XPS a surface sensitive technique.

4.3. Surface sensitivity

4.3.1. Inelastic mean free path (IMFP)

As the excited photoelectrons propagate through the solid towards the surface, they can be scattered either elastically or inelastically by scattering centres within the solid. If an electron is elastically scattered it suffers no loss in energy but can experience a change in direction and upon detection will provide information on the energy state of the core level it was emitted from. Inelastically scattered electrons undergo a loss of energy and may also experience a change in direction. Typically electrons may lose up to several eV due to inelastic scattering, although scattering by phonons results in a loss of energy of only a few meV and is negligible compared to the resolution of the spectrometer. Electrons that do encounter inelastic scattering may do so on a random number of occasions and hence may lose a significant amount of energy on the way to the surface. If the electrons still have enough energy to escape from the solid surface, they will have a kinetic energy significantly different to that of the elastically scattered electrons and will contribute in a random way to the featureless background to lower kinetic energy on the EDC. Inelastic scattering occurs due to the creation of electron-hole pairs or by the generation of plasmons, which involve a collective oscillation of conduction, valence or shallow core level electrons. Plasmon loss features are not random and give rise to peaks at about 10 to 30 eV on the lower kinetic energy side of the unscattered elastic emission peak.

The inelastic mean free path (λ) of an electron is defined as the average distance that an electron of energy E , can travel through the solid before being inelastically scattered¹⁰. The value of λ for electrons in a solid is greatly dependent on the kinetic energy of the electron. The relationship between the two parameters is represented by the "universal curve" shown in figure 4-3.

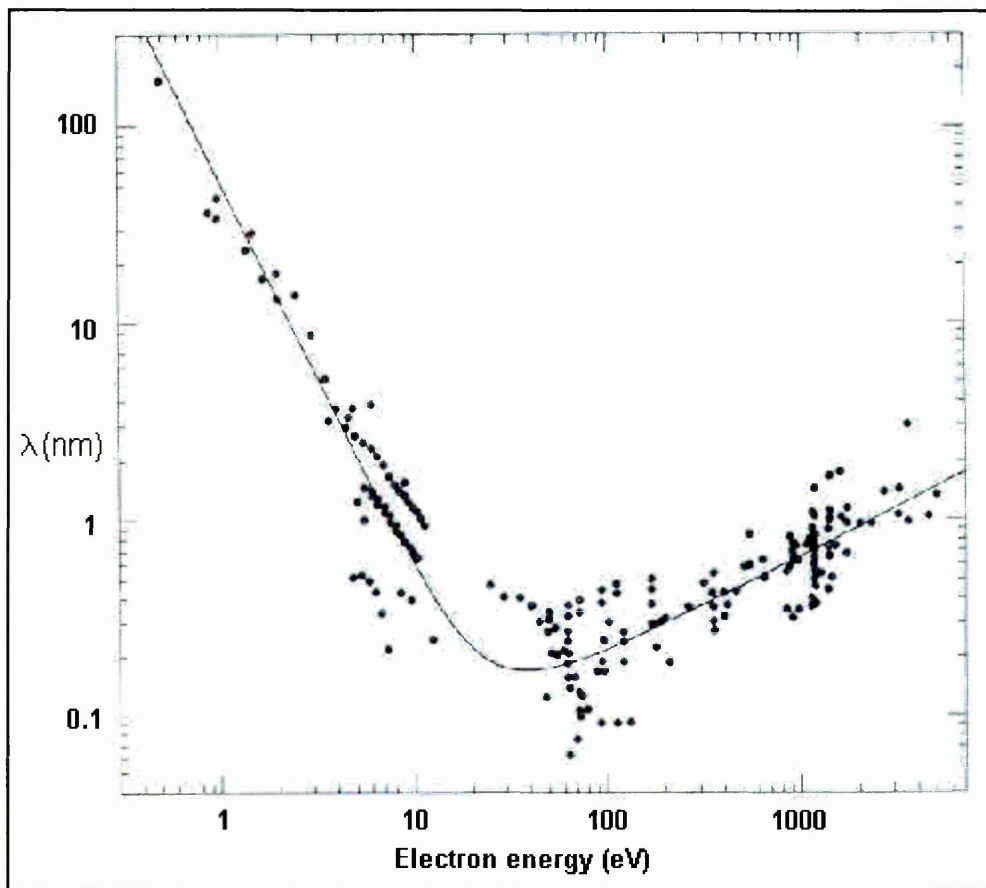


Figure 4-3: Evolution of the attenuation length as a function of electron energy for elements (from ref. [10]).

The shape of the curve is determined by the formation of electron-hole pairs and plasmons typically in the energy range 20-100 eV. At low energies (below the plasmon energy) electron scattering is dictated by single-particle electron excitations involving valence electrons and the ionisation of core levels¹¹. The associated cross sections of these processes are small compared to other processes and hence the mean free path for such collisions is about two orders of magnitude greater than for plasmon scattering.

On the other hand, at energies above the plasmon energy, the plasmon scattering cross section rises sharply which increases the probability of inelastic scattering. This reduces the mean free path to about a few Å. When λ becomes this small, electrons emerging from the surface without loss of energy must have originated from within the first few monolayers of the solid. It is this aspect of photoemission that makes it a surface sensitive technique. Then, as the energy of the electrons increases above ≈ 100 eV, the IMFP increases. This is the result of high velocity electrons that become less influenced by scattering centres. Therefore, the surface sensitivity can be altered by

changing the photon energy and hence the kinetic energy (according to equation [4-1]) using a tuneable radiation source such as monochromated synchrotron radiation source.

4.3.2. Escape depth and surface sensitivity

The escape depth d is defined as the distance from the surface that photoelectrons will have to travel in order to be ejected from the solid. Hence, by changing the angle of detection from normal emission β , it is possible to alter the surface sensitivity and scan different depths in the surface as shown in figure 4-4.

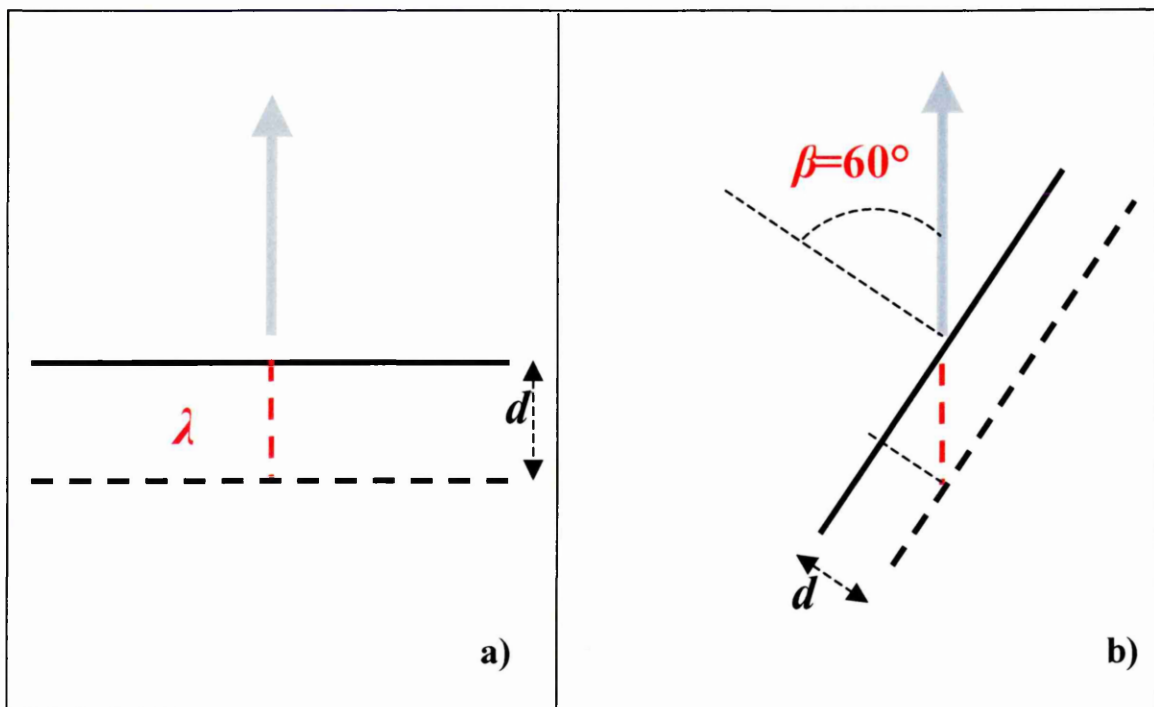


Figure 4-4: Variation of the escape depth d with take off angle: a) normal emission where $\beta = 0^\circ$ and b) a more sensitive surface where $\beta = 60^\circ$.

Using the notations shown in this figure, the escape depth may be expressed as follows:

$$d = \lambda \cos \beta \quad [4-9]$$

When the sample is facing the detectors (normal emission where $\beta = 0^\circ$), the photoelectrons will have to travel a distance λ from the surface as shown in figure 4-4 a). If the sample is oriented at an angle $\beta = 60^\circ$ from normal emission, then the photoelectrons will have to travel from a distance $d = \lambda/2$ from the surface. This case is seen as a more sensitive surface.

4.3.3. Photo-ionisation cross-section

The probability of a transition per unit time for excitation of a single photoelectron from the core level of interest due to an incident photon flux of $1 \text{ cm}^{-2}\text{s}^{-1}$ is given as the photo-ionisation cross section (σ) and is related to the matrix element $|\langle \psi_f | W | \psi_i \rangle|$ discussed in section 4.2. The intensity of the transition between the initial state and the final state is determined by the cross section and since the final state energy depends on the energy of the incident photon beam, σ will also vary with the photon energy¹². The resulting intensity of a given core level emission peak will vary with photon energy and the majority of core level emission peaks encounter a minimum in σ at certain photon energies known as a Cooper minimum¹³.

Experimentally observed values of σ for individual core levels have been collected and tabulated as a function of photon energy by Yeh and Lindau¹². These tables are of great use when performing experiments using a synchrotron radiation source as it is possible to maximise the emission intensity of the core level being studied by tuning the photon energy to exhibit the maximum possible cross section. However, this can result in a loss of surface sensitivity and hence a compromise between surface sensitivity and cross section usually needs to be found.

4.4. Spectrum features

The identification of core-level peaks on the XPS spectrum is a central step for the extraction of information. Hence, it is vital to be able to distinguish the core-level peaks from the other features in order to understand the surface composition and/or electronic changes at the surface or sub-surface. This section will present a basic interpretation of the main "parasitic" features and a more accurate discussion of the core-level peak and its analysis.

4.4.1. Auger peaks

After the emission of a photoelectron extracted from the K-shell, the relaxation process gives rise to the Auger process as shown in figure 4-5.

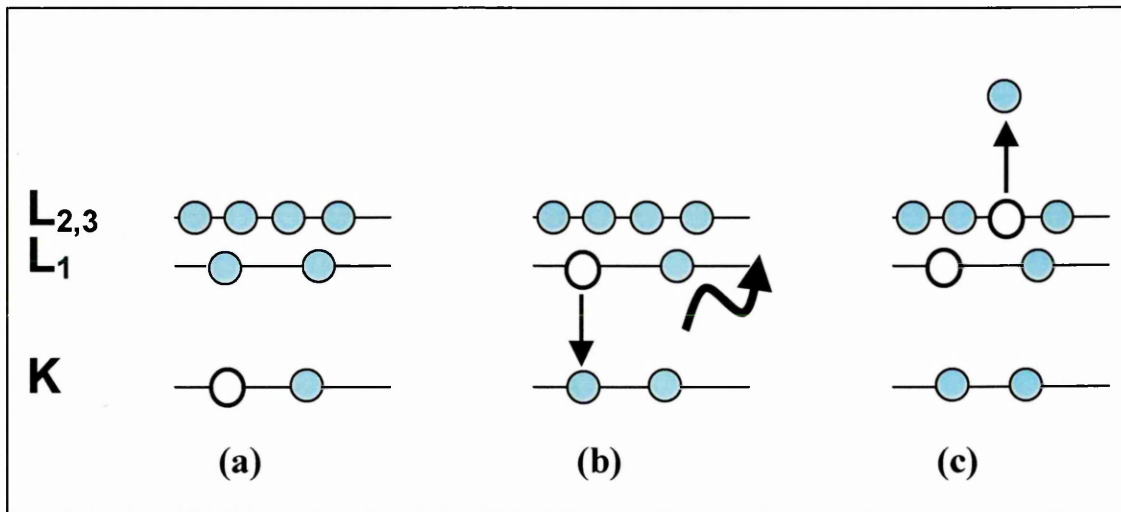


Figure 4-5: Schematic diagram of energy transfer mechanisms following the ejection of a photoelectron. (a) a hole is left in the K-shell due to photoelectron emission. (b) the hole is filled by a L₁-shell electron. The excess energy results in the creation of a photon $h\nu$ (x-ray fluorescence). (c) The excess energy is transmitted to a L_{2,3}-shell electron which is ejected from the solid and leaves a hole in the doubly ionised final state.

When the hole is filled by a L₁-shell electron, an excess energy $h\nu = E_K - E_{L1}$ is created. This excess energy can be used by the atom in two different ways shown in figure 4-5(b) and 4-5(c).

In the first situation, the energy may be released by a photon whose energy will be $h\nu = E_K - E_{L1}$ in the case shown in the figure. This process is known as x-ray fluorescence and is independent of the excitation x-ray source.

In the second situation, the energy is transmitted to another electron either in the same level or in a more shallow level, ejecting this second electron. This process is known as Auger process and the ejected electron is called Auger electron. The energy of this electron may be expressed as follows:

$$E_{KL_1L_{2,3}} = E_K - E_{L_1} - E_{L_{2,3}} \quad [4-10]$$

After the Auger electron emission, the doubly ionised atom will relax and the following electron transitions may produce more and less energetic Auger electrons.

These electrons will then have specific, discrete energies depending on the energy levels filled due to the atom relaxation.

The Auger electrons are collected in the same way as core-level electrons and will give rise to Auger peaks in the XPS spectrum. However, according to equation [4-10], above the excitation threshold, the Auger electron energy is not dependent on the x-ray energy. Hence, it is possible to distinguish Auger peaks from core-level peaks by changing the x-ray excitation energy.

4.4.2. X-ray satellites and ghosts

The fact that standard X-ray sources are not monochromatic gives rise to satellite peaks. Besides the principal $K\alpha_{1,2}$ line, ($2p_{3/2,1/2}$ to $1s$ transition) Mg and Al targets also produce a series of lower intensity peaks which results in satellite peaks on the low binding energy side of the main core level peak. The line positions and intensities (noted in brackets) are given in table 4-1.

Ghost peaks are due to excitation arising from impurity elements in the X-ray source. The most common ghost is Al $K\alpha_{1,2}$ from a Mg $K\alpha$ source. This arises from secondary electrons produced inside the source hitting the thin Al window used to prevent these same electrons from hitting the sample. This radiation will therefore produce weak ghost peaks 233.0 eV above excited by the dominant Mg $K\alpha_{1,2}$. Old or damaged targets can give rise to ghost peaks excited by Cu $L\alpha$ radiation, the main line from the exposed Cu base of the target⁴.

X-ray line	Separation from $K\alpha_{1,2}$ (eV) and relative intensity ($K\alpha_{1,2}=100$)	
	Mg	Al
$K\alpha'$	4.5 (1.0)	5.6 (1.0)
$K\alpha_3$	8.4 (9.2)	9.6 (7.8)
$K\alpha_4$	10.0 (5.1)	11.5 (3.3)
$K\alpha_5$	17.3 (0.8)	19.8 (0.4)
$K\alpha_6$	20.5 (0.5)	23.4 (0.3)
$K\beta$	48.0 (2.0)	70.0 (2.0)

Table 4-1: High energy satellite lines from magnesium and aluminium targets (from ref. [14]).

Both satellite and ghost features can be avoided by using monochromated X-rays produced by dispersion of X-ray energies by diffraction in a crystal such as quartz.

4.4.3. Core-level data analysis

The binding energy of an atom core-level is directly related to its chemical and electrical environment. If a change in environment of the emitting atom occurs, the binding energy of the core level emission peak will also change, with the difference in energy being described as a shift.

These shifts can be due to structural, chemical or electronic changes in the surface region, with the total binding energy shift being a convolution of the various shifts. Hence, it is important to be able to discern one category of shifts from another in order to quantify the changes that caused these shifts. In that way, the extraction of the precise core-level binding energy and intensity from the XPS scans taken after different surface treatments or metal deposition is an important issue. The seven following subsections will present the phenomena giving rise to these spectral features in order to analyse XPS data.

4.4.3.1. Broadening effects

The observed core-level lineshape in the EDC is limited by the natural linewidth which will eventually be broadened and characterised by the full width at half maximum (FWHM) of the core-level peak. This parameter also depends on the photon source linewidth and extrinsic broadening such as instrumental broadening as shown in the following equation:

$$\Delta E = (\Delta E_n^2 + \Delta E_p^2 + \Delta E_a^2)^{1/2} \quad [4-11]$$

where ΔE_n is the natural or inherent linewidth of the core level, ΔE_p is the linewidth of the photon source and ΔE_a is the analyser resolution.

The natural width of the core level is the inherent line of a core level, i.e. the range in KE of the emitted photoelectron is a direct reflection of uncertainty in the lifetime of the ion state remaining after photoemission.

The natural width of the core level is given by:

$$\Delta E_n = \frac{h}{\tau} = \frac{4.1 \times 10^{-15}}{\tau} eV \quad [4-12]$$

where h is the Planck's constant (eV.s) and τ is the lifetime (s).

The lifetime varies from 10^{-13} s to about 10^{-15} s for the broader core levels (e.g. Ag 3s) and is governed by the dissipation processes of the excess energy remaining after the photoemission.

The linewidth of the irradiation source is an important parameter which depends on the metal used as anode. The energy resolution of the X-ray source is determined by the natural linewidth of the fluorescence line (typically less than 1 eV for Al and Mg sources) and is characteristic of the irradiation source. Most commonly used anode targets are magnesium and aluminium but other materials may be used as shown in table 4-2.

Anode Material	Emission Line	Energy (eV)	Width (eV)
Mg	K α	1253.6	0.7
Al	K α	1486.6	0.85
Zr	L α	2042.4	1.7
Cr	K α	5415	2.1

Table 4-2: Characteristic energies and linewidths for some commonly used X-ray sources (from ref. [4]).

The broadening due to the analyser is dependent on the analyser pass energy and other analyser parameters and will be discussed in section 4.5.

4.4.3.2. Spin-orbit splitting

Many core level peaks form doublets due to the coupling of the orbital and spin angular momenta of the electrons. Only core levels with an angular quantum momentum number $\ell > 0$ will exhibit doublets and hence core levels such as $1s$, $2s$ and $3s$ will be singlets.

The outcome of coupling is the new total angular momentum given by:

$$j = \ell + s \quad [4-13]$$

where ℓ is the orbital angular momentum and s is the spin quantum number ($\pm 1/2$)¹⁵.

Hence, it is clear that electrons with a total angular momentum of $j = \ell + 1/2$ will have a different energy to those with $j = \ell - 1/2$. Electrons with $j = \ell + 1/2$ are shifted to higher binding energy than those with $j = \ell - 1/2$. The resulting difference in energy is known as the spin orbit splitting. The relative intensities of the photoemission peaks in a doublet are given by the ratio of their respective degeneracies ($2j + 1$) as follows:

$$R = \frac{2(\ell - s) + 1}{2(\ell + s) + 1} \quad [4-14]$$

Therefore, for the d core levels where $\ell = 2$, the ratio of the 3/2 spin orbit component to the 5/2 spin orbit component is 2:3.

4.4.3.3. Chemical shifts

When chemical reactions occur at the surface, the atoms that partake in these reactions will have their chemical environment changed. Core-level binding energies of these atoms will therefore present a shift in the EDC. The transfer of charge may also be affected by the electronegativities of the different elements consequently altering the electronic properties of the reacted species¹⁶.

For example, figure 4-6 shows an illustration of the chemical shift effect for the three different types of nitrogen (NH_2 , NO_2 , and NO_3) in the spectrum. It clearly points out the fact that the N 1s binding energy increases with an increase in formal oxidation number of the nitrogen atoms⁴. The general rule is that the core-level binding energy of the central atom increases as the electronegativity of attached atoms or groups increases.

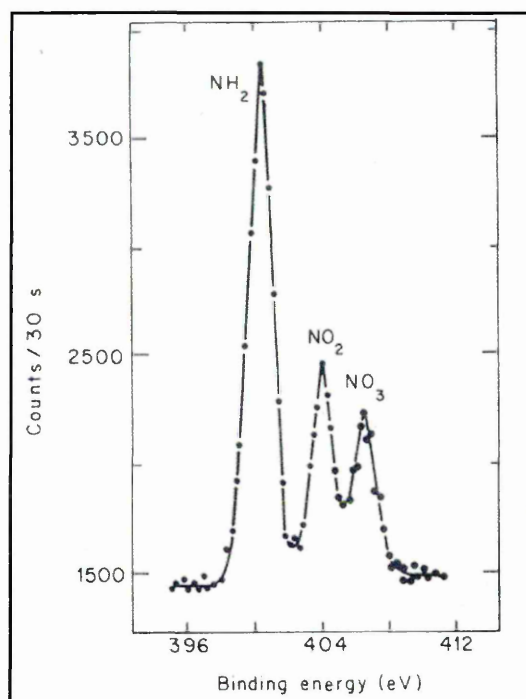


Figure 4-6: XPS spectra showing N 1s core-level peak under three different chemical environments (ref. [4]).

4.4.3.4. Fermi shifts

The position of the Fermi level in a semiconductor may shift due to the presence of surface states and/or the deposition of metals onto the surface. The resulting shift is known as Fermi shift or band bending. This is the result of an electronic effect that occurs due to charge transfer at the surface or interface as described in Chapter 3. This band bending induces a change in the Fermi level position at the surface compared to its position relative to the valence and conduction band edges in the bulk. The band bending occurs within the depletion region, which is usually much larger than the sampling depth of the photoemission technique. Hence, all core level electrons that are detected will have been subjected to band bending with a subsequent shift in the core level peaks in the EDC. It is therefore possible to observe the development of the Schottky barrier during the initial stages of metal-semiconductor interface formation.

The magnitude of core-level shifts must be measured using a reference energy point. For this reason, it is common practice to measure the Fermi level of the system (in electrical contact with the sample) in order to obtain an exact position for the Fermi level. This is easily achieved by scanning the Fermi edge of a metal, usually high purity

metal such as gold. The high density of states at the Fermi level in a metal ensures that emission from this region will be distinct and hence the Fermi level is easy to measure. Unfortunately this is not the case for a semiconductor, where the Fermi level often lies within the forbidden energy gap. In this case it is more productive to determine the valence band maximum (VBM) and this is found at the cut off point of the valence band signal and the background signal. By subtracting the valence band maximum from the Fermi level position (both measured at the same photon energy) it is possible to determine the clean surface pinning position of the Fermi level within the band gap.

The barrier height formed at metal-semiconductor interfaces (for low metal coverage) can therefore be estimated by adding the additional band bending due to metal deposition to the Fermi level pinning position. The meaningful determination of the energy position of the valence band and Fermi edges is however only possible when using monochromated X-rays; only relative energy shifts can be observed with a non-monochromated X-ray source.

4.4.3.5. Asymmetric metal core-levels

As the density of states is different from a metal to a semiconductor, the shape of the EDC is expected to be different. Metals have high density of states at the Fermi level which results in diminished ejected photoelectron energy due to high scattering. This results in high emission intensity at low kinetic energies and is observed as a tail to low kinetic energy side of the core level peak in the EDC.

4.4.3.6. Core-level intensities

Extraction of the chemical and electronic information from the analysed surface has been discussed in terms of core-level binding energy. It is also useful to investigate the core-level intensities in order to extract other information such as chemical composition or growth mode when a metal is deposited onto the surface.

During the metal deposition onto the semiconductor surface, the photoemission signal from the core levels within the semiconductor will be attenuated due to inelastic scattering in the growing overlayer. The growth mode can be identified using photoelectron intensities and three different growth modes may be identified. Hence it is possible to identify layer by layer growth by plotting the intensity of the attenuated signal as a function of metal overlayer thickness.

The Stranski-Krastanov (SK) mode represents the situation where the metal growth starts in the layer-by-layer or Frank-van der Merwe (FVDM) mode, and continues in islanding mode or Volmer-Weber (VW) mode as illustrated in figure 4-7.

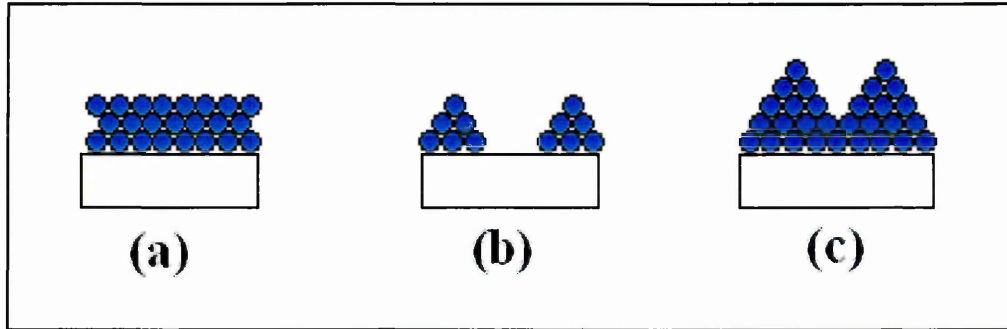


Figure 4-7: Schematic diagram of the three growth modes. (a) Layer-by-layer or Frank-van der Merwe (FVDM) mode, (b) islanding or Volmer-Weber (VW) mode, (c) layer-layer followed by islanding or Stranski-Krastanov (SK) mode.

Calculations can be made in order to predict the evolution of the intensity with metal coverage in the SK mode and have been described elsewhere^{17, 18}. However, this growth mode is simply a convolution of the other two, FVDM and VW modes. In this case, in order to avoid complex calculations, and because the model is valid at low metal coverage, only FVDM mode has been used to extract the photoelectron mean free path.

In the FVDM mode, the intensities of the substrate $I_S(z)$ and metal $I_M(z)$ photoemission lines can be calculated using the following formula¹⁷:

$$I_S(z) = I_S^0 \exp\left(-\frac{z}{\lambda}\right) \quad [4-15]$$

and

$$I_M(z) = I_M^\infty \exp\left(-\frac{z}{\lambda}\right) \quad [4-16]$$

where z is the metal thickness, λ the attenuation length, $I_S^0(z)$ the intensity from the clean surface and I_M^∞ the intensity from a thick metal layer.

4.4.3.7. Curve-fitting

It is essential to perform a detailed analysis of the individual components in order to understand the changes of the properties and the process involved. In spite of the limited equipment resolution, it is possible to deconvolute the raw photoemission spectra into individual components. This process is known as curve-fitting.

A mathematical technique developed by A.A. Cafolla, incorporating the conjugate gradient¹⁹ and Levenberg-Marquardt²⁰ curve fitting methods was used to generate the basic shape of a single core level, and then the curve fitting routine performed a least squares minimisation to produce the best fit. The software CasaXPS was used to process the raw data. A mix of Lorentzian and Gaussian functions, known as the Voigt function²¹, was used to fit core level spectra.

The Lorentzian function models the natural linewidth of the core hole lifetime and is given by the following equation:

$$L(E) = \frac{1}{1 + 4\left(\frac{E - E_L}{\Gamma_L}\right)^2} \quad [4-17]$$

where E_L is the energy peak centroid and Γ_L is the full width at half maximum (FWHM) of the peak.

The Gaussian function represents instrumental and other factors such as phonon broadening, and is given by the following equation:

$$G(E) = \exp\left[-4 \ln 2 \left(\frac{E - E_G}{\Gamma_G}\right)^2\right] \quad [4-18]$$

where E_G is the peak centroid and Γ_G is the full width at half maximum (FWHM) of the peak.

The Voigt function may be modified by changing various parameters such as the Lorentzian or Gaussian contribution, the spin orbit splitting of the core level, the intensity of individual components or the binding energy position of the peaks.

Before any peak quantification, a suitable background must be chosen and removed. This is routinely done using CasaXPS and a variety of backgrounds are available. The linear background, the simplest one, is drawn by taking a straight line between the first and the last data points and is useful when the signal to noise ratio is poor. Other more complex backgrounds^{22, 23, 24} have been introduced in order to remove as much asymmetry as possible and to allow a better characterization of the intensity and position under the peak. Shirley²⁵ backgrounds were introduced for that purpose.

Once a suitable background has been removed, the fitting can start. The clean surface spectrum is fitted with an estimate first, keeping the number of components as low as possible. Each individual component has a number of parameters that contribute to its lineshape. These are $L(E)$, $G(E)$, the spin orbit splitting (SOSP) of the core level being probed and their relative intensities, the peak position and the peak intensity. In addition, the software used for curve-fitting allows for the introduction of the asymmetric contribution occurring for metal core-levels.

Then, the quality of the mathematical fit is assessed by the calculation of the standard deviation of the window residual. Hence, it is possible to compare the quality of the peak fitting in order to add or remove components if the chemistry of the surface changes. However, it is important to note that a high quality of mathematical fit does not always have a physical meaning and any addition of new components in the curve fitting must be meaningful.

4.4.3.8. Charging

XPS analysis may be performed on insulating samples such as ceramics, polymers, glasses or biological materials. During analysis, the irradiation with X-rays followed by photoemission is only partly neutralised and causes charge accumulation at the surface. This process is known as charging.

The sample surface acquires a positive potential which varies from several volts to several tens of volts and the kinetic energies of the photoelectrons are decreased by the electronic field. This means that the Fermi levels of the sample and spectrometer are no longer in equilibrium, resulting in an unknown surface potential. For semiconductor

substrates with low surface conductivity such as AlGa_N, XPS analysis usually causes charging at the surface. This generally leads to different kind of problem:

- general instability leading to overall spectral noise and making analysis more difficult,
- excessive charge may damage the sample (only happens with delicate samples such as polymers),
- different charging at different region may lead to peak broadening or splitting,
- shifting of spectra to higher binding energy.

There are various methods to overcome the problem of charging during in XPS. The conductivity of the sample may be increased in order to facilitate the charge repartition at the surface and the contact to earth. A secondary energy source such as low energy electrons beam may be used to neutralize the charge potential at the surface. The main difficulty of this technique is to adjust the flood gun voltage to accurately balance the positive charge without getting an excess negative charge at the surface.

The main problem encountered during the AlGa_N substrates analysis was the shifting of the XPS spectra to higher binding energy. The most commonly used technique to correct charging is to reference via adventitious carbon-based contamination. In this method, the fact that most samples contain some kind of carbon contamination which might come from the adsorption of residual gases in the analysis chamber is used to reference the spectra. The C *1s* core-level binding energy position is usually used for this purpose and is assigned a value at 285 eV ± 0.2 eV.

However, this carbon referencing technique may lead to potential errors. The first source of error comes from the wide spread of values available in literature for C *1s* core-level position. The direct determination of a corrected core-level binding energy is subjected to the C *1s* value but these kinds of errors are systematic.

The other source of error comes from the assumption that the carbon contamination is not subjected to shifts. In fact, there is a distinct possibility that the carbon atoms are influenced by the semiconductor atoms because they might belong to the lattice. Therefore, the measurement of Fermi shifts after metal deposition or following various surface treatments may be subjected to errors.

Despite the apparent limitations and uncertainties associated with adventitious carbon referencing, it is the most convenient and commonly applied technique. This

method has been used to correct all core-level binding energy positions in the spectra during AlGa_N XPS analysis.

4.5. XPS at Materials and Engineering Research Institute

4.5.1. Experimental set-up

This XPS system was used for the experimental work on the influence of chemical treatment and thermal annealing on AlGa_N surfaces²⁶. A schematic VG Microlab description of the system is shown in figure 4-8. The analysis system consists of different parts that can be isolated from each other by gate valves in order to avoid contamination of the main chamber and to facilitate the realization of ultra high vacuum (UHV). The instrument is comprised of an analysis chamber, a preparation chamber, a custom built metallization chamber and a fast entry load lock. The vacuum inside the analysis and preparation chambers is maintained by two oil diffusion pumps with Liquid Nitrogen LN₂ cold traps to a base pressure of 10⁻¹⁰ mbar while the metallization chamber is connected to a turbo molecular pump. Samples are loaded into the preparation chamber through the load-lock and can be transferred to the metallization and analysis chambers by ways of a system of railtrack, linear drive and wobble sticks.

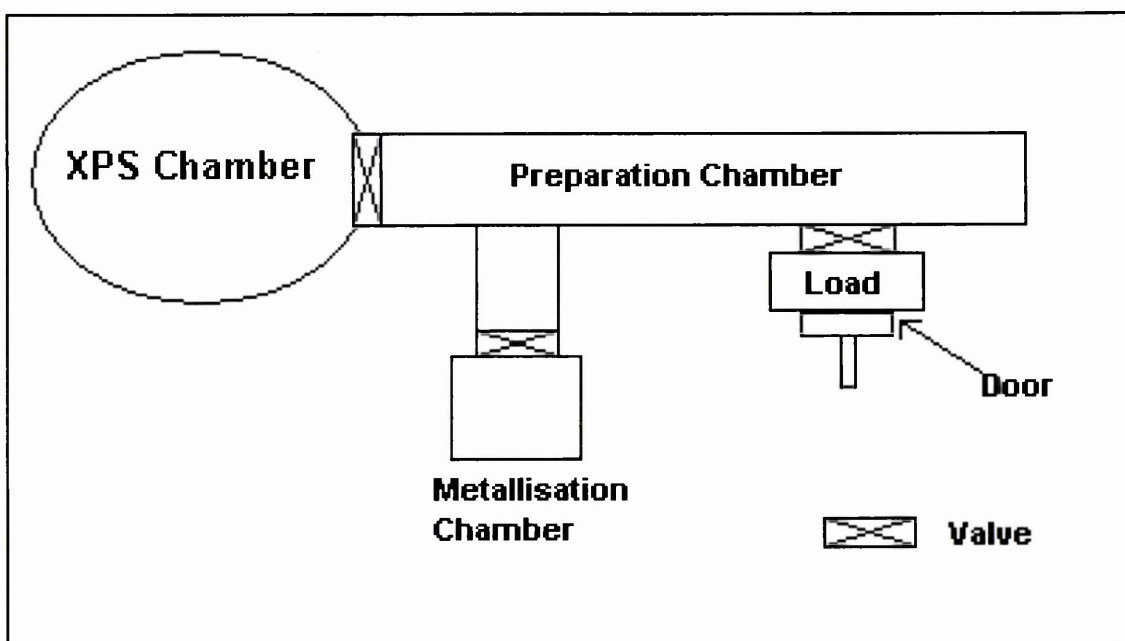


Figure 4-8: Schematic of the VG Microlab XPS and deposition chamber

The analysis chamber is equipped with a dual anode (Al/Mg) X-ray gun, as shown in figure 4-9, and a concentric hemispherical analyser (CHA), which will be described in more details in the next section. An electron lens is used to collect the photoelectrons from the sample.

Figure 4-9 also shows the process of generation of the X-rays for the irradiation source. The anode or metal target is kept close to ground potential whereas the filament is elevated at approximately 13 kV (20 mA) in order to create a difference of potential between the two parts. Electrons leaving the filament are accelerated before hitting the anode and will generate the X-rays. The Al window is placed between the anode and the sample in order to screen the sample from heating effects and any contamination originating from the source.

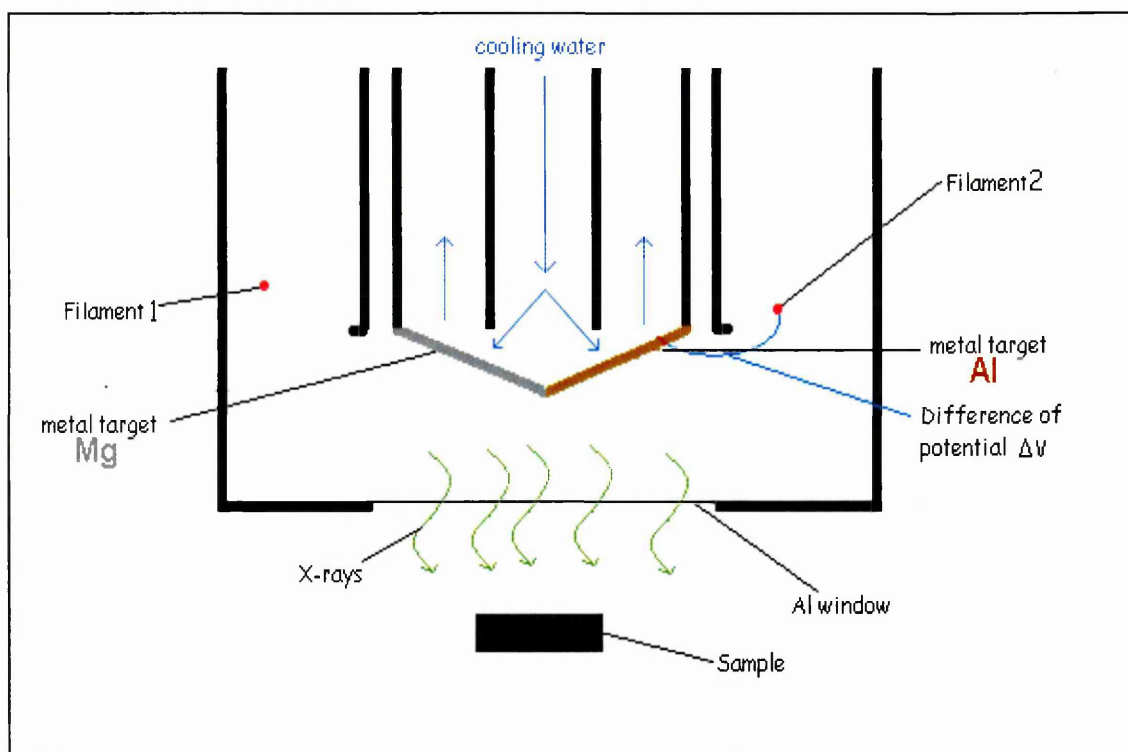


Figure 4-9: Schematic of dual-anode x-ray source (from ref. [4]).

The samples were annealed in UHV by passing an electric current through a high purity and low resistivity silicon plate as shown on figure 4-10. Both sample and silicon plate were held by two separate pieces of Tantalum foil. The crocodile clips were used to keep a uniform electrical contact between the silicon plate and the

Tantalum foil, and also to prevent the sample from moving if a metal deposition was made. One piece of Tantalum was connected to earth via the Ni stub whereas the other one acted as the other electrical contact via the bottom screw.

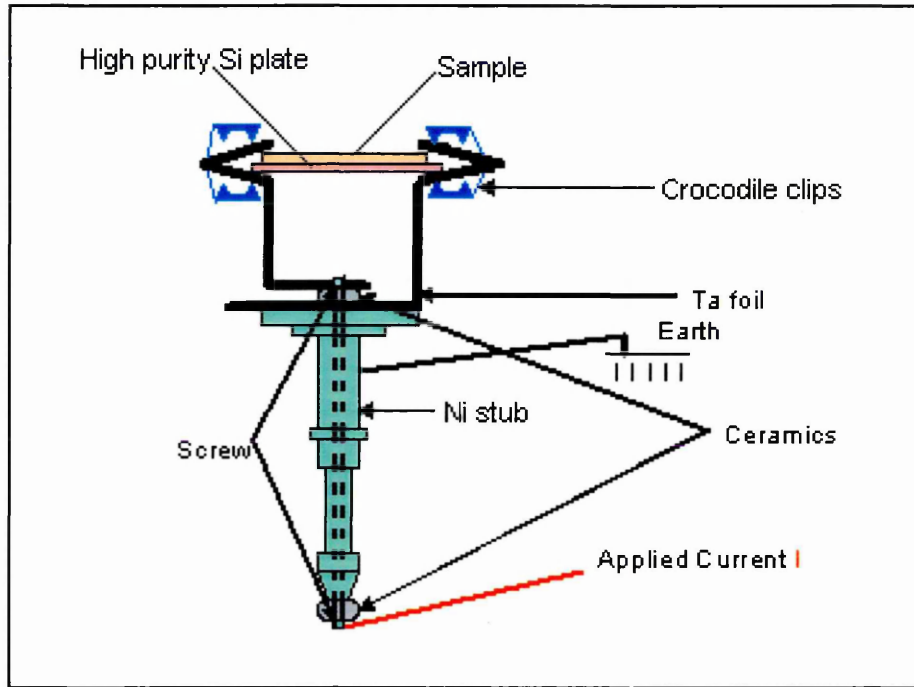


Figure 4-10: Heater stub used for *in-situ* annealing of AlGaN samples.

The relationship between the applied current and temperature at the silicon surface was calibrated using the LAND System 3 Short wavelength radiation thermometer GP212 (using Ge detectors with a response waveband of 0.9 to 1.8 μm and operating from 500°C to 1100°C) and LANDMARK 4 Signal Processor. The aluminium standard melting point was used for the calibration. Emissivities of 0.6 and 0.4 were used for silicon and aluminium, respectively. Figure 4-11 shows an example of a calibration curve.

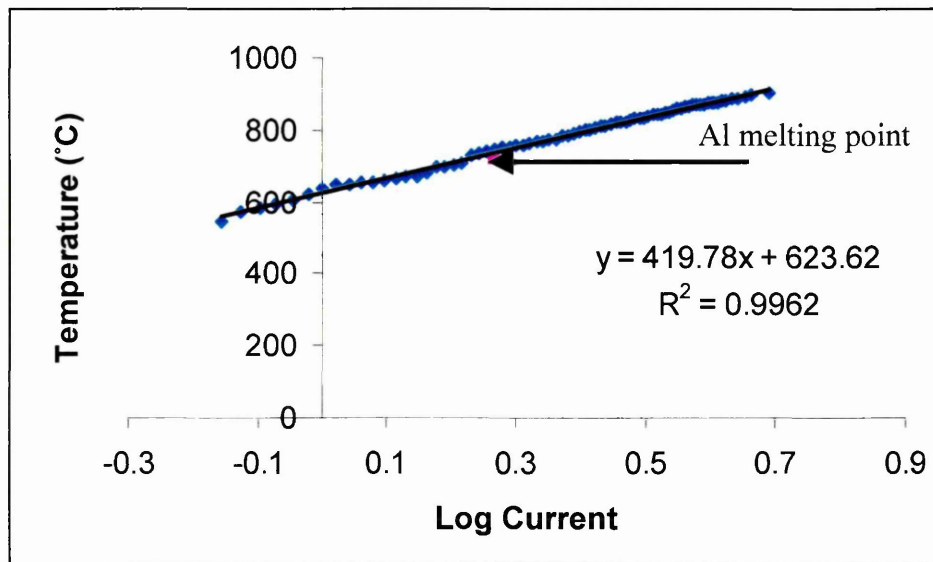


Figure 4-11: Example of a temperature calibration using the heater stub. The logarithmic value of the current I is represented in X axis.

4.5.2. Electron energy analyser

The electron analyser consists of 2 concentric hemispheres of radii R_1 and R_2 . Both hemispheres are elevated at different potentials $-V_1$ and $-V_2$ to inner and outer plates respectively, with V_2 greater than V_1 , in order to operate a selection of the photoelectrons to be analysed. The radius R_0 is the radius of the median equipotential surface of the hemispheres where the entrance and exit slits are centred. V_0 is the voltage along the median surface. We have the following relations for the analyser:

$$\bullet \quad V_1 = V_0 \left[3 - 2 \left(\frac{R_0}{R_1} \right) \right] \quad [4-19]$$

$$\bullet \quad V_2 = V_0 \left[3 - 2 \left(\frac{R_0}{R_2} \right) \right] \quad [4-20]$$

$$\bullet \quad V_2 - V_1 = V_0 \left(\frac{R_2}{R_1} - \frac{R_1}{R_2} \right) \quad [4-21]$$

$$\bullet \quad V_0 = \frac{V_1 R_1 + V_2 R_2}{2 R_0} \quad [4-22]$$

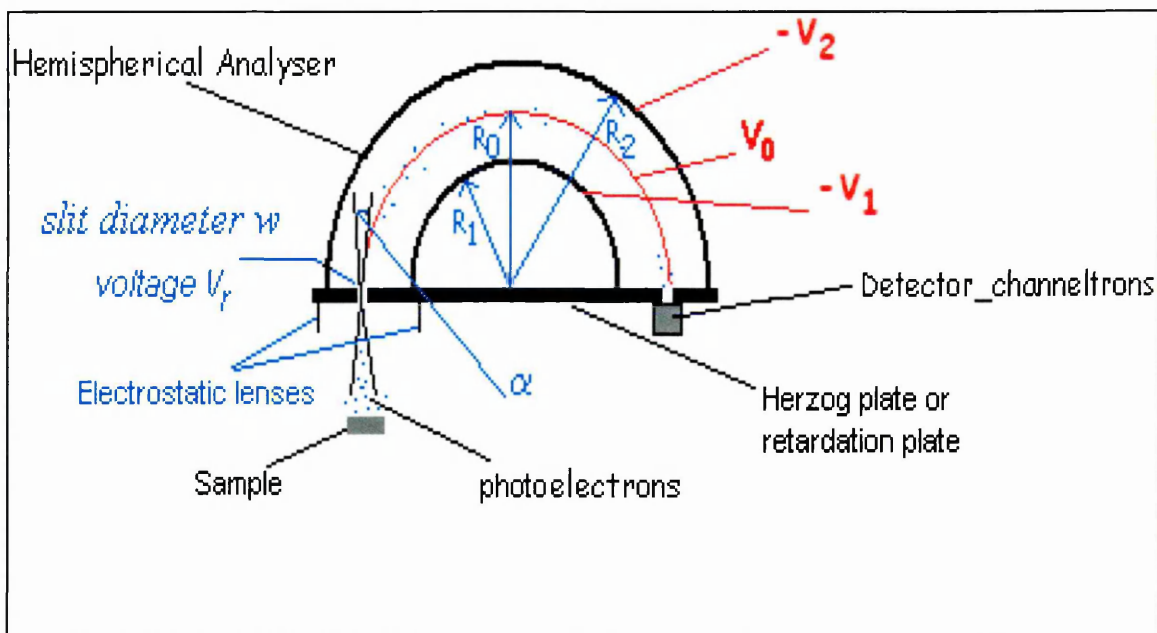


Figure 4-12: Details of the Concentric Hemispherical Analyser. The electron path is represented by the red line.

Figure 4-12 shows the different parameters to be taken into account for the calculation of the analyser's resolution. The electrostatic lenses aim to collect and lead the emitted photoelectrons to the entrance slit.

The Herzog plate or retardation plate has a width w and a retardation potential V_r is applied to the plate. The voltage across the plate is set in order to increase or decrease the photoelectron energy to the pass energy E_p as follows:

$$E_k = E_p + eV_r \quad [4-23]$$

where E_k is the electron kinetic energy (eV)
 V_r is the voltage to be applied across the Herzog plate (V)
 E_p is the pass energy (eV).

For example, if photoelectrons need to be scanned for kinetic energies of 300 eV with constant pass energy of 20 eV, then an energy of 280 eV must be applied across the plate (this represents the energy of the median equipotential surface or V_0).

In this case the EDC's are acquired in constant analyser energy (CAE) mode and the resolution of the spectra is kept constant (ΔE) for all core levels since the detected

Experimental techniques

electrons all have the same energy, E_p . The resolution of a CHA is given by the following equation:

$$\frac{\Delta E}{E_p} = \frac{w}{2R_0} + \frac{(\delta\alpha)^2}{4} \quad [4-24]$$

Here, w is the entrance slit width, R_0 is the radius of the electrons circumventing the hemispheres and $\delta\alpha$ is the acceptance angle of the analyser. From equation [4-24] it can be seen that the resolution of the analyser can be improved by either reducing the pass energy or the slit width. However, a reduction in the slit width will also reduce the signal intensity, and therefore a compromise between resolution and intensity must be established.

4.6. XPS at Swansea University

This system was used for the investigation of Schottky barrier formation of Ni/AlGaN interfaces. The system is both equipped with *in-situ* metal deposition which enabled the deposition of refractory metals, and *in-situ* scanning tunnelling microscope (STM), as illustrated in figure 4-13. The VG ESCALab MkII uses two LN₂ trapped diffusion pumps attached to the analysis chamber and preparation chamber maintaining the UHV environment in the system, and pressures in the order of 10⁻¹⁰ mbar were attained in both chambers.

In order to clean the sample, this system also allows *in-situ* UHV annealing. This can be achieved by e-beam heating, where the sample is bombarded by high energy electrons, thus heating the sample. The e-beam heater was carefully calibrated²⁷ (by plotting temperature versus emission current) at 1 kV in order to get the desired temperature. As Ni has relatively high melting point, it was deposited using an e-beam evaporator²⁸ (EGN4). The deposition rate was calibrated using a quartz crystal monitor and by XPS²⁷. The sample manipulation is very similar to that discussed in the section 4.5 and details of the system may be found elsewhere²⁷.

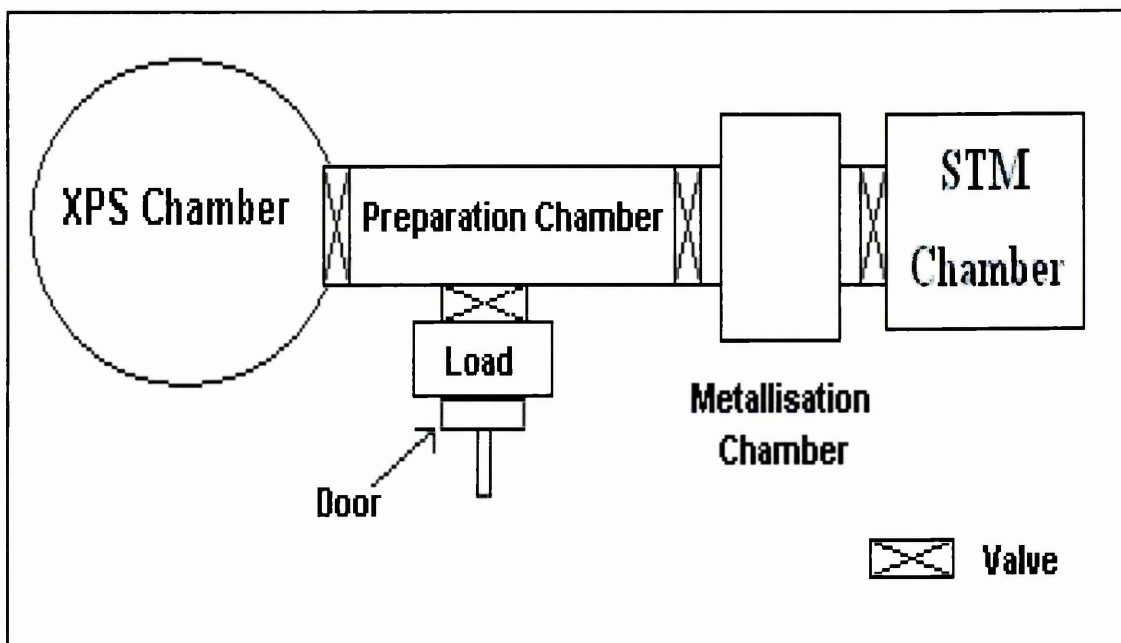


Figure 4-13: Schematic diagram of the XPS system used at Swansea University.

4.7. High resolution XPS at Daresbury Laboratory

XPS analysis of the core level and valence band spectra were performed using a Scienta ESCA 300 spectrometer at the National Centre for Electron Spectroscopy and Surface Analysis (NCESS), Daresbury Laboratory. This system was used for the chemical and electrical analysis of the $\text{Ag}/\text{Al}_x\text{Ga}_{1-x}\text{N}$ interface formation²⁹ presented in chapters 5 and 6. The set-up was very similar to that described in previous sections and illustrated in figure 4-8. However, this system is equipped with a more advanced X-ray source and electron transmission process in order to reach a much better total resolution.

The instrument employs a high power rotating anode monochromatised $\text{AlK}\alpha$ / $\text{Cr K}\beta$ ($h\nu = 1486.7 / 5946.7$ eV) X-ray source with selectable aluminium or chromium targets. The rotating anode has a maximum power rating of 8kW which is much higher than a typical power of 600W for a conventional fixed anode source. The system is equipped with a large, seven crystal, double focusing monochromator that focuses the X-rays to a line image, $6\text{mm} \times 0.5\text{mm}$, on the sample. The resulting $\text{Al K}\alpha$ (1486.7eV) line profile has a FWHM energy width of 0.26 eV, a factor of 3 narrower than for an unmonochromated $\text{Al K}\alpha$ source.

The computer-controlled lens system has two modes of operation: a high transmission mode for optimum acceptance of photoelectrons and an imaging mode for

Experimental techniques

high spatial resolution with $<50\ \mu\text{m}$ lateral resolution. The detection system consists of a 300mm radius hemispherical analyser and a multi-channel detector. During this work, the analyzer was operated at a pass energy of 150 eV with 0.8 mm slits. Pressures in the order of 10^{-10} were reached in both preparation and analysis chambers using turbomolecular and diffusion pumps. Gaussian convolution of the analyzer broadening with an effective linewidth of the 0.26 eV for the x-ray source gives an effective instrument resolution of 0.35 eV.

The sample was annealed using an e-beam heater, similar to that described in the previous section. The metal deposition was carried out by attaching a 4-way cross to the preparation chamber as shown in figure 4-14. The metal was evaporated by heating the filament and controlled using a quartz crystal monitor. Hence, it was possible to estimate a deposition rate and metal thickness after measurement of the distances R_1 and R_2 .

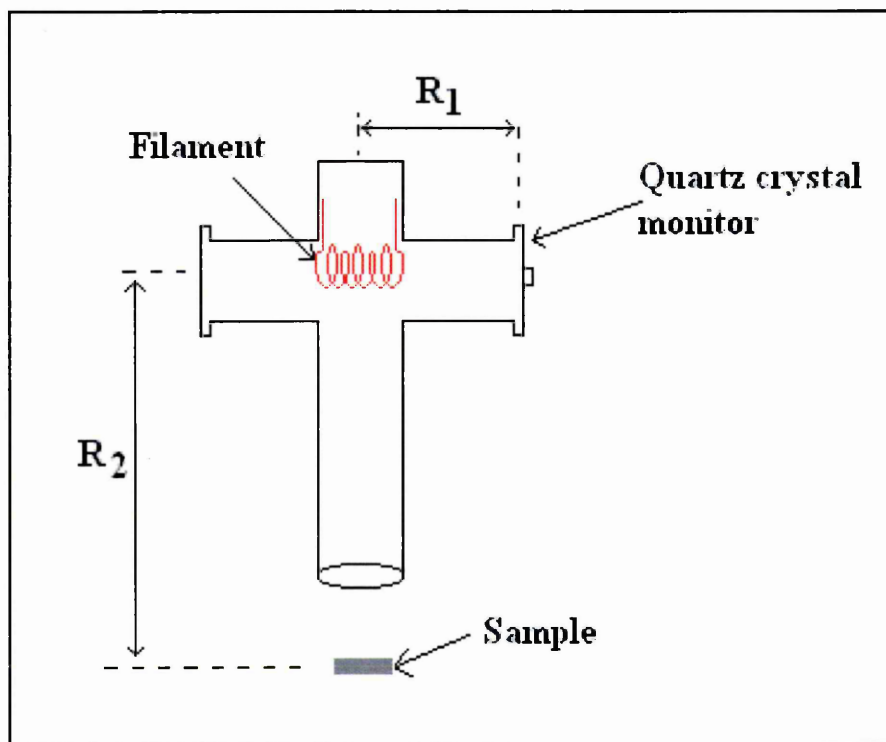


Figure 4-14: Schematic diagram of the 4-way cross used for Ag deposition. The sample is sitting on the holder in the preparation chamber

4.8. Scanning Probe Microscopy

During the course of this work, different microscopic techniques have been used in order to assess the properties of the surfaces and interfaces with the deposited metal. Atomic force microscopy (AFM) and scanning tunnelling microscopy (STM) have been chosen for this purpose. The AFM is closely related to the STM and other hybrid techniques that are based on these two instruments, such as magnetic force, electrochemical, and thermal microscopy. In this section, a brief description of these two techniques will be presented.

4.8.1. Atomic force microscope (AFM)

The atomic force microscope (AFM) is one of a class of recently developed instruments that are increasingly finding their way into the chemistry laboratory assisting scientists and engineers in their study of surfaces.

A sharp probe scans a sample surface at a distance over which atomic forces act. The forces between tip and sample cause the cantilever to deflect. A photo detector measures the cantilever deflection and from this information a map of the sample topography can be created as shown in figure 4-15.

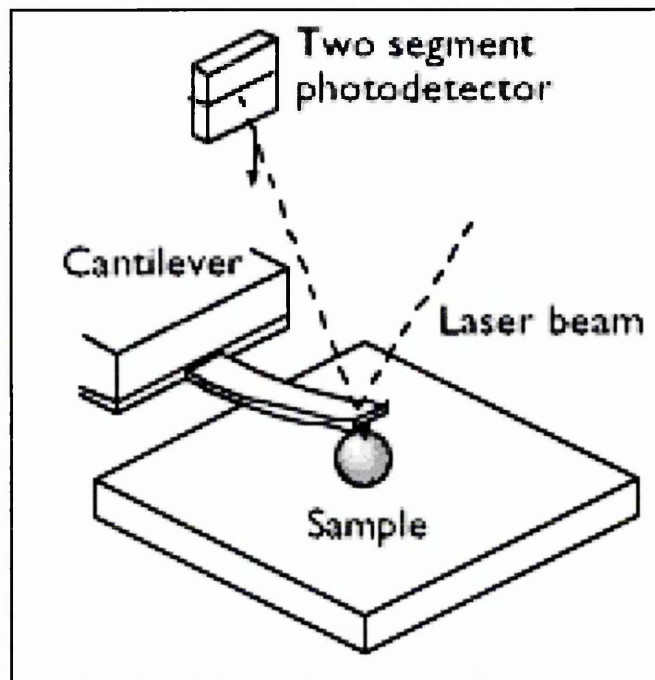


Figure 4-15: AFM working process

The technique can be processed in two different modes: the Tapping Mode and the Contact Mode. In Contact Mode, the tip is dragged across the surface which could cause damage to soft samples. In Tapping Mode a piezoelectric driver oscillates the cantilever at or near its resonance frequency at high amplitude. The tip lightly taps the surface, touching the sample through the absorbed fluid layer during each oscillation. The technique is successfully used for biological samples and for polymers since damaging frictional forces is avoided. The overall resolution can be of the order of nanometer.

4.8.2. Scanning Tunnelling Microscope (STM)

To get images of smaller size surfaces, other techniques such as STM may be used. A schematic diagram of a standard STM system is illustrated in figure 4-16. The basic principle of STM is based on the tunnelling effect. A bias voltage is applied between the tip and the sample. When the tip is brought within about 10\AA of the sample, electrons from the sample begin to "tunnel" through the 10\AA gap into the tip or vice versa, depending upon the sign of the bias voltage. The resulting tunnelling current varies with tip-to-sample spacing; both the sample and the tip must be conductors or semiconductors. Thus, STM cannot image insulating materials.

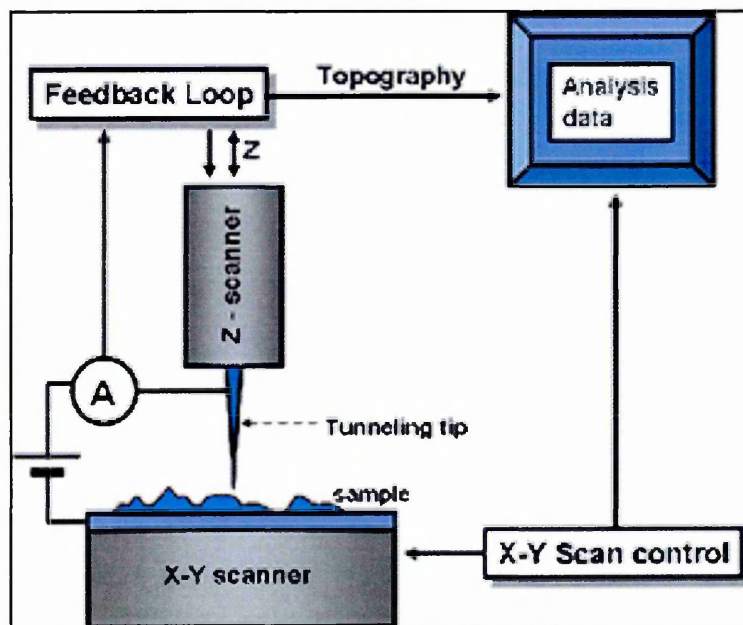


Figure 4-16: Schematic diagram of a standard STM system

The tunnelling current is an exponential function of distance. Based on quantum mechanics, the tunnelling current I can be expressed as:

$$I \approx e^{-2kd} \quad [4-25]$$

where d is the distance between tip and sample surface.

As an example, if the separation between the tip and the sample changes by 10% (on the order of 1 \AA), then the tunneling current changes by an order of magnitude. This exponential dependence gives STM its remarkable sensitivity. STM can image the surface of the sample with sub-angstrom precision vertically, and atomic resolution laterally. STM can be operated in two different modes: the constant-height mode and the constant-current mode.

In constant-height mode, the tip travels in a horizontal plane above the sample and the tunneling current varies depending on topography and the local surface electronic properties of the sample. The tunneling currents measured at each location on the sample surface constitute the data set.

In constant-current mode, STM uses feedback to keep the tunneling current constant by adjusting the height of the scanner at each measurement point. For example, when the system detects an increase in tunneling current, it adjusts the voltage applied to the Z-axis scanner to increase the distance between the tip and the sample.

Each mode has advantages and disadvantages. Constant-height mode is faster because the system doesn't have to move the scanner up and down, but it provides useful information only for relatively smooth surfaces. Constant-current mode can measure irregular surfaces with high precision, but the measurement takes more time. The constant-current mode was found more suitable for measuring the topography of $\text{Al}_x\text{Ga}_{1-x}\text{N}$ samples and all data collections have been taken using this mode.

4.9. I-V measurement

The characteristics of the metal- $\text{Al}_x\text{Ga}_{1-x}\text{N}$ have been assessed through current-voltage measurements (I-V). The experimental set-up is shown on figure 4-17.

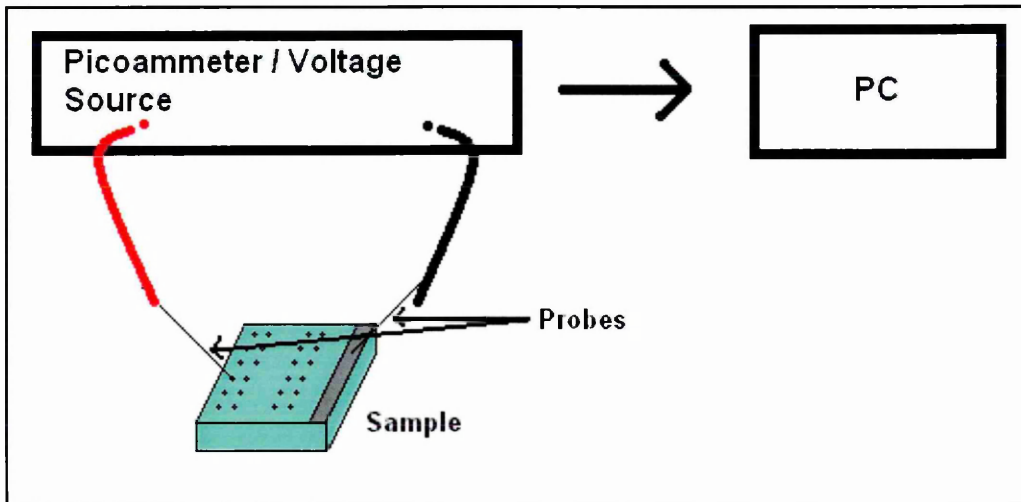


Figure 4-17: Schematic diagram of the I-V measurement experimental set-up

The Schottky contacts are represented by small spots and a large area contact has been used for Ohmic contact. One sharp probe was placed into contact with the different diodes whereas the other one was touching the Ohmic area. A bias is applied across the probes and the current flowing between the diode and the Ohmic contact is measured as a function of the applied voltage. The (I-V) measurements were done using a Hewlett-Packard programmable Picoammeter-Voltage source, Keithley Model 6487 system.

The voltage source is controlled by a personal computer (PC) where I-V characteristics of the diode are finally displayed through a LabView programme. This enabled the change of different parameters such as the voltage range, step size and acquisition time. Files were then saved in ASCII format and treated in Excel in order to extract the Schottky parameters.

References

1. A. Einstein, *Ann. Physik*, **17**, 132 (1905).
2. T. Koopmans, *Physica*, **1**, 104 (1933).
3. C.S. Fadley in "Electron Spectroscopy: Theory, Techniques and Applications, Vol. 2", edited by C.R. Brundle and A.D. Baker, Academic Press (1978).
4. "Practical Surface Analysis, 2nd Edition, Volume 1 Auger and x-ray Photoelectron Spectroscopy", edited by D. Briggs and M.P. Seah, John Wiley and Sons (1990).
5. P.J. Feibelman and D.E. Eastman, *Phys. Rev. B*, **10**, 4932 (1974).
6. B. Feuerbacher and R.F. Willis, *J. Phys. C: Solid St. Phys.* **9**, 169 (1976).
7. C.N. Berglund and W.E. Spicer, *Phys. Rev.* **136**, (4A), A1030 (1964).
8. E.W. Plummer and W. Eberhardt, *Advances in Chemical Physics*, **49**, 533 (1982).
9. C. Cohen-Tannoudji, B. Dui and F. Laloš, "Quantum Mechanics, Vol. 2", J. Wiley & Sons (1977).
10. M.P. Seah and W.A. Dench, *Surface and Interface Analysis*, **1**, 2 (1979).
11. D.P. Woodruff and T.A. Delchar, "Modern Techniques of Surface Science", Cambridge University Press (1990).
12. J.J. Yeh and I. Lindau, *Atomic Data and Nuclear Tables*, **32**,1 (1985).
13. J.W. Cooper, *Phys. Rev.* **128**, 681 (1962).
14. T.A. Carlson, "Photoelectron and Auger Spectroscopy", Plenum, New York (1976).
15. R.D. Rusk, "Introduction to Atomic and Nuclear Physics", Meredith Publications (1964).
16. W.A. Harrison, "Electronic Structure and Properties of Solids", W.H. Freeman and Co. (1980).
17. T. Conard, A.-C. Rousseau, L.M. Yu, J. Ghijsen, R. Sporcken, R. Caudano, R.L. Johnson, *Surf. Sci.* **359**, 82 (1996).
18. R. Sporcken, P.A. Thiry, E. Petit, J.J. Pireaux, R. Caudano, J. Ghijsen, R.L. Johnson, L. Ley, *Phys. Rev. B* **35**, 7927 (1987).
19. W.H. Press, B.P. Flannery, S.A. Teukolsky and W.T. Vetterling, "Numerical Recipes in Fortran", Cambridge University Press (1986).
20. D.W. Marquardt, *J. Soc. Ind. Appl. Math.* **11**, 431 (1963).
21. J.J. Joyce, M. Del Guidice and J.H. Weaver, *J. Electron. Spec. Rel. Phen.* **49**, 31 (1989).
22. S. Doniach, M. Sunjic, *J. Phys.* **4C31**, 285, (1970).
23. S. Tougaard, *Surf. Interface Anal.* **25**, 137, (1997).
24. S. Tougaard, *Surf. Interface Anal.* **11**, 453, (1988).
25. D.A. Shirley, *Phys. Rev. B*, **5**, 5, 4709 (1972).
26. B. Boudjelida, M.C. Simmonds, I. Gee, S.A. Clark, *Appl. Surf. Science* **252**, 5189, (2006).
27. W.Y. Lee, PhD Thesis, University of Wales, Swansea (2004).
28. Oxford Applied Research, "Operating and service manual for the mini e-beam evaporator EGN4".
29. B. Boudjelida, I. Gee, J. Evans-Freeman, S.A. Clark, M. Azize, J.-M. Bethoux, and P. De Mierry, *Phys. Stat. Sol. (c)* **3**(6), 1823, (2006).

Chapter 5

Cleaning of $\text{Al}_x\text{Ga}_{1-x}\text{N}$

5.1. Introduction

Surface preparation prior to metallization has become one of the most important steps in order to achieve a good Schottky contact¹ and a variety of surface cleaning² strategies have been employed with the aim of generating clean, defect-free, semiconductor surfaces. Hydrofluoric acid (HF) solution is commonly used to remove contamination layer from the III-Nitrides surfaces³. Ishikawa *et al.*⁴ identified a contamination layer at GaN surfaces mainly composed of GaO_x and adsorbed carbon, with a thickness layer of ~ 2 nm on the as-grown surface. This result is in agreement with Prabhakaran *et al.*⁵ who found the existence of an overlayer of native oxides, predominantly in the Ga_2O_3 form, on GaN surfaces. Exposure to HF and HCl has been found to be very effective in removing oxides from AlN and GaN surfaces but significant amounts of residual F and Cl were detected¹. Furthermore, complete thermal desorption of C contaminants occurred at temperatures higher than 900°C which

corresponds to the GaN sublimation temperature. Smith *et al.*⁶ found HF combined with methanol resulted in GaN surfaces which were more efficient for in-situ thermal desorption of C and O.

Ion bombardment and annealing technique (IBA) have also been studied to produce clean nitride surfaces. Ar⁺ and N⁺ sputtering have been the main candidates for GaN cleaning^{5, 7, 8}. On the other hand, atomic hydrogen clean (AHC) has been widely used to clean InN surfaces mainly because the temperature required for this technique is lower than for other ions⁹. H₂ is cracked and then deposited onto the surface to be annealed at temperature around 400°C. Recently, AHC was successfully used to produce clean AlN surfaces^{10, 11}. The application of this technique on AlGaN remains uninvestigated.

In this chapter, the XPS results of Al_xGa_{1-x}N surface cleaning using chemical cleaning followed by 600°C UHV annealing are shown. The structural and electronic consequences of UHV annealing on HF etched surfaces, by annealing the sample up to 600°C in increments of 100°C are then developed. Finally, an investigation of sample cleaning using AHC is presented.

The samples used in this study will be described at the beginning of each section and all samples were thick epitaxial layers.

In essence, the first generation samples have been used to investigate the effect of temperature on the semiconductor surfaces, whereas the second generation samples, of very high quality, have been mainly used to understand the effect of various surface treatments and the formation of the Schottky barrier which will be discussed in the next chapter.

5.2. Solvents cleaning and wet chemical etch

The two $\text{Al}_x\text{Ga}_{1-x}\text{N}$ samples ($x = 0.20$ and $x = 0.30$) were grown by metal-organic chemical vapor deposition (MOCVD) on sapphire substrates. A 2 μm thick GaN was used as buffer layer followed by 2 μm of $\text{Al}_x\text{Ga}_{1-x}\text{N}$ and threading dislocation densities as low as 5 to $7 \times 10^8 \text{ cm}^{-2}$ were measured by planview TEM and confirmed by AFM. X-ray diffraction (XRD) has also been used to assess the crystalline quality. The narrowness of the diffraction peaks gives information on the layer quality. The full width at half maximum (FWHM) of the XRD (002) ω -scan rocking curve was less than 350 arcsec. The Al mole fraction was measured by energy dispersive x-ray spectroscopy (EDX) and XRD. Details of the sample growth and the dislocation characterisation have been published elsewhere^{12,13}.

XPS analysis of the Ga 3*d*, Ga 2*p*, Al 2*p*, N 1*s*, O 1*s* and C 1*s* photoelectron spectra was performed using a Scienta ESCA300 spectrometer at the National Centre for Electron Spectroscopy and Surface Analysis, Daresbury Laboratory, as discussed in chapter 4. In the subsequent XPS studies, for each sample, three successive preparation stages were employed: solvent rinsing, acid etching (HF:H₂O) (1:10) for 1 min and ultra high vacuum (UHV) thermal annealing (600°C for 30 min).

The samples were annealed using an e-beam heater and monitored by an infrared pyrometer. AnalaR 48% HF was used in the experiments. As significant sample charging occurred for all measurements, the C 1*s* binding energy was used as a reference and assigned a value of 284.8 eV¹⁴. It should be noted that the results interpreted as Fermi shifts were obtained using the charging reference technique as explained in section 4.4.3.8. and might induce potential errors.

Figure 5-1 shows the evolution of the O 1*s* core level intensity with the successive surface treatments on $\text{Al}_{0.20}\text{Ga}_{0.80}\text{N}$ and $\text{Al}_{0.30}\text{Ga}_{0.70}\text{N}$ surfaces at normal emission. The intensity ratio O/Ga follows the same trend for the two Al concentrations and is found to be reduced by HF etching, and further reduced by 600°C temperature annealing. The O/Ga ratio for $x = 0.20$ is always higher than for $x = 0.30$, it is very probable that this is due to the difference in the Ga concentration between the two surfaces.

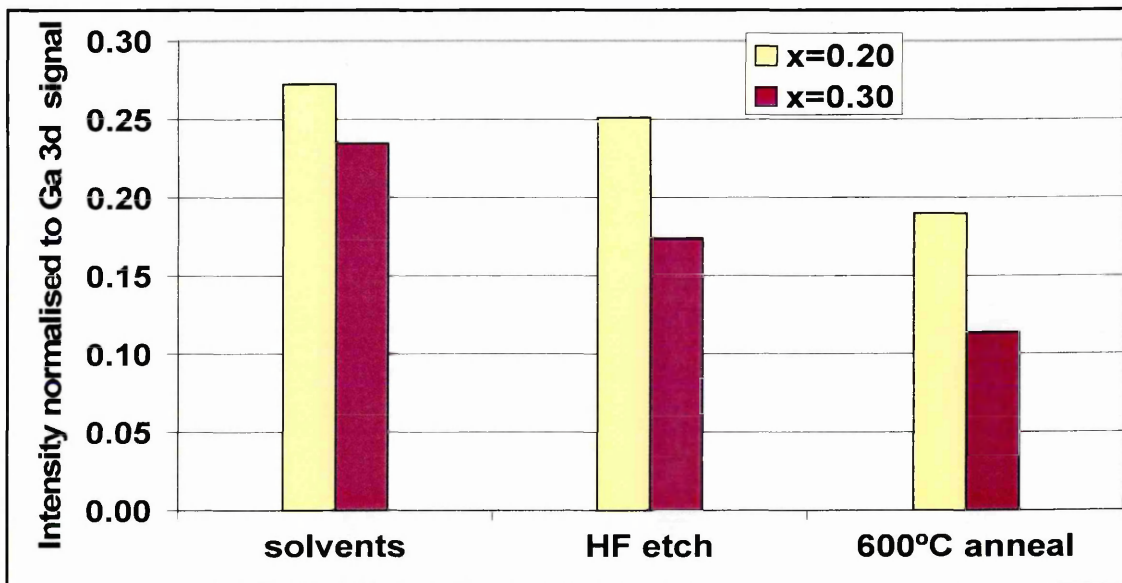


Figure 5-1: Evolution of the normalised O *1s* core level intensity after the successive surface treatments to $\text{Al}_x\text{Ga}_{1-x}\text{N}$ surfaces for $x = 0.20$ and $x = 0.30$ at normal emission. The intensities have been divided by an empirical sensitivity factor and normalised to the Ga *3d* intensity.

Figure 5-2 shows the evolution of the normalised Ga *3d*, Al *2p* and N *1s* core level lineshapes after the different surface treatments, for the lower Al content surface. All semiconductor core levels exhibit the same evolution of peak position in direction and in magnitude, and for the two different Al concentration materials.

Furthermore, no changes in lineshape (no significant change in FWHM), characteristic of chemical reactions at the interface were resolved. These observations indicate that the interface is unreacted and that the rigid shifts in binding energy result from Fermi shifts as the interface is formed. The Fermi shifts measured between the solvent treatment surface and the 600°C annealed surface were $\Delta E_F = +0.87\text{eV}$ and $\Delta E_F = +0.99\text{eV}$ for the $x = 0.20$ and $x = 0.30$ surfaces, respectively, indicating a downward band bending.

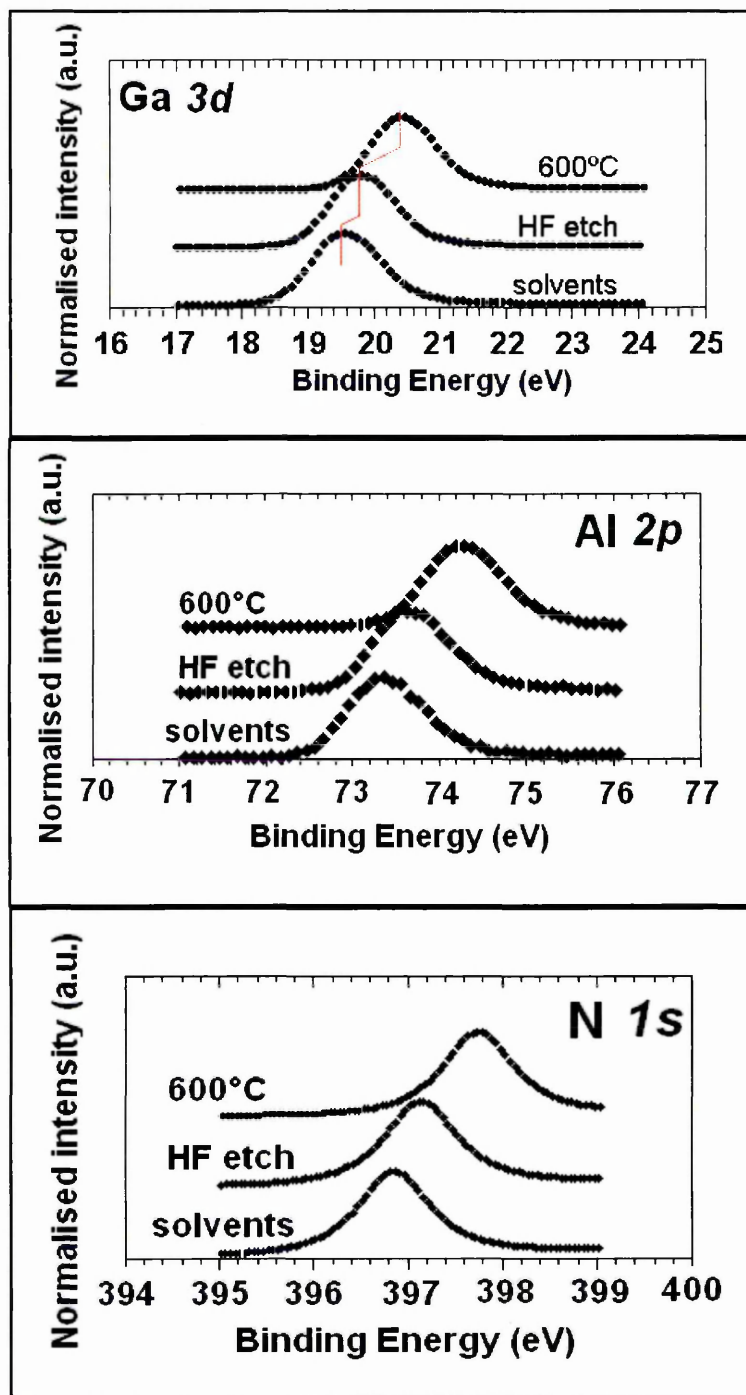


Figure 5-2: Evolution of the normalised Ga 3d, Al 2p and N 1s core level lineshapes after the successive surface treatments on $\text{Al}_{0.2}\text{Ga}_{0.8}\text{N}$ surfaces at normal emission.

Some of the results in figure 5-2 are, however, at variance with those previously reported for GaN and AlGa_N surfaces. Maffei *et al.*¹⁵ found that a 600°C anneal of GaN HF-etched surfaces resulted in a 0.35 eV upward band bending. Other studies of surface preparation of GaN have also, in the main, resulted upward band bending^{7, 16}. However, Wu *et al.*⁸ reported upward band bending of 0.75 eV for clean n-type, but witnessed a reduction of the upward banding as the surface was progressively cleaned

and annealed. Similar behaviour was also observed on an $\text{Al}_{0.2}\text{Ga}_{0.8}\text{N}/\text{GaN}$ HFET¹⁷ and very recently on an n-type $\text{Al}_{0.2}\text{Ga}_{0.8}\text{N}$ surface¹⁸.

Although the precise mechanisms causing this variance remain undefined, there is a distinct possibility that they relate to changes in the electronic structure and stoichiometry of the AlGaN surface, in comparison with GaN.

5.3. In-situ UHV annealing

HF is a powerful etchant, capable of removing hydrocarbon contamination¹⁹ and combined with subsequent annealing under UHV conditions can yield smooth surfaces and ultimately, abrupt metal-semiconductor interfaces. However, additional work is necessary to fully understand the mechanisms of structural and electronic changes at the surface at different temperatures. In this section, effects of HF etching combined with subsequent successive annealing stages are investigated using X-ray photoelectron spectroscopy (XPS).

The structure of the samples examined is shown schematically in figure 5-3. The 1 μm thick $\text{Al}_x\text{Ga}_{1-x}\text{N}$ ($x=0.20$) epilayer over a combination of GaN and AlN layers was grown by molecular beam epitaxy (MBE), on a sapphire substrate.

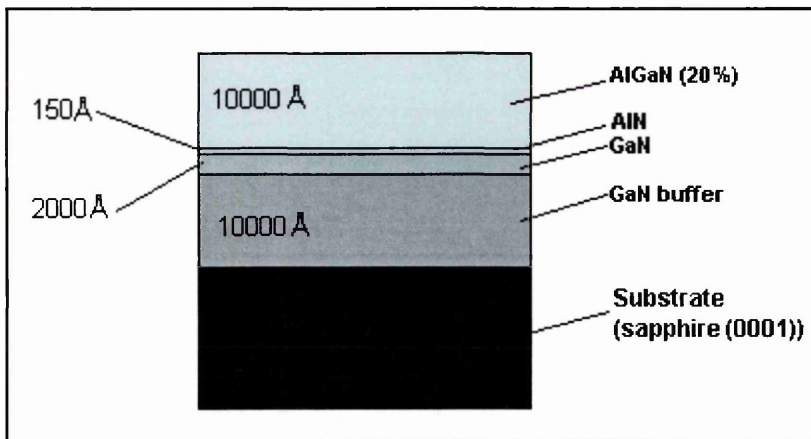


Figure 5-3: Schematic diagram of the $\text{Al}_x\text{Ga}_{1-x}\text{N}$ sample grown by MBE

For the subsequent XPS studies, for each sample, three successive preparation stages were employed: solvent rinsing, acid etching and thermal annealing. The preparation stages are detailed below:

Solvent rinse

- Acetone (3min)
- Ethanol (3 min)
- De-ionised H_2O .

Etch

- Acetone (3 min)
- Ethanol (3 min)
- De-ionised H_2O
- HF: H_2O (1:10) (1 min).

Thermal anneal

The samples were annealed in UHV by passing an electric current through a high purity and low resistivity silicon plate upon which the sample was placed. The sample and the silicon plate were held together by two separate pieces of Tantalum foil. The stub used for these experiments is described elsewhere¹⁵. The relationship between the applied current and the temperature at the silicon surface was calibrated using the LAND System 3 Short wavelength radiation thermometer (operating from 500°C to 1100°C). The aluminium standard melting point was used for calibration and emissivities of 0.60 and 0.40 were used for Si and Al, respectively. The sample was annealed in increments of 100°C for 10 min, to a maximum of 600°C.

After each chemical treatment and annealing stage, XPS scans of the Ga 3*d*, Ga 2*p*, N 1*s*, Al 2*p*, C 1*s*, O 1*s* core levels were recorded at normal emission and 60° off normal emission (30° take-off angle). The XPS spectra were acquired in a VG Microlab system operating at an average pressure in the range 10⁻¹⁰ - 10⁻⁹ mbar.

Intensity calibration:

Data were collected by the 5-channeltron detector as number of counts per 0.1 eV (BE). The intensity was normalised in the same way for all core-levels in order to have the same height for each peak, between 0 and 1.

In parallel, in order to demonstrate relative concentration changes between elements, calculations have been made on core-level intensities, by applying appropriate sensitivity factors. In this case, peak areas have been determined after removal of a Shirley background (see section 4.4.3.7.).

All core-level spectra were recorded using a MgK α X-Ray source. However, due to the significant overlap of the C 1*s* with the Ga KLL Auger transition, the C 1*s* core-level spectra were recorded using an AlK α source. As the core-level intensity is a function of the incident photon energy, absolute comparison between the peak intensities is not possible. However, examination of the relative intensity evolution can yield information about the surface and subsurface.

BE calibration:

The energy scale of the spectrometer was calibrated from the binding energy of Ag 3*d* at 367.9 eV. Because significant sample charging occurred for all measurements,

this has been reported for materials mounted into a foil²⁰, correct interpretation of the spectra requires an internal energy reference.

For each stage, Ga *3d* and C *1s* core-levels were recorded using the AlK α source. The C *1s* binding energy was assigned a value of 284.8 eV¹⁴ and the absolute position of the Ga *3d* peak was calculated. These peaks were then used as an internal reference to correct the core-level binding energies for charging. It should be noted that the results interpreted as Fermi shifts were obtained using the charging reference technique as explained in section 4.4.3.8. and might induce potential errors.

Figure 5-4 shows the evolution of the Ga *3d* and Al *2p* core-level peak positions as a function of chemical treatment and annealing temperature. Both peaks exhibit the same shift to higher binding energies resulting from the chemical treatment. For the Ga *3d* peak, cleaning the surface using organic solvents shifts the peak position by 0.4 eV to higher binding energy; HF cleaning in an additional shift of 0.5 eV in the same direction. When the temperature changes, the different core-levels seem to exhibit the same trend: up to 400°C, shifting to successively lower binding energies and from 500°C to 600°C, shifting to successively higher binding energies. For the Ga *3d* core-level, annealing from 100°C to 600°C produced a total shift of 0.3 eV to higher binding energy. These results are in accordance with those of Bermudez *et al.*⁷ who also found a shift to higher binding energy when annealing GaN from 300°C to 700°C. Although the shift observed by Bermudez *et al.* was more profound (0.7 eV), it is important to note that in the current study, overall the Ga *3d* core-level peak position shifted by 0.8 eV from the "as received" to 600°C. In other studies¹⁵, annealing etched surfaces of GaN to 600°C produced a similar shift in Ga *3d* core level peak position of 0.35 eV¹⁵. Conversely, cleaning AlGaN surfaces using a HF/HCl treatment did not change the Al *2p* and Ga *3d* peak positions but a (NH₄)₂S treatment shifted Ga *3d* position by about 0.85 eV to lower binding energy²¹.

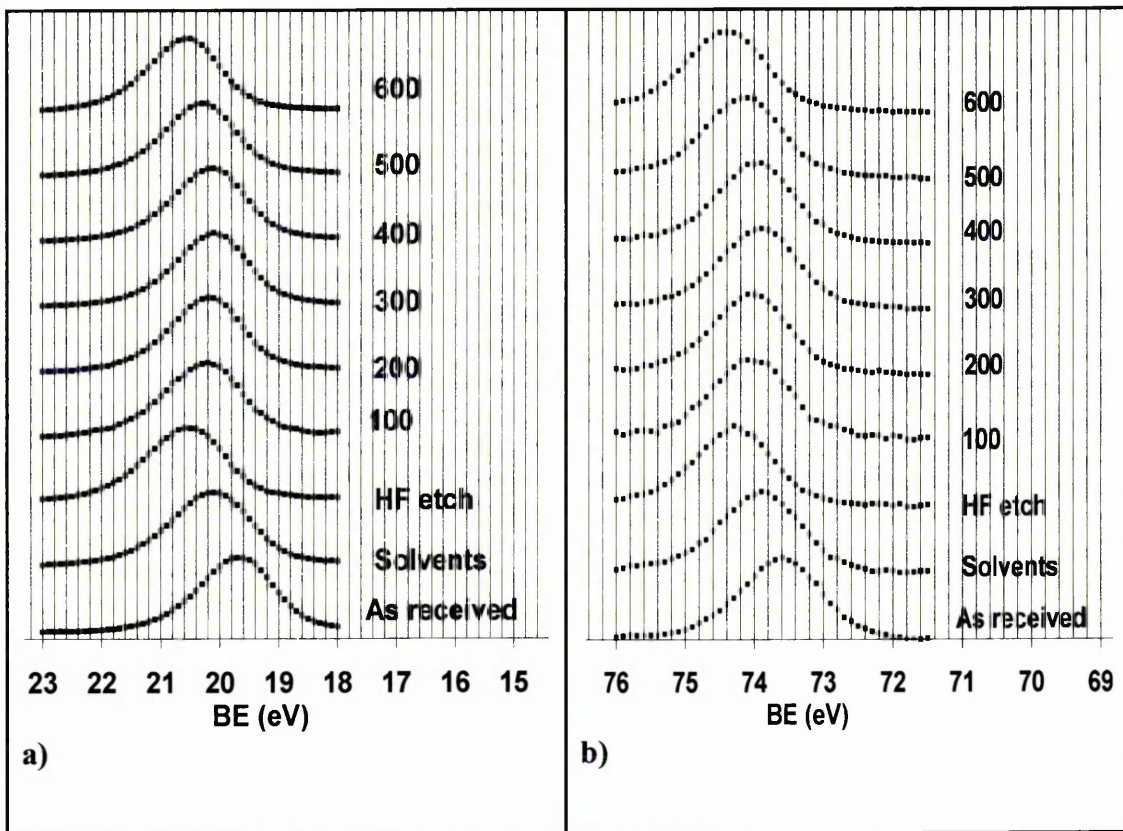


Figure 5-4: Evolution of (a) Ga 3d, and (b) Al 2p core-level peak position with chemical treatment and temperature

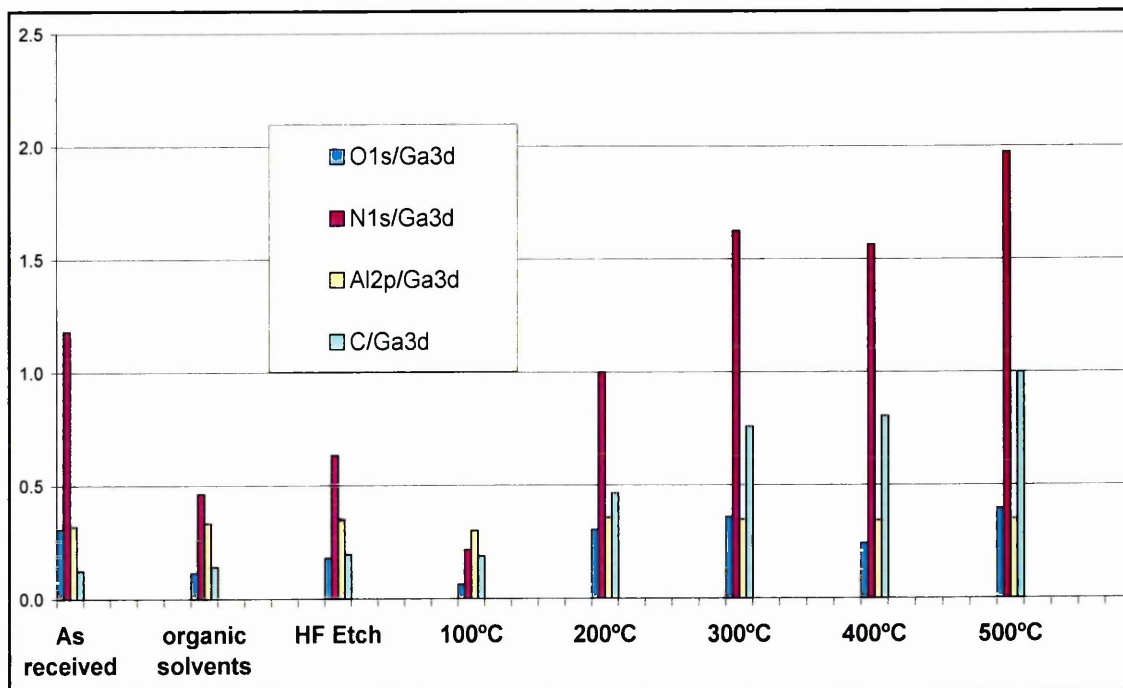


Figure 5-5: Evolution of the different ratios as a function of the treatment and temperature

Figure 5-5 shows the evolution in the relative ratios of O *1s*, N *1s*, Al *2p* and C *1s* core level intensities to Ga *3d* core level intensity following the different treatments and annealing stages. The first thing to note is the level of O-contamination at the Al_xGa_{1-x}N surface, "as received", with an O/Ga intensity ratio of 0.3. This is very low in comparison with previous reports on GaN^{15, 22, 23} and AlGaN²⁴ surfaces. This ratio was further decreased by the organic solvent treatment. The O/Ga ratio is low and roughly stable with subsequent surface treatment and temperature. The Al/Ga ratio also shows little change from 100°C to 600°C. However, an increase of the C/Ga ratio with the chemical treatment and increasing annealing temperature is evident. Effectively, C is always present at the surface.

HF etch treatment did not decrease the C/Ga ratio; the intensity of the C peak was not diminished. Ishikawa *et al.*³ also found that for GaN surfaces, employing solvent rinsing followed by buffered HF etching did not decrease C *1s* peak intensity. Figure 5-6 shows curve fitted C *1s* core level peaks obtained following the 600°C anneal at normal emission and 60° off. It shows that carbon contamination is significantly detectable by XPS after annealing at 600°C and the bond with O has not been removed. It appears that C and H react at Al_xGa_{1-x}N surfaces, as shown in the more surface sensitive 60° off spectrum.

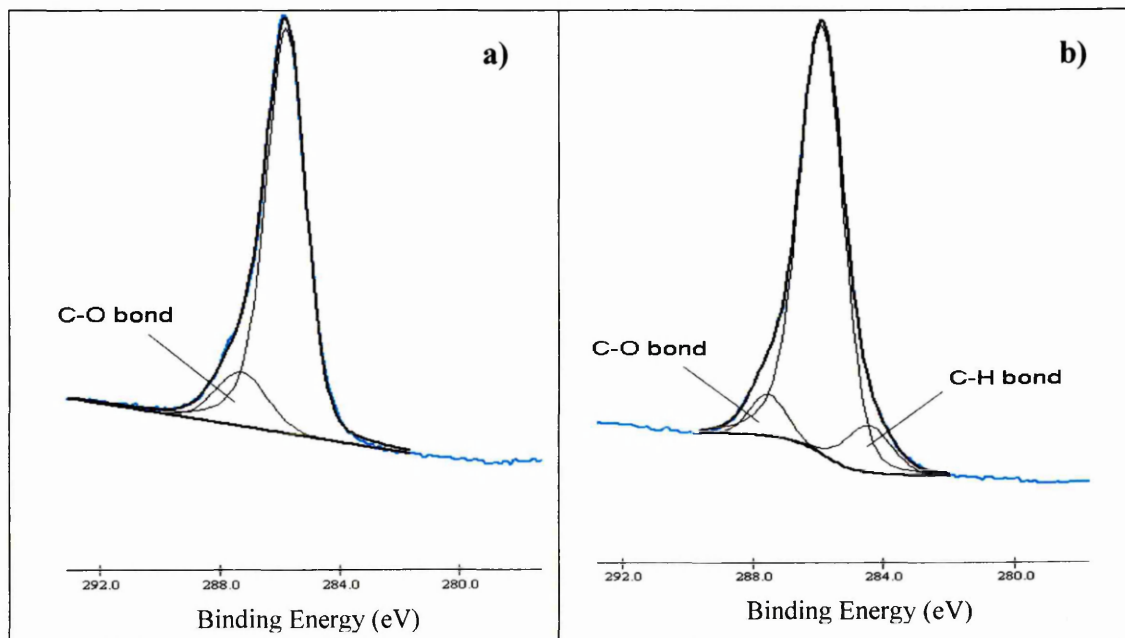


Figure 5-6: Curve fitted C *1s* peak for AlGaIn sample following 600°C anneal (a) taken at normal emission and (b) taken at 60° off normal emission.

Figure 5-7 shows curve fitted O $1s$ spectra taken, (a) following HF etching and (b) following the 600°C anneal. Curve fitting these spectra clearly shows the evolution of two components that result from annealing. It is highly likely that annealing generates more complex oxides at the surface and subsurface which appear to contain O^{2-} and OH^- species¹.

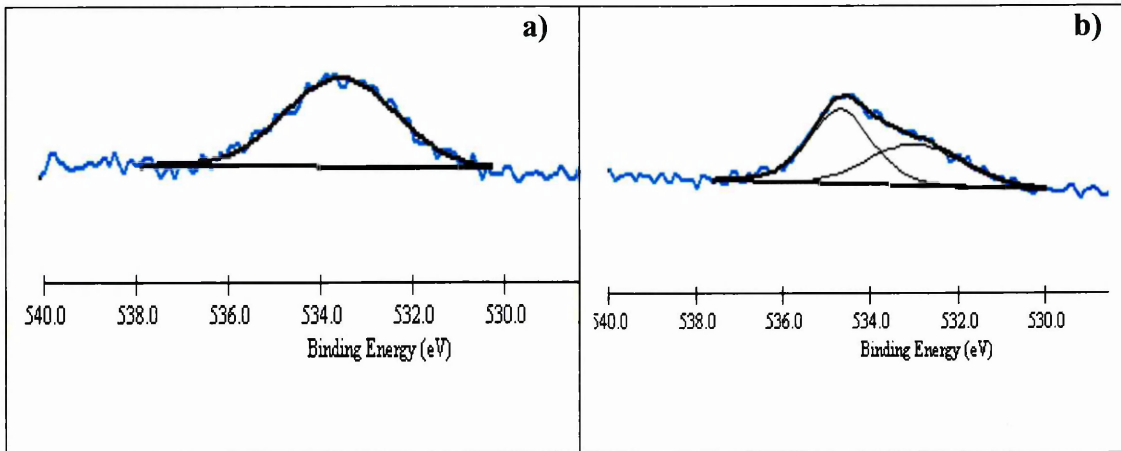


Figure 5-7: Curve fitting O $1s$ spectra obtained following (a) HF etch, normal emission, (b) 600°C anneal, normal emission.

Figure 5-8 shows the Ga $3d$ peaks obtained (a) following the HF etch and (b) after annealing for 10 mins at 600°C. Two components are evident in both cases. The larger component at higher binding energy is attributed to emission from the Ga $3d$ core-level in $\text{Al}_x\text{Ga}_{1-x}\text{N}$. The identification of the smaller component will be discussed later.

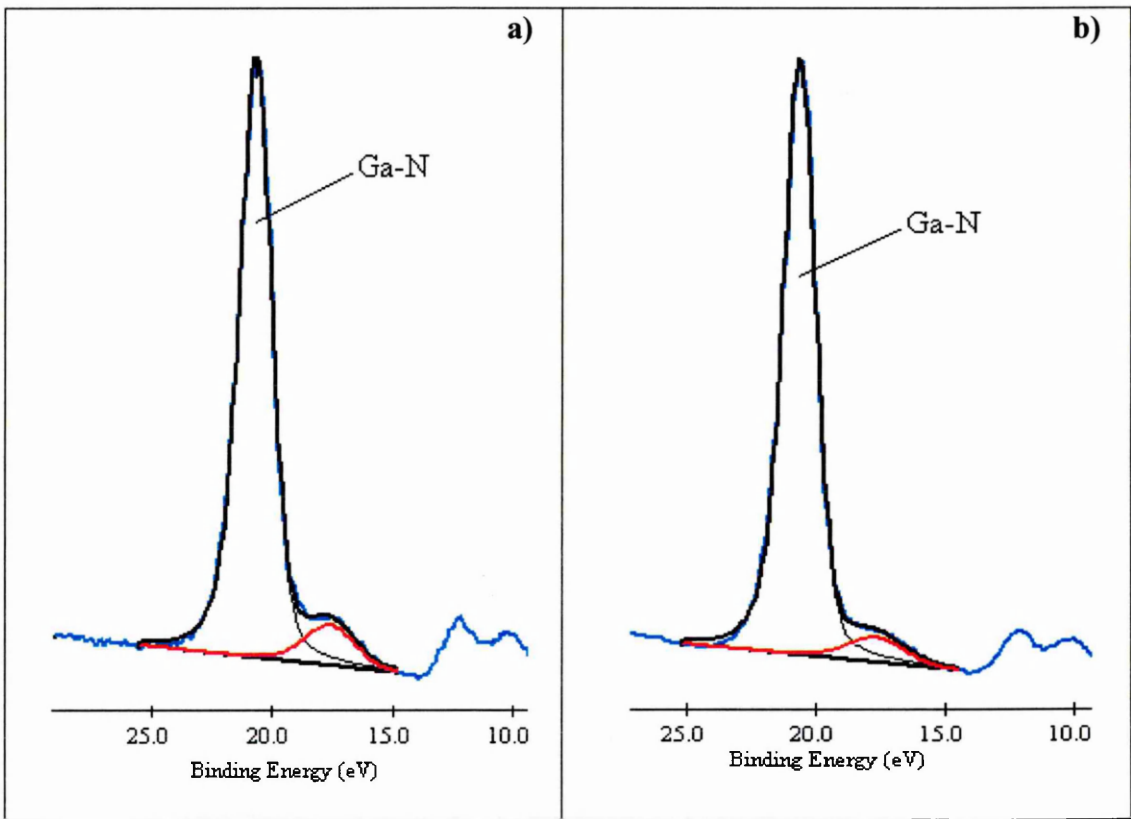


Figure 5-8: Ga 3d peak fitting obtained following (a) HF etch, normal emission, (b) 600°C, normal emission.

Figure 5-9 shows the differences in the $\text{Al}_x\text{Ga}_{1-x}\text{N}$ ($x = 0.20$) sample structure between the surface and the subsurface. The N/Al ratio increases with temperature; this change was more significant for the more surface sensitive scans taken at 60° off normal emission. There is a distinct possibility that these observations arise from an adaptation of the surface stoichiometry, with the concentration of N increasing, and Al decreasing.

Similar behaviour was evident in the N/Ga ratio, indicating that the surface concentration of N increases, whereas the Ga diminishes. This observation is supported by the nominally constant Al/Ga ratio throughout the experiments. This reduction in Ga population at the surface may, in part, explain the observed increases in C/Ga ratio with temperature. The fact that the C/Ga ratio increased with temperature and chemical treatments suggests a reduction in the Ga content at the surface, as most of the ratios to Ga decrease.

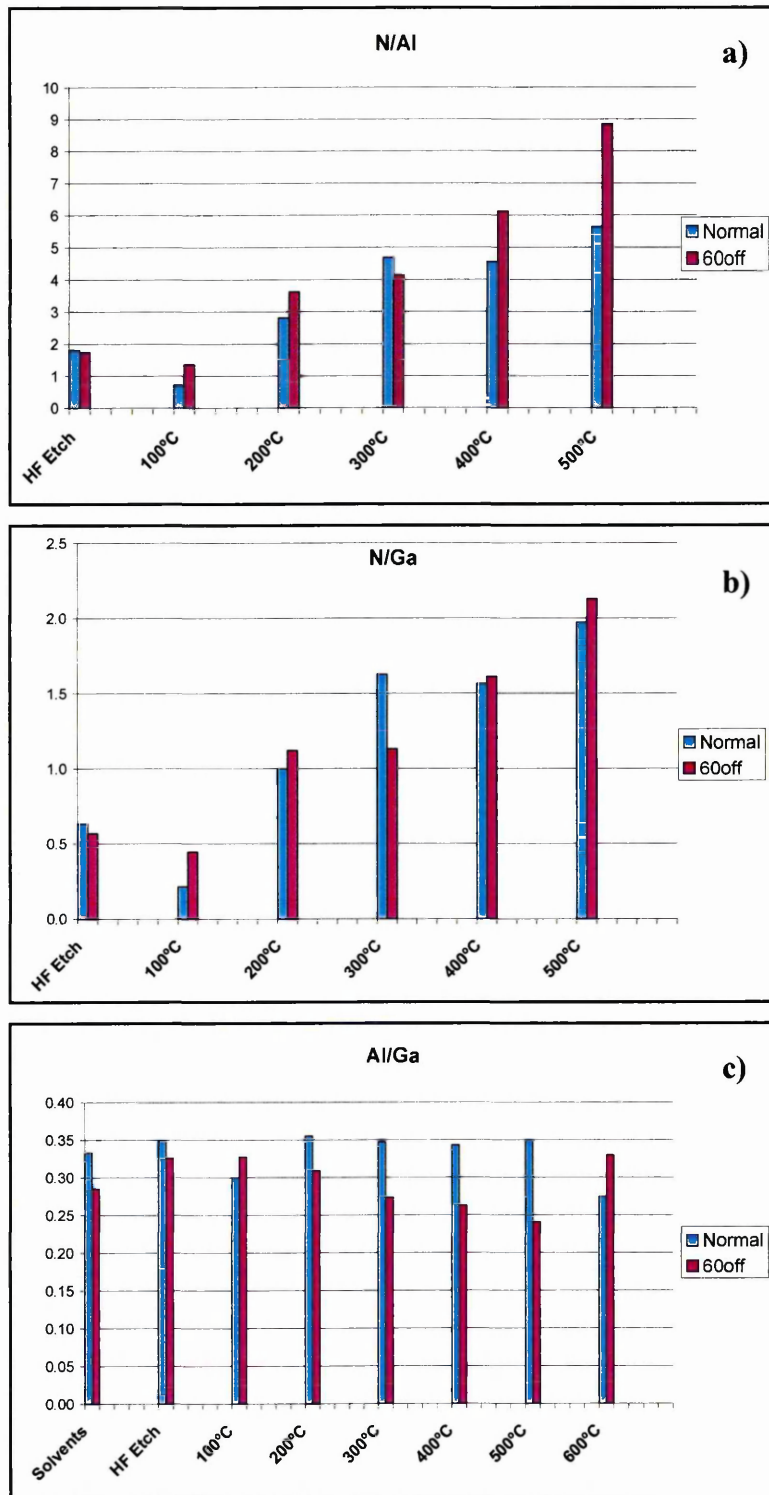


Figure 5-9: Normal emission and 60°off evolution of (a) N/Al ratio, (b) N/Ga ratio and (c) Al/Ga ratio.

In figure 5-10, the N/C ratio is significantly increased from 100°C to 200°C and remained stable at higher temperatures, whereas the N/Ga ratio increased to reach the

N/C value at 500°C. A reduction in C contamination between 100°C and 200°C would explain this behaviour.

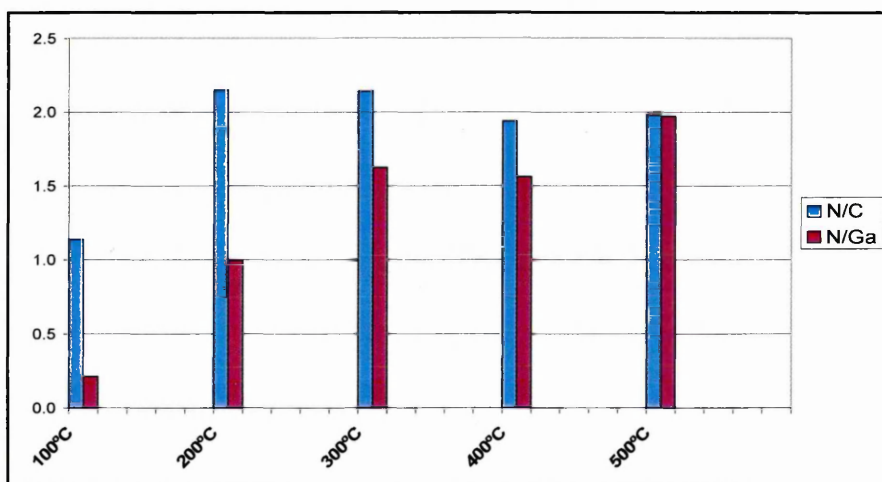


Figure 5-10: The effect of temperature on Carbon contamination

Structural composition:

Investigation of the relative peak intensity ratios reveals changes in the stoichiometry of the surface as the annealing temperature increased. Effectively, evolution of the peak ratios suggests a re-ordering at the $\text{Al}_x\text{Ga}_{1-x}\text{N}$ surface and subsurface. N/Al and N/Ga ratios show that Ga and Al are moving deeper into the surface and N goes to the top surface as the temperature is increased.

In figure 5-8, the overall lineshape and relative binding energy of the smaller component was expected to correspond to Ga_2O_3 at the surface³. However, the binding energy of this component is around 17.5 eV with a constant binding energy difference to Ga 3d of around 3 eV.

Oxygen being more electronegative than Nitrogen, a bond between Ga and O should have higher binding energy than a bond between Ga and N²⁵. In addition, Ga_2O_3 component is often detected in GaAs XPS scans at higher binding energy^{26, 27}. On the other hand, the binding energy of the component in figure 5-8 is also very close to metallic Ga (Ga^0) binding energy which is between 17.5 eV²⁰ and 18.5 eV²⁸.

It is highly likely that the smaller component on Figure 5-8 is N 2s because the different chemical treatments and consecutive increases of temperature did not remove the nitrogen. Additionally, it has previously been identified on GaN surfaces^{29, 30} at a binding energies around 18 eV.

The identification of this component might be facilitated by a higher resolution system. From the shape of this peak, it is highly possible to be due to the presence of the 2 components discussed above, namely the metallic Ga (Ga^0) and N 2s. This kind of investigation will be discussed in more detail in future work.

Even though the C contamination decreases slightly between 100°C and 200°C, a complex mixture of oxides and C are still detected at the surface following the 600°C anneal. Furthermore, peak fitting of the O 1s core-level suggests a complex composition for increasing temperatures and as we go to the top surface. This suggests the presence of a complex contamination layer at the $\text{Al}_x\text{Ga}_{1-x}\text{N}$ surface, mainly composed of oxides and C species reacted with O and H at the top surface, which is in good agreement with Ishikawa *et al.*³. However, the presence and origins of certain contaminants after the different surface treatments and at the subsurface is not yet fully understood.

Band bending:

Binding energy shifts occur at the $\text{Al}_x\text{Ga}_{1-x}\text{N}$ surface for Ga 3d, Al 2p, N 1s core-levels and follow the same trend. Effectively, the different core-level positions shift in the same direction with approximately the same amount, characteristic of Fermi shifts at the $\text{Al}_x\text{Ga}_{1-x}\text{N}$ surface. No changes in peak lineshapes were observed, which tend to support this view. However, the direction of the observed shift changes as a function of surface treatment. Bands bend downward with the successive chemical treatments and then upward after annealing to temperatures up to 400°C. Conversely, annealing at 500°C and 600°C, produced a shift to higher binding energy, indicative of downward band bending.

These phenomena may be interpreted in terms of the creation of surface states and control of their electronic activity. Alterations to the stoichiometry of the surface may produce surface states arising from the redistribution of atoms at the semiconductor surface. It should be noted that $\text{Al}_x\text{Ga}_{1-x}\text{N}$, as a ternary compound, is more complex than GaN and changes in the Al and Ga composition localised at the surface may, in turn, have an influence on the electronic structure of the alloy at the surface^{31, 32}.

Another possible interpretation of the observed evolution of band bending may be the creation of vacancies during the different treatments. Then surface annealing may activate/deactivate these vacancies and induce band bending upward/downward as the temperature increases. Annealing would therefore cause alterations in the density of states which will in turn adapt the band bending at the surface¹⁵. The precise role of these defects remains an open question and will be the subject of future investigation.

5.4. Ion bombardment and annealing (IBA)

In order to obtain clean, well ordered semiconductor surfaces, several techniques have been employed. The presence of various oxides and contaminations at the surface are the result of chemical reactions with air and are very difficult to eliminate. It is important to note that surface characterization should ideally be undertaken in a UHV chamber directly connected to the semiconductor growth chamber. However, when these facilities are not available, efforts have been made to physically etch the surface and analyse the bulk material. Ion bombardment or sputtering has been extensively used to achieve this goal. Sputtering leads to modification of various surface characteristics. These modifications are very important for ion implantation doping which is used at a large scale in the semiconductor industry. Moreover, efforts have to be made to understand the chemistry of the surface after ion bombardment, as well as the new electronic structure. The formation of the Schottky barrier will vary significantly depending on the pre-metallization surface treatment.

The basic principle of IBA is the same regardless of the target atoms used, sputtering time, dose or temperature and is similar to the chemical etch described in the previous section. Atoms are used to bombard the surface in order to break chemical bonds between contaminants and material, or to damage the topsurface below the contamination layer. Ion bombardment will cause structural damage. Annealing will reduce this.

5.4.1. Atomic H sputtering

An Oxford Applied Research thermal gas cracker, with a cracking efficiency of $\sim 50\%$ was used for atomic hydrogen irradiation. In the UHV preparation chamber, the atomic hydrogen clean consisted of 8kL ($1 \text{ kL} = 10^{-3} \text{ Torr s}$) of hydrogen. Then, the $\text{Al}_{0.2}\text{Ga}_{0.8}\text{N}$ sample was annealed under UHV to 400°C for 30 min in increments of 100°C , using an e-beam heater and monitored by an infrared pyrometer. After each step, XPS scans of the Ga $3d$, N $1s$, Al $2p$, C $1s$, O $1s$ core-levels were recorded at normal emission and 60° off normal emission.

Figure 5-11 shows the evolution of Ga $3d$ and Al $2p$ peak position core-levels with the H deposition and annealing temperature. Both peaks exhibit the same shift resulting from atomic H deposition. For Ga $3d$, atomic H deposition shifts the peak position by 0.3 eV to higher binding energy. When the temperature is increased, the

different core-level seem to exhibit the same evolution: 100°C annealing shifts the core-level peak positions to lower binding energy, and then slowly shifting to higher binding energy from 100°C to 400°C.

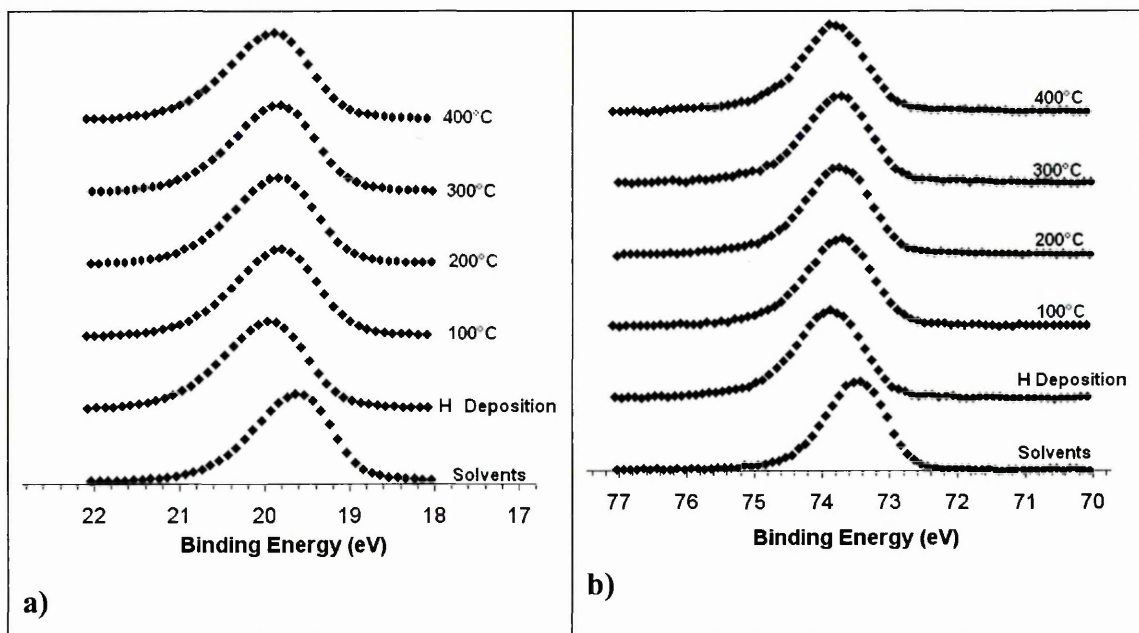


Figure 5-11: Evolution of (a) Ga 3d, and (b) Al 2p core-level peak position with atomic Hydrogen cleaning treatment and annealing.

Figure 5-12 shows the relative intensities of O 1s and C 1s to Ga 3d core-levels (intensities extracted from XPS scans) after H deposition and annealing temperature. Both elements show the same overall evolution: H deposition greatly decreases the relative intensities whereas 100°C temperature annealing clearly increases them (approximately doubled). Higher temperature annealing doesn't have any significant effect on the surface contaminants. The C and O ratios to Ga are significantly by H deposition but this disappears on annealing. Carbon is more reduced than oxygen at normal emission (about 60% and about 40% respectively) after H deposition. Analysis of the more sensitive surface scans taken at 60° off normal emission show a drastic difference in contaminant concentration. Oxygen and carbon ratios are 2 to 3 times higher from the surface to the topsurface which tends to confirm the spatial disposition of the oxide and hydrocarbon contamination layer.

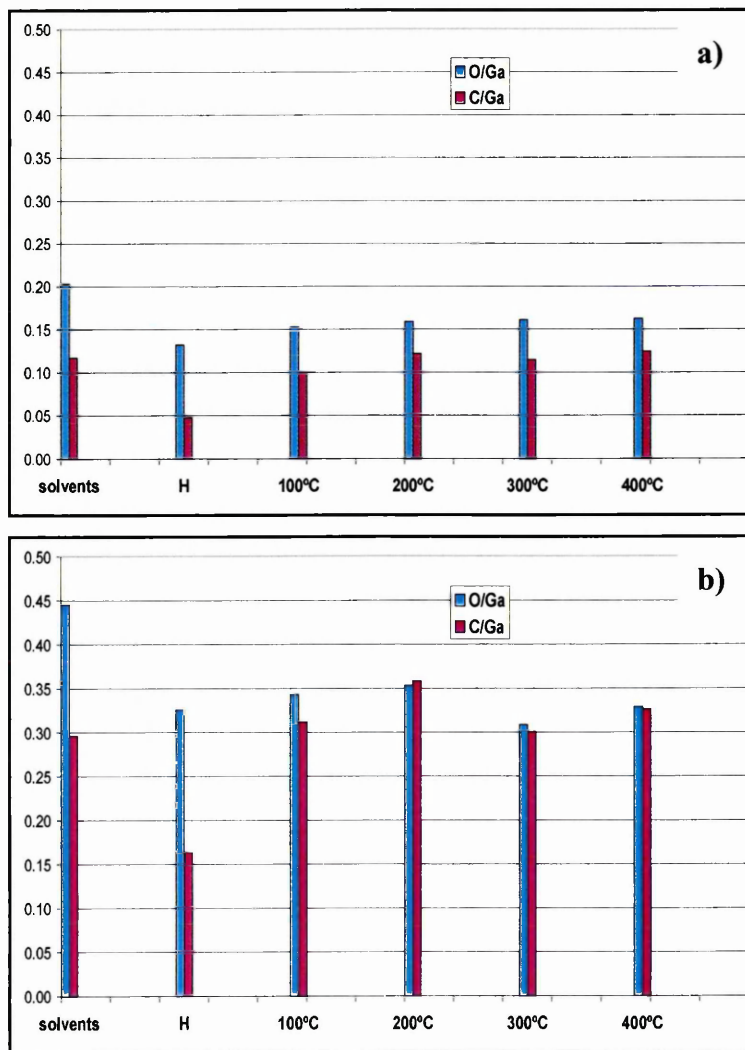


Figure 5-12: Evolution of O/Ga and C/Ga with H irradiation and temperature annealing at (a) normal emission, (b) 60° off normal emission. The intensities have been divided by the appropriate sensitivity factors.

5.5. Summary

In this chapter, we have presented XPS investigations of different Al concentrations of $\text{Al}_x\text{Ga}_{1-x}\text{N}$ using various cleaning techniques.

XPS study of $\text{Al}_x\text{Ga}_{1-x}\text{N}$ ($x=0.20$ and 0.30) surfaces showed that a wet chemical etch in a HF solution followed by annealing at 600°C under UHV was very effective in removing oxygen at the surface and induced Fermi shifts to higher binding energies. It is shown that total Fermi shifts occur between the solvent treatment surface and the 600°C UHV annealed surface of $\Delta E_F = +0.87\text{eV}$ and $\Delta E_F = +0.99\text{eV}$ for the $x = 0.20$ and $x = 0.30$ surfaces, respectively, indicating a downward band bending.

Analysis of the peak ratios showed a re-ordering at the surface and subsurface as the temperature is increased: Ga and Al are moving deeper in the surface, whereas N goes to the top surface. A slight diminution of C content is witnessed between 100°C and 200°C , but C is still detected at 600°C . The increased complexity of oxides at high temperatures and top surface suggests the presence of a contamination layer mainly composed of oxides and C species reacted with O and H at the top surface which is in good agreement with the literature. In parallel to the change in surface stoichiometry, downward band bending is observed with the successive surface treatments followed by upward band bending when annealing to 400°C , whereas higher temperatures result in downward band bending. These phenomena could be attributed to the change in the surface stoichiometry which may produce surface states. It may also be seen as a creation of vacancies due to the surface treatment, which will be activated or deactivated by subsequent temperature annealing.

AHC has been used to remove contamination from the $\text{Al}_x\text{Ga}_{1-x}\text{N}$ surface ($x = 0.2$). H deposition decreased O and C at the surface and topsurface, but annealing at 100°C increased the relative concentration of these contaminants which were not significantly changed at higher temperatures. The large difference in concentration from the surface to the topsurface suggests that the contamination layer is very thin (typically below 1nm). The reduction of Ga at the topsurface, as shown above, might as well explain the difference in the relative concentration in the growth axis.

References

1. S.W. King, J.P. Barnak, M.D. Bremser, K.M. Tracy, C. Ronning, R.F. Davis, R.J. Nemanich, *J. Appl. Phys.*, **84**(9), 5248, (1998).
2. L.D. Bell, R.P. Smith, B.T. McDermott, E.R. Gertner, R. Pittman, R.L. Pierson, G.J. Sullivan, *J. Vac. Sci. Technol. B* **16**(4), 2286, (1998).
3. S.N. Mohammad, *J. Appl. Phys.* **97**, 063703, (2005).
4. H. Ishikawa, S. Kobayashi, Y. Koide, S. Yamasaki, S. Nagai, J. Umezaki, M. Koike, M. Murakami, *J. Appl. Phys.* **81**(3), 1315, (1997).
5. K. Prabhakaran, T.G. Andersson, K. Nozawa, *Appl. Phys. Lett.* **69** (21), 3212, (1996).
6. L.L. Smith, S.W. King, R.J. Nemanich, R.F. Davis, *J. Electron. Mater.* **25**, 805, (1996).
7. V.M. Bermudez, D.D. Koleske, A.E. Wickenden, *Appl. Surf. Sci.* **126**, 69, (1998).
8. C.I. Wu, A. Kahn, N. Taskar, D. Dorman, D. Gallagher, *J. Appl. Phys.* **83**(8), 4249, (1998).
9. T. Ohashi, Y. Saito, T. Maruyama, Y. Nanishi, *J. Cryst. Growth* **237-239**, 1022, (2002).
10. T.D. Veal, I. Mahboob, L.F.J. Piper, C.F. McConville, Hai Lu, W.J. Schaff, *J. Vac. Sci. Technol. B* **22**(4), 2175, (2004).
11. L.F.J. Piper, T.D. Veal, M. Walker, I. Mahboob, C.F. McConville, Hai Lu, W.J. Schaff, *J. Vac. Sci. Technol. A* **23**(4), 617, (2005).
12. J.-M. Bethoux, P. Venegues, F. Natali, E. Feltin, O. Tottereau, G. Nataf, P. De Mierry, F. Semond, *J. Appl. Phys.* **94**(10), 6499, (2003).
13. J.-M. Bethoux, P. Venegues, *J. Appl. Phys.* **97**, 123504, (2005).
14. J.F. Moulder, W.F. Stickle, P.E. Sobol, K.D. Bomben, "Handbook of X-ray photoelectron spectroscopy", Parkin-Elmer, Eden Prairie, MN, (1994).
15. T.G.G. Maffei, M.C. Simmonds, S.A. Clark, F. Peiro, P. Haines, P.J. Parbrook, *J. Appl. Phys.* **92**(6), 3179, (2002).
16. S.M. Widstand, K.O. Magnusson, L.S.O. Johansson, E. Moons, M. Gurnett, H.M. Yeom, H. Miki, M. Oshima, *MRS Internet J. Nitride Semicond. Res.* **9**, 4, (2003).
17. D. Selvanathan, L. Zhou, V. Kumar, I. Adesida, *Phys. stat. sol. (a)* **194** (2), 583, (2002).
18. Y.J. Lin, Y.L. Chu, W.X. Lin, F.T. Chien, C.S. Lee, *J. Appl. Phys.* **99**(7), 073702, (2006).
19. Q.Z. Liu, S.S. Lau, *Solid-State Electronics* **42**(5), 677, (1998).
20. D.P. Butt, Y. Park, T.N. Taylor, *J. Nucl. Mater.* **264**, 71, (1999).
21. J. Liu, B. Shen, Y.G. Zhou, H.M. Zhou, M.J. Wang, Z.W. Zheng, R. Zhang, Y. Shi, Y.D. Zheng, *Optical Materials* **23**, 133, (2003).
22. J. Dumont, R. Caudano, R. Sporcken, E. Monroy, E. Munoz, B. Beamont, P. Gibart, *MRS Internet J. Nitride Semicond. Res.* **5S1** W11.79, (2000).
23. Y. Koyama, T. Hashizume, H. Hasegawa, *Solid-State Electronics* **43**, 1483, (1999).
24. T. Hashizume, S. Ootomo, R. Nakasaki, S. Oyama, M. Khara, *Appl. Phys. Lett.* **76**(20), 2880, (2000).
25. S. Pal, R. Mahapatra, S.K. Ray, B.R. Chakrobotky, S.M. Shivaprasad, S.K. Lahiri, D.N. Bose, *Thin Solid Films* **425**, 20, (2003).
26. K. Ohshika, J. Kuroda, H. Yanazawa, *Electronics and Communications in Japan, Part 2*, **85**(5), (2002).

27. D. Sadowska, A. Gladki, K. Mazur, E. Talik, *Vacuum* **72**, 217, (2004).
28. R. Carli, C.L. Bianchi, *Applied Surface Science* **74**, 99, (1994).
29. T. Hashizume, S. Ootomo, S. Oyama, M. Konishi, H. Hasegawa, *J. Vac. Sci. Technol. B* **19**(4), 1975, (2001).
30. E. A. Beach, E.C. Piquette, T.C. McGill, T.J. Watson, *MRS Internet J. Nitride Semicond. Res.* **4S1**, g6.26, (1999).
31. S.J. Pearton, F. Re, A.P. Zhang, K.P. Lee, *Mat. Sci. and Eng.* **R30**, 55, (2000).
32. D. Seghier, H.P. Gislason, *Physica B* **308-310**, 130, (2001).

Chapter 6

Metal - $\text{Al}_x\text{Ga}_{1-x}\text{N}$ Schottky contacts

6.1. Introduction

The Schottky barrier height is an important parameter for devices. A large barrier height leads to small leakage currents and high breakdown voltages, thus improving the noise level and the high voltage performance of the device. More importantly, a better understanding of the mechanisms of Schottky barrier formation may help in achieving the full potential of the semiconductor material.

While some groups have also used x-ray photoelectron spectroscopy (XPS) to study the formation of metal/AlGa_xN interfaces^{1,2}, to the best of our knowledge, no work using Ag on different Al contents has been reported. The low Ag work function (4.26 eV) would lead to a low Schottky barrier height on the basis of the Schottky-Mott model (see section 3.2.1.). Instead, Ag has been demonstrated to show strong rectifying behaviour with Schottky barrier heights in the range of 0.54 eV³ to 0.80 eV⁴ for Ag/GaN contacts. The wide spread of values calls for further investigations.

The high Ni work function (5.15 eV) has made it a commonly used metal for Schottky contact processing and Ni/GaN and Ni/AlGaN contacts have been extensively studied⁵⁻¹². The fact that Ni has shown to be a comparatively reactive metal was found to create interfacial reactions and/or intermixing with GaN¹³, hence having an influence on the formation of Schottky barrier. The discrepancy in reported barrier heights on GaN, the precise identification of chemical reactions at the interface and its impact barrier height are still under study. XPS would be a useful tool for this kind of investigation. In addition, the initial band bending at the surface has been investigated; GaN and AlGaN surfaces have shown to exhibit significant upward band bending in as-grown and chemically treated surfaces^{14, 15}.

In this chapter, we present an electronic and structural analysis of Ni/Al_{0.2}Ga_{0.8}N and Ag/Al_xGa_{1-x}N Schottky contact formation for x = 0.20 and x = 0.30. These results are compared with the I-V characterisation of Ag Schottky contacts on Al_{0.3}Ga_{0.7}N surfaces treated with N⁺ bombardment followed by 600°C UHV annealing, and discussed in terms of the current models of Schottky barrier formation.

6.2. Experimental details

6.2.1. Ag/ $\text{Al}_x\text{Ga}_{1-x}\text{N}$ contact formation

Two $\text{Al}_x\text{Ga}_{1-x}\text{N}$ samples ($x = 0.20$ and $x = 0.30$) have been used for this study, which were grown by metal-organic chemical vapor deposition (MOCVD) on sapphire substrates (see section 2.1.1.). Details of the sample growth and the dislocation characterisation have been published elsewhere^{16,17}.

Prior to evaporation and XPS studies, for each sample, three successive preparation stages were employed: solvent rinsing, acid etching (HF:H₂O (1:10) for 1 min) and ultra high vacuum (UHV) thermal annealing (600°C for 30 min). The samples have been annealed using an e-beam heater and monitored by an infrared pyrometer. We used AnalaR grade 48% HF for these experiments. Because significant sample charging occurred for all measurements, the C 1s binding energy was used as a reference and assigned a value of 284.8 eV¹⁸.

Investigation of the Ag contact formation on the 2 samples has been discussed through an XPS analysis of the Ga 3*d*, Ga 2*p*, Al 2*p*, N 1*s*, O 1*s*, C 1*s*, and Ag 3*d* photoelectron spectra recorded using a monochromated Al source at normal emission and 60° off normal emission. This was performed using a Scienta ESCA300 spectrometer at the National Centre for Electron Spectroscopy and Surface Analysis, Daresbury Laboratory (see chapter 4). Ag was deposited using a standard thermal evaporation technique, the evaporator was directly connected to the preparation chamber and deposition was monitored using a quartz crystal. The metal was deposited in steps of increasing thickness from 0.5 Å to 30 Å at a base pressure of about 10⁻⁹ mbar as shown in table 6-1.

6.2.2. Ni/ $\text{Al}_{0.2}\text{Ga}_{0.8}\text{N}$ contact formation

The study of Ni/ $\text{Al}_{0.2}\text{Ga}_{0.8}\text{N}$ interface formation was carried out using the same kind of sample as described in the previous section. XPS spectra of the Ga 3*d*, Ga 2*p*, Al 2*p*, N 1*s*, O 1*s*, C 1*s*, and Ag 3*d* core-levels were recorded using an ESCALab system equipped with a twin anode (Al and Mg) non-monochromated X-ray source at the Semiconductor Interface Lab, Swansea. Because of its high melting point (about 1450°C), Ni was deposited using an EGN4 mini e-beam UHV evaporator in steps of increasing thickness, identical to those with Ag as shown in table 6-1.

For the subsequent XPS studies, the same surface preparation was used. A Fischer grade 47-51% HF was used for these experiments.

All core-level photoelectron spectra were recorded using the Mg source in order to avoid the overlapping between Ga LMM Auger and N *1s*. Sample charging occurred for all experiments but the direct binding energy correction using C *1s* could not be applied in this case because of the overlapping between C *1s* and Ga satellites. Hence, for each subsequent XPS study, C *1s* and Ga *3d* were recorded using the Al source, in addition to all core-level spectra using the Mg source. The Ga *3d* binding energy was then calibrated using the C *1s* binding energy reference at a value of 284.8 eV¹⁸. Assuming that Ga *3d* binding energy was constant with the different X-ray sources; its value was used to calibrate the other core-level binding energies.

Deposited metal thickness (Å)	0	0.5	0.5	1	1	2	5	10	30	≈200 (a) 30 (b)
Total metal thickness (Å)	0	0.5	1	2	3	5	10	20	50	≈250 (a) 80 (b)

Table 6-1: Successive metal deposition thicknesses. These were the same for Ag (a) and Ni (b), except for the last deposition where Ag thickness was greater. The values have been measured using a crystal quartz monitor and a previous e-beam evaporator thickness calibration for Ag and Ni respectively.

Finally, the peak fitting procedure was kept the same for all experiments and was carried out using CasaXPS software. The peaks were fitting using the Voigt function, approximated with a Gaussian/Lorentzian product form after subtraction of the Shirley or linear background as discussed in chapter 3. The Ga *3d* core-level was deconvoluted in 3 components: Ga *3d* corresponding to the AlGaN bond, metallic Ga, and N *2s*. The Ga *3d* (AlGaN), Ni *2p_{3/2}* and Ag *3d_{5/2}* peaks were fitted in the same way with the addition of an asymmetric tail parameter, characteristic of the asymmetric metal peakshape.

6.2.3. Electrical measurements

I-V investigations were carried out on Ag/ $\text{Al}_x\text{Ga}_{1-x}\text{N}$ ($x = 0.20$). A thick Ag layer was first deposited on top of the $\approx 250 \text{ \AA}$ previously evaporated for XPS measurements. The conventional photolithographic lift-off technique was then used to define the Schottky diodes as shown in figure 6-1.

I-V measurements of the diodes were made at room temperature using a Keithley 6487 IV measurement system. From the I-V plots, the Schottky barrier height and the ideality factor were determined.

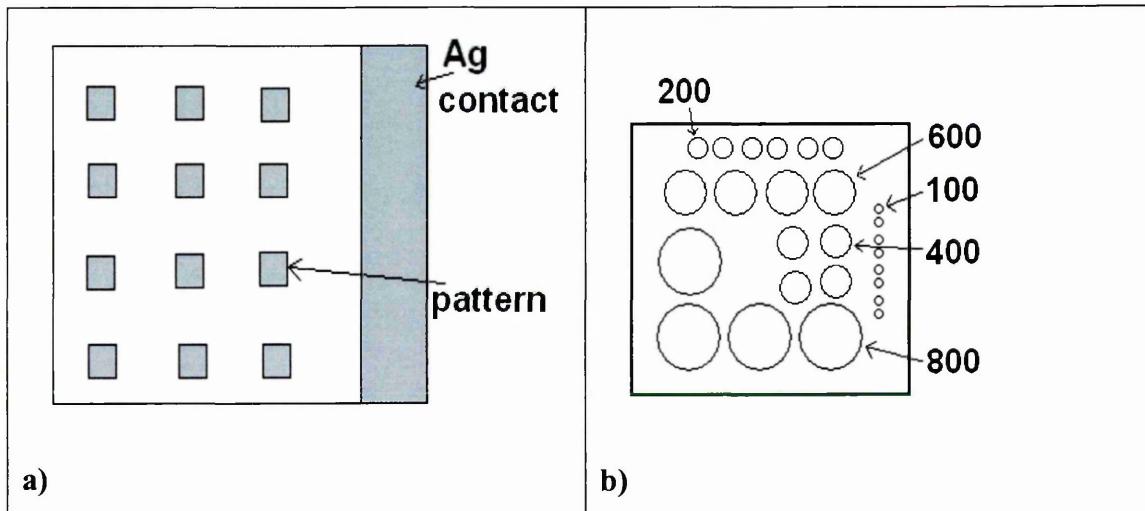


Figure 6-1: Diode processing showing a) the large Ag contact area used for ohmic contact, and b) the magnification of the pattern used. All values are shown in μm .

For the electrical characterization, the Schottky contact was formed by the small circular dots, whereas the Ohmic contact was simply formed by a large area Ag contact on the surface as shown in the figure above.

6.3. Ag - Al_xGa_{1-x}N contacts

This section presents an investigation of the formation of Ag/Al_xGa_{1-x}N Schottky barrier with two different Al concentrations and the same pre-metallization surface treatment. XPS has been extensively used to assess the Ag growth mode on these surfaces and the changes of the electronic properties during the barrier formation.

Therefore, the results are presented along two viewpoints: the variations of the XPS peak intensities and the variations of the XPS peak binding energies along the Ag coverage. In parallel, AFM results taken after the last deposition will also be discussed. Electrical investigation will briefly be described through I-V measurements of Ag/Al_{0.3}Ga_{0.7}N Schottky contacts.

6.3.1. Core-level intensity

a) Ag deposition on Al_{0.2}Ga_{0.8}N surfaces

For each Ag deposition, all XPS core-level intensities have been extracted at normal emission and 60° off normal emission. The evolution of the intensities in Al_{0.2}Ga_{0.8}N with increasing metal thickness is shown on figure 6-2. Because unpredictable intensity variation occurred at the first deposition, all intensities have been normalised to the same intensity at 1 Å. The anomalous intensity changes are likely to be due to an error in the sample position when the data were recorded. The intensity variation along the metal coverage differs at the same angle with the core-level. Ga 2p is found to have the highest intensity drop with Ag thickness which means that Ga 2p is the most surface sensitive core-level. This result is in agreement with theory as the photoelectron mean free path λ can be calculated using the equation¹⁹:

$$\lambda(nm) = 0.41 \left[\frac{A(gmol^{-1})10^{24}}{\rho(kgm^{-3})N(mol^{-1})} \cdot E_{kin}(eV) \right]^{\frac{1}{2}} \quad [6-1]$$

where A is the atomic mass of the element, ρ is the bulk density, N is the Avogadro's number, and E_{kin} the photoelectron kinetic energy.

In addition, figure 6-2(b) shows a faster intensity drop for all core-levels at a more sensitive surface which was due to the smaller photoelectron escape depth. The general attenuation plots trend is similar at both angles and presents a two-step evolution. Intensities drop quickly at low Ag coverage and then slow down at higher

metal thicknesses. The growth mode can be identified using photoelectron intensities and is characteristic of Stranski-Krastanov (SK) mode which means that the Ag growth starts in the layer-by-layer or Frank-van der Merwe (FVDM) mode, and continues in islanding mode or Volmer-Weber (VW) mode.

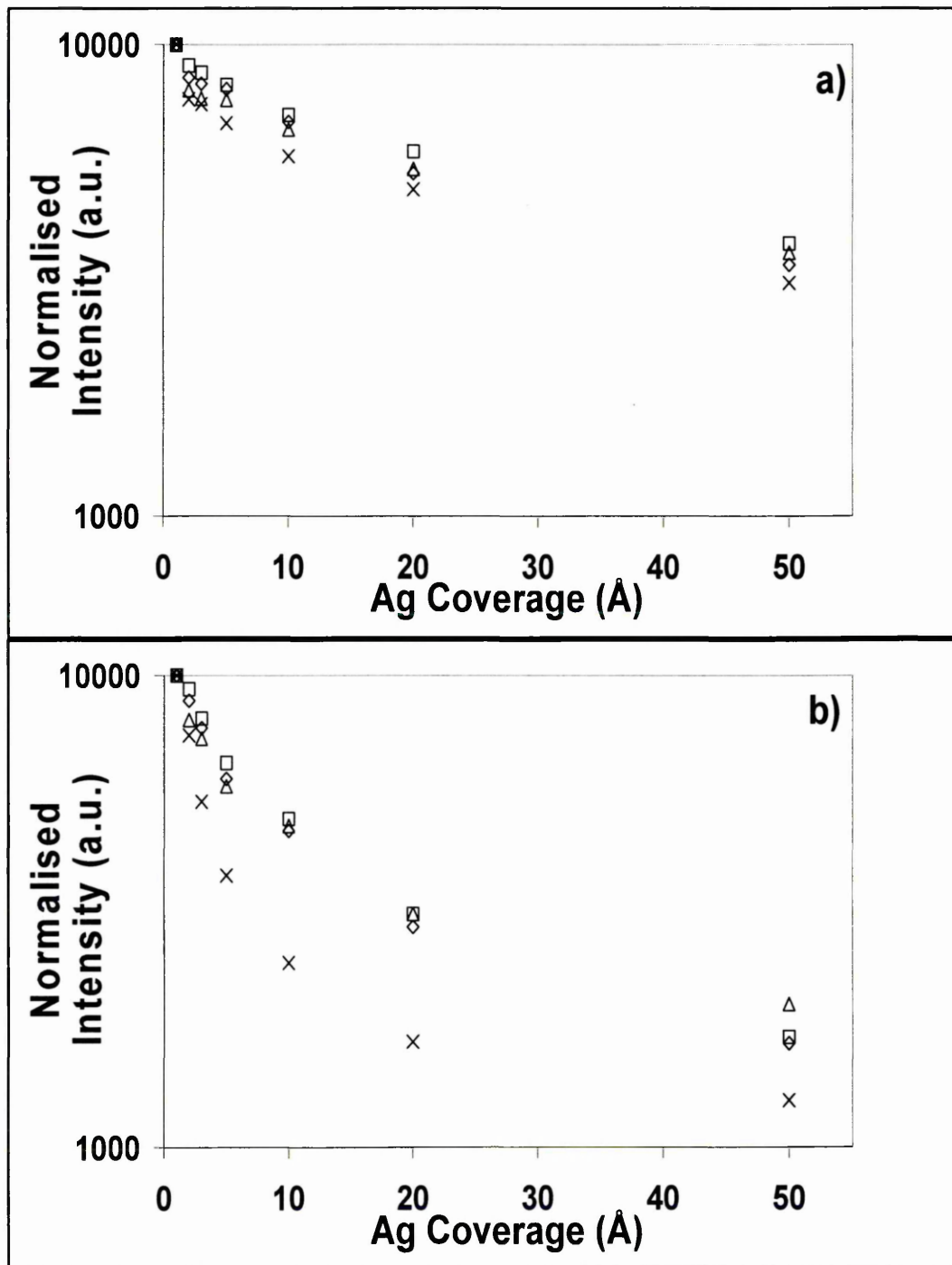


Figure 6-2: Semi-log plots of intensity versus Ag thickness on $\text{Al}_{0.2}\text{Ga}_{0.8}\text{N}$ measured at (a) normal emission and (b) 60° off normal emission. Al $2p$, Ga $3d$, Ga $2p$, and N $1s$ are represented by squares, diamond shapes, crosses, and triangles respectively.

Calculations can be made in order to predict the evolution of the intensity with metal coverage in the SK mode and have been described elsewhere^{20, 21}. However, this growth mode is simply a convolution of the other two, FVDM and VW modes. Hence, in this case, in order to avoid complex calculations, and because the model is valid at low metal coverage, FVDM mode only has been used to extract the photoelectron mean free path.

In the FVDM mode, the intensities of the substrate $I_S(z)$ and metal $I_M(z)$ photoemission lines can be calculated using the following formula²⁰:

$$I_S(z) = I_S^0 \exp\left(-\frac{z}{\lambda}\right) \quad [6-2]$$

and

$$I_M(z) = I_M^\infty \exp\left(-\frac{z}{\lambda}\right) \quad [6-3]$$

where z is the metal thickness, λ the attenuation length, $I_S^0(z)$ the intensity from the clean surface and I_M^∞ the intensity from a thick metal layer.

Figure 6-3 shows an example of the experimental escape depth extraction technique used for all semiconductor core-level intensities at normal emission and 60° off normal emission.

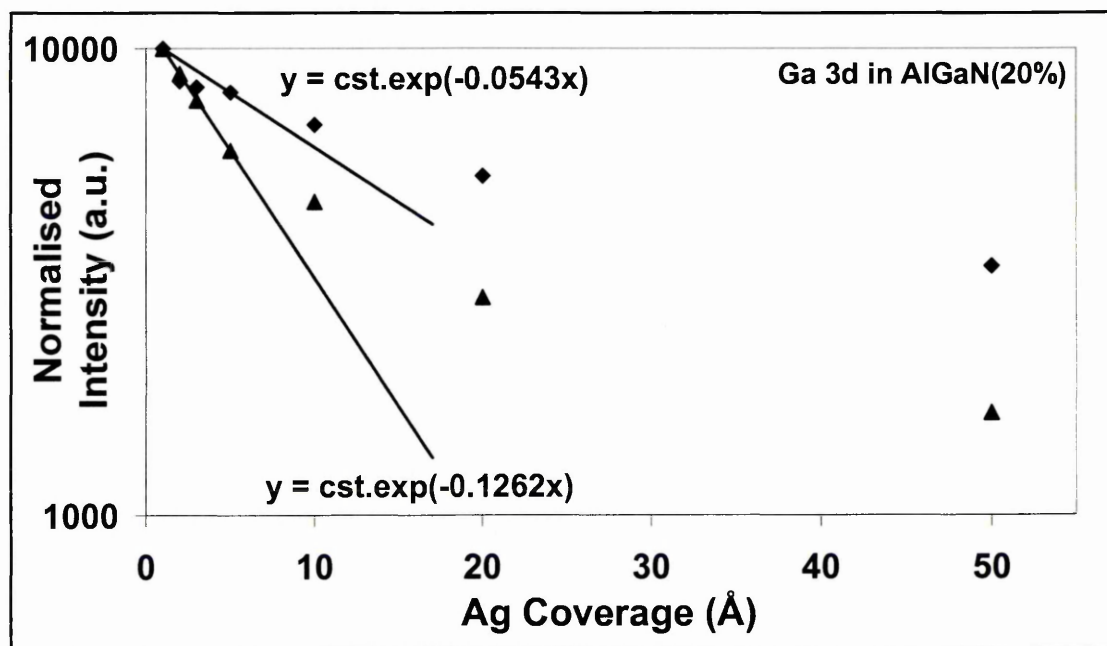


Figure 6-3: Escape depth extraction example on semi-log attenuation plot of Ga 3d core-level intensity versus Ag coverage in Al_{0.2}Ga_{0.8}N. Diamond shapes and triangles represent the Ga 3d intensities taken at normal emission and 60° off normal emission, respectively.

The same procedure was repeated for the different core-level and the general trend was very similar to that of Ga 3d shown in the above figure. The extrapolation line reasonably fits the first data points up to about 5 Å. These XPS results show that Ag grows in layer-by-layer in the first 2-3 monolayers (1 ML \approx 2 Å) and then grows in islands on Al_{0.2}Ga_{0.8}N under this specific surface treatment.

Table 6-2 presents the results on the determination of the escape depth extracted from the XPS data. Equations [6-1] and [6-2] were used to calculate the theoretical values for the photoelectron mean free path. At normal emission, the escape depth equals the mean free path, whereas at 60° off normal emission, the escape depth becomes half of it. These values were compared with the ones extracted from the attenuation plots.

	Experimental		Theory		Theory/exp	NE/60
	1/lambda	lambda	1/lambda	lambda		
Al2p 60	0.105	9.5	0.101	9.9	1.0	2.1
Al2p NE	0.049	20.4	0.050	19.8	1.0	
Ga3d 60	0.126	7.9	0.091	11.0	1.4	2.3
Ga3d NE	0.054	18.4	0.045	22.0	1.2	
Ga 2p 60	0.244	4.1	0.182	5.5	1.3	2.5
Ga 2p NE	0.096	10.4	0.091	11.0	1.1	
N 1s 60	0.154	6.5	0.108	9.2	1.4	2.3
N 1s NE	0.067	14.9	0.054	18.4	1.2	
Ag 3d 60	0.111	9.0	0.112	9.0	1.0	2.1
Ag 3d NE	0.054	18.5	0.056	17.9	1.0	

Table 6-2: Comparison of the experimental and theoretical escape depth values at normal emission and 60° off normal emission for Ag/Al_{0.2}Ga_{0.8}N.

The ratio $\lambda_{\text{theory}}/\lambda_{\text{exp}}$ is very close to unity and shows that the value given by the crystal quartz monitor is likely to be correct. Furthermore, the calibration of this device assumes a metal sticking coefficient of 1, which tends to suggest that most of the Ag evaporated sticks to this chemically treated/annealed Al_{0.2}Ga_{0.8}N surface. Au/GaN interface properties have been investigated by XPS using the same experimental procedure. Sporken *et al.*²² used hot KOH, aqua regia followed by 900°C UHV annealing and found a large overestimation of Ga 3d and N 1s escape depths (about 10 times). Maffei *et al.*²³ used HF followed by 600°C annealing and found an

underestimation of their escape depths (2 to 4 times) which they partially attributed to the design of the manipulator.

Whether the discrepancies observed are due to the pre-metallization surface treatment, the intrinsic chemical/electronic properties of the semiconductor used or the metal used remains an open question and will be discussed later.

The ratio NE/60 varies from 2.1 for Al $2p$ to 2.5 for Ga $2p$ and is in good agreement with what might be expected. However, there is a slight difference with values from theory as we have: $\lambda_{Ga2p} < \lambda_{Ni3s} < \lambda_{Ga3d} < \lambda_{Al2p}$ where λ_{Al2p} should be smaller than λ_{Ga3d} . This might be due to the close values of mean free paths for Ga $3d$ and Al $2p$.

b) Ag deposition on $Al_{0.3}Ga_{0.7}N$ surfaces

The same sets of experiments were conducted on $Al_{0.3}Ga_{0.7}N$ in parallel to the other Al concentration material. While one sample was being examined in the analysis chamber, the other one was in the preparation chamber where Ag was being deposited. The evolution of the intensities in $Al_{0.3}Ga_{0.7}N$ with increasing metal thickness is shown in figure 6-4. For the same reasons discussed earlier, all intensities have been normalised to that at 1 Å.

The intensity variations along the metal coverage differed at the same angle with the core-level and Ga $2p$ was found to be the most surface sensitive core-level, which is in agreement with theory.

The evolution of the core-level signals shows a similar trend to the one observed for the other Al concentration material and is consistent with SK growth.

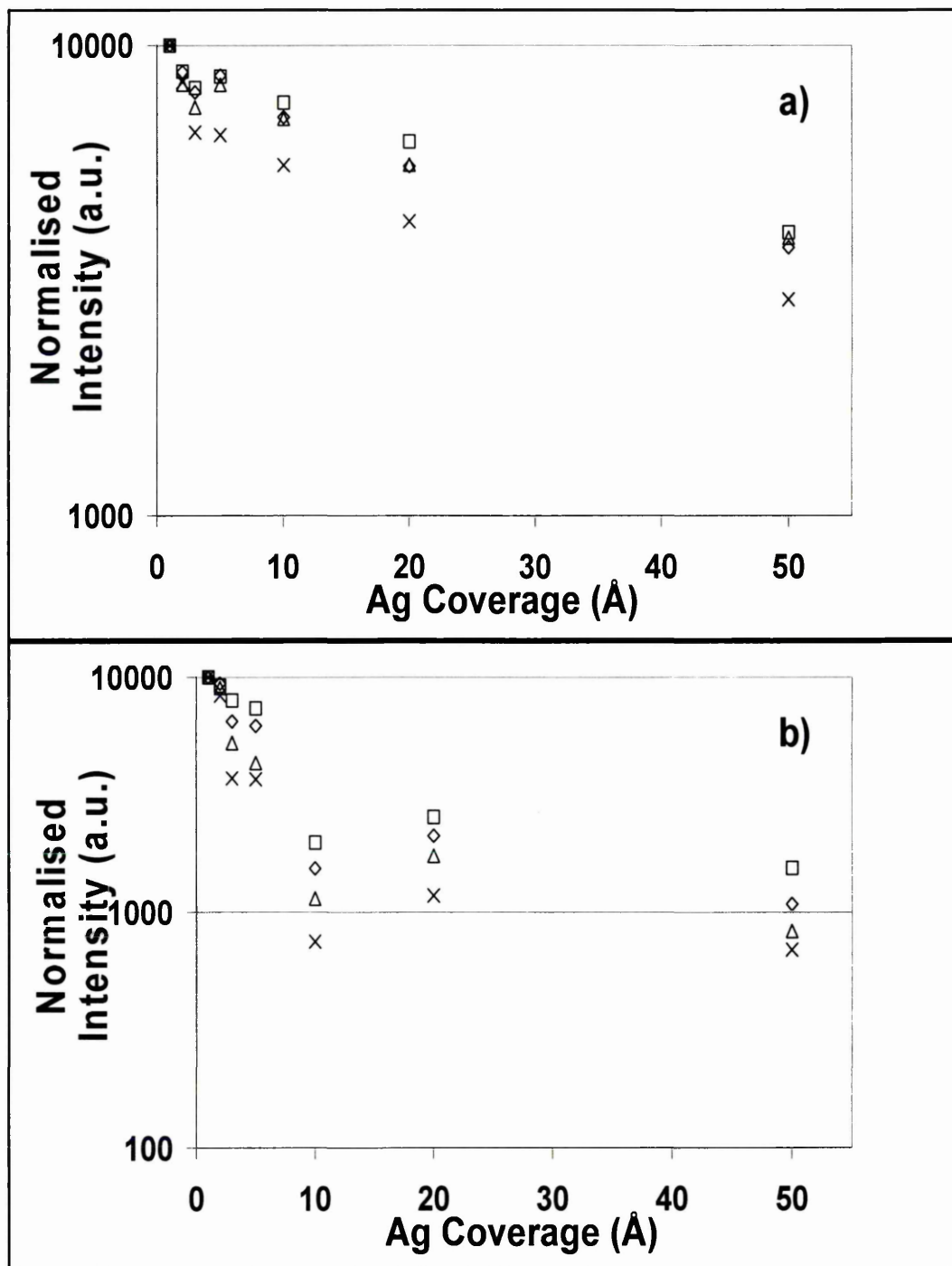


Figure 6-4: Semi-log plots of intensity versus Ag thickness on Al_{0.3}Ga_{0.7}N measured at (a) normal emission and (b) 60° off normal emission. Al 2*p*, Ga 3*d*, Ga 2*p*, and N 1*s* are represented by squares, diamond shapes, crosses, and triangles, respectively.

The general core-level intensity evolution at normal emission and 60° off normal emission seems to present some differences between the two materials and makes the escape depth extraction more difficult, as shown in figure 6-5.

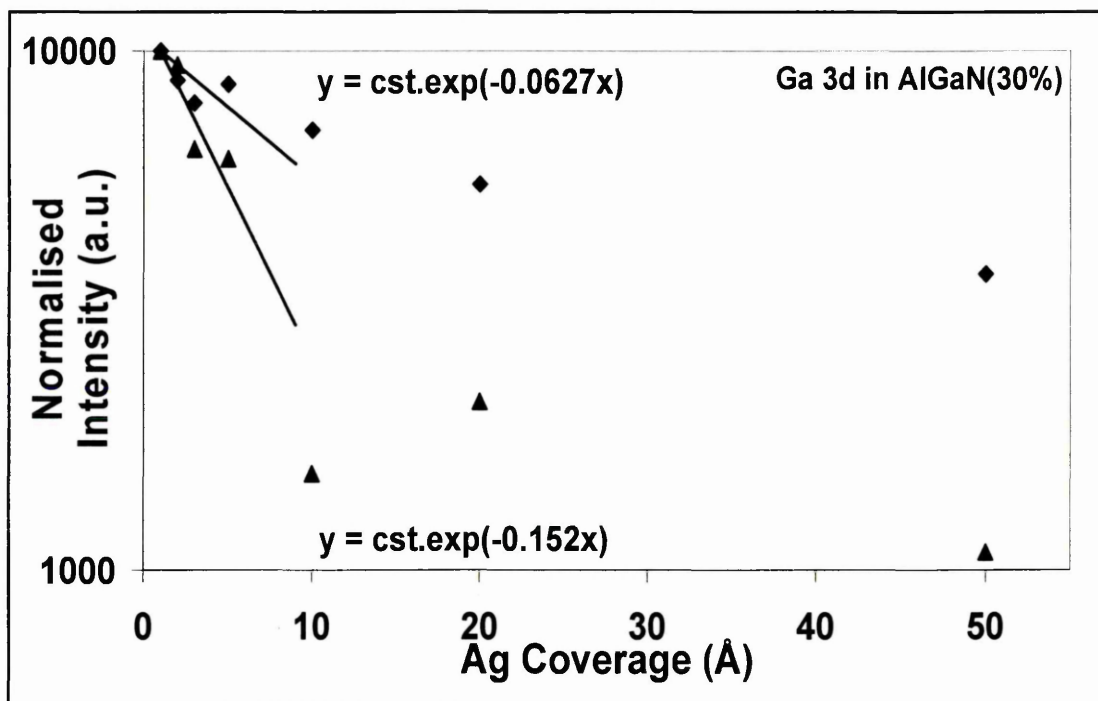


Figure 6-5: Escape depth extraction example on semi-log attenuation plot of Ga 3d core-level intensity versus Ag coverage in $\text{Al}_{0.3}\text{Ga}_{0.7}\text{N}$. Diamond shapes and triangles represent the Ga 3d intensities taken at normal emission and 60° off normal emission respectively.

The extrapolation lines (least squares fit) have been drawn in order to fit as reasonably as possible the first few data points, assuming a SK growth mode. However, it is highly likely that results obtained using this method contain more errors in the measurement of the escape depth compared to $\text{Al}_{0.2}\text{Ga}_{0.8}\text{N}$. Results of these measurements are shown in table 6-3.

	Experimental		Theory		Theory/exp	NE/60
	1/lambda	lambda	1/lambda	lambda		
Al2p 60	0.152	6.6	0.101	9.9	1.5	2.4
Al2p NE	0.063	15.9	0.050	19.8	1.2	
Ga3d 60	0.114	8.8	0.091	11.0	1.3	1.9
Ga3d NE	0.060	16.8	0.045	22.0	1.3	
Ga 2p 60	0.288	3.5	0.182	5.5	1.6	2.0
Ga 2p NE	0.144	6.9	0.091	11.0	1.6	
N 1s 60	0.210	4.8	0.108	9.2	1.9	2.6
N 1s NE	0.082	12.2	0.054	18.4	1.5	
Ag 3d 60	0.171	5.8	0.112	9.0	1.5	2.2
Ag 3d NE	0.078	12.8	0.056	17.9	1.4	

Table 6-3: Comparison between the experimental and theoretical escape depth values at normal emission and 60° off normal emission for Ag/ $\text{Al}_{0.3}\text{Ga}_{0.7}\text{N}$.

The ratio $\lambda_{\text{theory}}/\lambda_{\text{exp}}$ is still close to unity but is always greater than 1, and consistently higher than the one using $\text{Al}_{0.2}\text{Ga}_{0.8}\text{N}$. The fact that the same metal has been deposited on two different materials, under the same pre-metallization surface treatment, points out the different character of the surface with the metal. However, it is important to note that the values measured for the Al concentration $x = 0.30$ might be subjected to substantial errors.

The ratio $\text{NE}/60$ varies from 1.9 for Ga $3d$ to 2.6 for N $1s$ and is in good agreement with what we would expect and the relation $\lambda_{\text{Ga}2p} < \lambda_{\text{N}1s} < \lambda_{\text{Al}2p} < \lambda_{\text{Ga}3d}$ is respected.

6.3.2. Core-level binding energy

a) Ag deposition on $\text{Al}_{0.2}\text{Ga}_{0.8}\text{N}$ surfaces

Figures 6-6 to 6-8 show the evolution of the core-level binding energies Ga $3d$, Al $2p$ and N $1s$ respectively with increasing Ag thickness. The data labelled "600°C" correspond to the last surface treatment before the metal deposition and is considered as the clean surface. Hence, the changes related to Ag formation on the semiconductor material will be compared to this binding energy position. Effects of the surface treatment have been developed in the previous chapter, and will be used to explain the Schottky barrier formation.

By comparing the evolution of the substrate core-level binding energy positions, we can see that all of them follow the same trend. The first Ag deposition (0.5 Å) induces a shift of 0.3 eV to lower binding energy. Further metal depositions do not cause any shift, except for the third deposition (2 Å) which induces a small shift of 0.1 eV in the opposite direction but the following one shifts the positions back to the first metal deposition position.

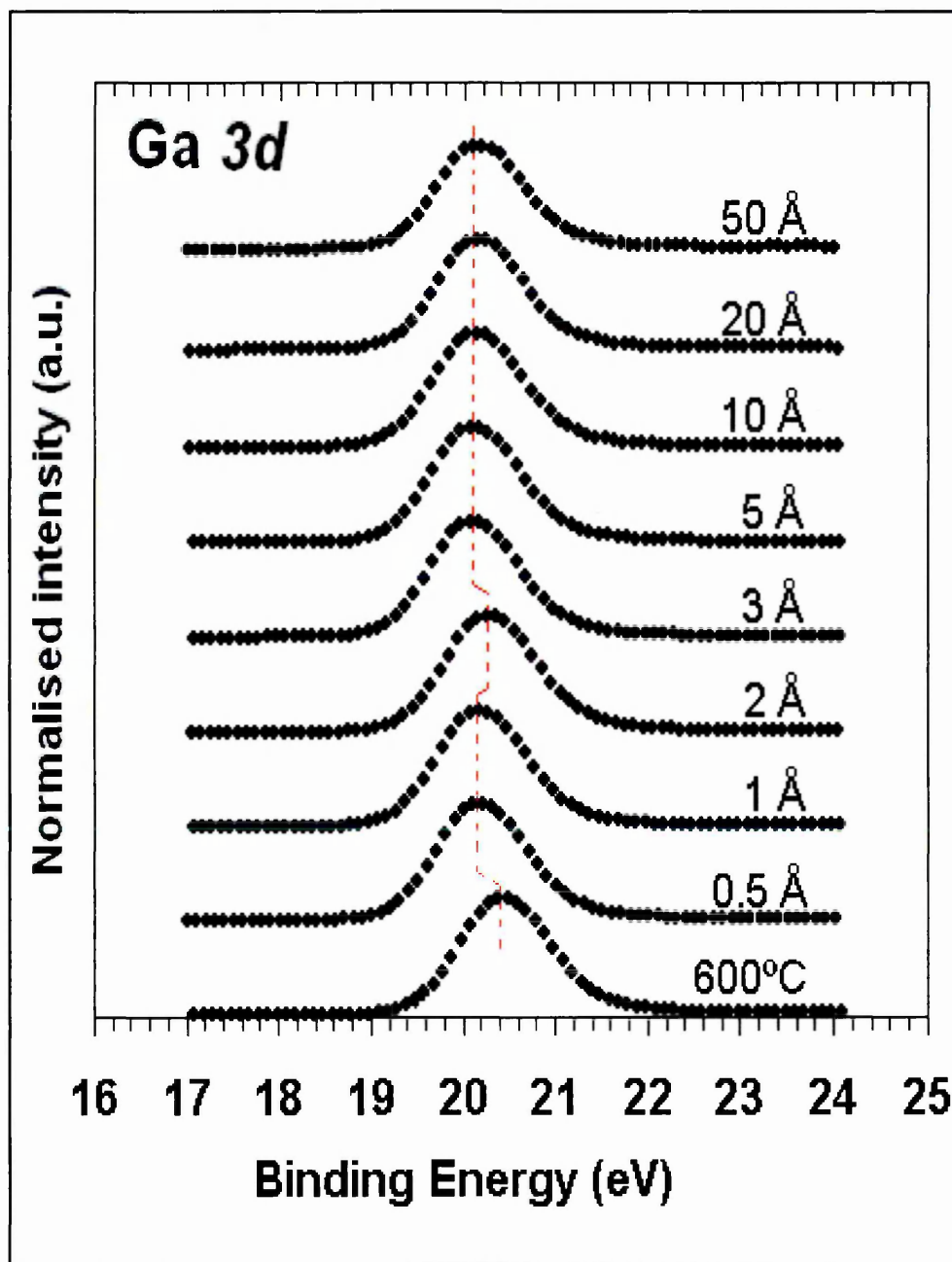


Figure 6-6: Evolution of the normalised Ga 3d lineshape at increasing Ag thickness on $\text{Al}_{0.2}\text{Ga}_{0.8}\text{N}$ surface at normal emission.

Additionally, the Ga 3d, Al 2p and N 1s peaks did not show any significant change in the full width at half maximum (FWHM), indicating that no chemical reaction was resolved at the interface.

These observations indicate that the interface is unreacted and that the rigid shifts in binding energy result from Fermi shifts as the interface is formed.

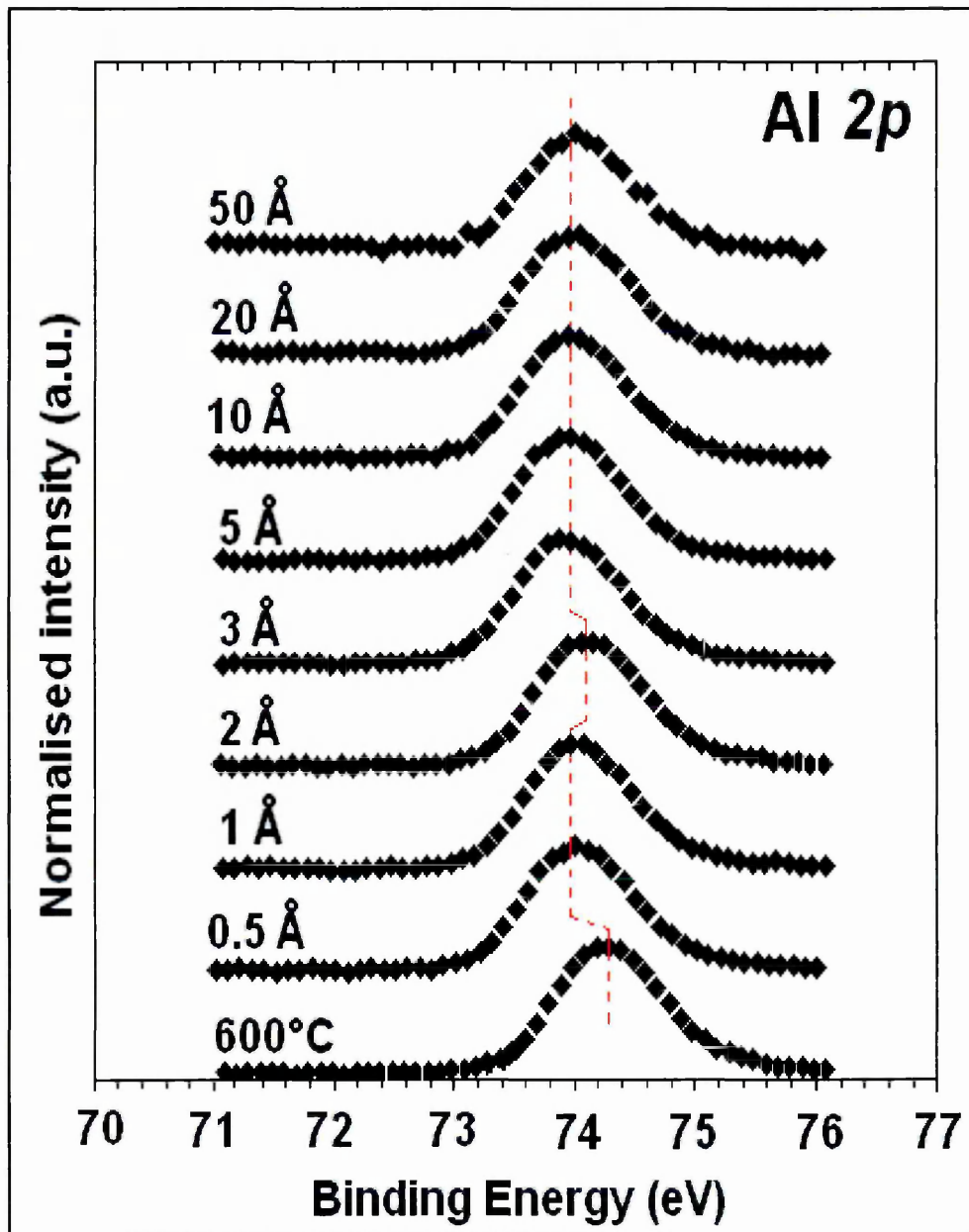


Figure 6-7: Evolution of the normalised Al 2p lineshape with increasing Ag thickness on Al_{0.2}Ga_{0.8}N surface at normal emission.

The Fermi shifts measured between the clean surface, subjected to HF etch and 600°C UHV annealing, and the last Ag deposition were $\Delta E_F = -0.30$ eV at Al_{0.2}Ga_{0.8}N surface, indicating an upward band bending.

Figure 6-9 shows the evolution of the Ag 3d_{5/2} core-level with Ag coverage at normal emission. In order to minimise errors in the peak fitting, the analysis has been done on the high intensity Ag core-level, Ag 3d_{5/2}.

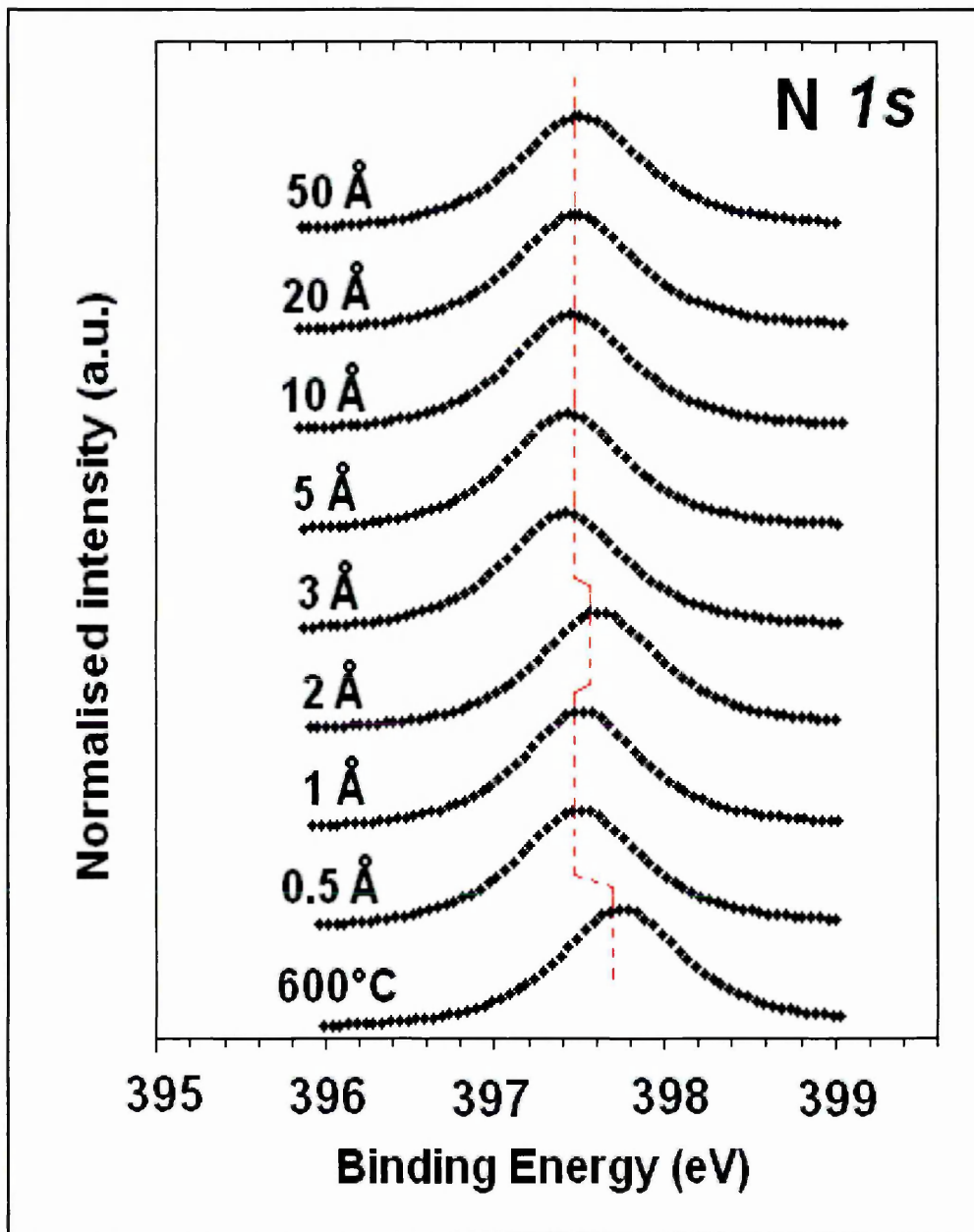


Figure 6-8: Evolution of the normalised N 1s lineshape at increasing Ag thickness on $\text{Al}_{0.2}\text{Ga}_{0.8}\text{N}$ surface at normal emission.

Two interesting features may be seen on figure 6-9. First of all, the core-level binding energy position is gradually shifted to lower binding energy as Ag thickness increases. The binding energy position of the Ag $3d_{5/2}$ core-level at 0.5 Å metal thickness is 368.5 eV, and decreases to reach 368.1 eV at 20 Å. That position remains unchanged at higher thickness which shows that pure metallic element is formed at the surface.

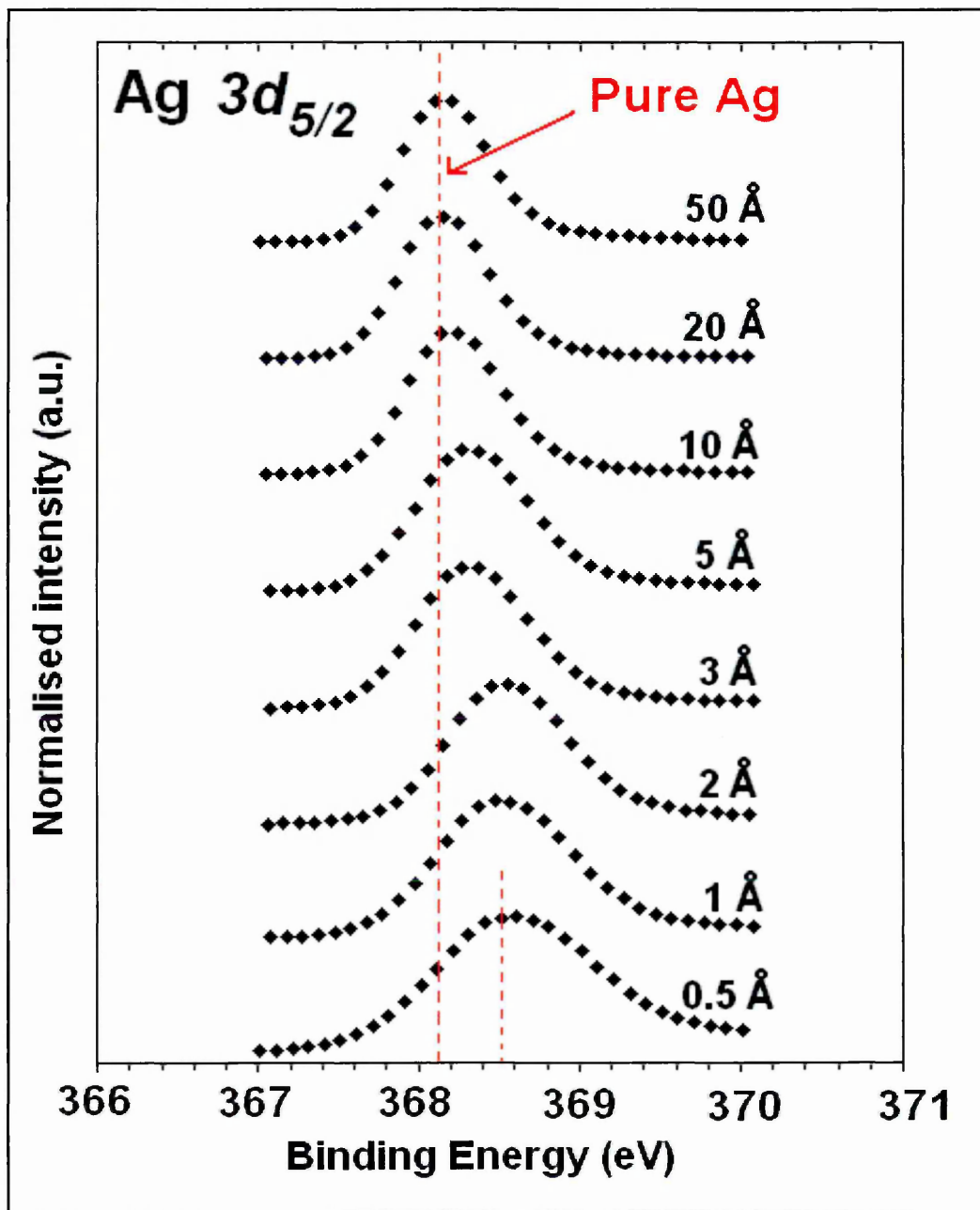


Figure 6-9: Evolution of the normalised Ag 3d_{5/2} lineshape at increasing Ag thickness on Al_{0.2}Ga_{0.8}N surface at normal emission.

The core-level position is found to be in good agreement with values from metallic Ag in literature²⁴. Then, the metal core-level peakshape is found to change with increasing thickness. The measurement of the full width at half maximum (FWHM) shows a decrease from about 1 eV at 0.5 Å to about 0.55 eV after the last deposition. This is indicative of Ag chemical shift. The origin of these shifts will be discussed later in the text.

b) Ag deposition on $Al_{0.3}Ga_{0.7}N$ surfaces

Figures 6-10 to 6-12 show the evolution of the core-level binding energies Ga $3d$, Al $2p$ and N $1s$ respectively, with increasing Ag thickness on $Al_{0.3}Ga_{0.7}N$. Analysis of the peak positions show unusual differences compared to surfaces with lower Al concentration. All core-levels follow the same trend with Ag coverage greater than 2 Å. However, Ga $3d$ and Al $2p$ follow the same trend with increasing metal thickness even below 2 Å, but Ga $3d$ shifts have higher magnitude.

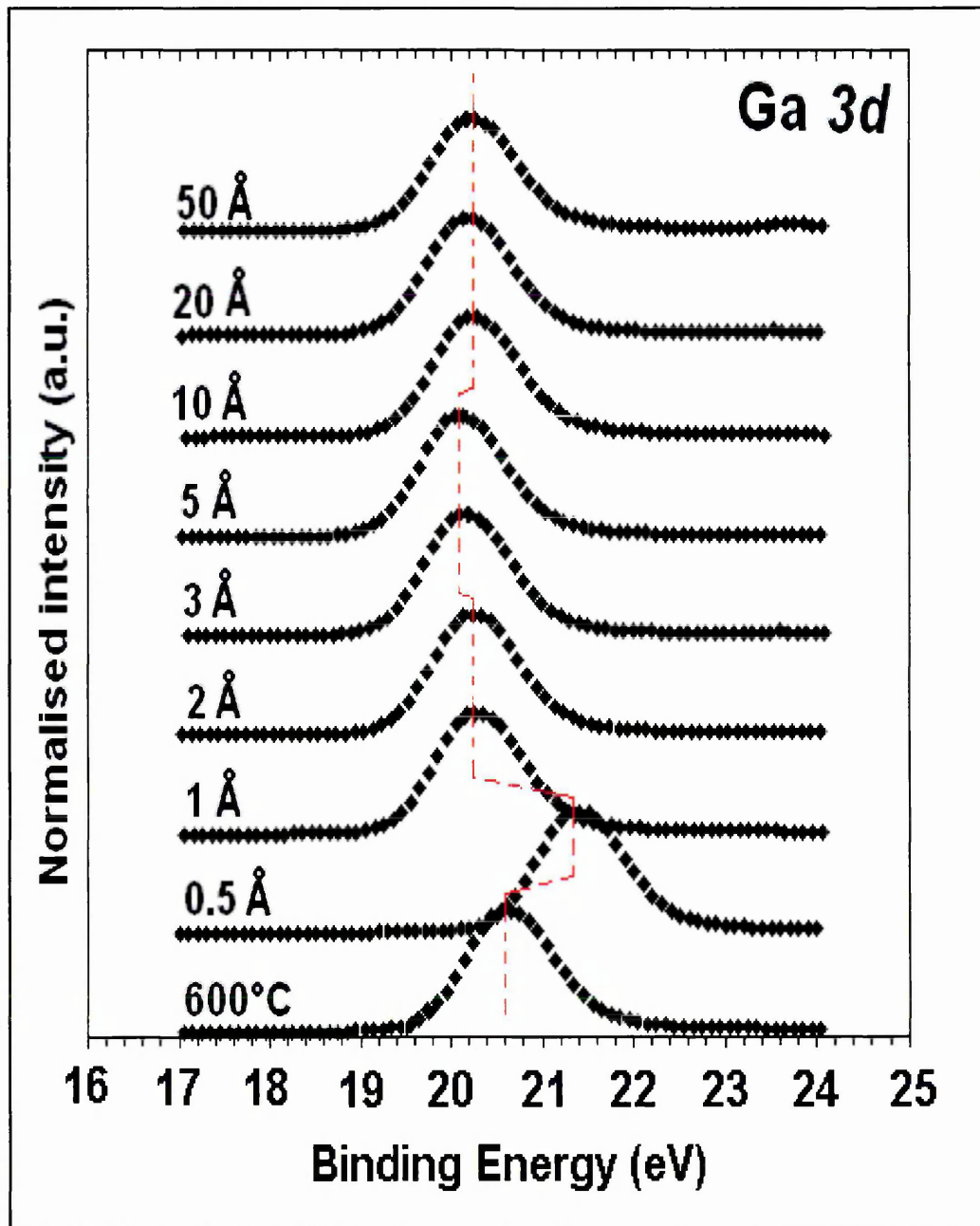


Figure 6-10: Evolution of the normalised Ga $3d$ lineshape at increasing Ag thickness on $Al_{0.3}Ga_{0.7}N$ surface at normal emission.

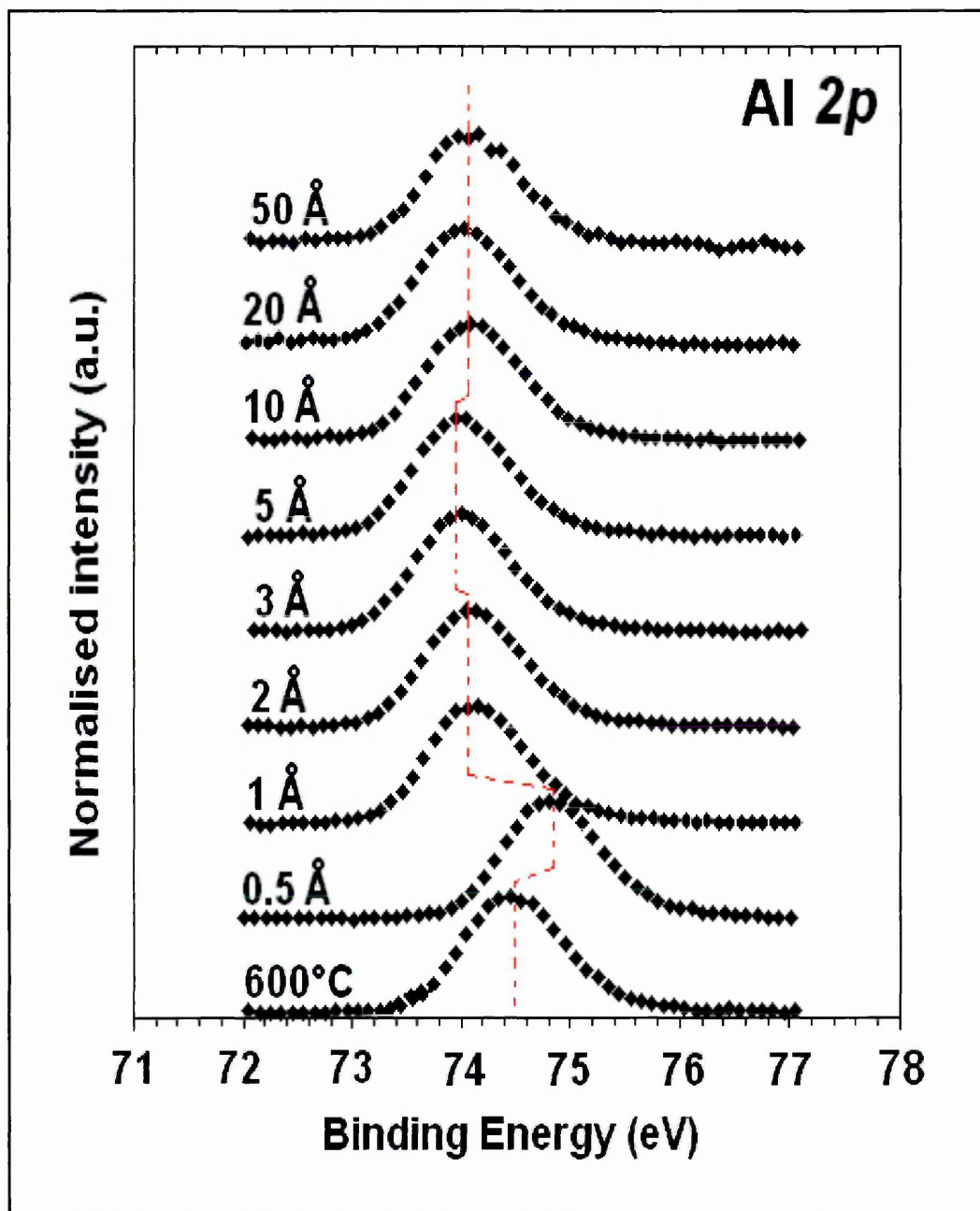


Figure 6-11: Evolution of the normalised Al 2p lineshape at increasing Ag thickness on $Al_{0.3}Ga_{0.7}N$ surface at normal emission.

For Ga 3d and Al 2p core-levels, the first Ag deposition induces a shift to higher binding energy of about + 0.7 eV and + 0.3 eV respectively. The second Ag deposition causes a shift to lower binding energy of about - 1.1 eV and - 0.7 eV for Ga 3d and Al 2p respectively. The positions remain unchanged until 3 Å Ag coverage where a small shift of - 0.1 eV to lower binding energy occurs. Finally, 10 Å coverage shifts the positions back to the value at 1 Å. The positions remain unchanged afterwards.

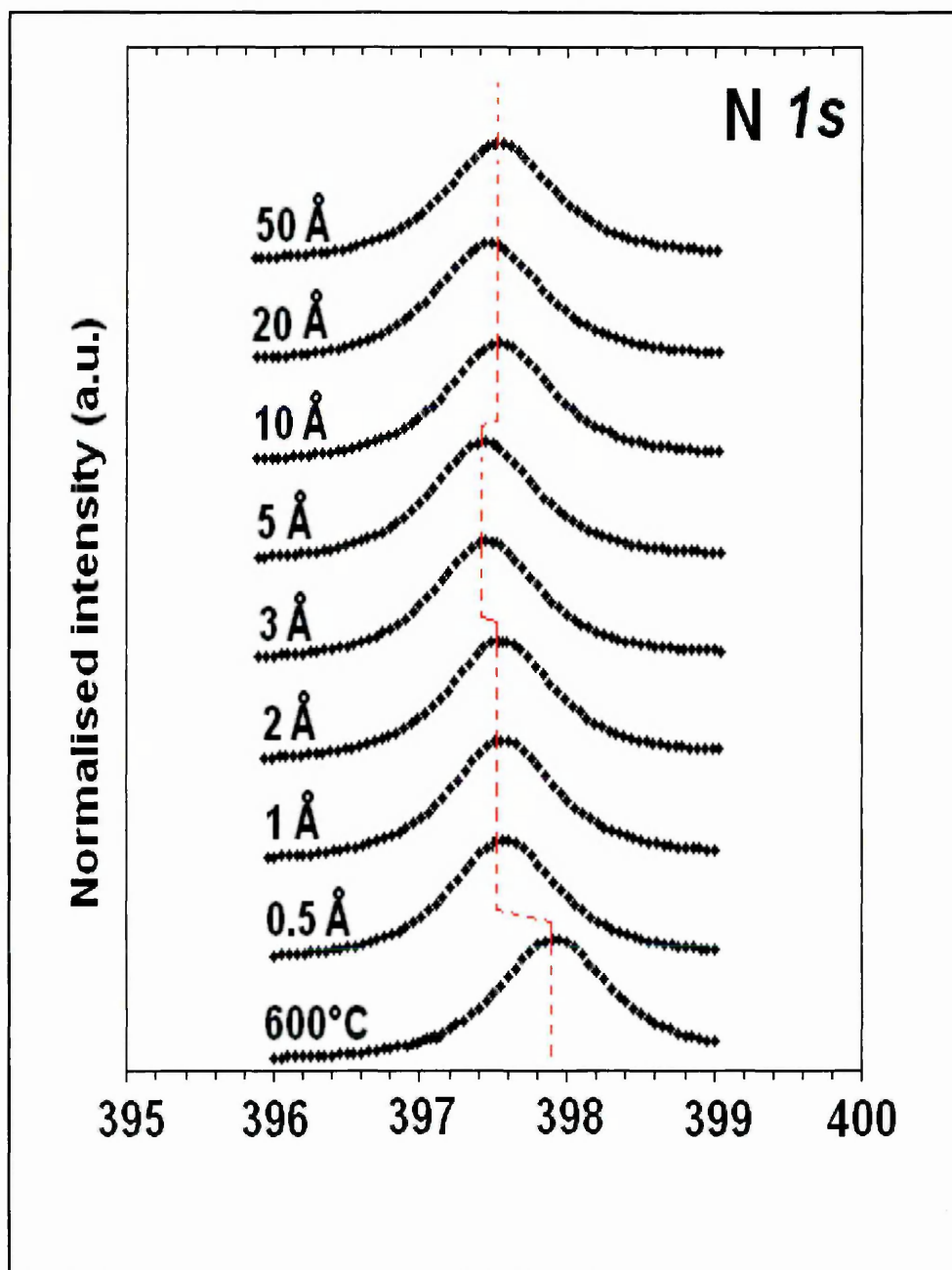


Figure 6-12: Evolution of the normalised N $1s$ lineshape at increasing Ag thickness on $\text{Al}_{0.3}\text{Ga}_{0.7}\text{N}$ surface at normal emission.

On the other hand, the N $1s$ core-level peak position shows a very similar evolution with increasing Ag coverage. However, the shifts to higher and lower binding energy following the first and second depositions, recorded for Ga $3d$ and Al $2p$, are not observable. Instead, the first deposition causes a shift to lower binding energy of -0.4 eV. The peak position remains unchanged until 3 \AA metal coverage and then follows the same trend as the other substrate core-levels. Similar to $\text{Al}_{0.2}\text{Ga}_{0.8}\text{N}$, the substrate peakshapes showed no significant change in the FWHM with increasing Ag thickness. Despite the anomalous position change in Ga $3d$ and Al $2p$ core-levels at 0.5 \AA , the

shifts undergone by all core-levels are similar in trend and magnitude from the clean surface to the last Ag deposition.

It is highly likely that the shifts observed above 1 Å are rigid Fermi shifts. The total Fermi shifts measured from the clean $\text{Al}_{0.3}\text{Ga}_{0.7}\text{N}$ and the last Ag deposition $\Delta E_F = -0.40$ eV, indicating upward band bending.

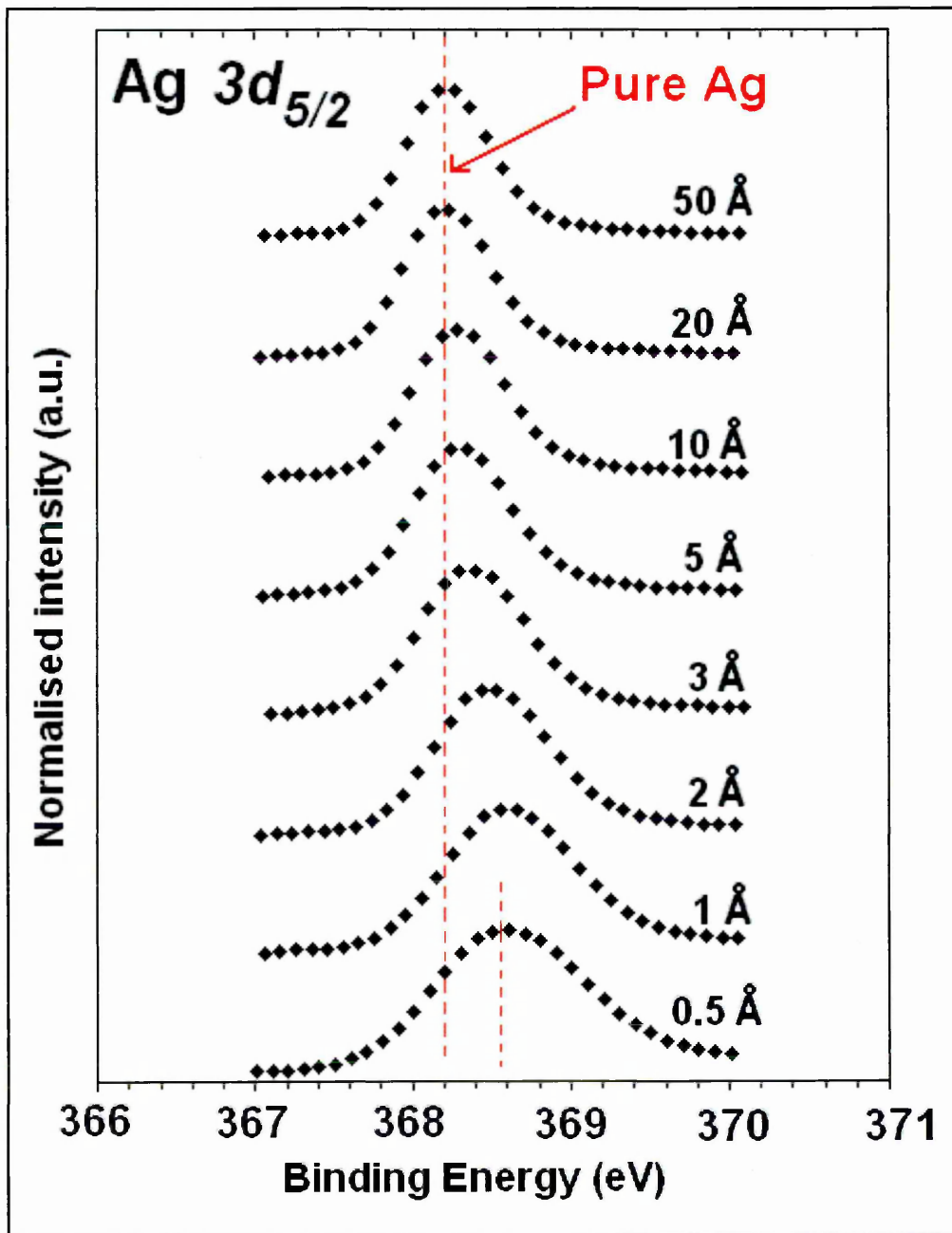


Figure 6-13: Evolution of the normalised Ag 3d_{5/2} lineshape at increasing Ag thickness on $\text{Al}_{0.3}\text{Ga}_{0.7}\text{N}$ surface at normal emission.

Analysis of the Ag 3d core-level shows the same characteristics as those observed on the other Al concentration surface ($x = 0.20$), as shown in figure 6-13. The peakshape is shifted from 368.5 eV at the first deposition to 368.2 eV at the last one. The FWHM is also found to decrease with increasing metal thickness which suggests that a chemical reaction is taking place at the metal interface.

Figure 6-14 summarizes the evolution of the Ga 3d core-level peak position at increasing Ag thickness on the different Al concentration materials at normal emission. Apart from the sudden increase for $\text{Al}_{0.3}\text{Ga}_{0.7}\text{N}$ at 0.5 Å, both substrates show a similar trend as the interface with Ag is formed which tends to suggest a comparable chemical interface formation.

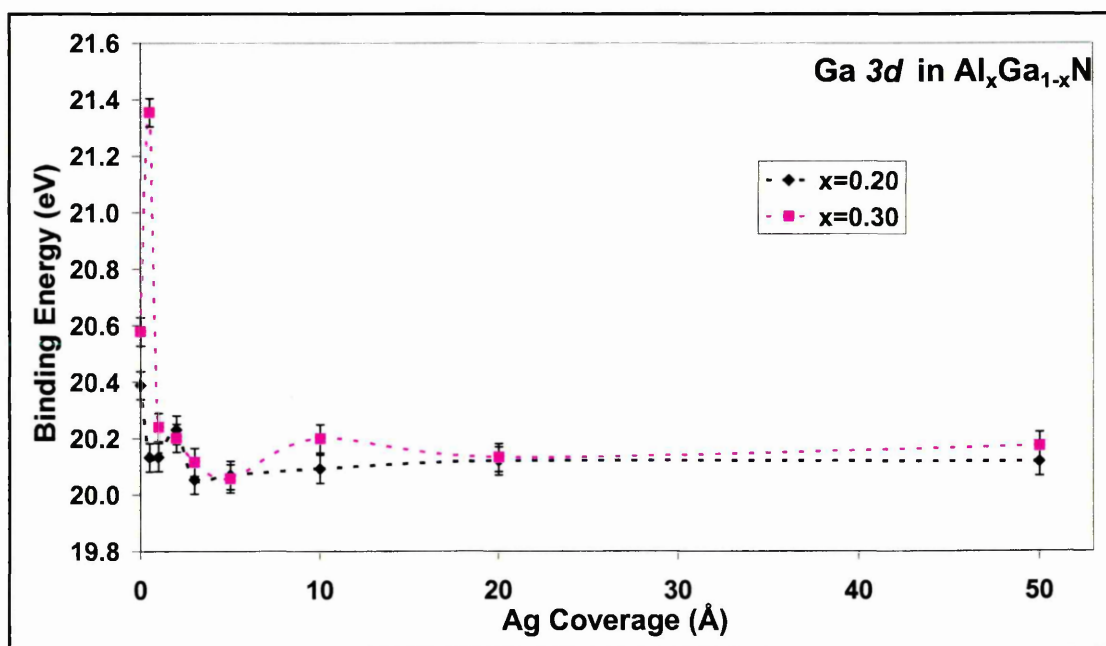


Figure 6-14: Evolution of the binding energy of the Ga 3d peak centre with Ag coverage at normal emission in $\text{Al}_x\text{Ga}_{1-x}\text{N}$ surfaces for $x = 0.20$ and $x = 0.30$. The dotted lines are intended to be a guide to the eye.

6.3.3. AFM results

XPS investigation on the growth mode showed signs of a different interface formation between the metal and the two Al concentration substrates, even though similar Fermi shifts were observed. In order to get a better understanding of the interface formation, a microscopic technique was used to assess the topography of the Ag covered surfaces.

After the last Ag deposition, the samples were taken out of the vacuum environment and analysed using tapping mode AFM. The overall metal thickness deposited on $\text{Al}_x\text{Ga}_{1-x}\text{N}$ surfaces was evaluated at about 250 Å.

Figure 6-15 shows AFM images taken of the two different metal covered surfaces. Islands of different sizes can be seen on the two pictures and present different shapes on the different Al concentrations.

On the 20% Al concentration material, Ag islands have a very well defined round shape and present a diameter of about 100 nm. Shapes and sizes do not show a significant variation over the surface which tends to suggest that island nucleation occurred at a similar thickness during the deposition.

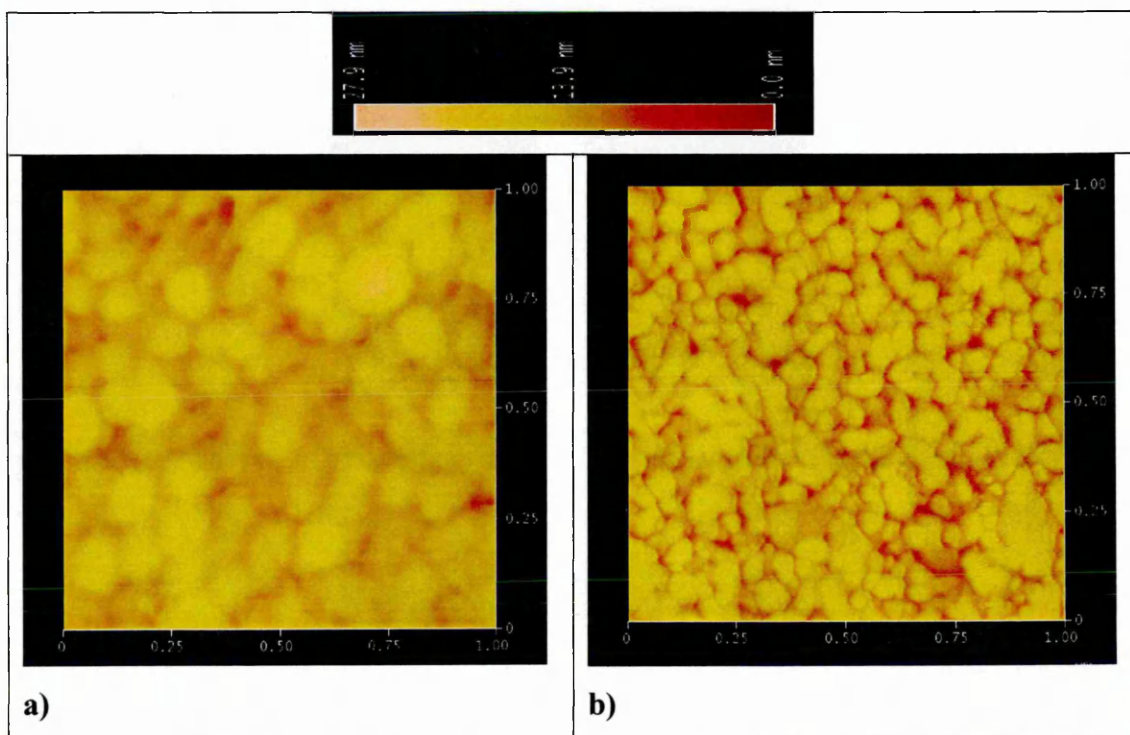


Figure 6-15: $1\mu\text{m}^2$ AFM images of the Ag covered $\text{Al}_x\text{Ga}_{1-x}\text{N}$ surfaces with a coverage of 250 Å for a) $x = 0.20$, and b) $x = 0.30$.

Figure 6-16 a) reinforces this statement. Additionally, measurement of the island dimensions shows a height in the order of tens of Angstroms. This is likely to be the results of layer-by-layer followed by islanding growth mode of Ag on $\text{Al}_x\text{Ga}_{1-x}\text{N}$ ($x = 0.20$), in good agreement with XPS results.

AFM images of the Ag covered $\text{Al}_x\text{Ga}_{1-x}\text{N}$ ($x = 0.30$) substrate show major differences in the interface formation. Clusters have random shapes as shown in figure 6-15 b) and present a nearly coalesced metal surface. Islands are smaller in dimensions and seem to be independent of each other and form various unpredictable shapes.

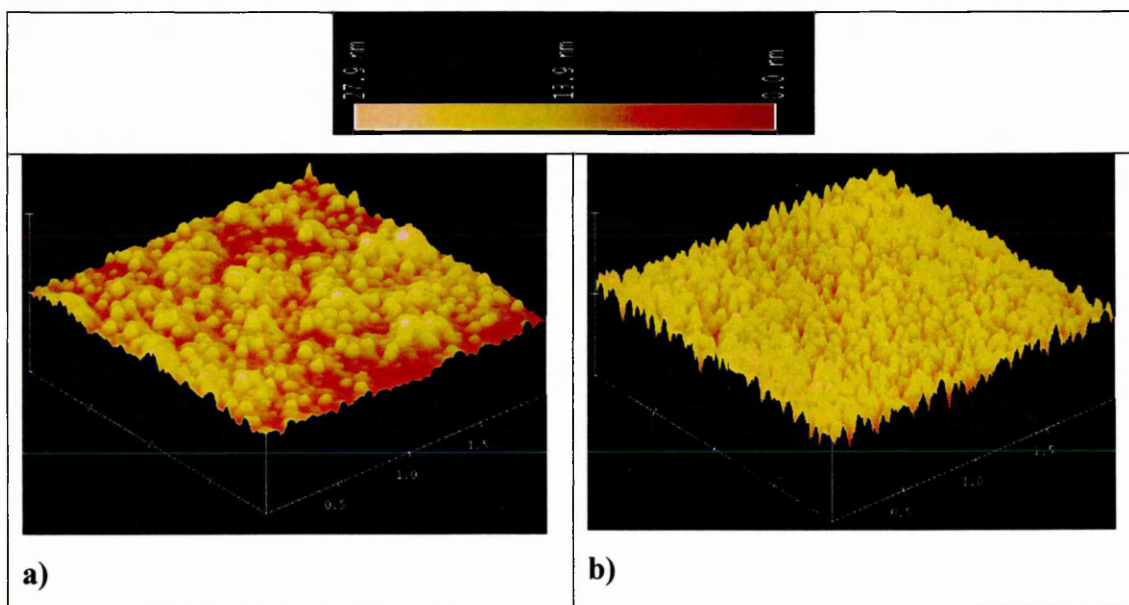


Figure 6-16: $2\mu\text{m} \times 2\mu\text{m}$ 3D AFM images of the Ag covered $\text{Al}_x\text{Ga}_{1-x}\text{N}$ surfaces with the Ag coverage of 250 \AA for a) $x = 0.20$, and b) $x = 0.30$.

From these observations, it is difficult to say that Ag growth mode was purely layer-by-layer followed by islanding on $\text{Al}_x\text{Ga}_{1-x}\text{N}$ ($x = 0.30$) surfaces. There is a distinct possibility that the growth mode was three dimensional which was pointed out by XPS results. Besides, increasing Al content in $\text{Al}_x\text{Ga}_{1-x}\text{N}$ might result in higher dislocation density (see chapter 2) which may, in turn, facilitate the formation of smaller Ag grains when Ag is deposited on the substrate.

6.3.4. Electrical characterisation

In order to get a better understanding of electron transport across the Schottky contacts, I-V measurements were performed on Ag/Al_{0.3}Ga_{0.7}N contacts as described in section 6.2.3.

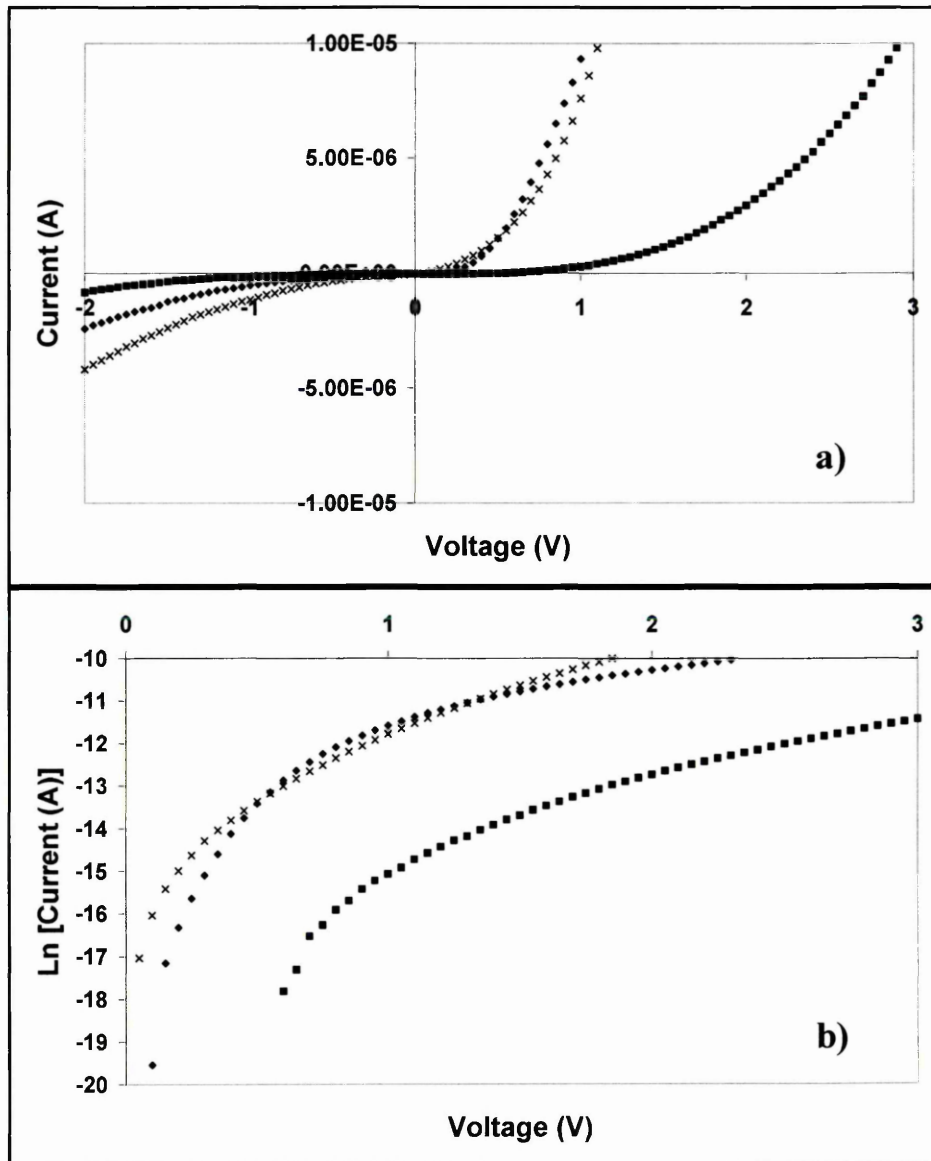


Figure 6-17: Current-voltage characteristics of three Ag/Al_{0.3}Ga_{0.7}N diodes measured in a) linear plot of reverse and forward voltage, and b) Ln I(A) versus forward voltage (V).

Unfortunately, it was only possible to measure the Al_xGa_{1-x}N (x = 0.30) sample. In addition, it is important to note that the sample was subjected to a different surface treatment as those investigated by XPS and showed in this chapter.

The $\text{Al}_{0.3}\text{Ga}_{0.7}\text{N}$ sample was first rinsed in solvents (acetone, ethanol, and methanol) and deionised H_2O . It was then taken in the preparation chamber where the sample was bombarded in a N^+ flux for 10 min at room temperature. The particles were accelerated by a 1 kV voltage and the drain current was kept at $2 \mu\text{A}$. The sample was finally annealed to 600°C for 30 min and 300 \AA thick Ag was deposited on the surface.

Current-voltage measurements of the diodes formed on this surface exhibit a rectifying behaviour as shown on figure 6-17. The diodes exhibited a non-ideal behaviour for Schottky contacts as the reverse voltage induced a significant reverse current even at low bias which indicated diode leakage. There is a distinct possibility that the leakage is due to the high dislocation density related to the Al content in the substrate. The dislocations will disrupt the lattice periodicity, hence creating surface states in the bandgap which may allow electrons to tunnel through the barrier.

The experimental I-V characteristics were analysed using the following equations as described in chapter 3:

$$I = I_0 \exp\left(\frac{qV}{nkT}\right) \quad [6-4]$$

$$I_0 = AA^*T^2 \exp\left(\frac{-q\phi_B}{kT}\right) \quad [6-5]$$

where n is the ideality factor, A is the contact area, A^* is the Richardson constant.

The Richardson constant can be expressed using the following relation:

$$A^* = \frac{4\pi q m^* k^2}{h^3} \quad [6-6]$$

where m^* is the effective electron mass for $\text{Al}_{0.3}\text{Ga}_{0.7}\text{N}$. As the sample is an alloy varying between GaN and AlN depending on Al concentration, it is common to consider a linear correlation of m^* between the two materials and a theoretical value of $32 \text{ Acm}^{-2}\text{K}^{-2}$ was used^{6, 25}.

Hence, fitting [6-4] to the linear region of $\text{Ln}(I)$ versus V yield ideality factor n and saturation current I_0 .

Figure 6-18 shows the current voltage behaviour at forward and reverse bias for the diode with the lowest ideality factor ($n = 1.21$ and $\Phi_B = 0.82$ eV). All data were measured in the dark at room temperature.

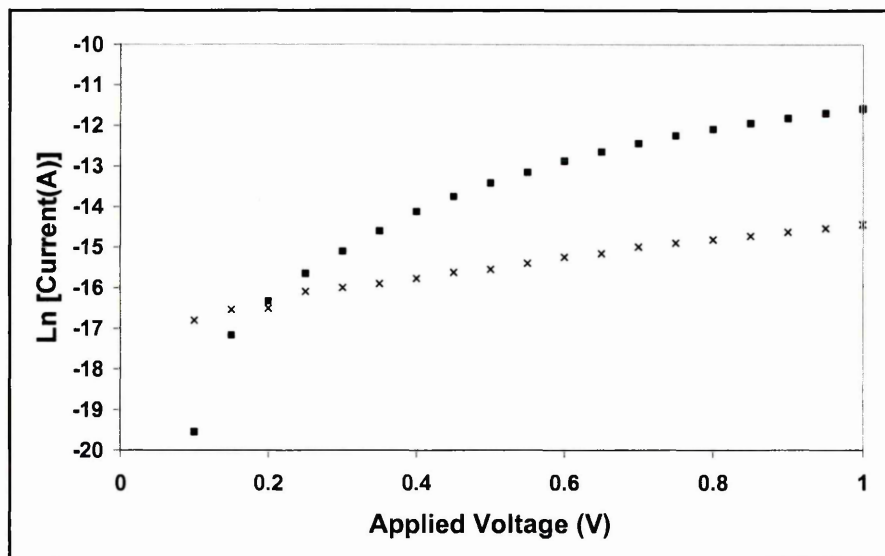


Figure 6-18: Ln(I) versus V plot showing I-V characteristics of the best diode (lowest ideality factor). Forward and reverse bias features are represented by squares and crosses, respectively.

For some diodes, the extraction of the Schottky parameters using the conventional method was not possible because of the high series resistance and the linear region at low bias was completely hidden. In addition, significant tunnelling and recombination current made the fitting procedure more difficult. 30 diodes have been measured and most of them showed a rectifying behaviour.

Experimental values for Schottky barrier height and ideality factor ($\Phi_B; n$) spread from the lowest barrier height (0.61 eV; 3.64) to the highest one (1.18 eV; 4.48) and lowest ideality factor (0.82 eV; 1.21) to highest one (1.18 eV; 4.48), with an average barrier height of 0.77 eV.

The large values measured for the ideality factor clearly shows that thermionic emission is not the only electron transport mechanism, even if the best diode presents a very low ideality factor compared to those reported for Ag/GaN contacts. The fact that values widely vary from diode to diode on the same sample is highly likely to be related

to the high and variable series resistance, in turn determined by the diode position relative to the ohmic contact as shown in figure 6-1.

Tracy *et al.*²⁶ investigated the formation of Schottky barriers between clean n-GaN and Ag using electrical and chemical characterizations. They measured a barrier height of 0.58 eV and an ideality factor of 1.20 via I-V characterization, in perfect agreement with XPS and UPS measurements.

Similarly, Kampen *et al.*⁴ found a barrier height of 0.7 eV with an ideality factor of 1.58 for a Ag/GaN contact using the same technique. Moreover, they calculated an extrapolated barrier height of 0.82 eV, assuming a linear correlation between the ideality factor and the Schottky barrier height and considering an ideality factor of 1.01.

6.4. Ni - Al_{0.2}Ga_{0.8}N contacts

The formation of the Ni/Al_{0.2}Ga_{0.8}N Schottky contacts has been investigated by XPS. Pre-metallization surface treatment was kept the same as Ag/Al_xGa_{1-x}N contact formation in order to facilitate the comparison between the different results. *In-situ* STM was used in parallel to view the topography of the Ni covered surface after the last deposition. Unfortunately, STM failed to get reasonable picture of the surface before metal deposition, probably because of the lack of conductivity of the sample.

In the same way, results are presented through two perspectives: the intensity of core-level signals which should give information on the growth mode, and the core-level binding energy positions which might assess changes in electronic properties with Ni coverage.

6.4.1. Core-level intensity

After subsequent Ni deposition, intensities from Al *2p*, Ga *3d*, Ga *2p*, N *1s* and Ni *2p_{3/2}* core-levels have been extracted from XPS spectra taken at normal emission only. Evolution of peak intensities with Ni coverage is shown in figure 6-19.

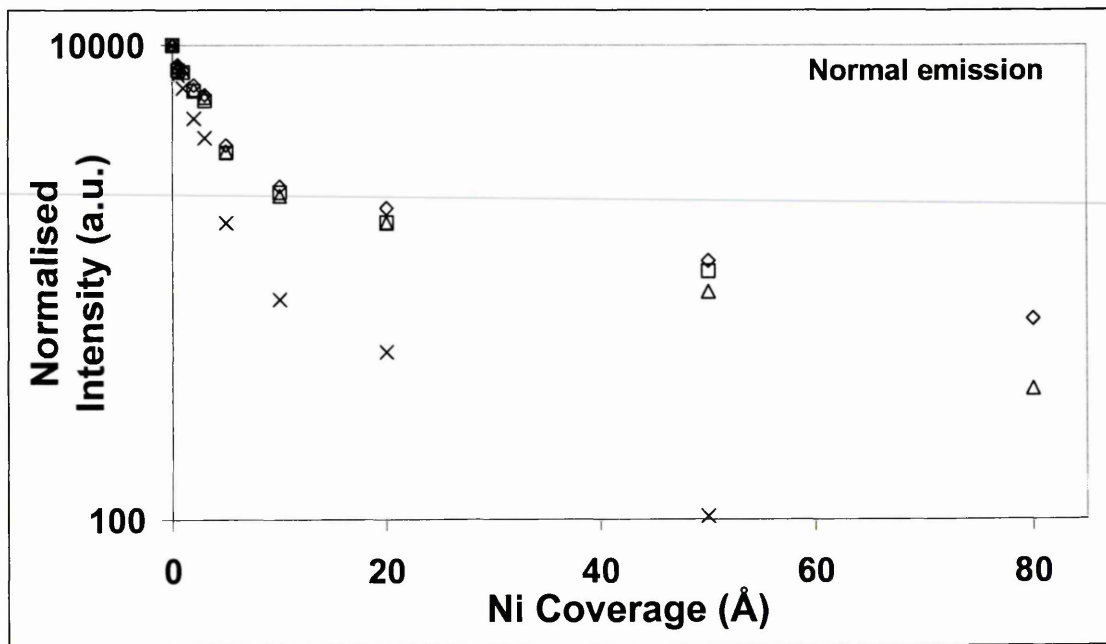


Figure 6-19: Semi-log plots of intensity versus Ni thickness on Al_{0.2}Ga_{0.8}N measured at normal emission. Al *2p*, Ga *3d*, Ga *2p*, and N *1s* are represented by squares, diamond shapes, crosses, and triangles, respectively.

The evolution of peak intensities clearly shows the two-slope evolution characteristic of the SK growth mode. Hence, according to XPS results, Ni grows in layer-by-layer and then forms islands on $\text{Al}_{0.2}\text{Ga}_{0.8}\text{N}$ substrates. From the first few metal depositions, it is therefore possible to extract the photoelectron escape depth as shown in figure 6-20.

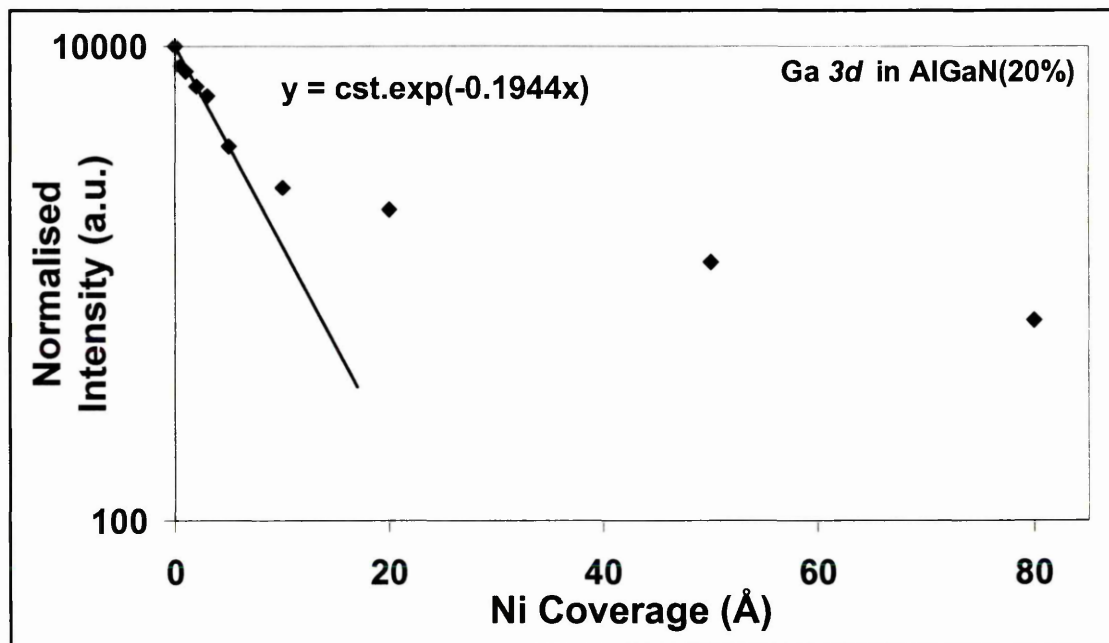


Figure 6-20: Escape depth extraction example on semi-log attenuation plot of Ga 3d core-level intensity versus Ni coverage in $\text{Al}_{0.2}\text{Ga}_{0.8}\text{N}$. Ga 3d intensities were taken at normal emission.

The same procedure was repeated for the different core-levels and the general trend was very similar to that of Ga 3d shown in the above figure. The extrapolation line reasonably fits the data points up to about 5 Å.

Table 6-4 presents the results on the determination of the escape depth extracted from the XPS data. Equations [6-1] and [6-2] were used to calculate the theoretical values for the mean free path used to compare with the ones extracted from the attenuation plots.

	Experimental		Theory		Theory/exp
	1/lambda	lambda	1/lambda	lambda	
Al 2p	0.208	4.8	0.055	18.2	3.8
Ga 3d	0.194	5.1	0.050	20.2	3.9
Ga 2p	0.345	2.9	0.148	6.8	2.3
N 1s	0.207	4.8	0.061	16.4	3.4
Ni 2p	0.452	2.2	0.116	8.6	3.9

Table 6-4: Comparison between the experimental and theoretical escape depth values at normal emission for Ni/ Al_{0.2}Ga_{0.8}N.

The ratio $\lambda_{\text{theory}}/\lambda_{\text{exp}}$ varies from 2.3 to 3.9 and is consistently higher than 3.5 which means that Ni thickness was overestimated by a factor of about 3.5. This might be due to the Ni effusion cell calibration process.

In addition, the relation $\lambda_{\text{Ga}2p} < \lambda_{\text{N}1s} < \lambda_{\text{Al}2p} < \lambda_{\text{Ga}3d}$ is respected but $\lambda_{\text{Ga}2p} > \lambda_{\text{N}1s}$ which might be related to the small values involved.

6.4.2. Core-level binding energy

Figures 6-21 to 6-23 show the evolution of the core-level binding energies Ga 3d, Al 2p and N 1s, respectively, with increasing Ni thickness on Al_{0.2}Ga_{0.8}N surfaces. The data labelled "600°C" correspond to the last surface treatment before the metal deposition and are considered as the "clean" surface.

From these figures, all substrate core-level binding energy positions change in the same way, in direction and magnitude. The first Ni depositions up to a total coverage of 5 Å induce a total shift of - 0.1 eV to lower binding energy. Then, additional metal coverage up to 50 Å causes a total shift of + 0.15 eV to higher binding energy. Finally, 80 Å Ni deposition induces a further shift of + 0.20 eV in the same direction for both Ga 3d and N 1s core-level positions.

The Al $2p$ core-level position followed the same evolution but no XPS signal was detected after the last metal deposition. This might be due to the relatively low Al cross-section.

It is highly likely that the shifts observed in the core-level material are rigid Fermi shifts. The fact that no significant change was observed in the material peakshape FWHM tends to rule out the possibility of changes in the semiconductor chemical environment.

Hence, total Fermi shifts $\Delta E_F = + 0.30$ eV are reported between the clean surface and the last Ni deposition, indicative of downward band bending. A similar result has been previously observed by Sporken *et al.*²² who noticed that Au induced a downward band bending of - 1.05 eV on GaN. Details on the Schottky barrier formation will be discussed later in the chapter.

Figure 6-24 shows the evolution of the Ni $2p_{3/2}$ peakshape with increasing Ni coverage at normal emission. Similarly to what was observed in Ag evolution, the peak gets narrower with increasing thickness which is indicative of increased purity material. The binding energy position also decreases and tends to that of metallic Ni at 853 eV²⁴ up to 50 Å but the last coverage shifts the position to that of the first deposition at 853.5 eV. This indicates a more reacted Ni interface even at high metal coverage, as opposed to the sharper Ag interface discussed earlier.

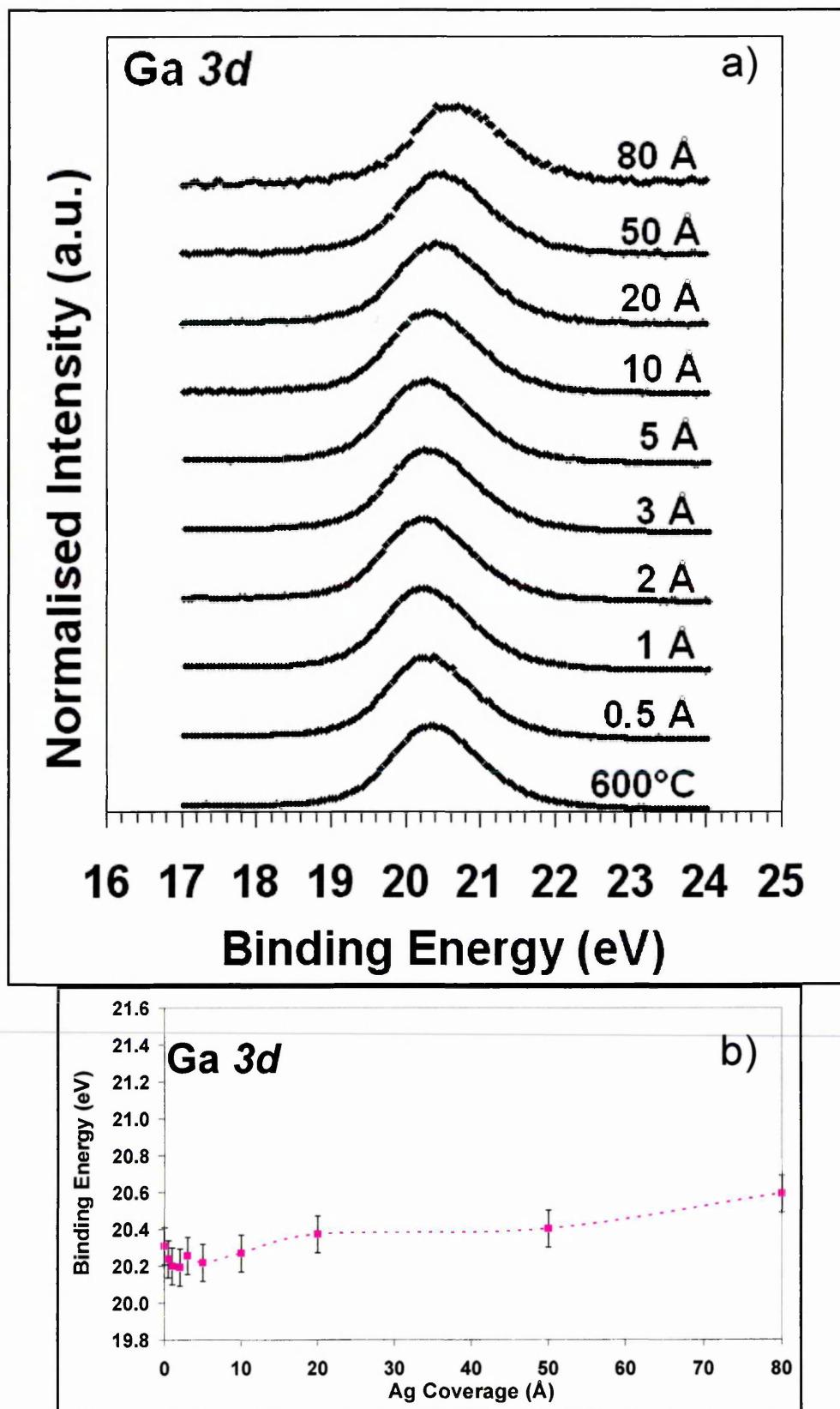


Figure 6-21: Evolution of (a) the normalised Ga 3d lineshape, (b) binding energy centre peak at increasing Ni thickness on Al_{0.2}Ga_{0.8}N surface at normal emission.

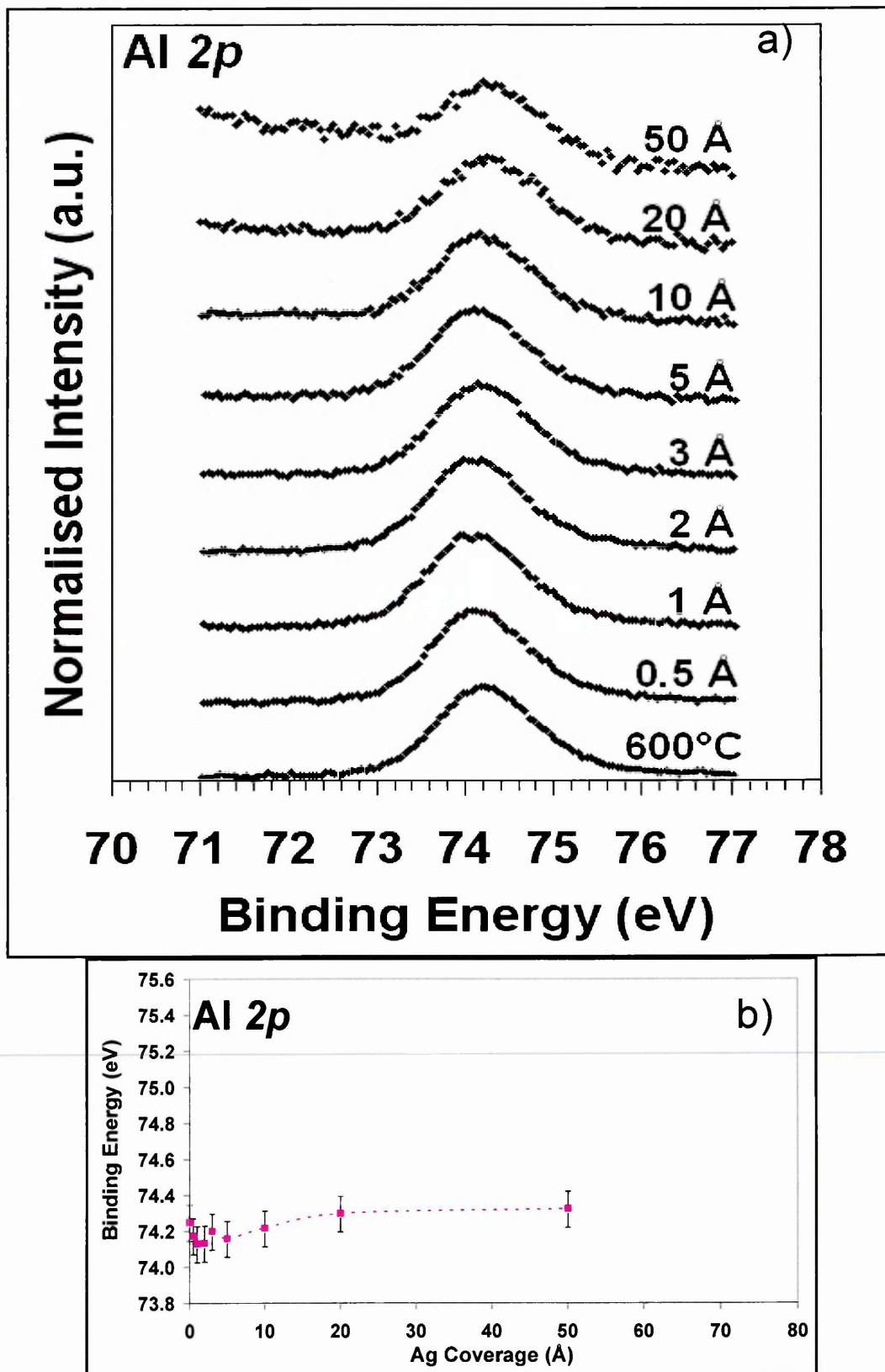


Figure 6-22: Evolution of (a) the normalised Al 2p lineshape, (b) binding energy centre peak at increasing Ni thickness on $Al_{0.2}Ga_{0.8}N$ surface at normal emission.

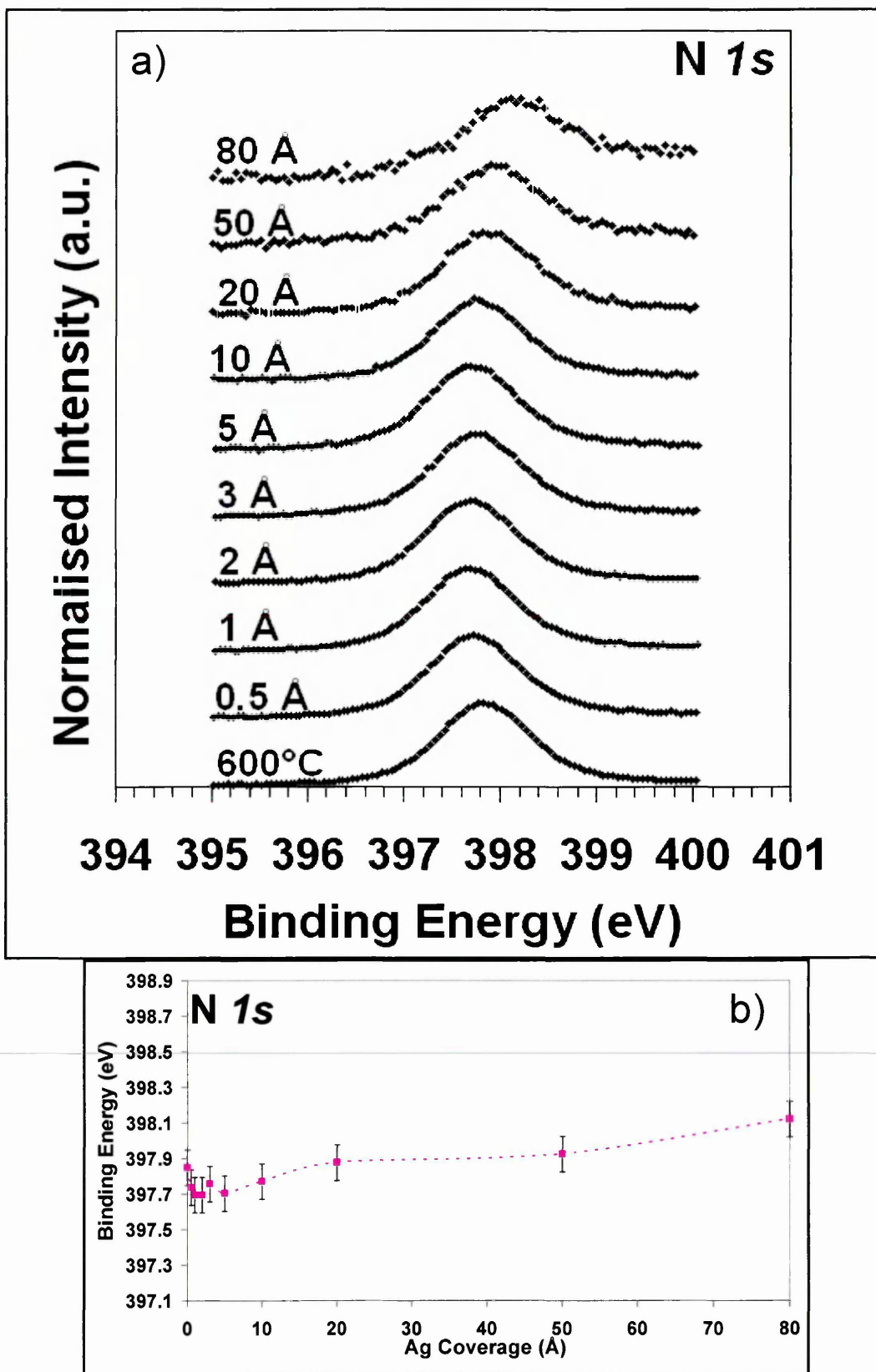


Figure 6-23: Evolution of (a) the normalised N 1s lineshape, (b) binding energy centre peak at increasing Ni thickness on $Al_{0.2}Ga_{0.8}N$ surface at normal emission.

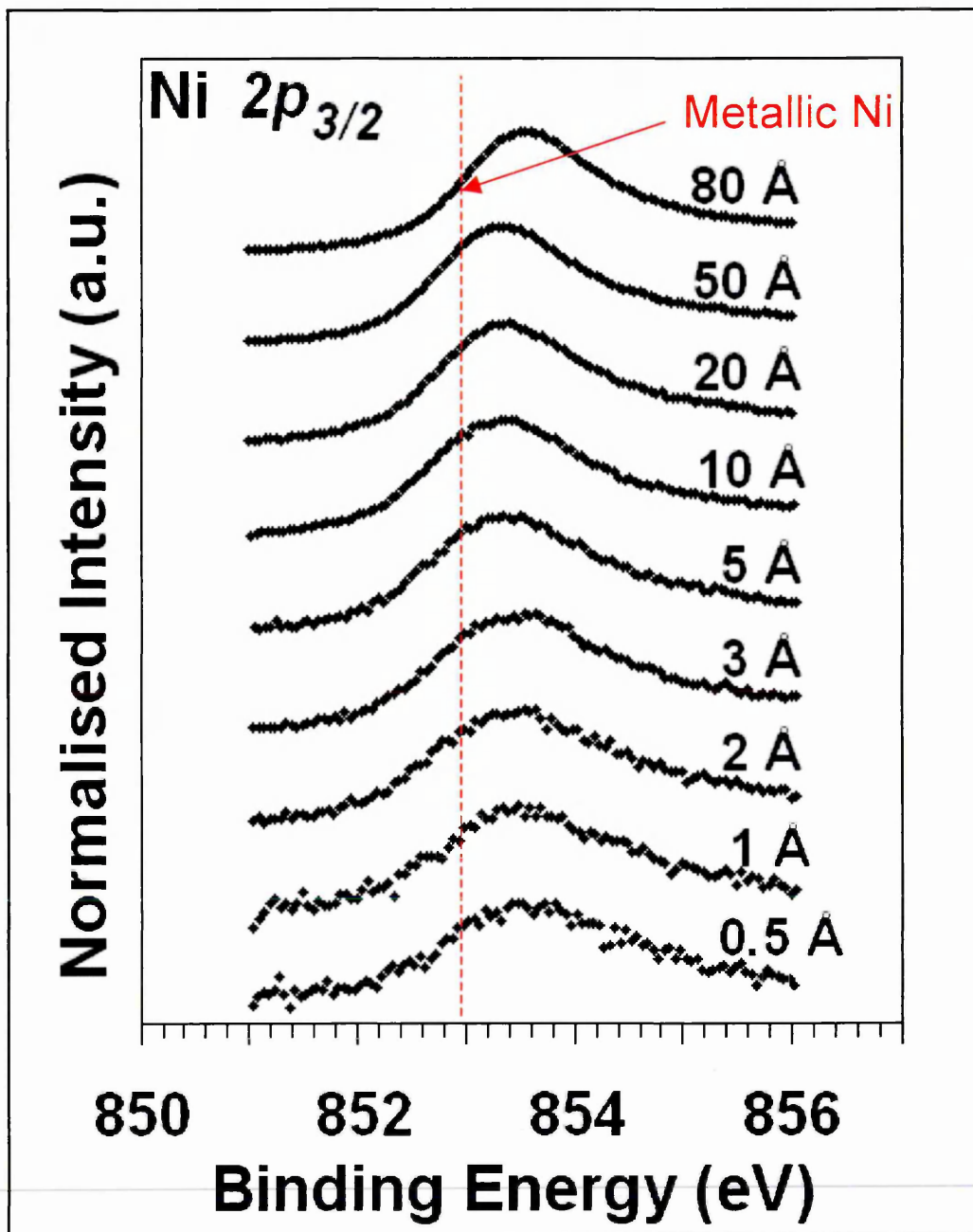


Figure 6-24: Evolution of the normalised Ni $2p_{3/2}$ lineshape at increasing Ni thickness on $\text{Al}_{0.2}\text{Ga}_{0.8}\text{N}$ surface at normal emission.

6.4.3. STM results

After the last Ni deposition, the sample was placed in a chamber where Scanning Tunneling Microscopy was carried out. It is important to note that STM was carried out *in-situ* following XPS studies. The pressure in the STM chamber was in the range 10^{-7} - 10^{-8} mbar. The metal covered surface being a lot more conductive than the uncovered one, STM was performed without problem at room temperature.

Figure 6-25 shows STM images of the Ni/ $Al_{0.2}Ga_{0.8}N$ surface in 2D and 3D views. The metal uniformly covers the substrate surface at a Ni thickness of 80 Å. Similarly to the Ag covered surface, Ni is clearly forming islands with well defined round shapes. Rickert *et al.*¹ investigated the formation of metal/GaN interfaces for different metals using X-ray photoemission and AFM. They carried out AFM analysis of Ni covered GaN surfaces with 10-nm-thick metal overlayers but did not observe island formation at the surface. On the other hand, they concluded that if islands were formed, they would be smaller than the resolution of the AFM measurement (about 10 nm). This is in perfect agreement with the results on Ni island measurements, as shown in figure 6-26.

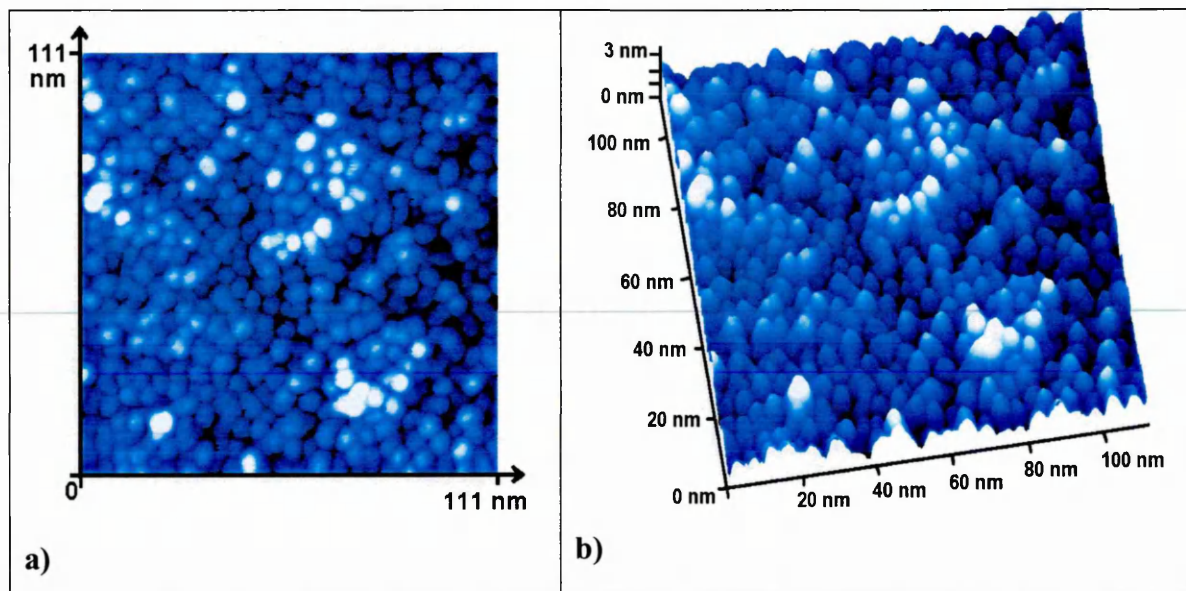


Figure 6-25: 111 nm × 111 nm × 2.49 nm STM images of the Ni covered $Al_{0.2}Ga_{0.8}N$ surface at Ni coverage of 80 Å in a) 2D view, and b) 3D view.

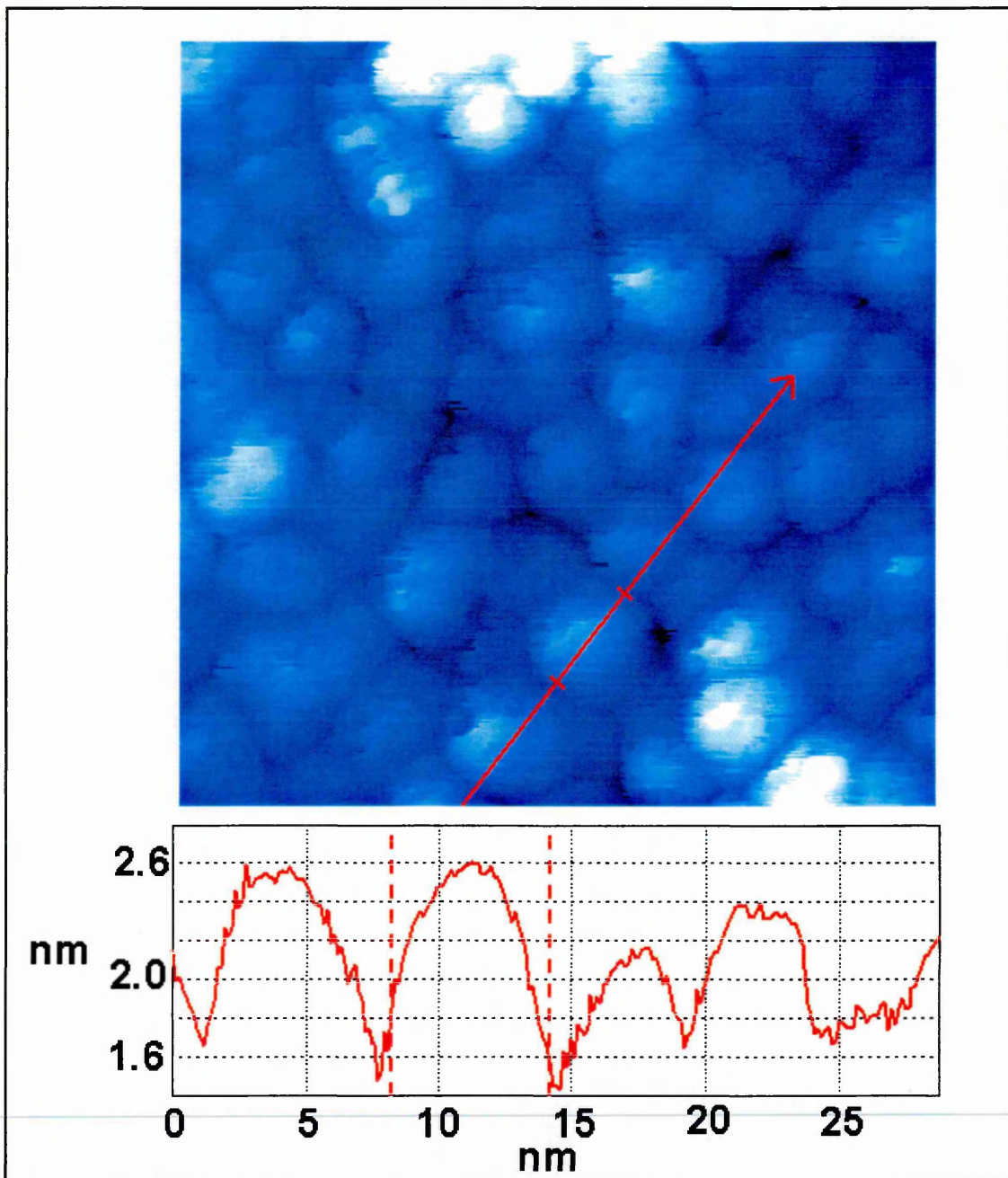


Figure 6-26: 29 nm × 29 nm STM line profile image of the Ni covered $\text{Al}_{0.2}\text{Ga}_{0.8}\text{N}$ surface at Ni coverage of 80 Å.

Figure 6-26 shows the investigation on the Ni island size measurement on the $\text{Al}_{0.2}\text{Ga}_{0.8}\text{N}$ surface. The surface presents randomly disposed round features of similar shape in diameter and height. The average island is found to be less than 10 nm in diameter and about 3 nm in height. This is about 10 times smaller than the Ag islands formed on the same surface. These results seem to be in agreement with the XPS data as the Ni growth mode on the $\text{Al}_{0.2}\text{Ga}_{0.8}\text{N}$ surface is clearly 3-dimensional at the Ni covered topsurface.

6.5. Discussion

XPS has been extensively used to investigate the chemical and electronic formation of $\text{Ag}/\text{Al}_x\text{Ga}_{1-x}\text{N}$ with two different Al concentrations ($x = 0.20$ and $x = 0.30$) and $\text{Ni}/\text{Al}_x\text{Ga}_{1-x}\text{N}$ with $x = 0.20$. Microscopic techniques such as AFM and *in-situ* STM have also been carried out to assess the topography of the metal covered surfaces. It is important to note that the samples used in this study have been carefully grown in order to obtain the best crystalline quality and have shown to achieve some of the lowest values ever reported in literature in dislocation density¹⁶.

An HF etch followed by 600°C *in-situ* annealing surface treatment has proven to be effective in removing contaminants from the surface even if full removal was not achieved, as developed in the previous chapter. Hence, the cleaning technique was the same for all samples studied with XPS in order to facilitate comparison between results. In parallel, (I-V) measurements were carried out on $\text{Ag}/\text{Al}_{0.3}\text{Ga}_{0.7}\text{N}$ diodes with the substrates subjected to N^+ bombardment and UHV annealing prior to metallization.

Results will be discussed from two view points: the interface formation in which chemical changes at the surface will be analysed, and the Schottky barrier formation in which electronic changes at the metal-semiconductor interface will be examined.

6.5.1. $\text{Ag}/\text{Al}_x\text{Ga}_{1-x}\text{N}$ interface formation

XPS has been used to identify the metal growth mode on $\text{Al}_x\text{Ga}_{1-x}\text{N}$ surfaces. Ag was deposited on the surface from sub-monolayer coverage up to a total thickness of 50 Å. The attenuation of the XPS core-level intensities gave information on how the metal grew on the surface.

It has been shown that Ag deposition on $\text{Al}_{0.2}\text{Ga}_{0.8}\text{N}$ substrates exhibits a Stransky-Krastanov (SK) growth mode which was demonstrated by the rapid intensity drop in the first few monolayers followed by a less steep intensity decrease. Considering this growth mode, experimental photoelectron mean free paths were calculated and compared to theoretical values arising from the universal curve, as explained in chapter 2. The parameter extraction was done by fitting the linear region of the graph intensity versus Ag coverage at low metal thickness.

The formation of islands has been confirmed by AFM pictures of Ag covered surface with metal thickness of about 250 Å. Large, well-defined round shaped islands

with a diameter of about 100 nm were clearly visible at the top surface. These observations tend to suggest a sharp and unreacted Ag/Al_{0.2}Ga_{0.8}N interface.

Similar to Al_{0.2}Ga_{0.8}N, the Al_{0.3}Ga_{0.7}N substrate also shows a SK growth mode of Ag. This is further emphasized by AFM images which show that the Ag layer is composed of partly coalescing metal islands of nonuniform shape.

As the two substrates were subjected to the same pre-metallization surface treatment (HF etch followed by 600°C UHV *in-situ* annealing), the differences might be explained by the substrate material itself. It has been shown that increasing the Al concentration in the Al_xGa_{1-x}N alloy induces an increased crack density at the surface^{16,17}. Rajasingam *et al.*²⁷ investigated the effects of high temperature on stress, structural and compositional changes. Using AFM, they observed that annealing enhanced the increase in the width of primary cracks and the formation of secondary cracks. Hence, it is highly likely that Ag interface formation on a more "damaged" Al_xGa_{1-x}N surface will alter the growth mode.

Ag growth has been investigated on various materials at different flux rates and different temperatures. The use of different deposition rates at room temperature (RT), where the low rate was 0.39 ML/min and higher rate was 3.7 ML/min, did not show a drastic influence on Ag growth mode and island shapes on Si(111):H surfaces²⁸ and resulted in VW (three-dimensional) growth. The temperature dependence of Ag on Si(111):H has been investigated using Auger electron spectroscopy (AES) and microscopic techniques such as AFM and scanning electron microscopy (SEM)²⁹. They found that low temperature (LT ≈ 210 K) deposition followed by annealing to RT leads to SK growth mode with large Ag islands, whereas RT deposition results in SK mode of smaller and irregularly shaped islands. The metal flux rate was kept at ≈ 3 ML/min. These results show a variance in the growth mode determination at RT.

Conversely, the Ag flux rate was found to be a key parameter in the growth of Ag on GaN³⁰, as a low flux rate (≈ 0.8 ML/min) induced a SK growth, whereas a high flux rate (≈ 60 ML/min) caused a layer-by-layer growth, where both types of deposition were performed at RT.

Results shown on Al_xGa_{1-x}N surfaces with $x = 0.20$ and $x = 0.30$ were taken from RT deposition at a constant flux rate of about 5 ML/min. Comparison with results from other groups shown above should be done with caution as Al_xGa_{1-x}N surfaces show drastic differences in cleanliness compared with Si(111):H surfaces, and an increased surface complexity compared to GaN. Our results seem to be agreement with

data from Ag/GaN as our flux rate would fall in the "low" flux rate category. A similar surface such as $\text{Al}_x\text{Ga}_{1-x}\text{N}$ ($x = 0.20$) would result in SK growth mode, whereas the increased Al concentration surface ($x = 0.30$) might cause a layer-by-layer or islanding growth mode. Additional work is still needed to understand the precise mechanisms of Ag growth formation on $\text{Al}_x\text{Ga}_{1-x}\text{N}$ surfaces, i.e. the measurement of surface roughness before metallization, the influence of metal flux rate and/or temperature deposition.

The chemical formation of Ag/ $\text{Al}_x\text{Ga}_{1-x}\text{N}$ interfaces can also be discussed through the binding energy variation of the Ag $3d_{5/2}$ XPS core-level as shown in figure 6-27.

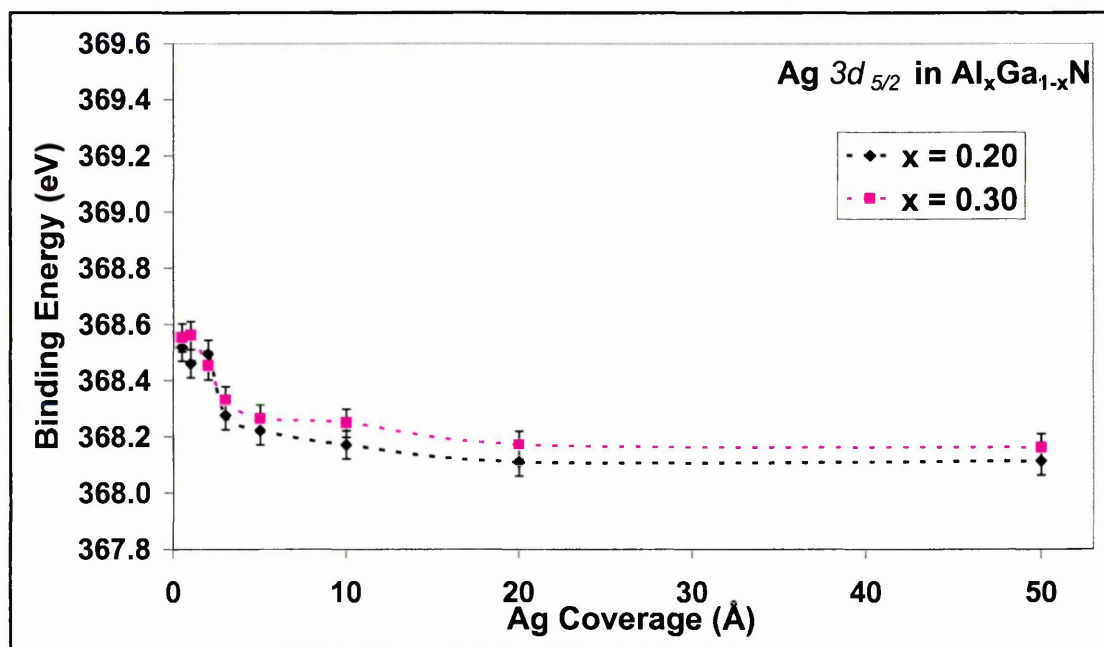


Figure 6-27: Evolution of the Ag $3d_{5/2}$ core-level binding energy centre peak at increasing Ag thickness on $\text{Al}_{0.2}\text{Ga}_{0.8}\text{N}$ and $\text{Al}_{0.3}\text{Ga}_{0.7}\text{N}$ surfaces. Data were taken at normal emission. Lines are guides to the eye.

The Ag $3d_{5/2}$ core-level binding energy decreases with increasing Ag thickness for the two Al concentration materials. The FWHM peakshape is also found to decrease with increasing Ag coverage. This behaviour is interpreted as a change in the chemical environment of Ag, from a Ag mixture near the interface to pure Ag at high metal coverage. It is important to note that no significant change in the FWHM core-level material peakshape is noticed which tends to rule out the possibility of chemical reactions between Ag and substrate.

It was highlighted in the previous chapter that O and C were still detectable at the surface after the pre-metallization treatment. Hence, it is suggested that Ag mixture is mainly composed of oxides and/or carboxides near the interface. Alternatively, with Al being very reactive, its reaction with Ag would be enhanced to form AlAg_2 compound which binding energy was about 368.5 eV ¹⁹ but no chemical shift in Al 2p core-level was witnessed to reinforce this possibility.

On the other hand, the Ag $3d_{5/2}$ core-level binding energy remains unchanged with Ag coverage above 20 \AA which tends to show that the reacted mixture is rapidly buried and the interface is sharp.

6.5.2. Ni/ $\text{Al}_x\text{Ga}_{1-x}\text{N}$ interface formation

XPS was used to determine the Ni growth mode on $\text{Al}_x\text{Ga}_{1-x}\text{N}$ ($x = 0.20$) in the same way as for Ag/ $\text{Al}_x\text{Ga}_{1-x}\text{N}$ contact formation and the evolution of peak intensities clearly shows the two-slope evolution characteristic of the SK growth mode. Hence, XPS results show that Ni grows in layer-by-layer and then forms islands on $\text{Al}_{0.2}\text{Ga}_{0.8}\text{N}$ substrates. This is confirmed by *in-situ* STM taken after the last Ni deposition. *In-situ* STM clearly shows the presence of small, well-defined round shaped islands at a Ni coverage of about 80 \AA . Islands have similar dimension throughout the surface and present a diameter of about 10 nm and about 3 nm in height. This is good agreement with Rickert *et al.*¹ who investigated the formation of Ni on GaN surfaces. They did not see islands on their metal covered surfaces using AFM, but mentioned that if islands were formed, they would be smaller than AFM resolution (about 10 nm).

Assuming this growth mode, experimental photoelectron escape depths were extracted for all core-levels at normal emission. Good agreement is found between experimental data and theory, although it is highly likely that the Ni thickness was underestimated by a factor of about 3.5. This might be linked to the Ni calibration procedure.

In parallel, the Ni $2p_{3/2}$ binding energy position decreases and tends to that of metallic Ni at 853 eV up to 50 \AA but the last coverage shifts the position to that of the first deposition at 853.5 eV . The exact origin of this behaviour remains an open question. Nevertheless, this indicates a more reacted Ni interface even at high metal coverage, as opposed to the sharper Ag interface discussed earlier.

Our results seem to be at variance with those reported by Bermudez *et al.*¹³ who examined the growth of thin Ni films on GaN using various spectroscopic techniques.

They concluded that Ni deposition near RT resulted in layer-by-layer growth mode where the Ni film was disordered. Additionally, they reported that chemical reaction at the interface between GaN and Ni occurred even at RT. The fundamental divergence with our results may be explained by the fact that they used a Ga reflux surface treatment before metallization which is believed to produce rougher, more reactive GaN surfaces²³.

Dumont *et al.*³¹ investigated the formation of metal-GaN and metal- $\text{Al}_x\text{Ga}_{1-x}\text{N}$ contacts using XPS depth profiles and electrical measurements. They found that Au, Pd and Pt contacts on GaN formed sharp unreacted interfaces, while Au and Ni contacts on $\text{Al}_x\text{Ga}_{1-x}\text{N}$ (x taken from 0 to 0.35) were very similar and presented a much broader interface compared to Au/GaN. However, apart from the more diffuse interface, they found no evidence of interfacial reaction or compound formation.

This result seems to be in accordance with our findings as no significant change in the core-level peakshape FWHM was observed which tends to rule out interfacial compound formation with Ni. Similarly to Ag contact formation, there is a distinct possibility that Ni reacts with the oxides and/or carboxides left at the surface prior the metallization surface treatment.

6.5.3. Metal- $\text{Al}_x\text{Ga}_{1-x}\text{N}$ Schottky barrier formation

Changes in the electronic properties at the surface after metal deposition have been investigated on Ag/ $\text{Al}_x\text{Ga}_{1-x}\text{N}$ ($x = 0.20$ and $x = 0.30$) and Ni/ $\text{Al}_x\text{Ga}_{1-x}\text{N}$ ($x = 0.20$) by XPS. Results show that binding energy shifts occur for all substrate core-levels and therefore are interpreted as rigid Fermi shifts at the surface. The absence of core-level peakshape broadening reinforces this statement. Ag deposition caused a total upward band bending of 0.30 eV and 0.40 eV on $\text{Al}_{0.2}\text{Ga}_{0.8}\text{N}$ and $\text{Al}_{0.3}\text{Ga}_{0.7}\text{N}$ surfaces, respectively. Ni deposition induced a downward band bending of 0.3 eV from the "clean" $\text{Al}_{0.2}\text{Ga}_{0.8}\text{N}$ surface to the last metal deposition. The pre-metallization surface treatment was the same for all experiments (solvents, HF etch followed by 600°C UHV anneal) and resulted in a downward band bending, measured between the "as-received" and annealed surface, of 0.87 eV and 0.99 eV for $\text{Al}_x\text{Ga}_{1-x}\text{N}$ ($x = 0.20$) and $\text{Al}_x\text{Ga}_{1-x}\text{N}$ ($x = 0.30$), respectively.

It should be noted that the results interpreted as Fermi shifts were obtained using the charging reference technique as explained in section 4.4.3.8. and might induce potential errors.

I-V measurements were also carried out on Ag/Al_{0.3}Ga_{0.7}N and led to a Schottky barrier height $\Phi_B = 0.82$ eV corresponding to the lowest ideality factor $n = 1.21$. The results also show a wide spread of values for ideality factors which was mainly attributed to the high and variable series resistances of the contacts. This has previously been observed for Ag/GaN and Pd/GaN and was attributed to the nonuniformity of real Schottky contacts along the interface⁴. This was further supported through a study of Au/Al_xGa_{1-x}N Schottky barrier formation, where the differences between I-V and C-V measurements was mainly attributed to spatial fluctuations in potential²⁵. In parallel, they reported that ideality factors were found to increase with increasing Al concentration in the alloy, whereas the data dispersion was attributed to alloy disorder and microscopic defects such as cracks¹². It is therefore likely that high ideality factors were caused by the increased material dislocation density which caused a random distribution of surface point defects, acting as tunnelling and recombination centres. Finally, it has been shown that changes in the Schottky barrier heights were mainly due to the local changes in the Al concentration^{8, 11}.

The Schottky-Mott model describes a simple prediction of the Schottky barrier height by taking into account the metal work function and the semiconductor electron affinity χ which is the energy needed to remove an electron from the bottom of the conduction band. In our case, the use of different Al concentrations induces a change of the material electron affinity. Grabowski *et al.*³² investigated the electronic properties and electron affinities of Al_xGa_{1-x}N over the whole composition range and found a linear decrease in electron affinity with increasing x . This was further emphasized²⁵ by a study on Au/Al_xGa_{1-x}N that resulted in a slope of ≈ 1 .

Hence, the electron affinity of Al_xGa_{1-x}N at a specified Al concentration can be estimated knowing electron affinities of GaN and AlN⁶. If we use the electron affinity reported³³ for GaN at 4.2 eV and AlN at 2.05 eV, χ_S for Al_{0.2}Ga_{0.8}N and Al_{0.3}Ga_{0.7}N should be about 3.8 eV and 3.6 eV, respectively.

For this reason, the evolution of band bending at the different Al concentration surfaces after Ag deposition may be explained in the Schottky-Mott model as we found an increasing band bending with decreasing electron affinity. Tracy *et al.*²⁶ calculated the Schottky barrier height from the XPS Fermi shift when the interface metal-GaN is formed by using the following equation:

$$\phi_B = E_g - E_{VBM}^i + (E_{core}^i - E_{core}^m) \quad [6-7]$$

where E_g is the band gap, E_{VBM}^i is the binding energy of the valence band maximum, E_{core}^i is the initial binding energy of the core-level peak, E_{core}^m is the binding energy of the material core-level peak following metal deposition.

The energy band gap for Al_xGa_{1-x}N can be expressed by using the following relation³⁴:

$$E_g^{AlGaN} = (1-x)E_g^{GaN} + xE_g^{AlN} + bx(1-x) \quad [6-8]$$

where $E_g^{GaN} = 3.39$ eV, $E_g^{AlN} = 6.20$ eV, and b is the bowing parameter with a value of 0.96.

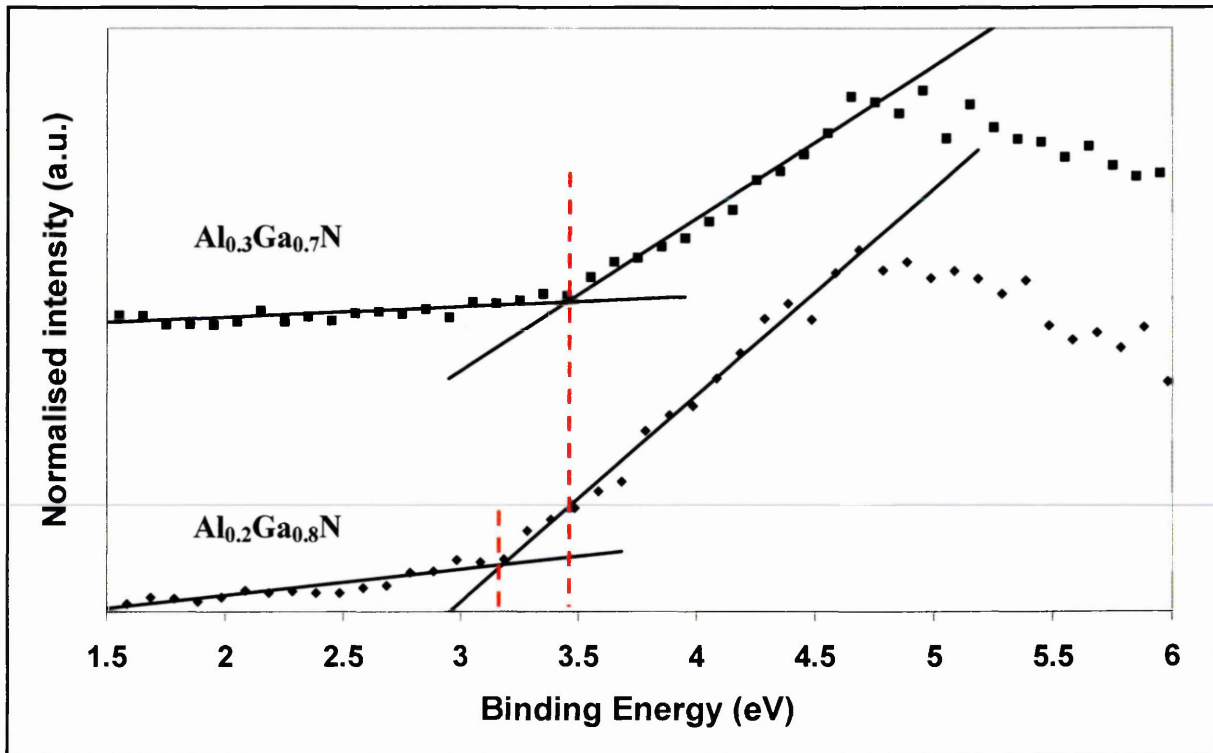


Figure 6-28: XPS binding energy of the valence band maximum for clean Al_{0.2}Ga_{0.8}N (diamond shapes) and Al_{0.3}Ga_{0.7}N (squares) surfaces. Binding energies have been measured relative to the Fermi level.

Figure 6-28 shows the determination of the valence band maximum using XPS. From this figure, E_{VBM} has been extracted and found to be 3.18 eV and 3.45 eV for clean Al_{0.2}Ga_{0.8}N and Al_{0.3}Ga_{0.7}N surfaces respectively. These results are in good agreement with reported values as E_{VBM} increase with increasing Al mole fraction and band gap.

Hence, replacing parameters in equations [6-7] and [6-8] yields values for Schottky barrier height of $\phi_b = 0.92$ eV and $\phi_b = 0.98$ eV for Al_{0.2}Ga_{0.8}N and Al_{0.3}Ga_{0.7}N substrates, respectively.

The barrier height is found to increase with decreasing electron affinity of the alloy as shown in figure 6-29. In addition, our XPS results are in perfect agreement with results reported by Kampen *et al.*⁴, Koyama *et al.*³⁵, and Maffei *et al.*³⁶ on Ag/GaN barrier heights, and therefore it would suggest a linear evolution of the barrier height as a function of electron affinity, according to the Schottky model. This result is however at variance with other barrier heights reported for Ag/GaN contacts (ref. [26] and [3]).

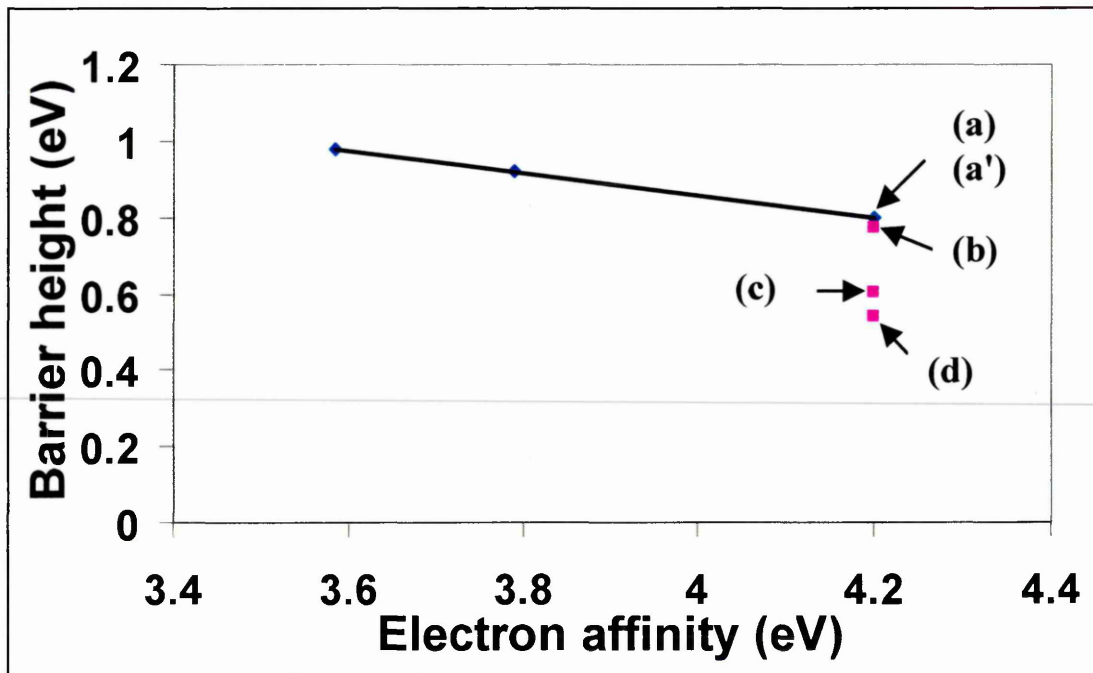


Figure 6-29: Evolution of the Schottky barrier height with semiconductor electron affinity for Ag/Al_xGa_{1-x}N contacts. Data points labelled (a), (a'), (b), (c), and (d) were taken from references 4, 35, 36, 26, and 3 respectively.

The Schottky barrier height of Ag/Al_{0.3}Ga_{0.7}N measured by I-V ($\phi_B = 0.82$ eV) is also lower than the one extrapolated from XPS Fermi shifts ($\phi_B = 0.98$ eV).

It is important to note that the electrically measured sample was subjected to N⁺ bombardment followed by 600°C UHV annealing, and the one investigated with XPS was cleaned in a HF solution followed by 600°C annealing. Hence, it is possible that the different pre-metallization surface treatment is responsible for the discrepancy in the barrier height. It is also highly likely that the mechanisms of Schottky barrier formation of Ag/Al_xGa_{1-x}N contacts fail to be predicted only by the Schottky model.

A summary of the results on Schottky barrier heights measured and extrapolated by XPS and I-V are shown in table 6-4. For Schottky-Mott model barrier heights, the values of 4.2 eV and 2.05 eV were used for GaN and AlN electron affinity, respectively, as discussed earlier in the text.

Al content	(XPS) ΔE_F (eV)	(XPS) ϕ_B (eV) (extrapolated from [7-7] and [7-8])	(I-V) ϕ_B (eV)	Schottky-Mott model ϕ_B (eV)
x = 0.20	-0.3	0.92		0.47
x = 0.30	-0.4	0.98	0.82	0.67

Table 6-4: Summary of results on Ag/Al_xGa_{1-x}N Schottky barrier height measurements using XPS and I-V. Schottky-Mott model predictions are also shown.

It can also be noted from this table that barrier heights obtained with I-V measurement are lower than those extrapolated from XPS Fermi shifts. This is highly likely to be related to the different pre-metallization surface treatment. N⁺ bombardment followed by annealing was found to produce N vacancies^{37, 38} and such surfaces exhibited surface states leading to 0.75 eV upward band bending³⁹. The high density of states would then result in tunnelling and recombination current, hence lowering the barrier height.

Besides, the discrepancy between barrier heights measured using I-V and XPS may be a result of the measurement process itself. In the case where the interface presents local variations of the barrier height, I-V measurement will favour the lowest

barrier because of electron flow mechanisms across the barrier, whereas the XPS technique will present an average over a large area and is therefore less sensitive to defects.

Unfortunately, the barrier height of Ni/Al_{0.2}Ga_{0.8}N contacts could not be measured using I-V and the Fermi shifts recorded using XPS after Ni deposition lead to an extrapolation of Schottky barrier height of 0.31 eV, using equation [6-7]. Therefore, Ni/Al_{0.2}Ga_{0.8}N barrier formation could not be explained by the Schottky model, based on XPS extrapolated results only.

The Cowley-Sze model⁴⁰ presents a more realistic prediction of the Schottky barrier height by separating the barrier height formation in two distinct steps: the state of the surface before metal contact, and the changes caused by the metallization, as discussed in chapter 3. Bermudez *et al.*⁴¹ investigated the formation of metal/GaN barrier heights and interpreted the results according to this model. The barrier height can be expressed as a sum of the "bare-surface barrier height" Φ_0 which is a measure of the band bending before metal contact, and a Schottky-Mott term as discussed earlier in the text. In this model, it is assumed a uniform distribution of surface states D_{SS} in the band gap, which would be $\approx 10^{13}$ (1-S)/S. For an ideal Schottky-Mott contact, S would be unity, whereas deviation from unity would give an indication of the density of gap states on the initial surface.

Tracy *et al.*²⁶ reported a bare-surface barrier height of 0.4 eV before metallization, whereas Ag deposition caused an additional upward band of 0.2 eV. Similarly, according to I-V measurements on Ag/Al_{0.3}Ga_{0.7}N, the bare-surface barrier height at the Al_{0.3}Ga_{0.7}N treated surface would be 0.42 eV and the Schottky-Mott contribution of 0.40 eV. This would mean that about half of the final barrier height is caused by initial band bending at the surface.

Considering the XPS measured barrier heights of Ag/AlGa_xN, the bare-surface barrier height at Al_xGa_{1-x}N for x = 0.20 and x = 0.30 would be 0.62 eV and 0.58 eV respectively, whereas the Schottky-Mott contribution would be 0.30 eV and 0.40 eV, respectively. This suggests that the Fermi level pinning is approximately identical for the two different surfaces subjected to the same pre-metallization surface treatment, in agreement with the model predictions where the bare-surface barrier height is strongly dependent on surface treatment.

It is also possible to calculate the bare-surface barrier height or band bending at the "clean" Al_xGa_{1-x}N surface using the measurement of the valence band maximum

shown in figure 7-28. The Fermi level position in the bulk, relative to the conduction band minimum, may be calculated using equation [3-3] where the density of states in the conduction band N_C is given by²⁵:

$$N_C = 2(2\pi m^* kT/h^2)^{3/2} \quad [6-9]$$

where m^* is the effective electron mass for $\text{Al}_x\text{Ga}_{1-x}\text{N}$. This value was estimated by linear extrapolation from $m^* = 0.35 m_0$ for AlN^7 and $m^* = 0.20 m_0$ for GaN^{25} . Using equations [3-3] and [6-9], considering a density of donors in the n-type $\text{Al}_x\text{Ga}_{1-x}\text{N}$ substrates $N_D \approx 1 \times 10^{17} \text{ cm}^{-3}$, leads to $V_n \approx 0.1 \text{ eV}$ for $x = 0.20$ and $x = 0.30$.

$\text{Al}_x\text{Ga}_{1-x}\text{N}$	$(E_F - E_V)_i$ (eV)	$(E_F - E_V)_b$ (eV)	Band bending (eV)
$x = 0.20$	3.18	3.70	0.52
$x = 0.30$	3.45	3.93	0.48

Table 6-5: Band bending at "clean" $\text{Al}_x\text{Ga}_{1-x}\text{N}$ surfaces before metallization. Indexes "i" and "b" stand for interface and bulk, respectively. $(E_F - E_V)_b$ was calculated using $(E_g)_{x=0.20} = 3.80 \text{ eV}$ and $(E_g)_{x=0.30} = 4.03 \text{ eV}$, as shown in equation [6-8]. $(E_F - E_V)_i$ was measured as described in figure 6-28.

The values for band bending shown in this table suggest a similar Fermi level pinning at the clean $\text{Al}_x\text{Ga}_{1-x}\text{N}$ surfaces ($x = 0.20$ and $x = 0.30$) subjected to the same surface treatment, in agreement with Bermudez *et al.*⁴¹. It also confirms the Schottky barrier is mainly caused by band bending prior to metallization.

The density of surface states can be calculated by taking an electron affinity of 3.59 eV and 3.79 eV for $\text{Al}_x\text{Ga}_{1-x}\text{N}$ ($x = 0.30$) and $\text{Al}_x\text{Ga}_{1-x}\text{N}$ ($x = 0.20$), respectively. However, the value of D_{SS} would not have a physical meaning and is likely to be related to the small difference between Ag work function and electron affinity used here compared to those reported used by Bermudez *et al.*⁴¹.

Results on $\text{Ni}/\text{Al}_x\text{Ga}_{1-x}\text{N}$ ($x = 0.20$) can not be interpreted by this model because Ni deposition to the surface induced a downward band bending which does not follow the Schottky-Mott prediction. As the surface was subjected to the same surface treatment as that for Ag contact, the fact that band bending was observed in the opposite direction of that predicted by the Schottky-Mott model calls for different model.

Metal - $\text{Al}_x\text{Ga}_{1-x}\text{N}$ Schottky Contacts

The unified defect model (UDM) was introduced by Spicer *et al.*⁴² and relies on the assumption that the Schottky barrier is caused by defects created near the semiconductor surface. Hence, according to this model, a wet chemical etch followed by a 600°C anneal induced defects at the $\text{Al}_{0.2}\text{Ga}_{0.8}\text{N}$ surface and caused a 0.87 eV downward band bending. Ni deposition induced defects and caused an additional 0.30 eV downward band bending.

Similarly, Ag/ $\text{Al}_x\text{Ga}_{1-x}\text{N}$ Schottky barrier formation can be interpreted within this model. The same surface treatment induced defects at the surface and caused a downward band bending of 0.87 eV and 0.99 eV at $\text{Al}_x\text{Ga}_{1-x}\text{N}$ ($x = 0.20$) and $\text{Al}_x\text{Ga}_{1-x}\text{N}$ ($x = 0.30$), respectively. Then, Ag deposition on the surface created additional defects and provoked an upward band bending of 0.30 eV and 0.40 eV at $\text{Al}_x\text{Ga}_{1-x}\text{N}$ ($x = 0.20$) and $\text{Al}_x\text{Ga}_{1-x}\text{N}$ ($x = 0.30$), respectively. Hence, according to this model, the created defects and/or activated/deactivated states caused the same effect on band bending at the two different surfaces.

The formation of the Schottky barrier of metal/ $\text{Al}_x\text{Ga}_{1-x}\text{N}$ contacts may also be interpreted in terms of metal-induced gap states (MIGS)^{43, 44} that might be in density sufficient enough to cause pinning of the Fermi level⁴⁵. The MIGS-and-electronegativity model⁴ was based on the concept of MIGS, considering that Schottky barrier height was also predicted to vary linearly as a function of the difference between the metal and the semiconductor electronegativities. According to this model, discussed in chapter 3, good agreement has been found on Ag/GaN⁴ and Au/GaN³¹ Schottky barrier heights by taking $S = 0.29$ eV/Miedema-unit and $\Phi_{bp} = 1.1$ eV.

Hence, according to the MIGS model, the different band bending observed after the deposition of Ag and Ni might be the result of the creation of MIGS at the metal- $\text{Al}_x\text{Ga}_{1-x}\text{N}$ interface, the magnitude of which depends on the metal. However, for Ag/ $\text{Al}_x\text{Ga}_{1-x}\text{N}$ ($x = 0.20$), the total band bending occurred after a deposition of only 0.5Å; whether this is a sufficient coverage for electron wavefunctions to form in the metal and decay into the semiconductor across this intimate interface is open to question.

6.5.4. Conclusions

The formation of Ag/ $\text{Al}_x\text{Ga}_{1-x}\text{N}$ contacts was investigated for $x = 0.20$ and $x = 0.30$ using XPS, AFM, and I-V measurements. Both contacts exhibited an unreacted, abrupt interface and showed no evidence of chemical reaction or intermixing between Ag and the substrate. Chemical shifts were observed on the Ag $3d_{5/2}$ core-level and were

attributed to chemical reactions with O and/or C left at the surface after pre-metallization surface treatment (HF etch followed by 600°C UHV annealing). Nevertheless, the reacted mixture was found to be rapidly buried as no change in Ag $3d_{5/2}$ binding energy position was observed after a metal thickness of 20 Å.

Ag was found to grow following the Stranski-Krastanov (SK) on $\text{Al}_x\text{Ga}_{1-x}\text{N}$ surfaces and was confirmed using AFM by the presence of islands at both metal covered surfaces. Increasing the Al concentration in the alloy induced slight deviations from this assumption, which was again witnessed with AFM by the different island shape and distribution.

The Ni/ $\text{Al}_{0.2}\text{Ga}_{0.8}\text{N}$ interface showed a much larger reacted interface compared to that of Ag/ $\text{Al}_{0.2}\text{Ga}_{0.8}\text{N}$, according to the chemical shifts observed in Ni $2p_{3/2}$. Similarly, it is suggested that Ni reacts with contaminants present at the surface, as no signs of chemical shifts were observed on substrate core-levels. XPS results also showed a SK growth mode of Ni on $\text{Al}_{0.2}\text{Ga}_{0.8}\text{N}$ surface. This was confirmed by small well-defined islands being found at the metal-covered surface using STM.

For Ag/ $\text{Al}_x\text{Ga}_{1-x}\text{N}$ contacts, the total upward band bending, measured from the clean surface to the last metal deposition, was 0.30 eV and 0.40 eV for $x = 0.20$ and $x = 0.30$, respectively. Ni/ $\text{Al}_{0.2}\text{Ga}_{0.8}\text{N}$ formation showed a 0.30 eV Fermi shift to higher binding energy. Schottky barrier parameters were extracted from XPS Fermi shifts and resulted in barrier heights of 0.92 eV and 0.98 eV for Ag/ $\text{Al}_{0.2}\text{Ga}_{0.8}\text{N}$ and Ag/ $\text{Al}_{0.3}\text{Ga}_{0.7}\text{N}$, respectively.

Transport measurements carried out on the N^+ bombardment followed by annealing (NBA) $\text{Al}_{0.3}\text{Ga}_{0.7}\text{N}$ surface resulted in an average barrier height of 0.77 eV, where the best diode had an ideality factor of 1.21 and a barrier height of 0.82 eV. It was suggested that the difference in barrier height was the consequence of the higher density of surface states produced by NBA, acting as tunnelling/recombination current lowering the barrier height.

Excellent agreement was found for Ag/ $\text{Al}_x\text{Ga}_{1-x}\text{N}$ XPS extrapolated barrier heights using the Schottky-Mott model. The results were discussed in the Cowley and Sze model which suggested that most of the Schottky barrier height was due to pre-metallization Fermi level pinning. Ni/ $\text{Al}_{0.2}\text{Ga}_{0.8}\text{N}$ could not be interpreted using this model because of the downward band bending induced after Ni deposition.

UDM and MIGS models were also put forward to interpret the formation of Ag and Ni on $\text{Al}_x\text{Ga}_{1-x}\text{N}$ surfaces at different Al mole fraction. It was suggested that the

creation and/or activation/deactivation of defects might be responsible for band bending after metal deposition. Finally, the investigation of metal/ $\text{Al}_x\text{Ga}_{1-x}\text{N}$ surfaces clearly showed the importance of pre-metallization surface treatment highlighted by the density of surface states that cause Fermi pinning at the surface.

References

1. K.A. Rickert, A.B. Ellis, Jong Kyu Kim, Jong-Lam Lee, F.J. Himpsel, F. Dwikusuma, T.F. Kuech, *J. Appl. Phys.* **92**(11), 6671, (2002).
2. J. Dumont, E. Monroy, E. Munoz, R. Caudado, R. Sporcken, *J. Cryst. Growth* **230**, 558, (2001).
3. A.C. Schmitz, A.T. Ping, M.A. Khan, Q. Chen, J.W. Yang, I. Adesida, *J. Electr. Mat.* **27**(4), (1998).
4. T. U. Kampen, W. Monch, *Appl. Surf. Sci.* **117/118**, 388, (1997).
5. C.C. Kim, S.K. Seol, J.K. Kim, J.-L. Lee, Y. Hwu, P. Ruterana, G. Magaritondo, J.H. Je, *Phys. Stat; Sol. (b)* **241** (12), 2771, (2004).
6. L.S. Yu, D.J. Qiao, Q.J. Xing, S.S. Lau, K.S. Boutros, J.M. Redwing, *Appl. Phys. Lett.* **73**(2), 238, (1998).
7. D. Qiao, L.S. Yu, S.S. Lau, J.M. Redwing, J.Y. Lin, H.X. Jiang, *J. Appl. Phys.* **87**(2), 801, (2000).
8. S.T. Bradley, S.H. Goss, J. Hwang, W.J. Schaff, L.J. Brillson, *J. Appl. Phys.* **97**, 084502, (2005).
9. Z. Lin, W. Lu, J. Lee, D. Liu, J. S. Flynn, G. R. Brandes, *Appl. Phys. Lett.* **82**(24), 4364, (2003).
10. T. Makimoto, M. Kashiwa, T. Kido, N. Matsumoto, K. Kumakura, N. Kobayashi, *Phys. Stat. Sol. (c)* **0** (7), 2393, (2003).
11. S.T. Bradley, S.H. Goss, J. Hwang, W.J. Schaff, L.J. Brillson, *Appl. Phys. Lett.* **85**(8), 1368, (2004).
12. E. Monroy, F. Calle, R. Ranchal, T. Palacios, M. Verdu, F.J. Sanchez, M.T. Montojo, M. Eickhoff, F. Omnes, Z. Bougrioua, I. Moerman, *Semicond. Sci. Technol.* **17**, L47, (2002).
13. V.M. Bermudez, R. Kaplan, M.A. Khan, J.N. Kuznia, *Phys. Rev. B* **48**(4), 2436, (1993).
14. S.-J. Cho, S. Dogan, S. Sabuktagin, M. A. Reshchikov, D.K. Johnstone, H. Morkoc, *Appl. Phys. Lett.* **84**(16), 3070, (2004).
15. M. Kocan, A. Rizzi, H. Luth, S. Keller, U.K. Mishra, *Phys. Stat. Sol. (c)* **234** (3), 773, (2002).
16. J.-M. Bethoux, P. Vennegues, F. Natali, E. Feltin, O. Tottereau, G. Nataf, P. De Mierry, F. Semond, *J. Appl. Phys.* **94**(10), 6499, (2005).
17. J.-M. Bethoux, P. Vennegues, *J. Appl. Phys.* **97**, 123504, (2005).
18. J.F. Moulder, W.F. Stickle, P.E. Sobol, K.D. Bomben, "Handbook of X-ray photoelectron spectroscopy", Parkin-Elmer, Eden Prairie, MN, (1994).
19. M.P. Seah, W.A. Dench, *Surf. Interface Anal.*, **1**, 2, (1979).
20. T. Conard, A.-C. Rousseau, L.M. Yu, J. Ghijsen, R. Sporcken, R. Caudano, R.L. Johnson, *Surf. Sci.* **359**, 82, (1996).
21. R. Sporcken, P.A. Thiry, E. Petit, J.J. Pireaux, R. Caudano, J. Ghijsen, R.L. Johnson, L. Ley, *Phys. Rev. B* **35**, 7927, (1987).
22. R. Sporcken, C. Silien, F. Malengrau, K. Grigorov, R. Caudano, F. J. Sánchez, E. Cajella, E. Munoz, B. Beaumont and P. Gibart, *MRS Internet J. Nitride Semicond. Res.* **2**, 23 (1997).
23. T.G.G. Maffei, M.C. Simmonds, S.A. Clark, F. Peiro, P. Haines, P.J. Parbrook, *J. Appl. Phys.* **92**(6), 3179, (2002).
24. "Practical Surface Analysis, 2nd Edition, Volume 1 - Auger and X-ray Photoelectron Spectroscopy", edited by D. Briggs and M.P. Seah, John Wiley and Sons (1990).

25. M.R.H. Khan, H. Nakayama, T. Detchprohm, K. Hiramatsu, N. Sawaki, *Solid-State Electronics* **41**(2), 287, (1997).
26. K.M. Tracy, P.J. Hartlieb, S. Einfeldt, R.F. Davis, E.H. Hurt, R.J. Nemanich, *J. Appl. Phys.* **94**(6), 3939, (2003).
27. S. Rajasingam, A. Sarua, M. Kuball, A. Cherodian, M.J. Miles, C.M. Younes, B. Yavich, W.N. Wang, N. Grandjean, *J. Appl. Phys.* **94**(10), 6366, (2003).
28. A. Nishiyama, G. ter ttorst , P.M. Zagwijn , G.N. van den Hoven, J.W.M. Frenken, F. Garten, A.R. Schlattmann, J. Vrijmoeth, *Surface Science* **320**, 229, (1996).
29. T. Muller, H. Nienhaus, *J. Appl. Phys.* **93**(2), 924, (2003).
30. Kehui Wu, Q. Z. Xue, R. Z. Bakhtizin, Y. Fujikawa, X. Li, T. Nagao, Q. K. Xue, T. Sakurai, *Appl. Phys. Lett.* **82**(9), 1389, (2003).
31. J. Dumont, R. Caudano, R. Sporcken, E. Monroy, E. Munoz, B. Beamont, P. Gibart, *MRS Internet J. Nitride Semicond. Res.* **5S1** W11.79, (2000).
32. S.P. Grabowski, M. Schneider, H. Nienhaus, W. Monch, R. Dimitrov, O. Ambacher, M. Stutzmann, *Appl. Phys. Lett.* **78**(17), 2503, (2001).
33. M.W. Wang, J.O. McCaldin, J.F. Swenberg, T.C. McGill, R.J. Hauenstein, *Appl. Phys. Lett.* **66**, 1974, (1995).
34. A. Motayed, A. Sharma, K.A. Jones, M.A. Derenge, A.A. Iliadis, S.N. Mohammad, *J. Appl. Phys.* **96**(6), 3286, (2004).
35. Y. Koyama, T. Hashizume, H. Hasegawa, *Solid-State Electronics* **43**, 1483, (1999).
36. T.G.G. Maffei, S.A. Clark, P.R. Dunstan, S.P. Wilks, D.A. Evans, F. Peiro, R. Riechert, P.J. Parbrook, *Phys. Status Solidi (a)* **176**, 751, (1999).
37. V.M. Bermudez, D.D. Koleske, A.E. Wickenden, *Appl. Surf. Sci.* **126**, 69, (1998).
38. V.M. Bermudez, *J. Appl. Phys.* **80**(2), 1190 (1996).
39. C.I. Wu, A. Kahn, N. Taskar, D. Dorman, D. Gallagher, *J. Appl. Phys.* **83**(8), 4249, (1998).
40. A. M. Cowley and S. M. Sze, *J. Appl. Phys* **36**, 3212, (1965).
41. V.M. Bermudez, *J. Appl. Phys.* **86**(2), 1170, (1999).
42. W.E. Spicer, I. Lindau, P. Skeath, C.Y. Su and P. Chye, *Physical Review Letters* **44**, 420, (1980).
43. V. Heine, *Physical Review A* **138**, 1689, (1965).
44. W. Monch, *J. Vac. Sci. Technol. B* **17**(4), 1867, (1999).
45. S.G. Louie, M.L. Cohen, *Physical Review B* **13**, 2461, (1976).

Chapter 7

Conclusion and Future Work

III-V nitrides have attracted a lot of interest in the last decade or so mainly because of their wide bandgaps and the possibility of tuning the bandgap by selecting the appropriate alloy. The demonstration and commercialisation^{1,2,3} of the first bright, blue GaN-based LED and LD have opened a new potential market worldwide. GaN-based applications range from optical devices such as blue and green LEDs, blue LDs, UV detection⁴, to high power high frequency devices⁵ and now represent economic reality with increasing market size⁶. In addition, new applications still need to be investigated such as spin-transport electronics (spintronics) in which the spin of charge carriers is exploited⁷. The full exploitation and reliability of these devices are however closely related to the quality of metal- $\text{Al}_x\text{Ga}_{1-x}\text{N}$ Schottky contacts. Hence, it is important to understand the precise mechanisms leading to the formation of Schottky barrier and the electron transport mechanisms across the metal-semiconductor interface.

Schottky contacts on GaN have been widely investigated during the last decade whereas contacts on $\text{Al}_x\text{Ga}_{1-x}\text{N}$ still need additional work. The discrepancies in Schottky

barrier heights, as discussed in chapter 2, may be linked to the pre-metallization surface treatment, the band bending of the clean surface prior metal deposition, the measurement technique or the quality of the substrate. The quality of $\text{Al}_x\text{Ga}_{1-x}\text{N}$ substrates is found to decay with increasing Al content x , according to dislocation density measurements⁸. Besides, removing oxide contaminants from $\text{Al}_x\text{Ga}_{1-x}\text{N}$ surface is found to be more difficult than for GaN, especially for high Al concentrations⁹. This was related to the difficulty in growing $\text{Al}_x\text{Ga}_{1-x}\text{N}$ which leads to the presence of cracks allowing O to move more easily^{10,11}.

The main goal of this research was to gain more understanding of Schottky contacts formation on $\text{Al}_x\text{Ga}_{1-x}\text{N}$ substrates. This was achieved through a combination of spectroscopic technique (XPS), scanning probe microscopy (AFM and STM) and electrical characterisation (I-V). Pre-metallization surface cleaning was also investigated in order to assess the electronic and structural changes that may occur at the surface and topsurface. This work was presented in two main parts; the influence of various cleaning techniques and UHV temperature annealing on $\text{Al}_x\text{Ga}_{1-x}\text{N}$ surfaces was discussed in chapter 5 while chapter 6 showed the results on Ag/ $\text{Al}_x\text{Ga}_{1-x}\text{N}$ and Ni/ $\text{Al}_x\text{Ga}_{1-x}\text{N}$ interface formation.

XPS study of $\text{Al}_x\text{Ga}_{1-x}\text{N}$ ($x = 0.20$ and 0.30) surfaces showed that a wet chemical etch in a HF solution followed by 600°C UHV annealing was found to be very effective in removing oxygen at the surface. This surface treatment also induced total Fermi shifts, measured between solvents-rinsed surface and the annealed surface, to higher binding energies where $\Delta E_F = +0.87\text{eV}$ and $\Delta E_F = +0.99\text{eV}$ for the $x = 0.20$ and $x = 0.30$ $\text{Al}_x\text{Ga}_{1-x}\text{N}$ surfaces, respectively, indicating a downward band bending.

The influence of temperature was investigated through an experiment where an $\text{Al}_x\text{Ga}_{1-x}\text{N}$ ($x = 0.20$) HF-etched surface was annealed under UHV up to 600°C , in increments of 100°C , and XPS scans were taken after each step, at normal emission and 60° off normal emission. Analysis of the peak ratios showed a re-ordering at the surface and subsurface as the temperature is increased: Ga and Al are moving deeper in the surface, whereas N goes to the top surface. The surface presented a contamination layer, even at high temperatures, mainly composed of C and oxides. In addition, Fermi level movement was observed when the temperature was increased. This was related to change in surface stoichiometry, creating surface states, and to the possible creation of vacancies being activated/deactivated by temperature annealing. Finally, atomic

hydrogen cleaning (AHC) was successfully used to produce $\text{Al}_x\text{Ga}_{1-x}\text{N}$ ($x = 0.20$) with a lesser degree of O and C contamination.

In chapter 6, the formation of Ag and Ni contacts on $\text{Al}_x\text{Ga}_{1-x}\text{N}$ substrates was mainly assessed with XPS. Ag and Ni were deposited in steps of increasing thickness, from sub-monolayer to thick coverage, on the HF etched followed by 600°C UHV annealed surfaces. XPS results suggested a SK (layer-by-layer followed by islanding) growth mode of Ag on $\text{Al}_x\text{Ga}_{1-x}\text{N}$ ($x = 0.20$ and 0.30) and Ni on $\text{Al}_x\text{Ga}_{1-x}\text{N}$ ($x = 0.20$). This was confirmed by the presence of Ag islands on the metal-covered $\text{Al}_x\text{Ga}_{1-x}\text{N}$ ($x = 0.20$ and 0.30) surfaces, as shown on the AFM study. STM images of Ni-covered $\text{Al}_x\text{Ga}_{1-x}\text{N}$ ($x = 0.20$) clearly showed small Ni islands, in agreement with the XPS study.

XPS measurements of the Fermi level position relative to the valence band maximum at the "clean" surface, together with Fermi shifts recorded between the "clean" surface and the last metal deposition led to the extraction of Schottky barrier heights. The total upward band bending, from the clean surface to the last Ag deposition, of 0.30 eV and 0.40 eV led to extracted barrier heights of 0.92 eV and 0.98 eV for Ag/ $\text{Al}_{0.2}\text{Ga}_{0.8}\text{N}$ and Ag/ $\text{Al}_{0.3}\text{Ga}_{0.7}\text{N}$, respectively. I-V measurements were carried out on Ag/ $\text{Al}_{0.3}\text{Ga}_{0.7}\text{N}$ diodes where the substrate was subjected N^+ bombardment followed by 600°C annealing (NBA) and yielded a barrier height $\Phi_B = 0.82$ eV with ideality factor $n = 1.21$ for the best diode. The difference between XPS and I-V barrier heights may be explained by the different pre-metallization surface treatment; NBA might induce a higher density of surface states which may, in turn, act as tunneling/recombination current lowering the barrier. Ag/ $\text{Al}_x\text{Ga}_{1-x}\text{N}$ were interpreted in terms of Cowley and Sze model as initial band bending of ≈ 0.5 eV was measured at $\text{Al}_x\text{Ga}_{1-x}\text{N}$ ($x = 0.20$ and 0.30), and Fermi shifts followed the Schottky-Mott model. This reinforced the possibility that Schottky barrier heights were significantly caused by band bending prior metal deposition and further highlighted the role of pre-metallization surface treatment. Ni deposition on $\text{Al}_x\text{Ga}_{1-x}\text{N}$ substrates ($x = 0.20$) caused a 0.3 eV downward band bending between the clean surface and the last metal deposition. UDM and MIGS models were also put forward to interpret the formation of Ag and Ni on $\text{Al}_x\text{Ga}_{1-x}\text{N}$ surfaces.

Additional work is still needed in order to fully understand Schottky contact formation on $\text{Al}_x\text{Ga}_{1-x}\text{N}$. The difficulty found in growing these alloys, especially for high Al concentration, results in the formation of structural defects and cracks at the surface. This is found to have a crucial influence on surface contamination. Hence, it is

more difficult to compare and identify mechanisms of Schottky barrier formation for substrates with different Al content as they might have different defect densities. If the substrate quality could be kept identical for different Al contents, it would be interesting to assess the evolution of the barrier height with increasing Al concentration of the alloy. Besides, the relatively low Ni/Al_{0.2}Ga_{0.8}N barrier height extrapolated from XPS Fermi shifts calls for further investigation. Alternative electrical techniques such as I-V, capacitance-voltage (C-V) or scanning tunnelling spectroscopy (STS) could be used in order to compare the average XPS barrier height to more local barrier measurements.

References

1. S. Nakamura, N. Iwasa, M. Senoh, T. Mukai, *Jpn. J. Appl. Phys.* **31**, 1258, (1992).
2. S. Nakamura, T. Mukai, M. Senoh, *Appl. Phys. Lett.* **64**, 1687, (1994).
3. S. Nakamura, S. Pearton, G. Fasol, "The Blue Laser Diode. The Complete Story", 2nd Ed., Springer, Berlin, (2000).
4. E. Munoz, E. Monroy, J.L. Pau, F. Calle, F. Omnes, P. Gibart, *J. Phys.: Condens. Matter* **13**, 7115, (2001).
5. M.S. Shur, R. Gaska, B. Bykhovski, *Solid-State Electronics* **43**, 1451, (1999).
6. J.Y. Duboz, *Phys. Stat. Sol. (a)* **176**, 5, (1999).
7. S.J. Pearton, C.R. Abernathy, M.E. Overberg, G.T. Thaler, A.H. Onstine, B.P. Gila, F. Ren, B. Lou, J. Kim, *Materialstoday*, 24, June 2002.
8. J.-M. Bethoux, P. Vennegues, F. Natali, E. Feltin, O. Tottereau, G. Nataf, P. De Mierry, F. Semond, *J. Appl. Phys.* **94**(10), 6499, (2003).
9. H. Nienhaus, M. Schneider, S.P. Grabowski, W. Monch, R. Dimitrov, O. Ambacher, M. Stutzmann, *Mat. Res. Soc. Symp. Proc.* **680E**, E4.5.1, (2001).
10. S. Rajasingam, A. Sarua, M. Kuball, A. Cherodian, M.J. Miles, C.M. Younes, B. Yavich, W.N. Wang, N. Grandjean, *J. Appl. Phys.* **94**(10), 6366, (2003).
11. S.P. Grabowski, M. Schneider, H. Nienhaus, W. Monch, R. Dimitrov, O. Ambacher, M. Stutzmann, *Appl. Phys. Lett.* **78**(17), 2503, (2001).